Missouri S&T Library and Learning Resources

Scholars' Mine

Doctoral Dissertations | Student Theses and Dissertations

Summer 2020

# Bond behavior of advanced fiber reinforced composite-concrete joints

Xingxing Zou

Follow this and additional works at: https://scholarsmine.mst.edu/doctoral_dissertations

 Part of the Civil Engineering Commons

Department: Civil, Architectural and Environmental Engineering

## Recommended Citation

Zou, Xingxing, "Bond behavior of advanced fiber reinforced composite-concrete joints" (2020). *Doctoral Dissertations*. 2928.
https://scholarsmine.mst.edu/doctoral_dissertations/2928

This thesis is brought to you by Scholars' Mine, a service of the Missouri S&T Library and Learning Resources. This work is protected by U. S. Copyright Law. Unauthorized use including reproduction for redistribution requires the permission of the copyright holder. For more information, please contact scholarsmine@mst.edu.

# BOND BEHAVIOR OF ADVANCED FIBER REINFORCED COMPOSITE-CONCRETE JOINTS

by

XINGXING ZOU

A DISSERTATION

Presented to the Faculty of the Graduate School of the

MISSOURI UNIVERSITY OF SCIENCE AND TECHNOLOGY

In Partial Fulfillment of the Requirements for the Degree

DOCTOR OF PHILOSOPHY

in

CIVIL ENGINEERING

2020

Approved by:

Dr. Lesley H. Sneed, Advisor
Dr. Genda Chen
Dr. Mohamed A. ElGawady
Dr. Guirong (Grace) Yan
Dr. Kristen M. Donnell

© 2020

Xingxing Zou

All Rights Reserved

## PUBLICATION DISSERTATION OPTION

This dissertation consists of the following five articles, formatted in the style used by the Missouri University of Science and Technology:

Paper I, found on pages 8-42, has been published in the Journal of Materials in Civil Engineering (American Society of Civil Engineers (ASCE)).

Paper II, found on pages 43-87, has been published in the Journal of Composite Structures (ELSEVIER).

Paper III, found on pages 88-123, has been published in the International Journal of Concrete Structures and Materials (SPRINGER).

Paper IV, found on pages 124-160, has been submitted to submission to the Journal of Composites Part B: Engineering (ELSEVIER).

Paper V, found on pages 161-186, is intended for submission to the Journal of Composites Part B: Engineering (ELSEVIER).

## ABSTRACT

Externally bonding advanced composite materials to concrete structures is an effective way to improve their strength, ductility, and durability. The interfacial bond behavior is fundamental to understand the overall structural performance of concrete structures strengthened with advanced composite materials. This study includes a comprehensive investigation of the bond behavior of composite-concrete joints with different fiber reinforced composite types. First, a direct approach to determine the bond-slip relationship for fiber reinforced cementitious matrix (FRCM)-concrete joints based on fiber strain measurements was proposed. Then, an analytical solution to predict the full-range response of FRCM-concrete joints was derived by assuming a trilinear bond-slip relationship. The analytical results were compared with experimental load responses to indirectly determine the bond-slip relationship. Next, the experimental load response of steel fiber reinforced polymer (SRP)-concrete joints was explored by single-lap direct shear tests. Lastly, a novel non-destructive evaluation method – active microwave thermography – was used to detect the existence of initial interfacial defects in carbon fiber reinforced polymer (CFRP)-concrete joints, and to monitor the progressive debonding between CFRP and concrete.

# ACKNOWLEDGMENTS

First of all, I would like to express my sincere gratitude to my supervisor Dr. Lesley Sneed. Her great support, patient guidance, and insightful views in this field have encouraged my study and research. She creates a comfortable and efficient academic atmosphere which inspires my motivation to study throughout the Ph.D. program.

I would also like to thank my committee members, Drs. Genda Chen, Mohamed ElGawady, Guirong (Grace) Yan, and Kristen Donnell for their valuable suggestions and guidance. My thanks also go to Prof. Tommaso D'Antino and Prof. Christian Carloni for their enlightening discussions and constructive contribution to the first two papers.

Many thanks and appreciation also go to the staff in the High Bay Structural Engineering Research Lab at Missouri S&T, including Gary Abbott, John Bullock, Brian Swift, and Greg Leckrone. My colleagues Ali Mirala, Christopher Moore, Keenan McBurney, Sarah Jemison, Nikkolas Edgmond, Giacomo Fraioli, Lia Vanzant, Daniel Bishof, Liang Fan, and Le Teng also helped me a lot throughout my experimental work. The following friends of mine are highly appreciated: Jianqiao Leng, Haibin Zhang, Xinzhe Yuan, Zhaochao Li, Yi Bao, Mohanad Abdulazeez, and Eslam Gomaa.

I am extremely grateful to my parents and my sister for their spiritual support. My special thanks go to my wife, Qing Tang, for her support, love, and cooking skills.

This project was partially funded by the National Science Foundation (NSF) Electrical, Communication, and Cyber Systems (ECCS) Award 1609470, and some of the composite material was donated by Kerakoll S.p.A. of Sassuolo, Italy. This financial and donation support is highly appreciated.

# TABLE OF CONTENTS

# LIST OF ILLUSTRATIONS

PAPER I



PAPER II

PAPER III

PAPER V

# LIST OF TABLES

# SECTION

# 1. INTRODUCTION

## 1.1. BACKGROUND

Numerous civil structures all over the world are currently in need of strengthening to prolong their service lives. The high strength-to-weight ratio and good chemical resistance make fiber reinforced composites such as fiber reinforced polymer (FRP) and fiber reinforced cementitious matrix (FRCM) composites attractive materials to repair, retrofit, strengthen, and rehabilitate concrete structures. In such applications, the composites are typically externally bonded to the structure by a polymeric or cementitious matrix. The interfacial bond plays a pivotal role in obtaining composite action between the FRP/FRCM composite and the substrate, which is required for load sharing.

Carbon and glass FRP (CFRP and GFRP), with organic polymer matrix (usually epoxy or polyester resin), have been widely used to strengthen existing concrete buildings and bridges. However, interfacial debonding between the FRP and concrete substrate can considerably weaken the composite action, limiting the effectiveness of the composite and resulting in an undesirable failure mode. It has been well documented that debonding of FRP-concrete joints tested in direct shear typically occurs due to fracture of the concrete within a thin layer directly beneath the composite. However, other debonding failure modes are possible depending on the composite and substrate materials employed. For example, in the case of FRCM composites, with inorganic mortar matrix, the predominant failure mode observed for FRCM-concrete joints with a single fiber layer is slippage of the fiber bundles with respect to the matrix. In general, experimental results reported in the literature

show that debonding of fiber reinforced composite-concrete joints can occur: (a) within the concrete substrate (cohesive failure), (b) at the concrete-composite interface (detachment), (c) at the fiber-matrix interface, (d) within the matrix (matrix delamination), or (e) with a combination of these failure modes. Thus, it is critical to understand the bond behavior of the composite system employed and the factors that influence it.

While FRP composites are commonly used in many strengthening applications, poor vapor compatibility with existing structures, low heat resistance, and susceptibility to UV rays have weakened the competitiveness of FRP systems in some cases. One solution to avoid these disadvantages is to use FRCM composite systems, a relatively new type of composite that typically consists of a fabric mesh with continuous fibers that is bonded to the substrate with a cementitious mortar. This type of composite has also been referred to as textile reinforced concrete (TRC), textile reinforced mortar (TRM) and inorganic matrix composites in the recent literature. As mentioned above, the debonding failure mode and mechanisms of FRCM-concrete joints are different from those of FRP-concrete joints, owing to the inorganic matrix. Thus, bond-slip $\tau(s)$ relationships for FRP-concrete joints may not be applicable, and the FRCM-concrete bond-slip relationship must be investigated. Generally, the FRCM-concrete bond-slip relationship has been characterized with a constant residual shear stress by adding a contribution of friction and interlocking to form the relationship that has a non-zero residual shear stress. The parameters of the FRCM-concrete bond-slip relationship could be determined by measuring the longitudinal strain in the fibers along the composite bonded length. However, few studies have accomplished this successfully, since the presence of the mortar matrix makes the strain measurement difficult. Therefore, alternative approaches to determine the bond-slip $\tau(s)$ relationship of

FRCM-concrete joints based on the global load response should be explored. Furthermore, a closed-form solution of the $\tau(s)$ relationship is desirable to provide the basis for analytical and numerical simulations of FRCM-strengthened members.

Another new type of composite that has shown promise in structural strengthening applications is steel reinforced polymer (SRP). SRP comprises high tensile strength steel fiber cords and a polymeric resin. SRP has been shown to exhibit comparable, or even better, tensile and bond behavior than CFRP (Ascione et al. 2017), and when applied as flexural reinforcement or for confinement, provides equivalent or higher improvement of structural performance in terms of load bearing and displacement capacity (Figeys et al. 2008). Unlike the fibers used in traditional FRP (namely carbon and glass), steel fiber cords can be bent around members to conform to sharp corners of rectangular cross sections (Mukhtar and Faysal 2018). However, the fundamental bond behavior of SRP-concrete joints is an open issue that has not been fully investigated and must be characterized before it can be used effectively and efficiently.

In many external strengthening applications, the fiber reinforced composite is installed in situ using a wet-layup procedure. Surface irregularities, material inhomogeneities, inadequate curing, and/or poor workmanship can result in voids or flaws along the composite-concrete interface, which in turn can interrupt the bond. In addition, many studies have reported that environmental conditions of FRP-strengthened concrete buildings and bridges can cause interfacial debonding (Cromwell et al. 2011, Tuakta and Büyüköztürk 2011). Interfacial voids, flaws, and debonding can be challenging to detect since they cannot be visually identified from the external surface of the composite. Thus, methods are needed to detect the presence of composite-concrete interfacial defects.

Nondestructive evaluation (NDE) methods, such as surface acoustic waves (Mahmoud et al. 2010), guided waves (Li et al. 2017), ground-penetrating radar (Yazdani et al. 2019), and infrared thermography (Yazdani et al. 2019, Shih et al. 2003) have been used to determine whether CFRP layers are well bonded and to detect possible interfacial imperfections. Active thermography is an inspection method that has shown promise to detect interfacial imperfections hidden internally within structures in the form of defects, flaws, and debonding. Active thermography generally includes the following steps: (i) utilizing an external heat excitation to penetrate a certain thickness in structures, (ii) capturing the thermal field on the outer surface of the structure with a thermal camera, and (iii) correlating the surface temperature with the inner imperfections. Several electromagnetic thermography techniques have been developed including eddy current (He et al. 2014), induction (Genest and Li 2018), and microwave (Mirala et al. 2018). Among these heating methods, the combination of microwave heating and subsequent thermography is referred to as active microwave thermography (AMT). AMT has been used successfully to inspect flat-bottom holes (FBHs) underneath CFRP sheets (Mirala et al. 2018), covered surface cracks in metal structures (Foudazi et al. 2018), and chopped steel fiber distribution in cementitious materials (Foudazi et al. 2016). Since debonding of the composite involves the formation of an interfacial crack, methods that can detect deflects and flaws could also be used to detect damage due to the initiation and propagation of debonding, thus enabling further study of the debonding phenomenon. Such methods could also be used to study how initial defects influence the initiation and propagation of debonding.

In summary, the effective application of the FRP/FRCM strengthening technique requires the knowledge of the complex bond behavior. To date, the bond behavior of FRP/FRCM composites bonded to a concrete substrate has been studied intensively, but there are still some challenges including, but not limited to:

1. Describing the bond-slip relationship of the FRP/FRCM composite-concrete interface to provide the basis for analytical evaluation and numerical simulation of FRP/FRCM-strengthened members.

2. Characterizing the bond behavior of new fiber reinforced composite systems with alternative fiber and/or matrix types.

3. Detecting interfacial damage along the composite-concrete interface.

4. Understanding how defects along the composite-concrete interface affect the bond behavior of fiber reinforced composites.

## 1.2. OBJECTIVE AND SCOPE OF WORK

The overarching objective of this work was to explore the bond behavior of the fiber reinforced composite-concrete interface. Experimental, analytical, and numerical studies were carried out to achieve this objective. In particular, the scope of work included the following:

1. The bond-slip $\tau(s)$ relationship for FRCM-concrete joints that exhibit debonding at the fiber-matrix interface was determined using direct measurements of strain along the composite bonded length. A closed-form solution of the bond-slip relationship was determined to provide the basis for analytical and numerical simulations of FRCM-strengthened members;

2. A method was developed to determine the nonlinear debonding process of composite-concrete joints based on global load response measurements (i.e., in the absence of strain measurements). The method developed can be applied to either FRP or FRCM composites.

3. The bond behavior of newly developed steel-reinforced polymer (SRP) composite was studied. The bond-slip $\tau(s)$ relationship of SRP-concrete was determined based on global load response measurements, and the maximum transferrable load and effective bond length were determined.

4. The initiation and propagation of debonding along the CFRP-concrete interface was explored using time-history NDE with AMT.

5. The effect of interfacial flaws on the bond behavior of CFRP bonded to concrete was studied using AMT.

## 1.3. RESEARCH SIGNIFICANCE

The importance of the work presented in this dissertation is to understand the fundamental bond behavior between advanced composite materials and concrete. When composite systems are externally bonded to existing structural members, the stress transfer is accomplished through fiber-matrix and matrix-substrate bonding (Brückner et al. 2008; Awani et al. 2015; Donnini et al. 2017). However, for many composite-strengthened members, premature interfacial debonding occurs that can result in failure of the member. Therefore, it is of pivotal significance to the design of composite-strengthened members to determine the degree of composite action between the composite and the substrate.

## 1.4. DISSERTATION ORGANIZATION

This dissertation includes three sections. Section 1 gives a brief introduction to the subject area and explains the need for the current research study. The first section also presents the overarching objective and scope of work of the investigation.

Section 2 presents the results of this study in the form of five manuscripts: two published journal papers, one journal paper under review, and two that will be submitted for review. The first paper presents a strain measurement based approach to determine the bond-slip relationship $\tau(s)$ for fiber reinforced cementitious matrix (FRCM)-concrete joints. The second paper presents an analytical solution of the full-range response of shear test of FRCM-concrete joints was derived by using a trilinear $\tau(s)$. The approach is also valid for FRP-concrete joints. The third paper presents an experimental and analytical study on the load response of steel fiber reinforced polymer (SRP)-concrete joints. The fourth paper presents a novel non-destructive evaluation method – active microwave thermography, and explores the feasibility of using AMT to conduct time-history monitoring of the bond behavior of CFRP-concrete joints. The fifth paper presents the results of a study in which AMT was to detect the existence of initial defects in the CFRP-concrete interface, and to monitor the progressive debonding of CFRP-concrete joints with initial defects.

Section 3 summarizes the findings and conclusions of this study and proposes future research.

# PAPER

## I. ANALYTICAL BOND-SLIP MODEL FOR FIBER REINFORCED CEMENTITIOUS MATRIX-CONCRETE JOINTS BASED ON STRAIN MEASUREMENTS

Xingxing Zou, Lesley H. Sneed, Tommaso D'Antino, and Christian Carloni

## ABSTRACT

An accurate bond-slip model is of fundamental importance to analyze the response of fiber reinforced cementitious matrix (FRCM) composite-strengthened structures. This study proposes a method to determine the bond-slip model of FRCM-concrete joints based on longitudinal fiber strains. First, discrete strain profiles measured with strain gauges were fitted by a continuous function $\varepsilon(y)$, where $y$ is the coordinate along the bonded length. Then, the slip $s(y)$ and shear stress $\tau(y)$ along the composite bonded length were obtained by integration and derivation of $\varepsilon(y)$, respectively. The debonding load and peak load from single-lap direct shear specimens were predicted by the fitted function $\varepsilon(y)$ and showed good agreement with test results. From the plot of the $\tau(s)$ relationship obtained from $\varepsilon(y)$, an alternative, closed-form, continuous bond-slip relationship was obtained based on the maximum shear stress $\tau_m$ and the corresponding slip $s_m$. The fracture energy was compared for both relationships and was in reasonable agreement with values reported in previous studies.

**Keywords:** Bond-slip model, debonding, fiber reinforced cementitious matrix (FRCM) composite, fracture energy, strain profile, stress transfer.

# 1. INTRODUCTION

Numerous civil structures all over the world are currently in need of strengthening to prolong their service lives. The high strength-to-weight ratio and good chemical resistance make fiber reinforced composites an attractive material to repair, retrofit, strengthen, and rehabilitate civil engineering structures (Teng et al. 2002; Hollaway 2010). Organic polymers, which exhibit good bond properties with masonry and concrete substrates, have been widely used as the matrix and bonding adhesive for fiber reinforced polymer (FRP) composites. However, poor vapor compatibility with existing structures, low heat resistance, and susceptibility to ultraviolet (UV) rays have weakened the competitiveness of FRP systems in some situations. One of the solutions to avoid the disadvantages of FRP composites is to replace the organic matrix with an inorganic (usually cementitious) matrix. Inorganic matrix composite materials have been referred to in the literature by different names including fiber or fabric reinforced cementitious matrix (FRCM) composites (ACI Committee 549, 2013), textile reinforced mortar (TRM) (Bournas et al. 2007), textile reinforced concrete (TRC) (Brückner et al. 2008), and mineral based composites (MBC) (Blanksvärd et al. 2009). In this paper, inorganic matrix composites will be referred to as FRCM composites. The feasibility of using FRCM composites to strengthen concrete and masonry structures has been explored in laboratory tests and in-situ field applications (e.g., Trapko 2013; Azam and Soudki 2014; Alecci et al. 2016).

FRCM composite systems typically consist of a fabric mesh with continuous fibers oriented along two orthogonal directions and bonded to the substrate with a cementitious mortar. Different fiber types have been studied including carbon, glass, basalt, and

polyparaphenylene benzobisoxazole (PBO). PBO FRCM composite, which is considered in the present study, has proven able to increase the flexural, shear, and torsional strength of reinforced concrete (RC) members in laboratory tests (e.g., D'Ambrisi et al. 2013; Babaeidarabad et al. 2014; Gonzalez-Libreros et al. 2017; Alabdulhady et al. 2017; Wakjira and Ebead 2018). When FRCM systems are externally bonded to existing structural members, the stress transfer is accomplished through fiber-matrix and matrix-substrate bond (Brückner et al. 2008; Awani et al. 2015; Donnini et al. 2017). However, for many FRCM-strengthened members, premature interfacial debonding occurs that could result in failure of the member. Therefore, it is of pivotal significance to the design of FRCM-strengthened concrete members to determine the degree of composite action between the FRCM and concrete. It is worth noting that in most strengthening applications, the composite is generally designed considering a pure Mode II condition and the fibers acting in tension only. Mode I effects should be prevented in practice (e.g., by using anchorage) or the contribution of the composite neglected depending on the direction of action.

Unlike FRP-concrete joints, in which interfacial crack propagation typically occurs within a thin layer of substrate beneath the bonded composite, the predominant failure mode observed in PBO FRCM-concrete or -masonry joints with one layer of fiber mesh is debonding at the matrix-fiber interface characterized by slippage of the fiber bundles with respect to the embedding matrix (D'Ambrisi et al. 2012; D'Antino et al. 2014; Sneed et al. 2015; Alecci et al. 2016). Similar results have been observed for carbon FRCM-concrete or -masonry joints (Ombres et al. 2017; Younis and Ebead 2018). Results have shown that the mechanical properties of the substrate may not play a significant role in the mechanical response of PBO FRCM-concrete joints (D'Antino et al. 2015; Gonzalez-Libreros et al.

2017). A fracture mechanics approach, based on pure Mode-II fracture, has been used to study the debonding phenomenon in single-lap direct shear test setups of PBO FRCM-concrete joints (D'Antino et al. 2014). Assuming a zero-thickness interface, the interfacial bond behavior can be described by introducing a bond-slip relationship between the interfacial shear stress and the relative slippage of the contact surfaces.

Analogously to some studies on FRP-concrete joints, a direct method to determine the bond-slip relationship based on fiber longitudinal strains measured along the composite bonded length has been applied to FRCM-concrete joints (D'Antino et al. 2014). However, measuring fiber strains in FRCM composites is a more difficult task compared with FRP systems because for FRCM composites the fibers are usually covered by an external layer of cementitious matrix that is relatively thick (approximately 2-4 mm). Since fiber slippage occurs relative to the embedding matrix, values of strain determined on the matrix surface are not representative of those in the fibers (Sabau et al. 2017). Therefore, fiber strains in FRCM composites were generally measured by attaching strain gauges onto the fiber bundles of FRCM composite strips either with (D'Ambrisi et al. 2012) or without (Carloni et al. 2014; Sneed et al. 2014) the external matrix layer. Digital image correlation (DIC) technique has also been used in an attempt to detect the slip and strain field of FRCM-substrate joints (D'Antino et al. 2016; Bilotta et al. 2017; Sabau et al. 2017; Caggegi et al. 2018). An indirect method to calibrate the bond-slip relationship of FRCM-concrete joints, based on the values of the peak load measured in direct shear tests with different composite bonded lengths, was also proposed (Focacci et al. 2017).

D'Antino et al. (2014) proposed Eq. (1) for curve fitting longitudinal strain profiles obtained from strain measurements along the fibers in PBO FRCM-concrete joints, where

Eq. (1) was obtained from a modification of a function used for FRP-concrete joints (Carloni and Subramaniam 2012) to take into account the presence of friction between fiber filaments and between fibers and matrix observed in the experimental tests:

$$\varepsilon(y) = \varepsilon_0 + \frac{\alpha + ky}{1 + e^{-(y-y_0)/\beta}} \quad (1)$$

In Eq. (1), $y$ is the distance along the composite bonded length with the origin at the free end of the bonded area, $\varepsilon_0$, $\alpha$, $\beta$, and $y_0$ are parameters determined using nonlinear regression analysis of the measured strains, and $k$ is a parameter that depends on the contribution of friction. The derivative of Eq. (1) can be used to compute the shear stress $\tau(y)$. However, the integral of Eq. (1), which provides the interfacial slip $s(y)$, cannot be obtained in a closed-form solution. Therefore, an alternative equation that can accurately describe the strain profile and that can be analytically integrated is desirable in order to determine both the $\tau(y)$ and $s(y)$ functions. Furthermore, a closed-form solution of the bond-slip relationship $\tau(s)$ is desirable to provide the basis for analytical and numerical simulations of FRCM-strengthened members. This paper attempts to address these needs using the analytical approach described in the following section.

## 2. OBJECTIVE AND APPROACH

The present study proposes a method to determine the bond-slip relationship of FRCM-concrete joints that fail due to debonding at matrix-fiber interface and determines expressions to predict key values of the load and slip based on discrete measurements of longitudinal fiber strain. Experimental results from single-lap shear test specimens of PBO FRCM-concrete joints with strain gauges mounted to the longitudinal fiber bundles along

the composite bonded length were used to calibrate the model. The paper is organized in the steps summarized below. Notation used is defined in the Notation section.

Step 1: fit the discrete strain profiles at the debonding load $P_{deb}$ of specimens equipped with strain gauges with a continuous function $\varepsilon(y)$;

Step 2: compute the slip $s(y)$ and shear stress $\tau(y)$ functions from integration and derivation of $\varepsilon(y)$, respectively;

Step 3: determine key values of the load and slip using the functions defined in Steps 1~ 2, and assess their accuracy using test data from additional specimens without strain gauges;

Step 4: combine the $\tau(y)$ and $s(y)$ functions to determine a bond-slip relationship $\tau(s)^{Eq.2}$ and obtain the maximum shear stress $\tau_m$ and corresponding slip $s_m$ values from the $\tau(y)$ and $s(y)$ functions;

Step 5: develop an alternative, closed-form, continuous, two-parameter bond–slip relationship $\tau(s)^{Eq.17}$ using $\tau_m$ and $s_m$ determined in Step 4;

Step 6: validate the relationship $\tau(s)^{Eq.17}$ by comparing it with $\tau(s)^{Eq.2}$; and

Step 7: determine the fracture energy from $\tau(s)^{Eq.2}$and $\tau(s)^{Eq.17}$ and compare the values with values reported in the literature (Carloni et al. 2014).

## 3. PREVIOUS EXPERIMENTAL RESULTS

Experimental results of single-lap direct shear tests presented by Carloni et al. (2014) were employed in this paper to calibrate a bond-slip relationship of PBO FRCM-concrete joints. All specimens included a concrete prism with a strip of PBO FRCM composite bonded to the surface. One layer of fibers was embedded within two layers of matrix for most of the specimens, whereas the external layer of matrix was omitted for

certain specimens to study the role of each matrix layer. The individual longitudinal bundles in the fiber net had a thickness $t_f$ = 0.092 mm, assuming a rectangular cross-section of the fiber bundle with a nominal width $b^*$=5 mm. Mechanical properties of the fibers, matrix, and concrete are reported in D'Antino et al. (2014).

Two linear variable displacement transformers (LVDTs) were mounted on the concrete surface, one on each side of the composite strip near the loaded end, and reacted off of a thin aluminum Ω-shaped plate attached to the bare fibers just outside the bonded area. The average of the two LVDT measurements, which is defined as global slip $g$ and assumed equal to the fiber loaded end slip in this paper, was used to control the tests. The test setup is illustrated in Figure 1. Strain gauges were attached to the central fiber bundle along the bonded length of certain specimens to measure the strain distribution in the direction of the applied load. The strain gauge locations are identified in D'Antino et al. (2014). Additional information on the experimental tests is provided in Carloni et al. (2014).

Specimens were named as DS_X_Y_(L, S, T, and/or D)_$Z^{(T)}$, where X is the composite bonded length ℓ (in mm) (shown in Figure 1), Y is the composite bonded width $b_1$ (in mm), L (if present) indicates that the external layer of matrix was omitted, S (if present) indicates that strain gauges were mounted onto the longitudinal fiber bundles, T (if present) indicates that the transversal fiber bundles were removed from the fiber net before applying the matrix, D (if present) indicates that the test was conducted until a constant applied load due to friction only was attained, Z is the specimen number of replicate specimens, and superscript T (if present) indicates that the fiber net was oriented with the transversal fiber bundles placed toward the concrete prism.

Fifty-one of the 79 specimens reported in Carloni et al. (2014) are considered in the present study. Specimens selected from Carloni et al. (2014) include seven FRCM-concrete joints that had strain gauges, whereas fiber strains were not measured for the remaining 44 FRCM-concrete joints considered. Only specimens that had a relatively uniform distribution of the applied load among the fiber bundles as described in Carloni et al. (2014) were considered in this paper. Specimens without the external matrix layer with the transversal fiber bundle oriented towards the concrete prism were not considered because their behavior was affected by the orientation of the fiber net (Carloni et al. 2014). Table A1 lists the specimens included in the present study.

The applied load $P$ - global slip $g$ response obtained for the seven specimens with strain gauges, listed in Table 1, is plotted in Figure 2. The experimental results show a wide scatter, which has also been reported for different FRCM composites (De Felice et al. 2014). Distinct stages of the $P$ - $g$ response were identified in D'Antino et al. (2014) for specimens with bonded lengths longer than the effective bond length $l_{eff}$, defined as the minimum length required to develop the load-carrying capacity of the interface. Herein the effective bond length is evaluated from the strain profiles along the bonded length by measuring the distance between the two points of the strain profiles in which the derivative is equal to zero at the free end and the derivative is constant at the loaded end (D'Antino et al. 2015). The idealized load response (D'Antino et al. 2014) is shown in Figure 3. The first stage is defined as an initial linear branch (OA). After the linear branch, the idealized $P$ - $g$ curve becomes nonlinear due to interface micro-damage until debonding at $P=P_{deb}$ (point B), where the zone in which the stress is transferred from the embedded fibers to the matrix, i.e., the stress transfer zone (STZ), is fully established. Next, a near-linearly

ascending branch occurs (BC) until the peak load is reached ($P=P^*$). The increase in applied load between points B and C is the result of friction that occurs in the debonded area of the composite as the STZ self-translates toward the free end of the composite. After the peak load is reached, which is assumed to occur when the STZ has reached the free end, the applied load decreases until the bond mechanism is no longer present (point D). The final branch (DE) represents a constant applied load associated with friction (matrix-fiber interlocking). Due to the presence of friction, bond-slip models developed for FRP-concrete joints are generally not applicable to FRCM-concrete joints.

## 4. ANALYTICAL APPROACH

### 4.1. ANALYTICAL STRAIN PROFILE

For the case of composite bonded length equal to or longer than the effective bond length, i.e., $\ell \geq l_{eff}$, the longitudinal strain profiles can be approximated by Eq. (2), which is a modified version of Eq. (1):

$$\varepsilon(y) = \frac{\alpha}{1 + e^{-(y-y_0)/\beta}} + ky \tag{2}$$

where $y$ is the location along the composite bonded length from the beginning of the fully established STZ (see Figure 1). Eq. (2) is strictly valid for $y \geq 0$. Similar to Eq. (1), $\alpha$, $\beta$, and $y_0$ are parameters determined using nonlinear regression of the measured strains.

There are three differences between Eq. (2) and Eq. (1), namely:

(i) Unlike in Eq. (1), the term $ky$ is not coupled with the term $\frac{\alpha}{1+e^{-(y-y_0)/\beta}}$ in Eq. (2), which allows for a closed-form integral of Eq. (2).

(ii) The origin of the *x*-*y* coordinate system considered for Eq. (2) does not have a fixed position during the loading process. When the applied load is equal to the debonding load (i.e., $P = P_{deb}$), the origin of the *y* axis is located a distance $l_{eff}$ from the loaded end (i.e., $y = l_{eff}$ corresponds to the loaded end of the bonded composite). After debonding occurs, with further increase of the global slip the STZ self-translates towards the composite free end together with the *x*-*y* coordinate system origin. Accordingly, Eq. (2) describes the strain response of the bonded composite along the STZ and the debonded region. Alternatively, an *x*-*y* coordinate system with a fixed origin could be employed, but it complicates the equations and therefore was not adopted in this paper. The strain profile associated with the debonding load is the only profile needed to determine all parameters in Eq. (2) using nonlinear regression. Analytically, the origin moves to the free end when the peak load is obtained. However, since only one strain profile is needed to obtain the fitting results of $\alpha$, $\beta$, and $y_0$, only the debonding load is used.

(iii) The term $\varepsilon_0$ in Eq. (1) is not included in Eq. (2), which results in one fewer parameter needed. In Eq. (1), $\varepsilon_0$ vertically translates the strain distribution associated to the STZ. Neglecting this term entails for a nonzero strain at the beginning at the STZ. However, this does not significantly affect the accuracy of the results obtained because values of $\varepsilon_0$ are generally much smaller than values of strain at the composite loaded end.

In Eq. (2), the term *ky* is associated with the presence of friction at the matrix-fiber interface, which will be discussed in the following sections (see Figure 4). The term $\frac{\alpha}{1+e^{-(y-y_0)/\beta}}$, which was employed to describe the strain distribution for the FRP-concrete interface (Carloni and Subramaniam 2012), is associated with the bond stress-transfer mechanism (see Figure 4). Decoupling the bond and friction contributions to the joint

capacity is important to clearly understand the relation between the bonded length and the load carrying capacity of the joint or the effective bond length.

Figure 5 illustrates the strain profiles along the composite bonded length at the debonding load $P_{deb}$ and peak load $P^*$. The effective bond length $l_{eff}$ is also indicated in Figure 5.

Assuming the matrix and concrete are rigid, the interfacial slip along the fiber direction can be obtained by integrating Eq. (2) using the boundary condition $s(0) = 0$:

$$s(y) = \alpha\beta\left[\ln\left(e^{\frac{y}{\beta}} + e^{\frac{y_0}{\beta}}\right) - \frac{y_0}{\beta} - \ln\left(1 + e^{-\frac{y_0}{\beta}}\right)\right] + \frac{ky^2}{2} \tag{3}$$

When $P$=$P_{deb}$, the global slip, i.e., the slip at the loaded end $s(y = l_{eff})$, is referred to as $g_{deb}$. Based on the fracture mechanics approach proposed by Carloni et al. (2014), $g_{deb} = s_f$, where $s_f$ denotes the slip at the end of the bond-slip model:

$$g_{deb} = s_f = \alpha\beta\left[\ln\left(e^{\frac{l_{eff}}{\beta}} + e^{\frac{y_0}{\beta}}\right) - y_0/\beta - \ln\left(1 + e^{-\frac{y_0}{\beta}}\right)\right] + \frac{kl_{eff}^2}{2} \tag{4}$$

When the applied load attains the peak load $P^*$, the STZ is assumed to have reached the composite free end, as shown in Figure 5. The validity of this assumption depends on the shape of the stress-transfer relationship and on the contribution of friction for the composite. If the contribution of friction is small compared to that of the bond stress-transfer mechanism, assuming that $P$=$P^*$ when the STZ reaches the composite free end provides accurate results (D'Antino et al. 2018). At $P^*$, the loaded end slip $g^*$ can be obtained by imposing $y$=ℓ in Eq. (3):

$$g^* = \alpha\beta\left[\ln\left(e^{\frac{\ell}{\beta}} + e^{\frac{y_0}{\beta}}\right) - y_0/\beta - \ln\left(1 + e^{-\frac{y_0}{\beta}}\right)\right] + k\ell^2/2 \tag{5}$$

Force equilibrium condition for an infinitesimal segment of fibers gives the shear stress along the surfaces of the fiber bundles as:

$$\tau(y) = E_f t_f \frac{d\varepsilon(y)}{dy} = E_f t_f \frac{\alpha}{\beta} \frac{e^{-(y-y_0)/\beta}}{[1+e^{-(y-y_0)/\beta}]^2} + E_f t_f k \quad (6)$$

where $E_f$ is the elastic modulus of the fibers, and $t_f$ is the thickness of a single longitudinal fiber bundle, which is assumed to have a rectangular cross section of width $b^*$. Note that in this paper, values of the shear stresses associated with both internal and external matrix layer-fiber interfaces are reported.

The maximum shear stress of the matrix-fiber interface $\tau_m$, referred to as the shear strength, is obtained at $y = y_0$, which corresponds to the coordinate where $d\tau(y)/dy = 0$. Therefore, $\tau_m$ is:

$$\tau_m = \tau(y_0) = E_f t_f \left(\frac{\alpha}{4\beta} + k\right) \quad (7)$$

For large values of $y$, i.e., large values of interfacial slip $s(y)$, the shear stress approaches the residual shear stress $\tau_f$:

$$\tau_f = E_f t_f k \quad (8)$$

$\tau_f$ can be also computed as $\tau_f = P_f/(nb^*\ell)$, where $n$ is the number of longitudinal fiber bundles included in the composite strip (Carloni et al. 2014). $P_f$ can be determined from the applied load-global slip curve as the tail of the post-peak descending branch where the applied load is constant as discussed in the "Previous experimental results" section.

The shear stress at $y = 0$, termed $\tau_0$, can be obtained by:

$$\tau_0 = E_f t_f \frac{\alpha}{\beta} \frac{e^{y_0/\beta}}{[1+e^{y_0/\beta}]^2} + E_f t_f k \quad (9)$$

According to this result, a certain value of initial shear stress exists when the slip is zero. $\tau_0 = 0$ was assumed for some $\tau(s)$ models for FRCM-concrete joints (D'Ambrisi et al. 2012; Focacci et al. 2017). In the case of the FRCM composite considered in this study, it is worth noting that the non-zero value of $\tau_0$ does not significantly influence the fracture energy and the predicted values of load and slip.

The interfacial slip $s_m$ associated with the maximum shear stress $\tau_m$ can be obtained by Eq. (3) imposing $y=y_0$:

$$s_m = \left[0.69 - \ln\left(1 + e^{-\frac{y_0}{\beta}}\right)\right]\alpha\beta + ky_0^2/2 \tag{10}$$

The axial force in the fibers can be obtained by:

$$P(y) = nb^*t_fE_f\varepsilon(y) = nb^*t_fE_f\left(\frac{\alpha}{1 + e^{-(y-y_0)/\beta}} + ky\right) \tag{11}$$

The applied load at the onset of debonding $P_{deb}$ and the peak load $P^*$ can be obtained from Eq. (11) enforcing $y=l_{eff}$ and $y=\ell$, respectively:

$$P_{deb} = nb^*t_fE_f\left(\frac{\alpha}{1 + e^{-(l_{eff}-y_0)/\beta}} + kl_{eff}\right) \tag{12}$$

$$P^* = nb^*t_fE_f\left(\frac{\alpha}{1 + e^{-(\ell-y_0)/\beta}} + k\ell\right) \tag{13}$$

Alternatively, if it is assumed that the difference between the debonding load $P_{deb}$ and the peak load P* is related only to friction, Eq. (2) can be used to depict the strain profile within the STZ, and a linear slope $k$ can be used to represent the friction effect (D'Antino et al. 2014) (see Figure 4). Thus, P* can be given as:

$$P^* = P_{deb} + \tau_f nb^*(\ell - l_{eff}) \tag{14}$$

Similarly, the global slip at peak load $g^*$ can be obtained by:

$$g^* = g_{deb} + (\ell - l_{eff})\left[\frac{\alpha}{1 + e^{-(l_{eff} - y_0)/\beta}} + \frac{k(\ell + l_{eff})}{2}\right] \quad (15)$$

The difference resulting from these two approaches is discussed in the "Validation of the model" section.

## 4.2. FITTING OF PARAMETERS

The parameters in Eq. (2) were determined by using a nonlinear regression analysis of the experimental results. The procedure to determine the parameters was: i) determine the debonding load $P_{deb}$ from the applied load $P$-global slip $g$ response, ii) determine the effective bond length $l_{eff}$ from the strain profiles at the debonding load $P_{deb}$, and iii) best-fit the experimental strain profile. Steps i) and ii) were conducted previously by the authors as described in Carloni et al. (2014). The effective bond length $l_{eff}$ determined for each specimen equipped with strain gauges is reported in Table 1. Assuming that $l_{eff}$ is not influenced by the presence or absence of the external matrix layer, as discussed in detail and supported by experimental results in (Carloni et al. 2014), the average value for the 11 specimens with strain gauges presented in (Carloni et al. 2014) (seven of which were considered in this paper, and four were excluded for the reasons explained in the "Previous experimental results" section) was equal to $\bar{l}_{eff}$= 260 mm with a coefficient of variation (CoV) of 0.084 (Carloni et al. 2014). Considering only the specimens with strain gauges employed in this study, the average effective bond length is $\bar{l}_{eff}$ =251 mm (with CoV=0.081) for the five specimens with the external matrix layer, and $l_{eff}$=250 mm for the two specimens without the external matrix layer (see Table 1).

Values of $\alpha$, $\beta$, and $y_0$ obtained by the nonlinear regression analysis of the results of the seven specimens considered are summarized in Table 1. Before the fitting process, $k$ was predefined as $\tau_f/(E_f t^*)$ for all specimens (Carloni et al. 2014). The average value of $\tau_f$ determined experimentally from specimens in (D'Antino et al. 2014; Carloni et al. 2014) with both internal and external layers of matrix is 0.12 MPa, whereas for specimens without the external layer of matrix is 0.08 MPa (Carloni et al. 2014).

Strain values measured at discrete locations along the bonded length at $P$=$P_{deb}$ and their fitting with Eq. (2) using the parameters determined for the corresponding specimen (Table 1) are plotted in Figure 6 for specimens equipped with strain gauges. Figure 6(c) shows the comparison of the curves of Eqs. (1) and (2) when the same fitting parameters are used and $\varepsilon_0 = 0$ for Eq. (1). Figure 6(c) shows that the difference between Eqs. (1) and (2) is small at the loaded end and that the strain determined by Eq. (1) is close to, but slightly lower than, the strain determined Eq. (2) along the STZ.

## 5. VALIDATION OF THE MODEL

The accuracy of Eq. (2) in describing the bond behavior of FRCM-concrete joints that fail at the matrix-fiber interface was assessed by comparing values of the applied load and global slip obtained from the experimental results with the corresponding analytical predictions. In this section, the subscript "e" denotes the experimental value, whereas the subscript "a" denotes the analytical value. Eqs. (12) and (4) provide the analytical debonding load $P_{deb,a}$ and the corresponding global slip $g_{deb,a}$, respectively. Eqs. (13) and (5) provide the analytical peak load $P_a^*$ and the corresponding global slip $g^*$, respectively.

The experimental values of the debonding load and peak load ($P_{deb,e}$ and $P_e^*$, respectively) were reported by Carloni et al. (2014), whereas the corresponding slips ( $g_{deb,e}$ and $g_e^*$, respectively) were obtained directly from the *P*-*g* response of the corresponding specimen. Results are summarized in Table 2.

Results in Table 2 show that the analytical values of the debonding and peak loads are in reasonable agreement with the corresponding experimental values. The average value of the ratio $P_{deb,a}/P_{deb,e}$ is 1.216 (CoV= 0.203), and the average value of the ratio $P_a^*/P_e^*$ is 1.214 (CoV=0.207). Possible reasons for the slight overestimation of the debonding and peak loads may be the result of stress concentration at the gauge closest to the loaded end (Carloni et al. 2013) and/or the shape of the chosen fitting function at the loaded end. The average of the ratio $g_{deb,a}/g_{deb,e}$ is 0.950 (CoV = 0.206), and the average value of the ratio $g_a^*/g_e^*$ is 0.918 (CoV = 0.413). The reason for the large CoV of the ratio $g_a^*/g_e^*$ can be attributed in part to the fact that the experimental response is highly sensitive to localized deformations along the composite bonded area as debonding propagates, see Figure 2. To be specific, when the load gradually approaches $P^*$, the value of $g$ highly increases, which results in substantial scatter of $g_e^*$. This has also been found by Focacci et al. (2017) where the analytical slip at peak load is larger than the experimental value.

Considering a larger data set, the peak load $P^*$ of the 51 specimens reported by Carloni et al. (2014) included in this study was estimated by applying the fitting procedure to the specimens equipped with strain gauges and then employing the average values of parameters of $\alpha$, $\beta$, and $y_0$ obtained (average values are reported in Table 1). Specimens with the same geometrical characteristics were grouped together, and the average value of

the experimental peak load of specimens in each group (series) $\overline{P_e^*}$ was determined. Table 3 reports the value of $\overline{P_e^*}$ and $P_a^*$ along with the corresponding CoV and the ratio $P_a^*/\overline{P_e^*}$ for each series. Values of $P_a^*/\overline{P_e^*}$ in Table 3 show that the peak load was well predicted using the analytical model, with an average value of 1.171 (CoV = 0.040).

Alternatively, if it is assumed that the difference between the debonding load and the peak load is related only to friction, Eq. (14) can be used to predict the analytical peak load $P_a^*$. The resulting values are summarized in Table 3. $P_a^*$ determined in this manner for the series considered are on average 5% lower than values determined by Eq. (13).

## 6. BOND-SLIP MODEL

The matrix-fiber shear stress-slip relationship $\tau(s)$ is a property of the matrix-fiber interface (D'Ambrisi et al. 2012; Carloni et al. 2014; D'Antino et al. 2014). The distribution of slip along the bonded length at the debonding load described by Eq. (3) is shown in Figure 7a for specimen DS_330_60_L_S_1. The global slip measured experimentally at the debonding load is included in Figure 7a for comparison. $\tau(y)$ at the debonding load described by Eq. (6) is also shown in Figure 7a, where the physical meaning of the parameter $y_0$ can be seen. Finally, Figure 7b shows the relationship $\tau(s)^{Eq.2}$ obtained by combining $\tau(y)$ with $s(y)$ derived from Eq. (2).

Table 4 reports the values of maximum shear stress $\tau_m$ and corresponding slip $s_m$ determined using Eqs. (7) and (10), respectively, with the average values of the parameters $\alpha$, $\beta$, and $y_0$ for the seven specimens with strain gauges (Table 1) for the corresponding series. For the DS_xxx_xx_L series, $\tau_m$ is 1.656 MPa, and $s_m$ is 0.224 mm. $s_f$ was

determined by Eq. (4), which provided $s_f$=0.957 mm. For the DS_xxx_xx series, the values of $\tau_m$, $s_m$ and $s_f$ are 1.321 MPa, 0.299 mm, and 1.081 mm, respectively.

Although both functions $\tau(y)$ and $s(y)$ derived from Eq. (2) are continuous, they do not provide a closed-form expression for the shear stress-slip function, i.e., the bond slip relationship $\tau(s)$. Several different bond-slip relationships with different shapes were evaluated by Focacci et al. (2017) for PBO FRCM-concrete joints. In this section, an alternative, continuous, closed-form solution for the $\tau(s)$ relationship is provided.

The results in Table 1 show that $e^{y_0/\beta}/[1+e^{y_0/\beta}]^2 \approx 0$, thus Eq. (9) can be rewritten as:

$$\tau_0 = E_f t_f k \tag{16}$$

which shows that the value of the initial shear stress $\tau_0$ is equal to $\tau_f$.

Herein a function is proposed by modifying the equation given by Dai et al. (2006) for FRP-concrete joints:

$$\tau(s)^{Eq.17} = E_f t_f A^2 B(e^{-Bs} - e^{-2Bs}) + \tau_f \tag{17}$$

A constant term $\tau_f$ has been added to the right hand side of Eq. (17) to account for friction, which is a peculiarity of certain FRCM composites, including the composite investigated in the present study. The parameters $A$ and $B$ can be obtained by forcing the peak point $(s_m, \tau_m)$ in Eq. (17) equal to the curve determined by Eqs. (3) and (6).

The maximum shear stress $\tau_m$ and corresponding slip $s_m$ by enforcing $\frac{d\tau(s)}{ds} = 0$ in Eq. (17) are:

$$\tau_m = \frac{A^2 B E_f t_f}{4} + \tau_f \tag{18}$$

$$s_m = 0.693/B \tag{19}$$

Eqs. (18) and (19) can be employed to determine the parameters $B$ and $A$:

$$B = 0.693/s_m \tag{20}$$

$$A = 2.4\sqrt{\frac{(\tau_m - \tau_f)s_m}{E_f t_f}} \tag{21}$$

where the values of $B$ and $A$ obtained by Eqs. (20) and (21), respectively, are summarized in Table 4.

The bond-slip relationship in Eq. (17) ($\tau(s)^{Eq.17}$) for the seven specimens equipped with strain gauges was obtained using the values of $s_m$ and $\tau_m$ in Table 4 which are plotted in Figure 8 together with $\tau(s)^{Eq.2}$ determined from the analytical procedure described previously for comparison. Figure 8 shows that Eq. (17) can be used as a reasonable approximation of the bond-slip relationship determined from Eq. (2) for the PBO-FRCM composite studied in this paper. However, the curve of $\tau(s)^{Eq.17}$ is slightly higher than $\tau(s)^{Eq.2}$, which indicates a higher fracture energy is provided by Eq. (17). This difference is discussed in the following section.

## 7. FRACTURE ENERGY

The fracture energy $G_F$ of the matrix-fiber interface in PBO FRCM-concrete joints is (Carloni et al. 2014):

$$G_F = \int_0^{s_f} \tau(s)\, ds \tag{22}$$

The fracture energy in Eq. (2), termed $G_F^{Eq.2}$, was determined for each series by calculating the area under the curve $\tau(s)^{Eq.2}$ for $0 \leq s \leq s_f$ employing the average values of parameters $\alpha$, $\beta$, and $y_0$ for the respective series (reported in Table 1). The resulting value of $G_F^{Eq.2}$ for each series is summarized in Table 4.

Considering the alternative bond-slip model in Eq. (17), the fracture energy can be computed as:

$$G_F^{Eq.17} = \frac{A^2 E_f t_f}{2}(1 - e^{-Bs_f}) + \tau_f s_f \tag{23}$$

The values of $G_F^{Eq.17}$ computed for series DS_xxx_xx_L and DS_xxx_xx using values of $A$, $B$, $\tau_f$, and $s_f$ given in Table 4 for the corresponding series are summarized in Table 4.

The fracture energy in Eq. (1), termed $G_F^{Eq.1}$, was reported in Carloni et al. (2014), where $G_F^{Eq.1}$ was determined for each specimen by calculating the area under the resulting curve $\tau(s)$ for $0 \leq s \leq s_f$ and employing values of parameters $\varepsilon_0$, $\alpha$, $\beta$, and $y_0$ for the corresponding specimen determined using nonlinear regression analysis of the measured strains. Considering the seven specimens with strain gauges included in this paper, average values of $G_F^{Eq.1}$ for the DS_xxx_xx_L and DS_xxx_xx series are reported in Table 4.

Results in Table 4 show that values of $G_F^{Eq.2}$ and $G_F^{Eq.1}$ are very close (within an average of 4%), which shows that Eqs. (1) and (2) provide similar results. Table 4 also shows that using Eq. (17) to depict the relationship derived by Eqs. (3) and (6) results in a difference in fracture energy of about 6% on average (see also Figure 8). This can be explained by the approach used in the previous section to determine parameters $A$ and $B$ in

Eq. (17), where values of $\tau_m$and $s_m$ were set. Another approach could be to determine the parameters by maintaining the same fracture energy $G_F$ and setting the value of either $\tau_m$ or $s_m$.

## 8. CONCLUSIONS

This paper presented an analytical procedure to determine the bond–slip model of FRCM-concrete joints based on discrete measurements of longitudinal fiber strains acquired from single-lap direct shear test specimens. A new curve fitting equation describing the longitudinal strain profile was proposed, and the parameters in the proposed equation were determined using a nonlinear regression analysis of experimental results reported in the literature. An advantage of the proposed equation $\varepsilon(y)$ is that it can be used to describe the distribution of slip $s(y)$ and shear stress $\tau(y)$ along the bonded length of the composite by integration and derivation, respectively. However, the resulting bond–slip model $\tau(s)^{Eq.2}$ could not be obtained in closed-form. Therefore, an alternative function of the bond–slip model $\tau(s)^{Eq.17}$ obtained from the maximum shear stress $\tau_m$ and corresponding slip $s_m$, was also proposed. The following main conclusions can be drawn from this study:

- The strain profiles of PBO FRCM-concrete joints can be described by the continuous function $\varepsilon(y)$ presented in Eq. (2). An advantage of Eq. (2) is that a closed-form equation of the slip $s(y)$ can be obtained by integrating $\varepsilon(y)$.
- The peak load $P^*$ and debonding load $P_{deb}$ from seven single-lap direct shear specimens were predicted by fitting parameters of the function $\varepsilon(y)$ and showed good agreement with test results. Values of global slip at the debonding load and

peak load were predicted with reasonable accuracy but with larger coefficient of variation. Considering test results from 51 specimens reported in the literature, the predicted values of $P^*$ were in reasonable agreement with the experimental results, with average predicted-to-experimental values of 1.171 (CoV = 0.040).

- An alternative, continuous, closed-form function of the bond–slip model was obtained from the maximum shear stress $\tau_m$ and corresponding slip $s_m$. The alternative function of the bond–slip model $\tau(s)^{Eq.17}$ showed good agreement with the bond slip model $\tau(s)^{Eq.2}$ obtained from the function $\varepsilon(y)$ presented in Eq. (2).
- The fracture energy obtained by function $\tau(s)^{Eq.2}$ agreed well with values given in the literature (within an average of 4%). The fracture energy obtained by the alternative function of the bond slip model $\tau(s)^{Eq.17}$ overestimated value obtained by function $\tau(s)^{Eq.2}$ by approximately 6%. This discrepancy could be removed by determining the parameters in the function $\tau(s)^{Eq.17}$ by maintaining the same fracture energy $G_F$ and setting the value of either $\tau_m$ or $s_m$ instead of setting values of $\tau_m$ and $s_m$.

The authors postulate that the procedure in this paper can be extended to other types of FRCM composites bonded to other substrates (such as masonry) as long as the failure mode is the same (cohesive failure within the substrate with residual friction stress) and the internal matrix layer is considered rigid. Previous experimental results have suggested that the failure mode was not significantly affected by the substrate considered (D'Antino et al. 2015; Gonzalez-Libreros et al. 2017). This hypothesis requires further study, for example the possible effect of mortar joints for the case of masonry substrates.

## APPENDIX

Table 5 lists the specimens considered in the present study and the corresponding values of peak load $P^*$ (Carloni et al. 2014). Test specimen notation is described in the "Previous experimental results" section.

## NOTATION

| | | |
|---|---|---|
| $A,B$ | = | parameter in bond-slip model; |
| $b_1$ | = | composite bonded width; |
| $b^*$ | = | nominal width of a single fiber bundle; |
| $E_f$ | = | elastic modulus of fibers; |
| $g$ | = | global slip, measured by the average of two LVDTs at the loaded end of composite in the experimental test and used to control the direct shear tests; |
| $g_{deb}$ | = | global slip at debonding load; |
| $g_{deb,a}$, $g_{deb,e}$ | = | analytical and experimental global slip at debonding load; |
| $g^*$ | = | global slip at peak load; |
| $g_a^*$ | = | analytical global slip at peak load; |
| $g_e^*$ | = | experimental global slip at peak load; |
| $G_F^{Eq.1}, G_F^{Eq.2}, G_F^{Eq.17}$ | = | fracture energy computed by Eq. (1), Eq. (2) or Eq. (17). |
| $\ell$ | = | composite bonded length; |
| $l_{eff}$ | = | effective bond length; |
| $k$ | = | parameter in Eqs. (1) and (2), related to friction and interlocking mechanism; |

$P$ = applied load;

$P_{deb}$ = debonding load;

$P_{deb,a}, P_{deb,e}$ = analytical and experimental debonding load;

$P_f$ = applied load due to friction and interlocking;

$P*$ = peak load;

$P_a^*$ = analytical peak load;

$P_e^*$ = experimental peak load;

$\overline{P_e^*}$ = average experimental peak load;

$s$ = slip between the fibers and the matrix;

$s_m, s_f$ = slip corresponding to the maximum shear stress and the complete debonding;

$t_f$ = thickness of fiber bundle, which is assumed to have a rectangular cross section of width $b^*$;

$y$ = longitudinal distance to loaded end in Eqs. (1) and (2);

$y_0$, $\alpha$, $\beta$, $\varepsilon_0$ = parameter in Eqs. (1) and (2);

$\varepsilon(y)$ = strain profile function;

$\tau_0$ = initial shear stress;

$\tau_f$ = shear stress due to friction and interlocking;

$\tau_m$ = maximum shear stress;

$\tau(s)^{\text{Eq.2}}$ = function for bond-slip model determined by Eq. (2);

$\tau(s)^{\text{Eq.17}}$ = function for alternative bond-slip model given in Eq. (17);

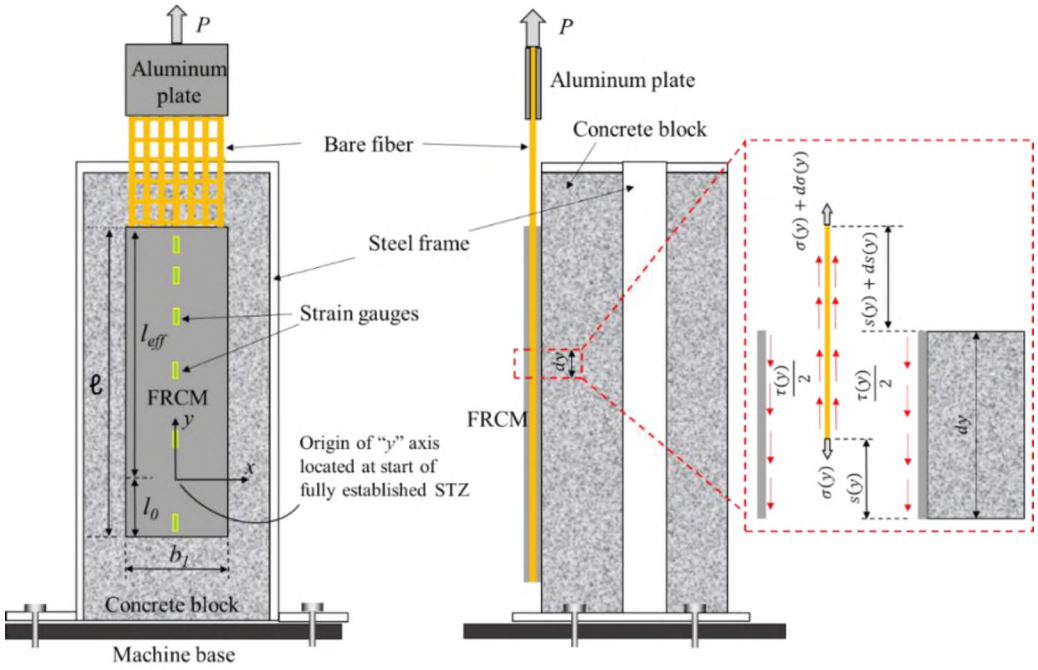


(a) (b)

Figure 1. Test setup and strain gauge locations (D'Antino et al. 2014; Carloni et al. 2014): (a) front view, and (b) side view.

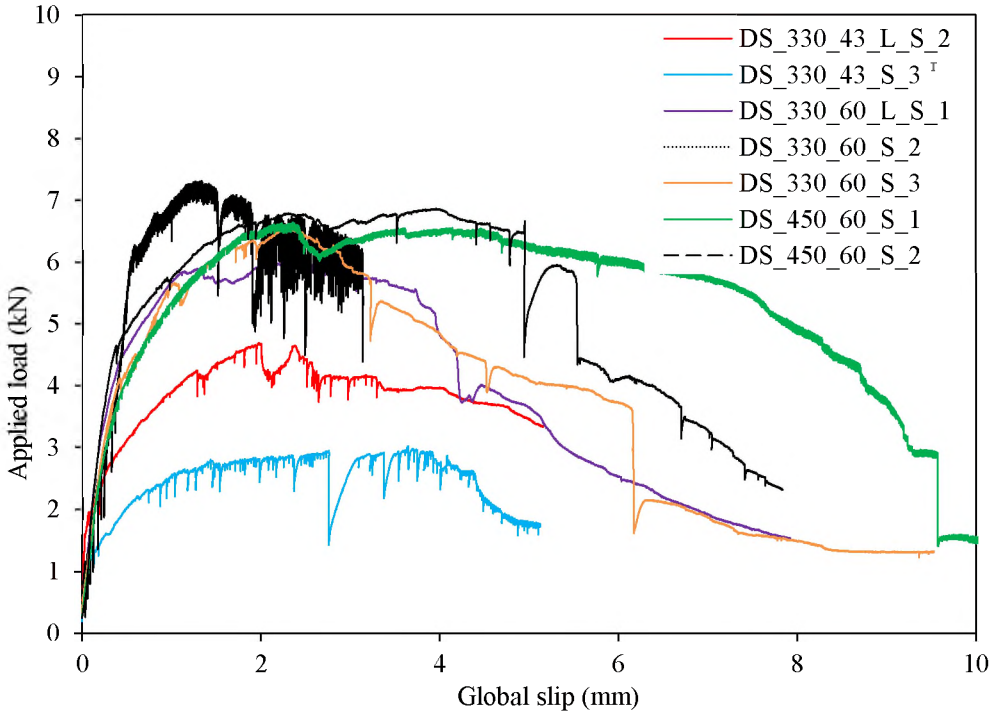


Figure 2. Applied load P - global slip g relationship of the seven specimens with strain gauges analyzed in the present study.

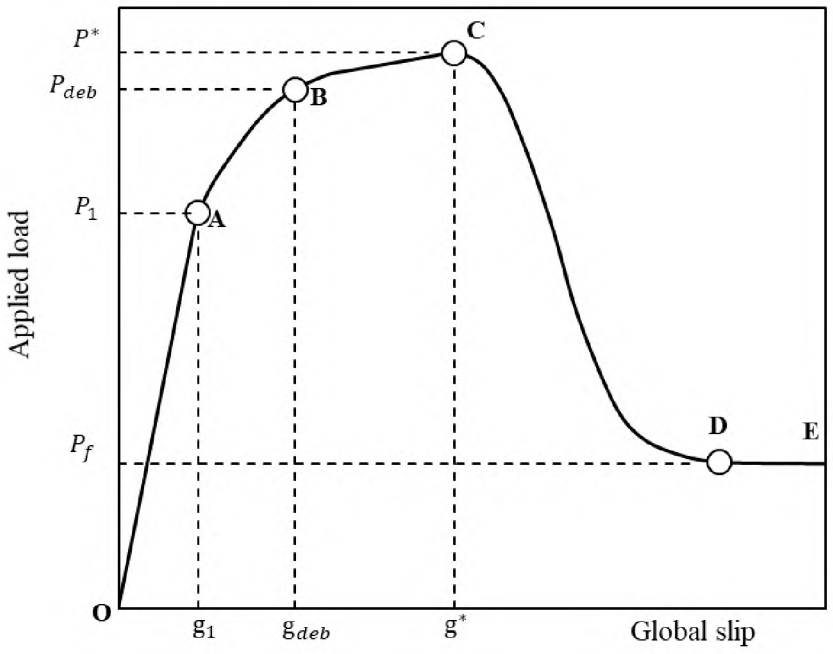


Figure 3. Idealized applied load P – global slip g curve.

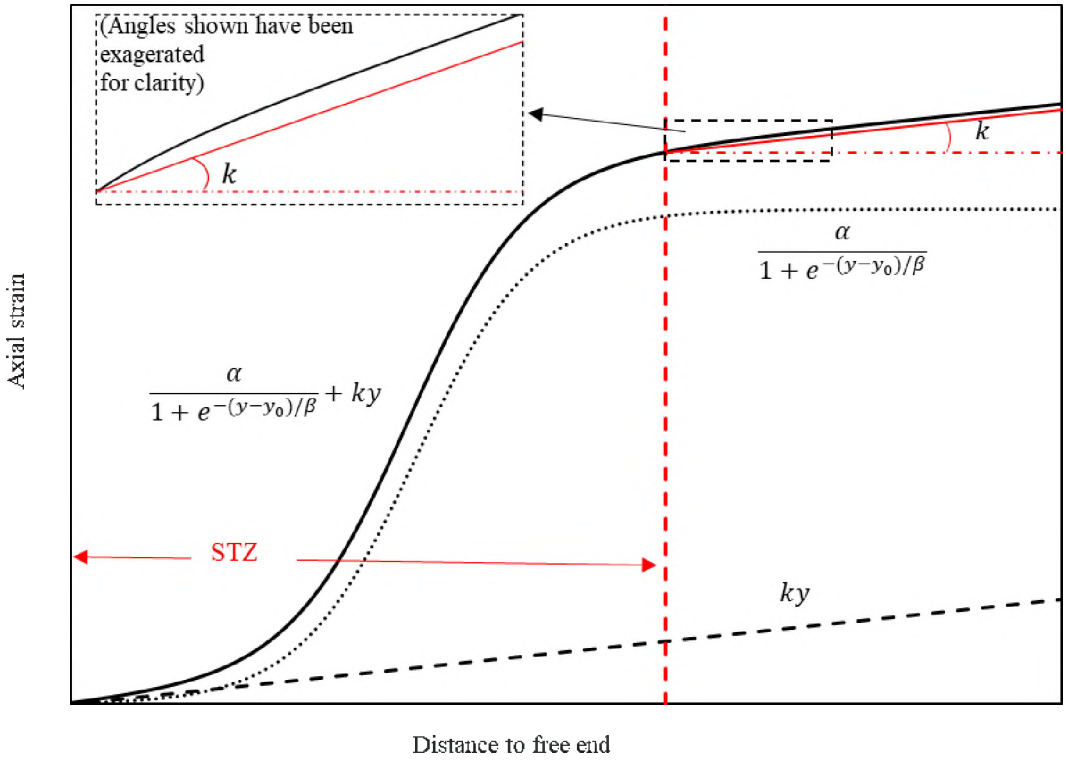


Figure 4. Plot of Eq. (2) and its two parts.

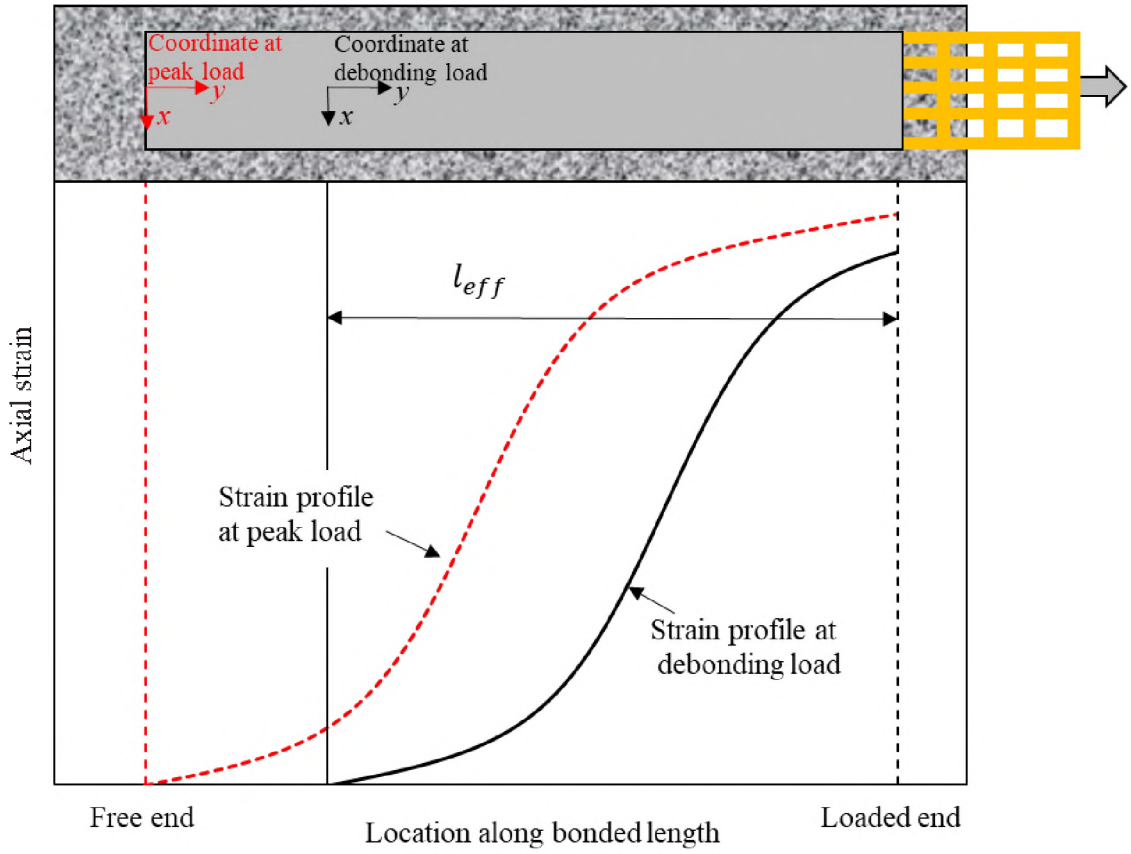


Figure 5. Axial strain profiles along the composite bonded length at the debonding load Pdeb and peak load P*.

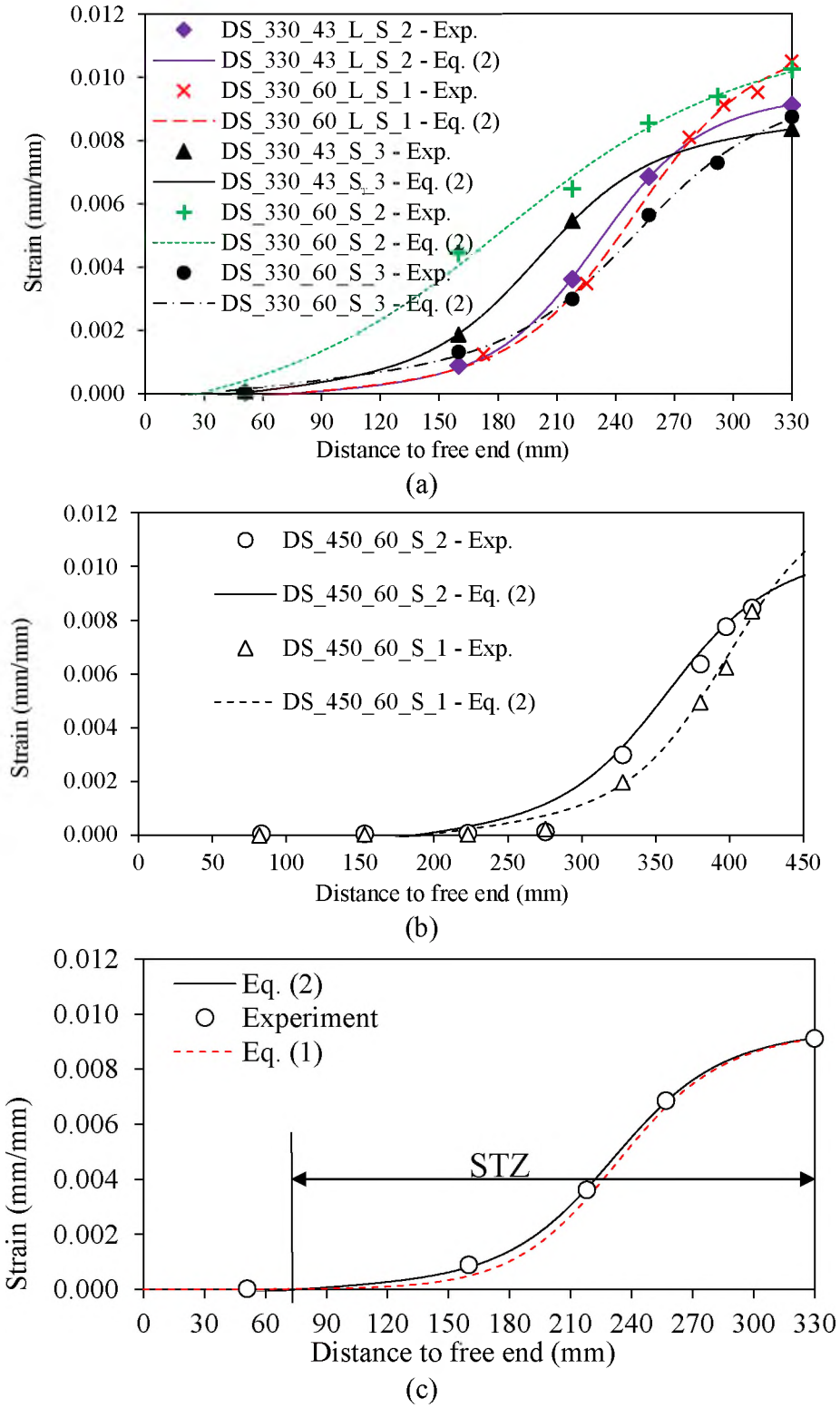


Figure 6. Curve fitting results for specimens with a bonded length of (a) 330 mm, and (b) 450 mm at the debonding load $P_{deb}$ (Table 1), and (c) comparison between Eqs. (1) and (2).

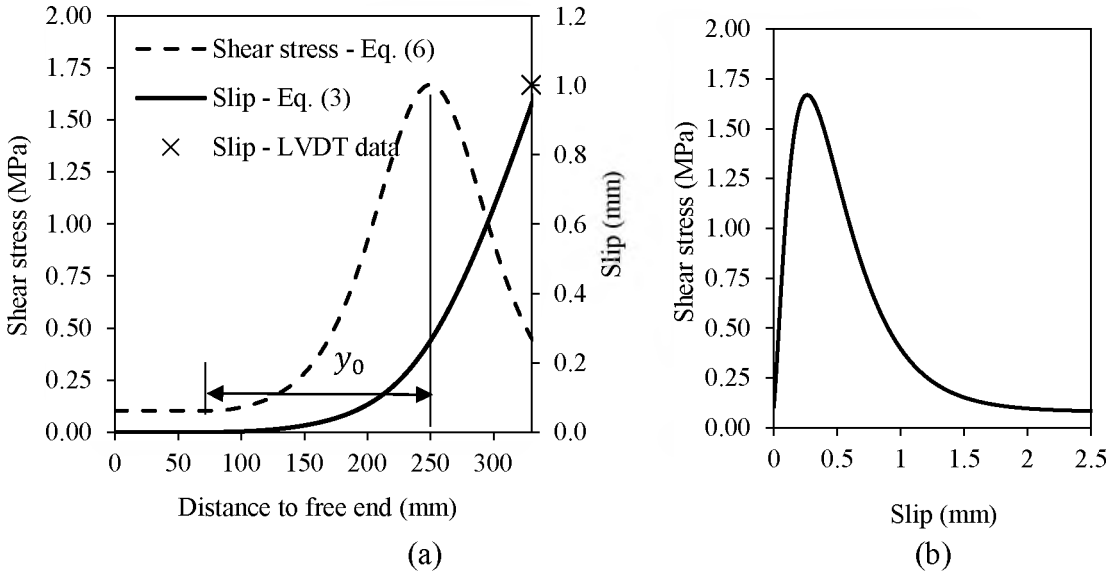


Figure 7. Specimen DS_330_60_ L_S_1: (a) slip distribution and shear stress at debonding load, and (b) shear stress-slip relationship.

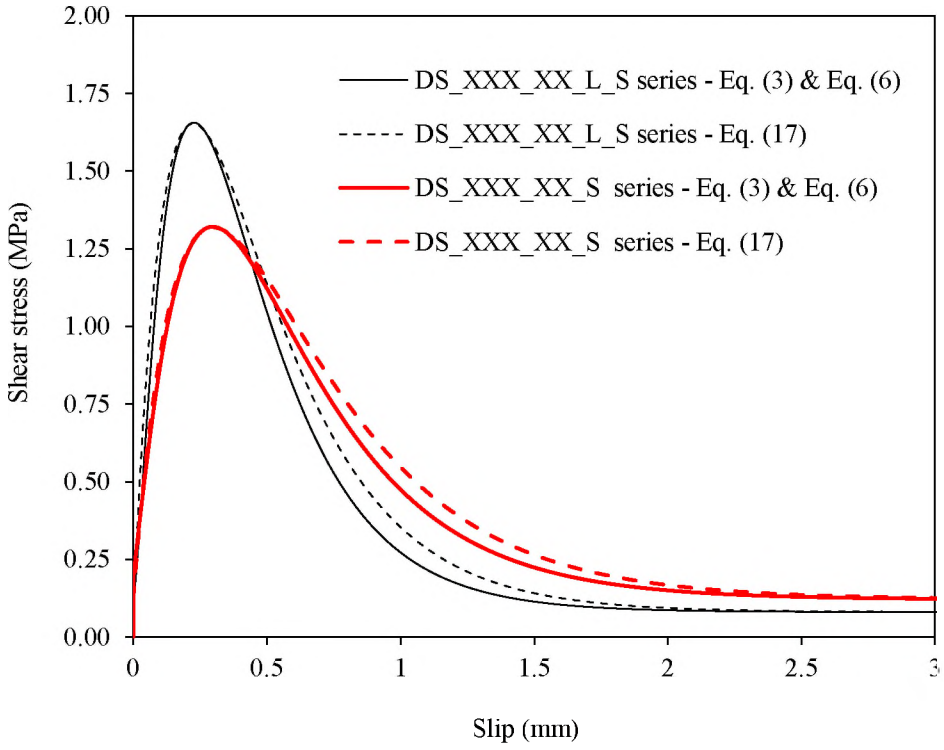


Figure 8. Shear stress vs. slip relationship of specimens in Table 4.

Table 1. Parameters in Eq. (2) determined by nonlinear regression analysis.

| Specimen | $l_{eff}$ (mm) | $k$ $(10^{-6}/mm)$ | $\alpha$ ($10^{-6}$) | $\beta$ (mm) | $\frac{\beta}{l_{eff}}$ | $y_0$ (mm) | $\frac{y_0}{l_{eff}}$ |
|---|---|---|---|---|---|---|---|
| DS_330_43_L_S_2 | 250 | 8.44 | 8321 | 25.3 | 0.101 | 151.0 | 0.604 |
| DS_330_60_L_S_1 | 250 | 8.44 | 9907 | 29.6 | 0.118 | 169.3 | 0.680 |
| Average | 250 | | 9114 | 27.4 | 0.110 | 160.4 | 0.642 |
| CoV | - | | 0.123 | 0.111 | 0.111 | 0.084 | 0.084 |
| DS_330_43_S_3 [T] | 280 | 6.33 | 6636 | 26.7 | 0.095 | 150.6 | 0.538 |
| DS_330_60_S_2 | 225 | 6.33 | 9327 | 54.1 | 0.240 | 77.6 | 0.345 |
| DS_330_60_S_3 | 240 | 6.33 | 10200 | 33.2 | 0.138 | 184.5 | 0.769 |
| DS_450_60_S_1 | 255 | 6.33 | 10610 | 31.8 | 0.125 | 202.8 | 0.795 |
| DS_450_60_S_2 | 255 | 6.33 | 8532 | 33.1 | 0.130 | 162.8 | 0.638 |
| Average | 251 | | 9061 | 35.8 | 0.146 | 155.7 | 0.617 |
| CoV | 0.081 | | 0.174 | 0.296 | 0.380 | 0.308 | 0.298 |

Table 2. Comparison of applied load and global slip determined from experiments and analytical model for specimens with strain gauges.

| Specimen | $P_{deb,e}$ (kN) | $P_{deb,a}$(kN) | $\frac{P_{deb,a}}{P_{deb,e}}$ | $P_e^*$ (kN) | $P_a^*$ (kN) | $\frac{P_a^*}{P_e^*}$ | $g_{deb,e}$ (mm) | $g_{deb,a}$(mm) | $\frac{g_{deb,a}}{g_{deb,e}}$ | $g_e^*$ (mm) | $g_a^*$ (mm) | $\frac{g_a^*}{g_e^*}$ |
|---|---|---|---|---|---|---|---|---|---|---|---|---|
| DS_330_43_L_S_2 | 4.20 | 4.66 | 1.115 | 4.69 | 4.97 | 1.060 | 1.3 | 1.0 | 0.72 | 2.0 | 1.8 | 0.90 |
| DS_330_60_L_S_1 | 5.80 | 6.52 | 1.124 | 5.97 | 6.96 | 1.165 | 1.1 | 1.0 | 0.88 | 2.2 | 1.8 | 0.81 |
| DS_330_43_S_3 [T] | 2.71 | 4.77 | 1.758 | 3.03 | 5.35 | 1.766 | 1.4 | 1.1 | 0.79 | 3.6 | 2.0 | 0.54 |
| DS_330_60_S_2 | 6.65 | 6.67 | 1.004 | 7.31 | 7.48 | 1.024 | 0.8 | 1.1 | 1.31 | 1.3 | 2.0 | 1.48 |
| DS_330_60_S_3 | 5.63 | 6.67 | 1.186 | 6.55 | 7.48 | 1.143 | 1.1 | 1.1 | 1.00 | 4.0 | 2.0 | 0.50 |
| DS_450_60_S_1 | 5.70 | 6.67 | 1.171 | 6.63 | 7.88 | 1.188 | 1.2 | 1.1 | 0.90 | 2.4 | 3.3 | 1.38 |
| DS_450_60_S_2 | 5.77 | 6.67 | 1.157 | 6.86 | 7.88 | 1.149 | 1.0 | 1.1 | 1.06 | 4.0 | 3.3 | 0.82 |
| Average | | | 1.216 | | | 1.214 | | | 0.95 | | | 0.92 |
| CoV | | | 0.203 | | | 0.207 | | | 0.206 | | | 0.413 |

Table 3. Comparison of experimental and analytical peak loads considering 51 specimens and using average values of parameters $\alpha$, $\beta$, and $y_0$ obtained.

| Series | Numbers of test specimens (Carloni et al. 2014) | $\overline{P_e^*}$ (kN) | CoV | $P_a^*$ (kN) | $P_a^*$ Determined by Eq. (14) (kN) | $P_a^*/\overline{P_e^*}$ |
|---|---|---|---|---|---|---|
| DS_330_43_L | 10 | 4.23 | 0.133 | 4.97 | 4.82 | 1.175 |
| DS_330_43 | 5 | 4.75 | 0.203 | 5.35 | 5.00 | 1.126 |
| DS_330_60_L | 10 | 5.63 | 0.089 | 6.96 | 6.75 | 1.236 |
| DS_330_60 | 15 | 6.65 | 0.010 | 7.48 | 7.01 | 1.125 |
| DS_450_60 | 11 | 6.60 | 0.060 | 7.88 | 7.51 | 1.194 |
| Average | | | | | | 1.171 |
| CoV | | | | | | 0.040 |

Table 4. Comparison of bond-slip models for one- and two-layer matrix specimens.

| Series | $s_m$ (mm) | $\tau_m$ (MPa) | $s_f$ (mm) | $\tau_f$ (MPa) | $A$ ($\times 10^{-3}$) | $B$ ($mm^{-1}$) | $G_F^{Eq.2}$ ($J/m^2$) | $G_F^{Eq.17}$ ($J/m^2$) | $\frac{G_F^{Eq.17}}{G_F^{Eq.2}}$ | $G_F^{Eq.1}$ ($J/m^2$) | $\frac{G_F^{Eq.1}}{G_F^{Eq.2}}$ |
|---|---|---|---|---|---|---|---|---|---|---|---|
| DS_xxx_xx_L | 0.224 | 1.656 | 0.951 | 0.08 | 10.4 | 3.09 | 917 | 992 | 1.082 | 915 | 0.998 |
| DS_xxx_xx | 0.299 | 1.321 | 1.081 | 0.12 | 10.4 | 2.32 | 960 | 997 | 1.039 | 892 | 0.929 |

Table 5. Summary of test specimens and corresponding values of peak load $P^*$ from (Carloni et al. 2014) included in the present study.

| Series | Numbers of test specimens (Carloni et al. 2014) | Specimen | $P^*$ (kN) |
|---|---|---|---|
| DS_330_43_L<br>$\overline{P_e^*}$= 4.23 kN<br>CoV = 0.133 | 10 | DS_330_43_L_1 | 4.96 |
| | | DS_330_43_L_2 | 4.63 |
| | | DS_330_43_L_3 | 4.61 |
| | | DS_330_43_L_4 | 3.98 |
| | | DS_330_43_L_5 | 3.96 |
| | | DS_330_43_L_6 | 3.82 |
| | | DS_330_43_L_8$^T$ | 3.67 |
| | | DS_330_43_L_11 | 4.72 |
| | | DS_330_43_L_S_1$^T$ | 3.24 |
| | | DS_330_43_L_S_2 | 4.69 |
| DS_330_43<br>$\overline{P_e^*}$= 4.75 kN<br>CoV = 0.203 | 5 | DS_330_43_2$^T$ | 5.25 |
| | | DS_330_43_3 | 5.27 |
| | | DS_330_43_6 | 5.09 |
| | | DS_330_43_S_2$^T$ | 5.12 |
| | | DS_330_43_S_3$^T$ | 3.03 |
| DS_330_60_L<br>$\overline{P_e^*}$= 5.63 kN<br>CoV = 0.089 | 10 | DS_330_60_L_1 | 5.80 |
| | | DS_330_60_L_2 | 5.49 |
| | | DS_330_60_L_3 | 6.60 |
| | | DS_330_60_L_4 | 5.46 |
| | | DS_330_60_L_5 | 5.26 |
| | | DS_330_60_L_D_1 | 5.19 |
| | | DS_330_60_L_D_2 | 6.13 |
| | | DS_330_60_L_D_3 | 5.47 |
| | | DS_330_60_L_D_4 | 4.90 |
| | | DS_330_60_L_S_1 | 5.97 |

Table 5. Summary of test specimens and corresponding values of peak load $P^*$ from (Carloni et al. 2014) included in the present study (continued).

| Series | Numbers of test specimens (Carloni et al. 2014) | Specimen | $P^*$ (kN) |
|---|---|---|---|
| DS_330_60<br>$\overline{P_e^*}$= 6.65 kN<br>CoV = 0.010 | 15 | DS_330_60_1$^T$ | 7.05 |
| | | DS_330_60_2$^T$ | 6.56 |
| | | DS_330_60_3$^T$ | 6.06 |
| | | DS_330_60_4$^T$ | 6.50 |
| | | DS_330_60_5$^T$ | 6.28 |
| | | DS_330_60_D_1 | 8.29 |
| | | DS_330_60_D_2 | 7.12 |
| | | DS_330_60_D_3 | 6.56 |
| | | DS_330_60_D_4 | 5.24 |
| | | DS_330_60_D_5 | 6.69 |
| | | DS_330_60_S_2 | 7.31 |
| | | DS_330_60_S_3 | 6.55 |
| | | DS_330_60_T_1 | 6.62 |
| | | DS_330_60_T_2 | 6.27 |
| | | DS_330_60_T_3 | 6.59 |
| DS_450_60<br>$\overline{P_e^*}$= 6.60 kN<br>CoV = 0.060 | 11 | DS_450_60_1 | 6.40 |
| | | DS_450_60_2 | 6.34 |
| | | DS_450_60_3 | 6.44 |
| | | DS_450_60_4 | 5.77 |
| | | DS_450_60_5 | 6.51 |
| | | DS_450_60_6 | 6.79 |
| | | DS_450_60_7 | 6.65 |
| | | DS_450_60_D_1 | 7.01 |
| | | DS_450_60_D_2 | 6.67 |
| | | DS_450_60_D_3 | 7.33 |
| | | DS_450_60_S_1 | 6.63 |
| | | DS_450_60_S_1 | 6.86 |

Note - Specimens included are those in the DS_330_43 series, the DS_330_43_L series, the DS_330_60 series, the DS_330_60_L series, and DS_450_60 series that had a relatively uninform distribution of the applied load across the longitudinal fiber bundles as defined in (Carloni et al. 2014).

# REFERENCES

ACI Committee 549. (2013). Guide to Design and construction of externally bonded fabric-reinforced cementitious matrix (FRCM) systems for repair and strengthening concrete and masonry structures, ACI 549.4R-13, American Concrete Institute, Farmington Hills, USA.

Alabdulhady, M. Y., Sneed, L. H., & Carloni, C. (2017). Torsional behavior of RC beams strengthened with PBO-FRCM composite–An experimental study. Engineering Structures, 136, 393-405.

Alecci, V., Focacci, F., Rovero, L., Stipo, G., & De Stefano, M. (2016). Extrados strengthening of brick masonry arches with PBO–FRCM composites: Experimental and analytical investigations. Composite Structures, 149, 184-196.

Awani, O., El Refai, A., & El-Maaddawy, T. (2015). Bond characteristics of carbon fabric-reinforced cementitious matrix in double shear tests. Construction and Building Materials, 101, 39-49.

Azam, R., & Soudki, K. (2014). FRCM strengthening of shear-critical RC beams. Journal of Composites for Construction, 18(5), 04014012.

Babaeidarabad S., Loreto G, & Nanni A. (2014). Flexural strengthening of RC beams with an externally bonded fabric-reinforced cementitious matrix. Journal of Composites for Construction,18(5), 04014009.

Bilotta, A., Ceroni, F., Lignola, G. P., & Prota, A. (2017). Use of DIC technique for investigating the behaviour of FRCM materials for strengthening masonry elements. Composites Part B: Engineering.

Blanksvärd, T., Täljsten, B., & Carolin, A. (2009). Shear strengthening of concrete structures with the use of mineral-based composites. Journal of Composites for Construction, 13(1), 25-34.

Bournas, D. A., Lontou, P. V., Papanicolaou, C. G., & Triantafillou, T. C. (2007). Textile-reinforced mortar versus fiber-reinforced polymer confinement in reinforced concrete columns. ACI Structural Journal, 104(6), 740.

Brückner, A., Ortlepp, R., & Curbach, M. (2008). Anchoring of shear strengthening for T-beams made of textile reinforced concrete (TRC). Materials and Structures, 41(2), 407-418.

Caggegi, C., Sciuto, D., & Cuomo, M. (2018). Experimental study on effective bond length of basalt textile reinforced mortar strengthening system: Contributions of digital image correlation. Measurement, 129, 119-127.

Carloni, C., & Subramaniam, K. V. (2012). Application of fracture mechanics to debonding of FRP from RC members. Special Publication, 286, 1-16.

Carloni, C., Sneed, L.H., & D'Antino, T. (2013). Interfacial bond characteristics of fiber reinforced concrete mortar for external strengthening of reinforced concrete members. In: FraMCos-8, 8th International Conference on Fracture Mechanics of Concrete and Concrete Structures, Toledo, Spain, 1-9.

Carloni, C., D'Antino, T., Sneed, L. H., & Pellegrino, C. (2014). Role of the matrix layers in the stress-transfer mechanism of FRCM composites bonded to a concrete substrate. Journal of Engineering Mechanics, 141(6), 04014165.

D'Ambrisi, A., Feo, L., & Focacci, F. (2013). Experimental analysis on bond between PBO-FRCM strengthening materials and concrete. Composites Part B: Engineering, 44(1), 524-532.

D'Ambrisi, A., Focacci, F., & Caporale, A. (2013). Strengthening of masonry–unreinforced concrete railway bridges with PBO-FRCM materials. Composite Structures, 102, 193-204.

D'Antino, T., Carloni, C., Sneed, L. H., & Pellegrino, C. (2014). Matrix–fiber bond behavior in PBO FRCM composites: A fracture mechanics approach. Engineering Fracture Mechanics, 117, 94-111.

D'Antino, T., Sneed, L.H., Carloni, C., & Pellegrino, C. (2015). Influence of the substrate characteristics on the bond behavior of FRCM-concrete joints. Construction and Building Materials, 101(1), 838-850.

D'Antino, T., Sneed, L. H., Carloni, C., & Pellegrino, C. (2016). Effect of the inherent eccentricity in single-lap direct-shear tests of PBO FRCM-concrete joints. Composite Structures, 142, 117-129.

D'Antino, T., Colombi, P., Carloni, C., & Sneed, L. H. (2018). Estimation of a matrix-fiber interface cohesive material law in FRCM-concrete joints. Composite Structures.

Dai, J., Ueda, T., & Sato, Y. (2006). Unified analytical approaches for determining shear bond characteristics of FRP-concrete interfaces through pullout tests. Journal of Advanced Concrete Technology, 4(1), 133-145.

De Felice, G., De Santis, S., Garmendia, L., Ghiassi, B., Larrinaga, P., Lourenco, P. B., Oliveira, D. V., Paolacci, F., & Papanicolaou, C. G. (2014) Mortar-based systems for externally bonded strengthening of masonry. Materials and Structures, 47:2021-2037.

Donnini, J., Lancioni, G., Bellezze, T., Corinaldesi, V. (2017). Bond behavior of FRCM carbon yarns embedded in a cementitious matrix: Experimental and numerical results. Key Engineering Materials, 747, 305-312.

Focacci, F., D'Antino, T., Carloni, C., Sneed, L. H., & Pellegrino, C. (2017). An indirect method to calibrate the interfacial cohesive material law for FRCM-concrete joints. Materials & Design, 128, 206-217.

Gonzalez-Libreros, J., D'Antino, T., & Pellegrino, C. (2017). Experimental Behavior of Glass-FRCM Composites Applied onto Masonry and Concrete Substrates. Key Engineering Materials, 747, 390-397.

Gonzalez-Libreros, J. H., Sabau, C., Sneed, L. H., Pellegrino, C., & Sas, G. (2017). State of research on shear strengthening of RC beams with FRCM composites. Construction and Building Materials, 149, 444-458.

Hollaway, L. C. (2010). A review of the present and future utilisation of FRP composites in the civil infrastructure with reference to their important in-service properties: review article. Construction and Building Materials; 24(12), 2419–45.

Ombres, L., Mancuso, N., Mazzucca, S., & Verre, S. (2017). Bond between carbon fabric-reinforced cementitious matrix and masonry substrate. Journal of Materials in Civil Engineering, 31(1), 1-11.

Sabau, C., Gonzalez-Libreros, J. H., Sneed, L. H., Sas, G., Pellegrino, C., & Täljsten, B. (2017). Use of image correlation system to study the bond behavior of FRCM-concrete joints. Materials and Structures, 50(3), 172.

Sneed, L.H., D'Antino, T., & Carloni, C. (2014). Investigation of bond behavior of PBO fiber-reinforced cementitious matrix-composite concrete interface. ACI Materials Journal, 111(5), 569-580.

Sneed, L. H., D'Antino, T., Carloni, C., & Pellegrino, C. (2015). A comparison of the bond behavior of PBO-FRCM composites determined by double-lap and single-lap shear tests. Cement and Concrete Composites, 64, 37-48.

Trapko, T. (2013). The effect of high temperature on the performance of CFRP and FRCM confined concrete elements. Composites Part B: Engineering, 54, 138-145.

Wakjira, T. G., & Ebead, U. (2018). Hybrid NSE/EB technique for shear strengthening of reinforced concrete beams using FRCM: Experimental study. Construction and Building Materials, 164, 164-177.

Younis, A., & Ebead, U. (2018). Bond characteristics of different FRCM systems. Construction and Building Materials, 175, 610-620.

# II. FULL-RANGE BEHAVIOR OF FIBER REINFORCED CEMENTITIOUS MATRIX (FRCM)-CONCRETE JOINTS USING A TRILINEAR BOND-SLIP RELATIONSHIP

Xingxing Zou, Lesley H. Sneed, and Tommaso D'Antino

## ABSTRACT

Interfacial debonding of fiber reinforced cementitious matrix (FRCM)-concrete joints can be considered as a mainly mode-II fracture process, a problem that can be solved by accounting for one-dimensional interfacial shear stress-slip relationships. This paper presents an analytical approach to predict the load response of FRCM-concrete joints by adopting a trilinear bond-slip relationship consisting of a linear-elastic branch, a softening branch, and a friction branch. The applied load-global slip response of FRCM-concrete joints with (relatively) long bonded length includes five stages: elastic, elastic-softening, elastic-softening-debonding, softening-debonding, and debonding stages. Closed-form solutions of the interfacial slip, shear stress, and axial stress (or strain) distribution along the bonded length are provided. The response of FRCM-concrete joints with (relatively) short bonded length is examined. The effective bond length and a critical length for the existence of the snap-back phenomenon are derived. Experimental results reported in the literature are used to calibrate the parameters needed for the analytical approach. The analytical results are then compared with experimental results and with numerical results determined using a finite difference method (FDM). Finally, the capability of determining the parameters in the trilinear bond-slip relationship using a neural network (NN) with the experimental load response as the input is investigated.

**Keywords:** Fiber reinforced cementitious matrix (FRCM) composite, trilinear bond-slip relationship, finite difference method (FDM), neural network (NN).

## 1. INTRODUCTION

A recent innovation in strengthening civil structures is the application of externally bonded reinforcement in the form of fiber-reinforced polymer (FRP) composites, which have a high strength-to-weight ratio, good corrosion resistance, and versatility of application to different cross-sections ([1],[2]). However, the use of polymeric matrix and adhesives makes FRP composites vulnerable to thermal cycles, heat exposure, and ultraviolet (UV) ray exposure ([3],[4],[5]). Fiber reinforced cementitious matrix (FRCM) materials are a new type of composite in which the polymeric matrix is replaced by an inorganic mortar. FRCM composites can provide higher heat resistance and better compatibility with concrete and masonry substrates than FRP composites [6]. Over the past decade, FRCM composites have been increasingly employed for strengthening and repairing civil structures in bending [7], shear ([8],[9],[10]), torsion [11], and confinement ([5],[12]) applications.

The effectiveness of externally bonded FRCM composites relies on the load transfer between the composite and the existing structure. Therefore, a large number of tests have been conducted to study the interfacial stress-transfer mechanism in FRCM-substrate joints ([6],[13],[14],[15]). These studies showed that for the majority of the tests (which include flexural and shear strengthened beams), when a limited number of composite layers is employed (generally up to two), debonding occurs at the fiber-matrix interface and is characterized by fiber-matrix slip ([16],[17]).

Single- and double-lap direct-shear tests are commonly conducted to study the bond at the FRCM-concrete interface [16]. In these tests, the applied load is parallel to the interface, and out-of-plane stresses and displacements are minimized. Though there is an inherent eccentricity between the applied load and support in single-lap shear tests, it was shown that for FRCM-concrete joints the fracture mechanics Mode-I component at the fiber–matrix interface can be neglected given the beneficial effect of the external layer of matrix, i.e., the layer that covers the fibers [17]. Therefore, single-lap shear tests were used to validate a bond-slip relationship based on the definition of an interfacial shear stress-slip relationship $\tau(s)$, also known as a cohesive material law (CML). D'Ambrisi et al. [18] and Focacci et al. [19] studied different $\tau(s)$ relationships for FRCM composites assuming a pure Mode-II interfacial crack propagation at the matrix-fiber interface. Generally, the $\tau(s)$ relationship of FRCM composite-substrate joints consists of an increasing branch until the shear stress reaches the peak value (i.e., shear strength) $\tau_m$, followed by a softening stage. For some FRCM composites, a friction (interlocking) stage characterized by a constant shear stress $\tau_f$ was observed at the end of the softening stage, whereas for others the interfacial shear stress decreased to zero after complete debonding [19]. However, for most continuous equations for $\tau(s)$ reported in the literature, a closed-form solution of the interfacial shear stress and axial stress distributions cannot be obtained for the full-range loading process, unless there is no friction stage after complete debonding ([20],[21]).

For FRP-concrete joints, Yuan et al. [22] derived closed-form solutions of the slip, shear stress, and axial strain distribution based on a bilinear $\tau(s)$. A similar approach was applied to FRCM-substrate joints using a trilinear $\tau(s)$ that is appropriate for situations in which the presence of friction (interlocking) should be taken into account (e.g., certain

externally bonded FRCM composites ([23],[24],[25],[26],[27]), FRP reinforcing bars embedded in concrete [28], FRP ground anchors [29], and grouted rockbolts ([30],[31])). In particular, Carozzi et al. [23] provided the solution for FRCM-masonry joints using a trilinear $\tau(s)$ and conducted a parametric analysis to investigate the effect of the parameters that control the shape of the $\tau(s)$. D'Antino et al. [25] applied a trilinear bond-slip relationship to study the bond behavior of FRCM-concrete joints providing a formulation to compute the effective bond length, i.e. the length of the bond stress transfer zone (STZ). However, the effect of generally-accepted assumptions, such as treating a long bonded length as an infinite bonded length, are in need of study. In addition, the response of FRCM-substrate joints with bonded lengths less than the effective bond length has not been fully investigated.

This paper presents an analytical solution to predict the full-range load response of FRCM-concrete joints that include a frictional branch by adopting a trilinear $\tau(s)$. Behaviors of (relatively) long and short bonded lengths are explored, and the critical length for the existence of snap-back phenomenon and the effective bond length are derived. Load responses of PBO FRCM-concrete joints available in the literature are compared to corresponding analytical solution. Furthermore, the accuracy of the analytical solution is validated by a numerical solution given by a finite difference method (FDM), which is also used to examine whether certain mathematical approximations are reasonable.

A neural network (NN) is then used to conduct an inverse determination of the parameters in the trilinear $\tau(s)$ from experimental load responses. The results obtained show that the analytical solution provides accurate estimations of the experimental load responses.

## 2. GOVERNING EQUATIONS AND BOND-SLIP RELATIONSHIP ADOPTED

Experimental results available in the literature showed that debonding in FRCM-concrete joints can occur: (a) within the concrete substrate, (b) at the concrete-composite interface, (c) at the fiber-matrix interface, (d) within the matrix (matrix delamination), or (e) with a combination of these failure modes [19]. This paper focuses on debonding at the fiber-matrix interface, which was observed for several FRCM composites bonded to concrete and masonry substrates (e.g. [6],[16],[18],[32],[33]). This failure mode is characterized by significant fiber-matrix slip and does not generally induce cracking within the matrix.

When debonding at the fiber-matrix interface occurs, the deformation of concrete and matrix can be usually neglected, as discussed by D'Antino et al. [17]. As a result, the fibers can be assumed to be under uniaxial tension and the fiber-matrix interface under interfacial shear deformation only [6]. In addition, the following assumptions are adopted in this paper: (i) the slip is assumed to be the same in each longitudinal fiber bundle across the width of the composite, and the externally applied load is assumed to be equally distributed among the longitudinal fiber bundles; (ii) a linear-elastic constitutive law is adopted for the longitudinal fiber bundles; (iii) a zero-thickness cohesive interface is assumed between the matrix and fibers, and its behavior is modelled with a trilinear $\tau(s)$ (see Figure 1a); and (iv) the presence and influence of FRCM transversal fiber bundles is neglected.

Based on the aforementioned assumptions, the governing equation can be obtained by enforcing force equilibrium of an infinitesimal portion, as shown in Figure 2a:

$$\frac{d\sigma(y)}{dy} - \frac{\tau(s)}{t^*} = 0 \tag{1}$$

where $y$ is the axial coordinate along the composite bonded length with the origin at the free end (see Figure 2), $\tau(s)$ is the total shear stress considering the entire contact surface of the outer and inner layers of matrix (see Figure 2), $t^*$ is the thickness of the longitudinal fiber bundles, and $\sigma(y)$ is the axial stress in the longitudinal fiber bundles along the bonded length. Assumption (ii) provides:

$$\sigma(y) = E_f \varepsilon(y) = E_f \frac{ds(y)}{dy} \tag{2}$$

where $E_f$ is the elastic modulus of the fibers. Substituting Eq. (2) into Eq. (1), the governing equation can be written as:

$$\frac{d^2 s(y)}{dy^2} - \frac{s_f}{\tau_m} \lambda^2 \tau(s) = 0 \tag{3}$$

where $\lambda = \sqrt{\frac{\tau_m}{s_f E_f t^*}}$. Eq. (3) can be solved once $\tau(s)$ is defined.

The trilinear $\tau(s)$ considered in this paper is composed of three branches shown in Figure 1a: (i) a linear-elastic branch from the origin to the peak shear stress $\tau_m$, which is associated with a slip $s_m$; (ii) a linear softening branch until the shear stress decreases to $\tau_f$, which is associated with a slip $s_f$; and, (iii) a debonding branch with a constant residual shear stress $\tau_f$ due to friction between the matrix and fibers. The last branch is assumed to be infinite.

The trilinear $\tau(s)$ is defined as:

$$\tau(s) = \begin{cases} \dfrac{\tau_m}{s_m} s, 0 \le s \le s_m \\ \tau_m \left[ \dfrac{(s_f - s) + \mu(s - s_m)}{s_f - s_m} \right], s_m \le s \le s_f \\ \mu\tau_m, s \ge s_f \end{cases} \quad (4)$$

where $\mu$ is defined as the ratio of the residual shear stress $\tau_f$ and the peak stress $\tau_m$, i.e., $\tau_f = \mu\tau_m$. It should be noted that $\mu = 0$ denotes that no friction exists at the debonding interface, such as usually assumed for FRP-concrete joints [22]. A non-zero value of $\mu$ has been reported for certain FRCM composites including a polyparaphenylene benzobisoxazole (PBO)-FRCM composite ([16],[18],[19],[34]), which is considered in the present study. Substituting Eq. (4) into Eq. (3), the governing differential equation can be rewritten as:

$$\frac{d^2 s(y)}{dy^2} = \begin{cases} \lambda_1^2 s(y), 0 \le s \le s_m \\ -\lambda_3^2 s(y) + \lambda_2^2 (s_f - \mu s_m), s_m \le s \le s_f \\ \lambda^2 \mu s_f, s \ge s_f \end{cases} \quad (5)$$

where $\lambda_1 = \lambda \sqrt{\frac{s_f}{s_m}}$, $\lambda_2 = \lambda \sqrt{\frac{s_f}{s_f - s_m}}$, $\omega = \sqrt{1 - \mu}$, and $\lambda_3 = \lambda_2 \omega$.

As indicated in ([25],[35]), when the composite bonded length is relatively long (see discussion in Section 3.3), five stages can be identified in the load response (see Figure 1b): I) elastic; II) elastic-softening; III) elastic-softening-debonding; IV) softening-debonding; and V) debonding stages. The general applied load $P$ versus global slip $g$ (i.e., loaded end slip) curve for long bonded length is shown in Figure 1b, whereas the corresponding shear stress distribution along the bonded length is illustrated in Figure 2. For direct-shear tests of FRCM-concrete joints that are controlled by monotonically increasing $P$, the test stops at the peak load (Point C). If the test is controlled by

monotonically increasing $g$, the snap-back phenomenon shown in Figure 1b cannot be captured ([36],[37]). Curve snap-back in FRP-concrete joints was observed by controlling the free end slip $s_F$ [37]. Further discussion on snap-back is provided in Section 7.1.

## 3. ANALYSIS OF THE FULL-RANGE BEHAVIOR OF FRCM-CONCRETE JOINTS WITH LONG BONDED LENGTH

In this section, the full-range behavior for FRCM-concrete joints with long bonded length is derived. The criterion for the critical length that differentiates the solutions given in Sections 3 and 4 will be discussed in Section 3.3. The full-range solutions are driven by the free end slip $s_F$, i.e., $s(0) = s_F$ serves as the boundary condition for all stages.

The following boundary condition will be used for the solutions of all stages:

$$\sigma(0) = 0 \tag{6}$$

Also, Eq. (7) will be used to compute the applied load:

$$\sigma(\ell) = \frac{P}{t^* b_f} \tag{7}$$

where $\ell$ is the composite bonded length (see Figure 2), and $b_f = nb^*$ is the total width of the longitudinal fiber bundles, where $n$ is the number of longitudinal fiber bundles, and $b^*$ is the width of a single fiber bundle.

### 3.1. ELASTIC STAGE (STAGE I)

As $s_F$ increases from zero to a small value, the applied load and global slip values are also small, and the entire bonded length is governed by the first piece of Eq. (5) (see Figure 2b and segment OA in Figure 1b). The slip $s(y)$, shear stress $\tau(y)$, and axial fiber stress $\sigma(y)$ can be obtained under the boundary condition of Eq. (6) as:

$$s(y) = s_F \cosh(\lambda_1 y) \tag{8}$$

$$\tau(y) = \frac{\tau_m}{s_m} s_F \cosh(\lambda_1 y) \tag{9}$$

$$\sigma(y) = \frac{\tau_m}{s_m \lambda_1 t^*} s_F \sinh(\lambda_1 y) \tag{10}$$

Eq. (8) can be used to obtain the slip at the loaded end $g = s(\ell) = s_F \cosh(\lambda_1 \ell)$, which indicates that $s_F \ll g$ for long bonded length because $\cosh(\lambda_1 \ell)$ is usually much larger than 1.0. Substituting Eq. (10) into Eq. (7), the applied load can be obtained as:

$$P = \left(\frac{b_f \tau_m}{\lambda_1}\right) \sinh(\lambda_1 \ell) \frac{s_F}{s_m} = \left(\frac{b_f \tau_m}{\lambda_1}\right) \frac{\tanh(\lambda_1 \ell)}{s_m} g \tag{11}$$

Eq. (11) indicates that $P$ increases proportionally with $g$ (see the linear segment OA in Figure 1b) and with $s_F$. The elastic stage ends when $g = s_m$, whereas $s_F = s_m / \cosh(\lambda_1 \ell)$ (Point A in Figure 1b and shear stress distribution A in Figure 2b). The applied load at the end of the elastic stage $P_A$ can be obtained by setting $g = s_m$ in Eq. (11) as:

$$P_A = \left(\frac{b_f \tau_m}{\lambda_1}\right) \tanh(\lambda_1 \ell) \tag{12}$$

### 3.2. ELASTIC-SOFTENING STAGE (STAGE II)

As $s_F$ increases, a softening branch commences at the composite loaded end, and the shear stress decreases along a softening length, $l_{sf}$ (see Figure 2b and segment AB in Figure 1b). The location of the peak shear stress $\tau_m$ moves towards the composite free end. When the shear stress at the loaded end attains $\tau_f$, debonding starts to occur (the applied load is the debonding load $P_{deb}$) and Stage II ends (Point B in Figure 1b and shear stress distribution B in Figure 2b).

During the elastic-softening stage, the first and second pieces of Eq. (5) can be solved considering the following compatibility conditions together with Eq. (6):

$$\sigma^{-}(l_{el}) = \sigma^{+}(l_{el}) \tag{13}$$

$$s(l_{el}) = s_m \text{ or } \tau(l_{el}) = \tau_m \tag{14}$$

where $l_{el}$ is the interface length engaged in the elastic stress-transfer mechanism, i.e., the elastic region. The solution for the elastic region of the interface where $s_F \leq s \leq s_m$ (or $0 \leq y \leq l_{el}$ ) can be expressed by Eqs. (8-10). Thus, $l_{el}$ can be obtained by solving $s^{-}(l_{el}) = s_m$ provided by Eq. (8) (see Figure 2b):

$$l_{el} = \frac{1}{\lambda_1}\operatorname{arccosh}\left(\frac{s_m}{s_F}\right) \tag{15}$$

Eq. (15) indicates that $l_{el}$ decreases with the increasing of $s_F$. The solution for the softening region ($s_m \leq s \leq s_f$ and $l_{el} \leq y \leq \ell$) is:

$$s(y) = \left(s_f - s_m\right)\left[\frac{\lambda_2}{\lambda_1\omega}\sin[\lambda_3(y-l_{el})]\tanh(\lambda_1 l_{el}) - \frac{\cos[\lambda_3(y-l_{el})]}{1-\mu}\right] + \frac{s_f - \mu s_m}{1-\mu} \tag{16}$$

$$\tau(y) = -\tau_m\left[\frac{\lambda_3}{\lambda_1}\sin[\lambda_3(y-l_{el})]\tanh(\lambda_1 l_{el}) - \cos[\lambda_3(y-l_{el})]\right] \tag{17}$$

$$\sigma(y) = \frac{\tau_m}{t^{*}\lambda_3}\left[\frac{\lambda_3}{\lambda_1}\cos[\lambda_3(y-l_{el})]\tanh(\lambda_1 l_{el}) + \sin[\lambda_3(y-l_{el})]\right] \tag{18}$$

Substituting Eq. (18) into Eq. (7), the applied load is obtained as:

$$P = \frac{b_f\tau_m}{\lambda_3}\left[\frac{\lambda_3}{\lambda_1}\cos(\lambda_3 l_{sf})\tanh(\lambda_1 l_{el}) + \sin(\lambda_3 l_{sf})\right] \tag{19}$$

Eq. (16) gives $g$ as:

$$g = s(\ell) = (s_f - s_m)\left[\frac{\lambda_2 \sin(\lambda_3 l_{sf}) \tanh(\lambda_1 l_{el})}{\lambda_1 \omega} - \frac{\cos(\lambda_3 l_{sf})}{1-\mu} + \frac{s_f - \mu s_m}{(1-\mu)(s_f - s_m)}\right] \quad (20)$$

At the debonding load $P_{deb}$, the shear stress at the loaded end is $\tau_f$, so substituting $\tau(\ell) = \tau_f$ into Eq. (17) leads to:

$$\frac{\lambda_1}{\lambda_3}\left(\frac{\cos(\lambda_3 l_{sf}) - \mu}{\sin(\lambda_3 l_{sf})}\right) = \tanh(\lambda_1 l_{el}) \quad (21)$$

Considering that $l_{el} = \ell - l_{sf}$, Eq. (21) can be solved iteratively to compute the value of the softening length at the debonding load, $l_{sf,d}$ (Figure 2b). Then $l_{el}$ at the debonding load can be obtained, and the corresponding value of $s_F$ at the debonding load, denoted as $s_{F,deb}$, can be determined by Eq. (15). Finally, the debonding load $P_{deb}$ can be determined by substituting $l_{sf,d}$ into Eq. (19):

$$P_{deb} = \frac{b_f \tau_m}{\lambda_3}\left[\frac{\lambda_3}{\lambda_1}\cos(\lambda_3 l_{sf,d}) \tanh(\lambda_1 l_{el}) + \sin(\lambda_3 l_{sf,d})\right] \quad (22)$$

### 3.3. ELASTIC-SOFTENING-DEBONDING STAGE (STAGE III)

With the increasing of $s_F$, a debonding branch associated with a constant shear stress and with a length of $l_{db}$ develops at the loaded end (see Figure 2c and segment BCD in Figure 1b). With the development of $l_{db}$, an approximately linear increase of the applied load $P$ due to the presence of friction occurs. The peak applied load, denoted by $P^*$ (see Point C in Figure 1b), is reached within this stage.

The three pieces of Eq. (5) that describe this stage are solved considering the following compatibility conditions together with Eq. (6):

$$\sigma^-(l_{el}) = \sigma^+(l_{el}) \quad (23)$$

$$\sigma^{-}(\ell - l_{db}) = \sigma^{+}(\ell - l_{db}) \tag{24}$$

$$s(\, l_{el}) = s_m \text{ or } \tau(\, l_{el}) = \tau_m \tag{25}$$

$$s(\ell - l_{db}) = s_f \text{ or } \tau(\ell - l_{db}) = \mu\tau_m \tag{26}$$

where $l_{db} = \ell - l_{sf} - l_{el}$ (see Figure 2c), and $l_{el}$ can still be computed by Eq. (15). The solutions for the elastic ($0 \le y \le l_{el}$) and softening ($l_{el} \le y \le \ell - l_{db}$) regions are in the same form of those obtained in Stages I and II, respectively. The solution for the debonding region of the interface where $s \ge s_f$ (or $l_{el} + l_{sf} \le y \le \ell$) is:

$$\begin{aligned} s(y) = s_f + \frac{s_f}{2}\lambda^2\left[y - \left(l_{el} + l_{sf}\right)\right]\Bigg\{\mu y - \mu\left(l_{el} + l_{sf}\right) \\ + 2\left[\frac{\sin\left(\lambda_3 l_{sf}\right)}{\lambda_3} + \frac{\cos\left(\lambda_3 l_{sf}\right)\tanh(\lambda_1 l_{el})}{\lambda_1}\right]\Bigg\} \end{aligned} \tag{27}$$

$$\tau(y) = \mu\tau_m \tag{28}$$

$$\sigma(y) = \frac{\tau_m}{t^*}\left[\mu\left(y - \left(l_{el} + l_{sf}\right)\right) + \frac{\sin(\lambda_3 l_{sf})}{\lambda_3} + \frac{\cos\left(\lambda_3 l_{sf}\right)\tanh(\lambda_1 l_{el})}{\lambda_1}\right] \tag{29}$$

Substituting $\tau\left(l_{el} + l_{sf}\right) = \mu\tau_m$ into Eq. (17) provides the same equation as Eq. (21). Increasing the free end slip $s_F$ from $s_{F,deb}$ (beginning of Stage III) to $s_m$ (end of Stage III), the general solution of Eq. (21) considering Eq. (15) is given as:

$$l_{sf} = \frac{1}{\lambda_3}\arccos\left(\frac{\mu + \frac{\lambda_3}{\lambda_1}\sqrt{1 - \left(\frac{s_F}{s_m}\right)^2}\sqrt{2 - \mu^2 - \left(\frac{s_F}{s_m}\right)^2}}{2 - \left(\frac{s_F}{s_m}\right)^2}\right) \tag{30}$$

Substituting Eqs. (15) and Eq. (30) into Eqs. (27-29) gives the solution of $s(y)$ and $\sigma(y)$ as a function of $s_F$. Eq. (30) indicates that with the increasing of $s_F$, the softening length $l_{sf}$ increases. Stage III ends when the length of the elastic zone is reduced to zero

($l_{el} = 0$ and $s_F = s_m$) and $l_{sf}$ attains its maximum value (denoted by $l_{sf,u}$):

$$l_{sf,u} = \frac{1}{\lambda_3}\arccos(\mu) \tag{31}$$

Eq. (31) indicates that $l_{sf,u}$ is an upper limit for $l_{sf}$ and is not a function of the bonded length. If $\mu = 0$, Eq. (31) gives $l_{sf,u} = \frac{\pi}{2\lambda_3}$, which is identical to the result for FRP-concrete joints given by [22]. If the bonded length is less than $l_{sf,u}$, the elastic and debonding regions will not coexist for any value of the free end slip, i.e., before the shear stress at the composite loaded end drops to $\mu\tau_m$, the shear stress at the free end reaches $\tau_m$, so the solution in this section no longer holds. Therefore, $l_{sf,u}$ is the minimum length needed to fully establish the softening stage. It should be noted that the minimum length required to attain $P_{deb}$ is the effective bond length $l_{eff}$, which is longer than $l_{sf,u}$ if a trilinear $\tau(s)$ is employed. $l_{sf,u}$ is equal to $l_{eff}$ only in the case a rigid-softening $\tau(s)$ is considered [38]. For bonded length $l_{sf,u} \leq \ell < l_{eff}$, the solution given in Section 3 applies, however $P_{deb}$ cannot be obtained.

For $\ell < l_{sf,u}$, the elastic-softening-debonding stage that exists for specimens with $\ell \geq l_{sf,u}$ will be replaced by a pure softening stage, as discussed in Section 4.

Substituting Eq. (29) and $y = \ell$ into Eq. (7) and considering $l_{el} + l_{sf} + l_{db} = \ell$, the applied load is given as:

$$P = b_f\tau_m\left[\mu l_{db} + \frac{\sin(\lambda_3 l_{sf})}{\lambda_3} + \frac{1}{\lambda_1}\cos(\lambda_3 l_{sf})\tanh[\lambda_1(\ell - l_{sf} - l_{db})]\right] \tag{32}$$

The applied load $P$ reaches its maximum value $P^*$ when the derivative of Eq. (32) with respect to $l_{db}$ is zero. If it is assumed that the variation of $l_{sf}$ is negligible with respect

to that of $l_{db}$ and its value is denoted as $l_{sf}^*$ at the peak load $P^*$, $P$ can be considered as a function of $l_{db}$ only; therefore, $\frac{\partial P}{\partial l_{db}} = 0$ gives:

$$\tanh^2\left[\lambda_1(\ell - l_{sf}^* - l_{db})\right] = 1 - \mu/\cos(\lambda_3 l_{sf}^*) \tag{33}$$

The solution of Eq. (33) provides $l_{db}$ at the peak load, denoted as $l_{db}^*$:

$$l_{db}^* = \ell - l_{sf}^* - \frac{1}{\lambda_1}\operatorname{arctanh}\left(\sqrt{1 - \frac{\mu}{\cos(\lambda_3 l_{sf}^*)}}\right) \tag{34}$$

It should be noted that $l_{sf,d} \leq l_{sf}^* \leq l_{sf,u}$ and for $l_{sf}^* = l_{sf,d}$, Eq. (34) provides the same result as the equation for the debonding length at the peak load obtained in [30].

Substituting $l_{db}^*$ into Eq. (32) gives the peak load $P^*$ as:

$$P^* = b_f \tau_m \left[\mu l_{db}^* + \frac{\sin(\lambda_3 l_{sf}^*)}{\lambda_3} + \frac{1}{\lambda_1}\cos(\lambda_3 l_{sf}^*)\tanh\left[\lambda_1(\ell - l_{sf}^* - l_{db}^*)\right]\right] \tag{35}$$

For infinite bonded length, the term $(\ell - l_{sf}^* - l_{db}^*)$ is also infinite, so $\tanh\left[\lambda_1(\ell - l_{sf}^* - l_{db}^*)\right] = 1$. Thus, considering Eq. (22), Eq. (35) can be written as:

$$P^* = P_{deb} + \mu \tau_m b_f l_{db}^* \tag{36}$$

which indicates that the contribution of friction is proportional to the shear stress $\mu\tau_m$ and to the contact area $b_f l_{db}^*$ as postulated in the literature ([6],[25]). It should be noted, however, that with the trilinear relationship adopted, Eq. (36) strictly holds only for infinite bonded length, whereas for finite bonded lengths, $P^* < P_{deb} + \mu \tau_m b_f l_{db}^*$. This result is common when bond-slip relationships with $\tau(0)=0$ and $d\tau/ds \neq \infty$ are employed [39].

$g$ in Stage III can be obtained from Eq. (27) as:

$$g = s(\ell) = s_f + s_f \lambda^2 l_{db}\left[\frac{\mu l_{db}}{2} + \frac{\sin(\lambda_3 l_{sf})}{\lambda_3} + \frac{1}{\lambda_1}\cos(\lambda_3 l_{sf})\tanh(\lambda_1 l_{el})\right] \tag{37}$$

At the peak load, the free end slip and loaded end slip can be obtained as:

$$s_F^* = \frac{s_m}{\cosh\left[\lambda_1\left(\ell - l_{db}^* - l_{sf}^*\right)\right]} \tag{38}$$

$$g^* = s_f + s_f\lambda^2 l_{db}^* \left[\frac{\mu l_{db}^*}{2} + \frac{\sin(\lambda_3 l_{sf}^*)}{\lambda_3} + \frac{\cos(\lambda_3 l_{sf}^*)\tanh\left[\lambda_1\left(\ell - l_{db}^* - l_{sf}^*\right)\right]}{\lambda_1}\right] \tag{39}$$

### 3.4. SOFTENING-DEBONDING STAGE (STAGE IV)

Stage III ends when $s_F = s_m$ and the peak shear stress reaches the free end, $\tau(0) = \tau_m$ (see shear stress distribution D in Figure 2c). Hereafter the interface is subjected to softening and friction shear stresses only (softening-debonding stage, see Figure 2c and segment DE in Figure 1b). Stage IV is described by the second and third pieces of Eq. (5), which can be solved considering the following compatibility conditions and Eq. (6):

$$\sigma^-\left(l_{sf}\right) = \sigma^+\left(l_{sf}\right) \tag{40}$$

$$s\left(l_{sf}\right) = s_f \text{ or } \tau\left(l_{sf}\right) = \mu\tau_m \tag{41}$$

The solution for the softening region with $0 \le y \le l_{sf}$ is:

$$s(y) = \frac{s_f - \mu s_m}{1-\mu} - \left(\frac{s_f - \mu s_m}{1-\mu} - s_F\right)\cos(\lambda_3 y) \tag{42}$$

$$\tau(y) = \left(\frac{1-\mu}{s_f - s_m}\right)\left(\frac{s_f - \mu s_m}{1-\mu} - s_F\right)\tau_m\cos(\lambda_3 y) \tag{43}$$

$$\sigma(y) = E_f\lambda_3\left(\frac{s_f - \mu s_m}{1-\mu} - s_F\right)\sin(\lambda_3 y) \tag{44}$$

Substituting $s\left(l_{sf}\right) = s_f$ into Eq. (42) gives the relationship between $l_{sf}$ and $s_F$:

$$l_{sf} = \frac{1}{\lambda_3}\arccos\left[\left(\frac{\mu}{1-\mu}\right)\frac{s_f - s_m}{\left(\frac{s_f - \mu s_m}{1-\mu} - s_F\right)}\right] \tag{45}$$

In this stage $s_F$ ranges from $s_m$ to $s_f$, and accordingly Eq. (45) indicates that the value of $l_{sf}$ ranges from $l_{sf,u}$ to 0. The solution for the debonding region with $l_{sf} \leq y \leq \ell$ is:

$$s(y) = s_f + s_f \left[ \frac{\tan(\lambda_3 l_{sf})}{\lambda_3} (y - l_{sf}) + \frac{1}{2} (y - l_{sf})^2 \right] \tag{46}$$

$$\tau(y) = \mu \tau_m \tag{47}$$

$$\sigma(y) = \frac{\mu \tau_m}{t^*} \left[ y - l_{sf} + \frac{\tan(\lambda_3 l_{sf})}{\lambda_3} \right] \tag{48}$$

Substituting Eq. (48) and $y = \ell$ into Eq. (7) gives the applied load $P$:

$$P = \mu \tau_m b_f \left[ \ell - l_{sf} + \frac{\tan(\lambda_3 l_{sf})}{\lambda_3} \right] \tag{49}$$

The global slip can be obtained by imposing $y = \ell$ in Eq. (46):

$$g = s_f \left[ 1 + \frac{\mu \lambda^2}{\lambda_3} \tan(\lambda_3 l_{sf}) (\ell - l_{sf}) + \frac{\mu \lambda^2}{2} (\ell - l_{sf})^2 \right] \tag{50}$$

### 3.5. DEBONDING STAGE (STAGE V)

The debonding stage (Stage V) starts when the softening zone disappears (Point E in Figure 1b). In this stage, the load-carrying capacity is solely provided by interface friction, as shown by the shear stress distribution E in Figure 2c. The solution for the debonding region with $0 \leq y \leq \ell$ is:

$$s(y) = s_F + \frac{s_f}{2} \mu \lambda^2 y^2 \tag{51}$$

$$\tau(y) = \mu\tau_m \tag{52}$$

$$\sigma(y) = \frac{\mu\tau_m}{t^*} y \tag{53}$$

The global slip at the end of the Stage IV (Point E in Figure 1b), denoted by $g_E$, can be obtained from Eq. (50) by setting $l_{sf} = 0$ or substituting $s_F = s_f$ in Eq. (51):

$$g_E = s_f + \frac{s_f}{2}\mu\lambda^2\ell^2 \tag{54}$$

The shear stress is constant along the entire bonded length and equal to $\mu\tau_m$. Therefore, the applied load maintains a constant value $P_f = 2b_f\mu\tau_m\ell$ (see segment EF in Figure 1b and the shear stress distribution in Figure 2c).

## 4. ANALYSIS OF THE BEHAVIOR OF FRCM-CONCRETE JOINTS WITH $\ell < l_{sf,u}$

For FRCM-concrete joints with bonded length $\ell < l_{sf,u}$, the softening stage cannot be fully established (see Section 3.3). In general, the load response can be subdivided into five stages (see Figure 1b): elastic (Stage I, segment OA'); elastic-softening (Stage II, segment A'C'D'); softening (Stage III, segment D'E'); softening-debonding (Stage IV, segment E'F'); and debonding (Stage V, segment F'G') stages. The shear stress distribution along the bonded length is shown in Figure 3.

The solution for the elastic stage can be determined by Eqs. (8)-(10). Eq. (13) can be used to compute the load at the end of the elastic stage.

The solution for the elastic-softening stage can be determined by Eqs. (16)-(18), and Eq. (19) can be used to compute the applied load. The peak load $P^*$ occurs in the elastic-

softening stage when $\frac{\partial P}{\partial l_{sf}} = 0$, which provides:

$$\frac{\lambda_3}{\lambda_1}\tan(\lambda_3 l_{sf}) = \tanh[\lambda_1(\ell - l_{sf})] \tag{55}$$

Eq. (55) is a transcendental equation that cannot be solved analytically and requires a numerical method to find its solution. Indicating the solution of Eq. (55) as $l_{sf}^*$ (see Figure 3), $P^*$ can be computed by replacing $l_{sf}$ with $l_{sf}^*$ in Eq. (19):

$$P^* = \frac{b_f \tau_m}{\lambda_3}\left[\frac{\lambda_3}{\lambda_1}\cos(\lambda_3 l_{sf}^*)\tanh[\lambda_1(\ell - l_{sf}^*)] + \sin(\lambda_3 l_{sf}^*)\right] \tag{56}$$

The elastic-softening stage ends when the entire bonded length enters the softening stage, i.e., $l_{sf} = \ell$. Thus, the corresponding load (Point D' in Figure 1b) is:

$$P_{D'} = \frac{b_f \tau_m}{\lambda_3}\sin(\lambda_3 \ell) \tag{57}$$

In the softening stage, all the shear stresses along the entire bonded length are within the softening branch (see Figure 1b and Figure 3). The shear stress distribution along the bonded length is described by the second piece of Eq. (5), which can be solved considering Eqs. (6) and (7):

$$s(y) = -\frac{\lambda_3 P}{\tau_m b_f}\frac{(s_f - s_m)}{(1-\mu)}\frac{\cos(\lambda_3 y)}{\sin(\lambda_3 \ell)} + \frac{s_f - \mu s_m}{1-\mu} \tag{58}$$

$$\tau(y) = \frac{\lambda_3 P}{b_f}\frac{\cos(\lambda_3 y)}{\sin(\lambda_3 \ell)} \tag{59}$$

$$\sigma(y) = \frac{P}{t^* b_f}\frac{\sin(\lambda_3 y)}{\sin(\lambda_3 \ell)} \tag{60}$$

$s_F$ and $g$ can be obtained by imposing $y = 0$ and $y = \ell$ into Eq. (58), respectively:

$$s_F = -\frac{\lambda_3 P}{\tau_m b_f}\frac{(s_f - s_m)}{(1-\mu)}\frac{1}{\sin(\lambda_3 \ell)} + \frac{s_f - \mu s_m}{1-\mu} \tag{61}$$

$$g = -\frac{\lambda_3 P}{\tau_m b_f}\frac{(s_f - s_m)}{(1-\mu)}\frac{1}{\tan(\lambda_3 \ell)} + \frac{s_f - \mu s_m}{1-\mu} \tag{62}$$

Eqs. (61) and (62) indicate that $P$ decreases proportionally with both $s_F$ and $g$. Stage III starts at $s_F = s_m$ and ends when $g = s_f$.

When $g > s_f$, the interface enters the softening-debonding stage (Stage IV). The solution for this stage can be determined by Eqs. (42)-(44) and Eqs. (46)-(48). When the interface is fully debonded, i.e., $l_{sf} = 0$, the load response is in the debonding stage (Stage V), and the applied load is equal to $P_f$. The solution for the debonding stage can be determined by Eqs. (51)-(53).

## 5. VALIDATION OF ANALYTICAL RESULTS

In this section, trilinear bond-slip relationships previously determined from the results of single-lap direct-shear tests of FRCM-concrete joints with different bonded lengths reported in the literature [40] are employed in the analytical solutions presented in Sections 3 and 4 and compared with corresponding experimental load responses. Then, a numerical solution for Eq. (5) is provided and compared with the analytical solutions given in Sections 3 and 4.

### 5.1 VALIDATION WITH EXPERIMENTAL RESULTS

In a previous study [40], the authors calibrated a bond-slip relationship for FRCM-concrete joints with one layer of fiber mesh and one or two layers of matrix using seven

specimens equipped with strain gauges attached to the fibers along the bonded length and tested using a single-lap direct-shear set-up originally reported in [41]. The fiber mesh was a PBO bidirectional fiber textile with fiber bundles, which were assumed to have rectangular cross-section, with thickness $t^*$ = 0.092 mm and width $b^*$=5 mm. The elastic modulus $E_f$ = 206 GPa of the fibers in the longitudinal direction was determined from tensile tests of the bare fiber bundles in ([6],[17]). Two different bonded widths (43 mm and 60 mm, which include $n$=5 and 7 longitudinal bundles, respectively) and two different bonded lengths (ℓ=330 mm and 450 mm) were adopted for the specimens. The characteristics of the five specimens with two layers of matrix are summarized in Table 1.

The bond-slip relationship calibrated in [40] for the specimens with one fiber layer embedded within two layers of matrix is named Model_0 and is shown in Figure 4. The parameters $s_m$, $s_f$, $\tau_f$, and $\tau_m$ were determined by fitting the strain gauge measurements with an analytical $\tau(s)$ [40] and are summarized in Table 2. Table 2 also provides the interfacial fracture energy $G_F$ (referred to as $G_{F,2}$ in [40]), which is the area under the $\tau(s)$ curve for $0 \leq s \leq s_f$. It should be noted that Model_0 was determined from non-linear regression analysis of experimentally measured fiber strain profiles along the bonded length. The $\tau(s)$ obtained provided close estimation of the debonding load, although the friction stress $\tau_f$ and corresponding slip $s_f$ determined were different from those previously reported in [6].

To analyze the capability of the analytical approach proposed to reproduce the load response of FRCM-concrete joints, three trilinear bond-slip relationships were defined by enforcing: (i) Model_1: the same parameters $s_m$, $s_f$, $\tau_f$, and $\tau_m$ of Model_0; (ii) Model_2: the same ascending branch and same fracture energy $G_F$ of Model_0; and (iii) Model_3:

the same parameters $s_m$, $s_f$, $\tau_f$, and $G_F$ of Model_0. Table 2 summarizes the parameters of each bond-slip relationship, and Model_1-3 are shown in Figure 4.

Figure 5 plots the strain profiles obtained by the analytical approach using Model_1-3 at the debonding load along with the values of strain experimentally measured by strain gauges at discrete locations. The strains close to the loaded end determined using Model_1 are lower than the values determined by Model_2-3 because Model_1 has a lower fracture energy (see Table 2).

Figure 6 compares the experimental and analytical $\sigma$-$g$ responses of the specimens, where $\sigma$ is the applied stress given by Eq. (7). The experimental results have a wide scatter, nevertheless, good agreement can be observed in the ascending region. Specimen DS_330_43_S_3$^T$, in particular, exhibited a lower stress response than other specimens in the same series (see the peak applied stress in Figure 7). The snap-back phenomenon provided by the analytical solution is different from the post-peak behavior observed in the experimental tests. The reason for this difference is the control mode adopted to obtain the experimental and analytical responses. In the analytical solution, the post-peak behavior was driven by increasing $s_F$, which allows the development of the snap-back process, whereas the experimental tests were controlled by monotonically increasing $g$ [6]. The snap-back phenomenon is discussed further in Section 7.1.

The analytical peak stresses $\sigma^*$, computed by Eqs. (37), (58), and (65) and using Model_1-3, were also validated using the results of 42 specimens of the same PBO FRCM composite with different bonded lengths and widths described in [19]. The experimental and analytical results are compared in Figure 7. Good agreement was achieved between the analytical results and the test data with long bonded lengths. For relatively short bonded

lengths ($\ell \leq 150$ mm), the analytical approach tended to overestimate the experimental peak stress. This can be explained in part by the fact that experimental results of specimens with short bonded length are more sensitive to Mode-I effects [17]. Further investigation is needed to determine if the model proposed can be applied to specimens with bonded length less than 150 mm.

## 5.2 VALIDATION USING NUMERICAL SOLUTION

The finite difference method (FDM) was used to numerically solve the governing equation Eq. (5) in order to validate the results obtained by the analytical approach considering the same PBO FRCM composite discussed in Section 5.1. The principles and applications of FDM to solve the differential equation with different bond-slip relationships were reported in [42] for FRP-concrete joints. The methodology adopted in this paper is summarized in the Appendix. The bonded length was discretized into 1000 elements, and a Matlab routine was used to generate the full-range behavior for different bonded lengths based on the equations in Sections 3 and 4. Table 2 provides the value of $l_{sf,u}$ determined for the three trilinear relationships considered, whereas Figure 8 compares the $P$-$g$ and $P$-$s_F$ responses for two long bonded lengths ($\ell$=330 mm and $\ell$=450 mm) (Figure 8a) and two short bonded lengths ($\ell$=50 mm and $\ell$=150 mm) (Figure 8b) determined by the analytical (solid lines) and FDM (dashed lines) approaches using Model_1 (see Figure 4 and Table 2). It can be seen in Figure 8 that the analytical solutions matched well with the numerical results for all bonded lengths considered.

Figure 9 shows the distribution of slip, strain, and shear stress along the bonded length at key values of the applied load for a bonded length $\ell$=330 mm obtained with the

FDM and with the analytical solutions with Model_1. Again, good agreement between the analytically and numerically determined values was achieved. At low load levels (equal to or lower than the debonding load), the numerical and analytical curves are almost identical. However, owing to the error caused by Eq. (34) (as discussed in Section 3.3), the peak load obtained by Eq. (35) is slightly different than the FDM solution, and therefore the analytical curves of slip, strain, and shear stress are slightly different than the results obtained with the FDM solution.

# 6. DETERMINATION OF PARAMETERS IN THE TRILINEAR BOND-SLIP RELATIONSHIP FROM MEASURED *P-g* RESPONSE USING NEURAL NETWORK METHOD

Obtaining the four parameters ($\tau_m, s_m, \mu, s_f$) in the trilinear bond-slip relationship may be challenging for specimens without measurements of longitudinal fiber strains. This section utilizes a neural network to determine the parameters in the trilinear bond-slip relationship from the measured applied load-global slip response, considering the same PBO FRCM composite discussed in Section 5.1. The main appeal of the approach presented in this section is that it reduces the demand on test instrumentation by not requiring strain readings.

If the friction stress $\tau_f$ can be determined from the load response (see Section 3.5), the number of unknown parameters can be reduced to three ($\tau_m, s_m, s_f$), which reduces the complexity of the neural network. In this study, the average value of $\tau_f$ determined experimentally from specimens in [6] with both internal and external layers of matrix (Figure 2) is 0.12 MPa.

Several features of the ascending part of the experimentally determined $P$-$g$ curve obtained for long bonded length specimens were used to obtain the parameters in the trilinear bond-slip relationship. Five features were selected: the slope of the $P$-$g$ curve in the elastic stage $k_e$, the load at the end of the elastic stage $P_A$ , the peak load $P^*$, the global slip at peak load $g^*$, and the area of ascending part of the $P$-$g$ curve denoted as $G_P$ (see Figure 10a). The steps needed to predict the parameters $(\tau_m, s_m, s_f)$ using a neural network are: (i) determine the ranges of the three parameters of $(\tau_m, s_m, s_f)$, and discretize them into $j$ values as $(\tau_{m1}, \tau_{m2}, \dots, \tau_{mj})$, $(s_{m1}, s_{m2}, \dots, s_{mj})$, and $(s_{f1}, s_{f2}, \dots, s_{fj})$; (ii) for each of the $j^3$ combinations of $(\tau_m, s_m, s_f)$, compute the $P$-$g$ curve and determine the values of $(k_e, P_A, P^*, g^*, G_P)$ using the analytical procedure described in Section 3; (iii) use the analytically determined results of $(k_e, P_A, P^*, g^*, G_P)$ as the input for the neural network (see Figure 10b) and the corresponding combinations of $(\tau_m, s_m, s_f)$ as the output and train the neural network with the $j^3$ combinations of data; and finally (iv) use the trained neural network to predict the values $(\tau_m, s_m, s_f)$ by inputting values of $(k_e, P_A, P^*, g^*, G_P)$ determined from a measured $P$-$g$ response.

It should be noted that the choice of reasonable ranges for the three parameters of $(\tau_m, s_m, s_f)$ is important to reproduce realistic load responses. The ranges of parameters of $(\tau_m, s_m, s_f)$ for the PBO FRCM composite considered in this study were defined based on the experimental data employed and results reported in ([23],[24],[25]). Herein, $\tau_m$ ranged from 0.5 to 3.0 MPa, $s_m$ ranged from 0 to 0.5 mm, and $s_f$ ranged from 0.5 to 3.0 mm. The value of $j$ was set to 200, thus $j^3 = 8 \times 10^6$ combinations of input data and corresponding output data were employed. A program was written in Matlab to generate the combinations

of parameters and to determine the corresponding analytical $P$-$g$ curves using the analytical solution with the trilinear relationship given in Section 3.

Three of the five specimens with strain gauges discussed in Section 5.1 were used to validate the results of the trained neural network. Specimens DS_330_43_S_3$^{T}$ and DS_330_60_S_2 were not considered since values of $P^*$ or $g^*$ were significantly different with respect to the other specimens. The input values employed are summarized in Table 3. The bond-slip relationship and $\sigma$-$g$ curve based on the values $(\tau_m, s_m, s_f)$ predicted by the neural network and then implemented using the analytical approach provided in Section 3 are plotted in Figure 4 and Figure 6, respectively. The results in Figure 6 show the predicted data of $(\tau_m, s_m, s_f)$ can provide a reasonable $\sigma$-$g$ curve as compared with the experimental results. A similar approach could be used for specimens with $\ell \leq l_{eff}$, however different features should be included.

## 7. DISCUSSION

### 7.1. CRITICAL LENGTH FOR SNAP-BACK PHENOMENON

The decrease of the global slip during the descending branch of the $P$-$g$ response, i.e., curve snap-back, is due to the recovering of the elastic deformation of the debonded fibers with decreasing the applied load. The snap-back phenomenon was observed experimentally for FRP-concrete joints tested in direct shear by controlling displacements along the bonded length [23],[43] and was determined by analytical study of FRP-concrete joints [37] and by analytical and numerical studies on FRCM-concrete joints [19],[44]. The trilinear model adopted in this paper correctly captured the snap-back phenomenon, which

was not observed experimentally because the tests were controlled by monotonically increasing the loaded end slip (as discussed in Section 5.1).

The presence of the snap-back depends on the shape of the bond-slip relationship and the bonded length available. The minimum length needed to observe the snap-back, referred to as $l_{sb}$ in this paper, was determined for certain $\tau(s)$ with [38] and without the contribution of friction [37]. With the trilinear $\tau(s)$ studied, an approximate formulation to obtain $l_{sb}$ can be determined from the global slip values associated with Points D and E in Figure 1b. As discussed in Section 3.3, the end of elastic-softening-debonding stage is reached when the softening length reaches its maximum value, $l_{sf,u}$. The global slip at this point can be obtained by substituting $l_{sf,u}$ into Eq. (52), which gives:

$$g_D = s_f + \frac{\mu\lambda_2(s_f - s_m)}{\omega}\tan\left(\lambda_3 l_{sf,u}\right)\left(\ell - l_{sf,u}\right) + \frac{s_f}{2}\mu\lambda^2\left(\ell - l_{sf,u}\right)^2 \tag{63}$$

There exists a bonded length that meets $g_D = g_E$ , which means that with the development of the softening-debonding stage, the global slip remains approximately constant. This bonded length can be considered as an estimation of $l_{sb}$ and is obtained by solving $g_D = g_E$, where $g_E$ is given by Eq. (54):

$$l_{sb} = \left(\frac{\sqrt{1-\mu^2} - \mu\lambda_2 l_{sf,u}/2}{\sqrt{1-\mu^2} - \mu\lambda_2 l_{sf,u}}\right) l_{sf,u} \tag{64}$$

$l_{sb}$ defined in Eq. (64) represents a critical length such that for $\ell > l_{sb}$ snap-back will occur, whereas for $\ell \leq l_{sb}$ snap-back will not occur. Also, since Eq. (64) indicates that $l_{sb} \geq l_{sf,u}$, snap-back will occur only if the bonded length is long enough to fully develop the softening stage. It is interesting to note that when there is no friction, $l_{sb} = l_{sf,u} = \frac{\pi}{2\lambda_3}$.

For the PBO FRCM composite considered in this study, the value of $l_{sb}$ for Model_1-3 is 156 mm, 179 mm, and 209 mm, respectively (see Table 2). The analytical $P-g$ curves for $\ell = l_{sb}$ are plotted in Figure 11 for Model_1-3 described in Section 5.1. It should be noted that the segment DE is not a perfect line [25], and thus the condition $g_D$=$g_E$ does not provide the general solution for $l_{sb}$. Nevertheless, Eq. (64) can be used with reasonable accuracy to determine the critical length at which snap-back will occur. Further studies should be carried out to confirm the accuracy of this approach for other FRCM composites.

## 7.2. RELATIONSHIP BETWEEN THE DEBONDING LOAD AND FRACTURE ENERGY

The relationship between the debonding load for infinite bonded length $P_{deb,G}$ and fracture energy has been well established as [45]:

$$P_{deb,G} = b_f \sqrt{2E_f t^* G_F} \tag{65}$$

where $G_F$ is the fracture energy that, for the trilinear relationship adopted, can be computed as [19]:

$$G_F = \int_0^{s_f} \tau(s)\, ds = \frac{\tau_m}{2}\left(s_f + \mu s_f - \mu s_m\right) \tag{66}$$

As discussed in Section 3.3, for infinite bonded length, $l_{el}$ is also infinite, which leads to $\tanh(\lambda_1 l_{el}) = 1$. Thus the softening length at the debonding load for infinite bonded length $l_{sf,d,\infty}$ can be determined by solving Eq. (21) as:

$$l_{sf,d,\infty} = \frac{1}{\lambda_3}\arccos\left(\frac{\mu + \frac{\lambda_3}{\lambda_1}\sqrt{1-\mu^2+\left(\frac{\lambda_3}{\lambda_1}\right)^2}}{1+\left(\frac{\lambda_3}{\lambda_1}\right)^2}\right) \tag{67}$$

Defining the effective bond length $l_{eff}$ as the length needed to attain $\alpha P_{deb,G}$, where $\alpha$ is a value less than but close to 1.0 [22], Eqs. (22), (65), and (67) provide:

$$l_{eff} = l_{sf,d,\infty} + \frac{1}{\lambda_1}\operatorname{arctanh}\left(\lambda_1\sqrt{\left(\frac{\alpha}{\tau_m}\right)^2 2E_f t^* G_F - \frac{1-\mu^2}{\lambda_3^2}}\right) \tag{68}$$

Eq. (68) has a different form than the equation proposed in [25] to obtain $l_{eff}$, however, they provide the same results when using the same bond-slip relationship and value of $\alpha$. In previous research on FRP-concrete joints, $\alpha = 0.97$ was used [22]. For the PBO FRCM composite considered in the present study, the value of $l_{eff}$ is given in Table 2 for Model_1-3 considering values of $\alpha$ = 0.97, 0.99, and 0.999. Values of $l_{eff}$ determined by Eq. (68) and $\alpha$ = 0.97 are 17-32% less than the value measured experimentally, i.e., 260 mm given in [6]. For $\alpha = 0.999$ as suggested in [25], the values of $l_{eff}$ are 7-28% larger than 260 mm, whereas the results given by the cohesive material laws in [25] match better with 260 mm. For $\alpha = 0.99$ and when Model_2 is used, $l_{eff}$ determined by Eq. (68) is only 2% less than 260 mm.

## 8. CONCLUSIONS

In this paper, an analytical approach to predict the full-range behavior of FRCM-concrete joints using a trilinear bond-slip relationship was presented. Closed-form expressions for the interfacial shear stress distribution and load-slip response for

(relatively) long and short bonded lengths were obtained, providing a rigorous and theoretical basis for understanding the full-range load-slip behavior of FRCM-concrete joints. Based on the results and discussion presented in the paper, the following conclusions can be drawn:

1. The applied load-global slip behavior for long bonded lengths features an elastic stage, an elastic-softening stage, an elastic-softening-debonding stage, a softening-debonding stage, and a debonding stage. For bonded lengths less than the fully established softening length, the third stage is a pure softening stage.

2. The trilinear $\tau(s)$ provides closed-form solutions for the debonding and peak loads and corresponding slips at the composite free and loaded ends.

3. The analytical solution is in good agreement with strain and peak load results of test specimens reported in the literature, as well as with the numerical results obtained using a finite difference method (FDM).

4. Results obtained by an inverse determination of the parameters in the trilinear bond-slip relationship using the experimental load-slip response as input of the neural network were in good agreement with the experimental load responses.

5. An approximate solution for the minimum length needed to develop the snap-back phenomenon was derived.

6. The effective bond length determined using the analytical approach was in good agreement with experimental results reported in the literature.

## FUNDING

This research did not receive any specific grant from funding agencies in the public, commercial, or not-for-profit sectors.

## ACKNOWLEDGEMENTS

The author Xingxing Zou would like to thank Haohan Li, a PhD student in the Department of Computer Science of Missouri University of Science and Technology, for his helpful discussion on the use of neural network.

## DECLARATION OF INTERESTS

Declarations of interest: none.

## APPENDIX

## FINITE DIFFERENCE METHOD SOLVING EQ. (3)

The basis of the numerical method used [42] consists of substituting Eq. (3) by finite differences and solving the system of equations with the Newton–Raphson iteration technique as follows:

$$\{s_i\}_{j+1} = \{s_i\}_j - \mathbf{J}^{-1}(s_i) * f_i(s_i) \tag{A1}$$

where $\{s_i\}_j$ and $\{s_i\}_{j+1}$ are the slip at the $j$-th and $j$+1-th iteration, respectively, $\mathbf{J}^{-1}$(s) is the inverse of the Jacobian matrix for this system, and $f_i(s_i)$ is the first member of Eq. (4) at point $i$. The central difference approximations for Eq. (3) lead to:

$$\frac{ds(y_i)}{dy} = \frac{s_{i+1} - s_{i-1}}{2h} \tag{A2}$$

$$\frac{d^2s(y_i)}{dy^2} = \frac{s_{i+1} - 2s_i + s_{i-1}}{h^2} \tag{A3}$$

where the discretization step ($h$) is $h = \frac{L}{N}$, $L$ is the bonded length, and $N$ is the number of discretizations. The distance $h$ between consecutive points $y_i$, $i$ = 0, 1, 2, . . . , $N$, was selected with $N$ as the largest integer above which no gain in accuracy was observed. The convergence of the system was defined according to:

$$\frac{\{s_i\}_{j+1} - \{s_i\}_j}{\{s_i\}_j} \leq 10^{-6} \tag{A4}$$

Before the applied load reaches the peak load, the boundary conditions are:

$$\varepsilon(0) = \frac{ds(0)}{dy} = 0 \tag{A5}$$

$$s(L) = g \tag{A6}$$

In order to capture the snap-back phenomenon after the applied load reaches the peak load, the boundary condition of Eq. (A6) is replaced as:

$$s(0) = s_F \tag{A7}$$

Note that according to Eq. (A2),

$$\varepsilon(0) = \frac{s_1 - s_{-1}}{2h} \tag{A8}$$

However, $s_{-1}$ is not in the domain, thereby creating a difficulty. The solution is to extend the original domain from $[0, Nh]$ to $[-1, Nh]$. This results in $N + 2$ nodes, the first one being a fictitious one. Values are solved for $(s_{-1}, s_0, s_1, \ldots, s_{N-1}, s_N)$, and the additional variable introduced due to the fictitious node $s_{-1}$ is discarded from the final solution.

Once the slip distribution is determined, the shear stress can be determined by:

$$\tau_i = \tau(s_i) \tag{A9}$$

The calculation of the applied load will use the following equation:

$$P = t^* \int_0^L \tau(y)dy \tag{A10}$$

and the load at the loaded end can be obtained by numerical integration of Eq. (A10). The strain can be computed as:

$$\varepsilon_i = \frac{s_{i+1} - s_{i-1}}{2h} \tag{A11}$$

It should be noted that when $i = N + 1$, there is no point for $s_{N+2}$, therefore $\varepsilon_{N+1}$, i.e., the strain at loaded end, is:

$$\varepsilon_{N+1} = \frac{P}{E_F t^* b_f} \tag{A12}$$

It should be noted that an initial slip distribution is needed at the beginning of the solution process. A linear distribution can be adopted:

$$s_i = \frac{i+1}{N} g \tag{A13}$$

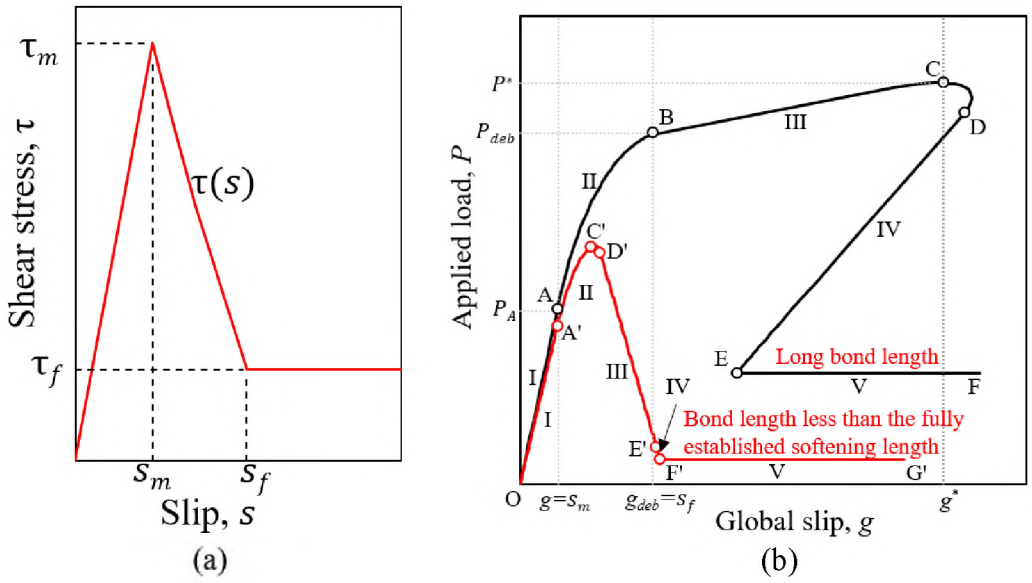


Figure 1. (a) Trilinear bond-slip relationship; and (b) general applied load-global slip curves.

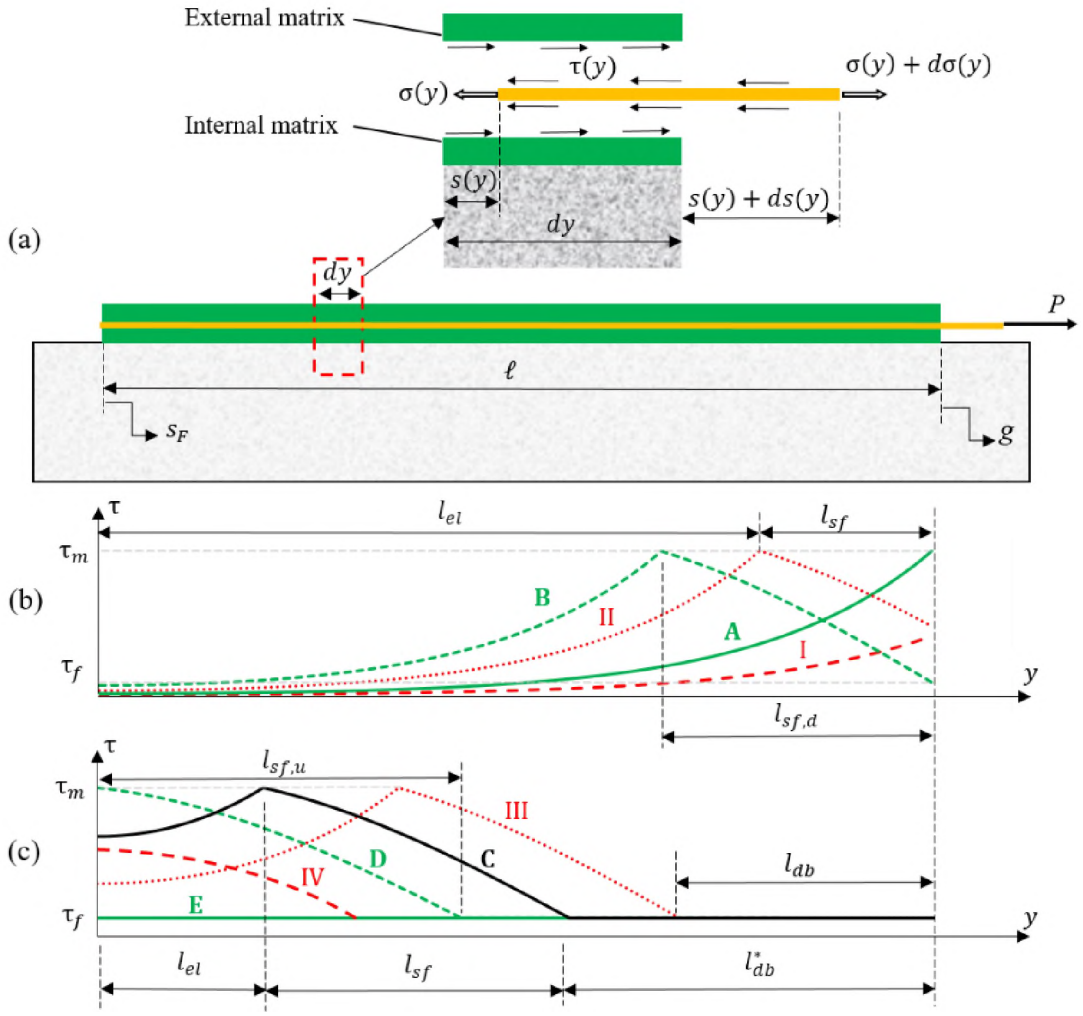


Figure 2. Evolution of interfacial shear stress distribution for long bonded length: (a) schematic side view of a single-lap direct-shear test; (b) elastic stage and elastic-softening stage (see Stages I, II and Points A, B in Figure 1b); and (c) elastic-softening-debonding stage, softening-debonding stage, and debonding stage (see Stage III and Points C, D, and E in Figure 1b).

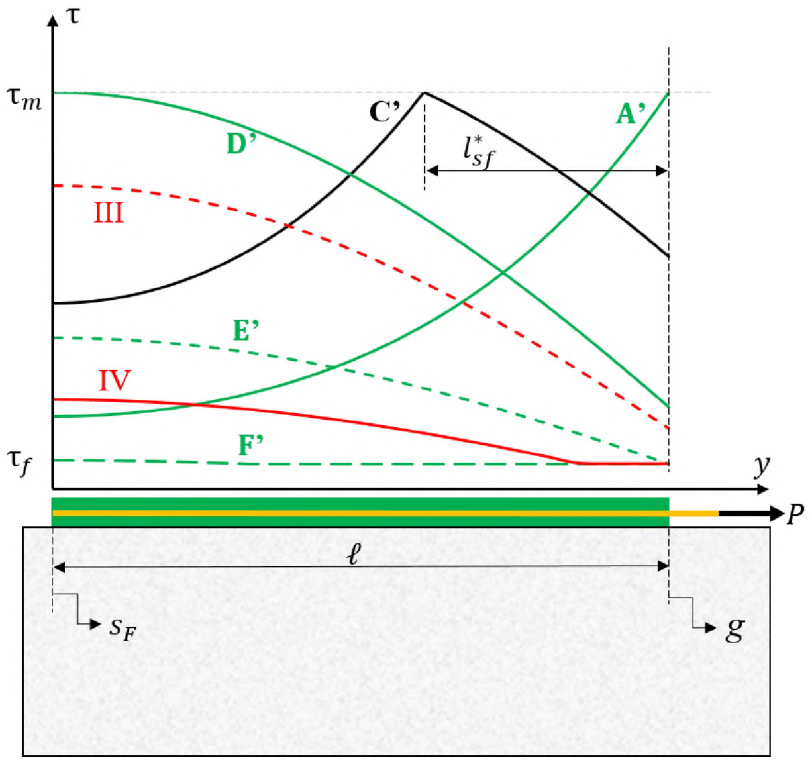


Figure 3. Evolution of interfacial shear stress distribution for bonded length less than the fully established softening length (see Stages III, IV and Points A', C', D', E', and F' in Figure 1b).

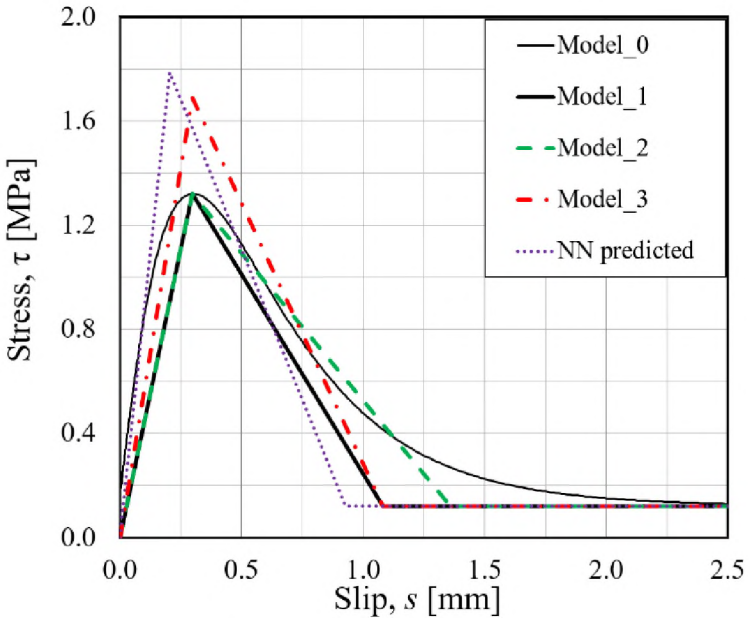


Figure 4. Bond-slip relationships considered.

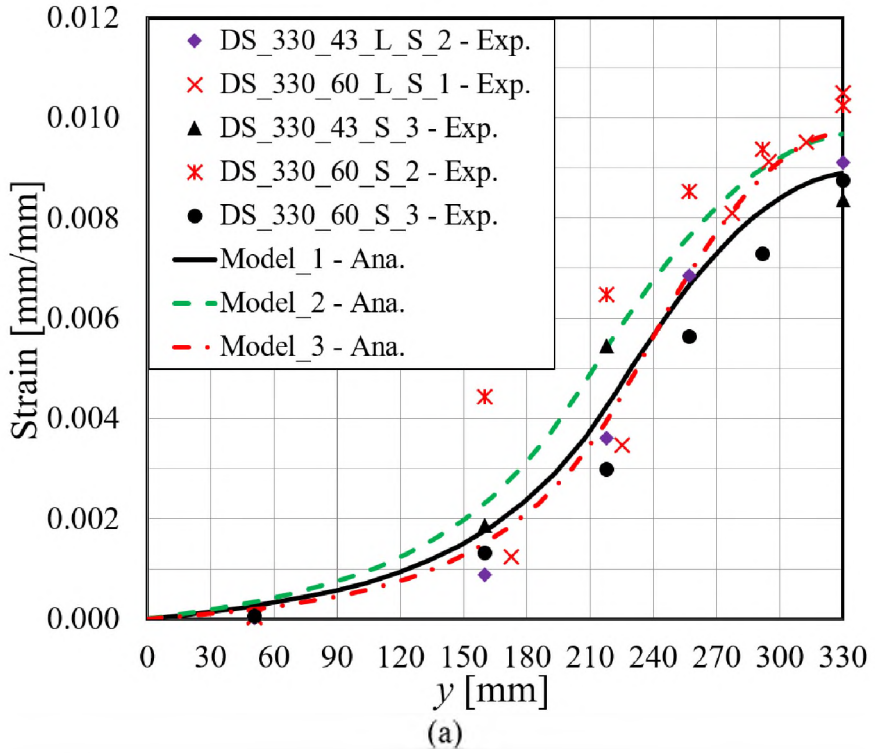


(a)

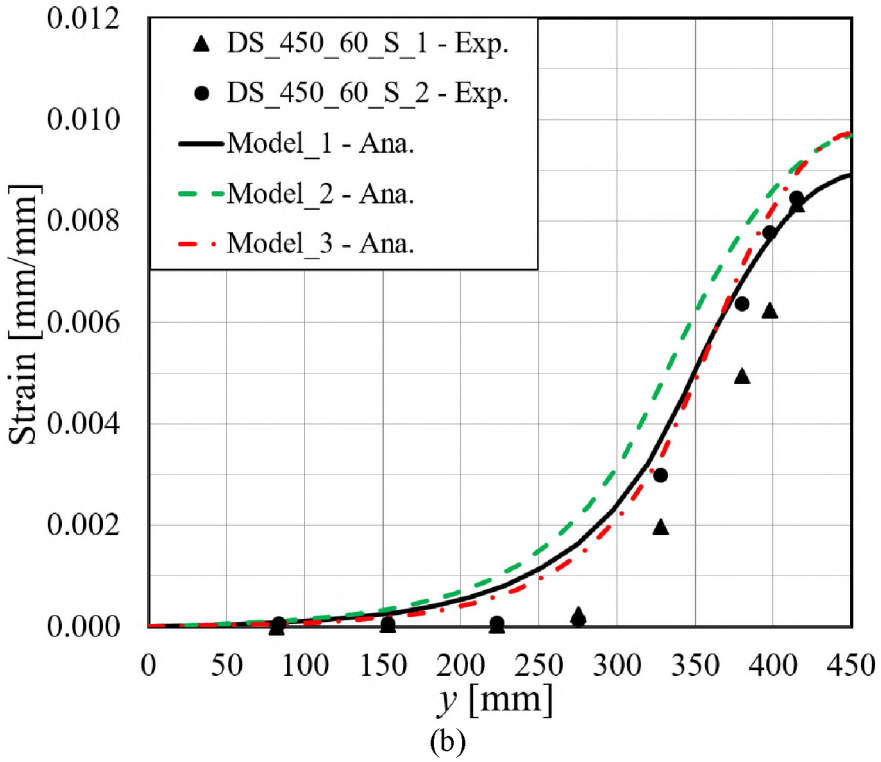


(b)

Figure 5. Comparison between analytical and experimental strain profiles at the debonding load, $P_{deb}$: (a) $\ell$=330 mm; and (b) $\ell$=450 mm.

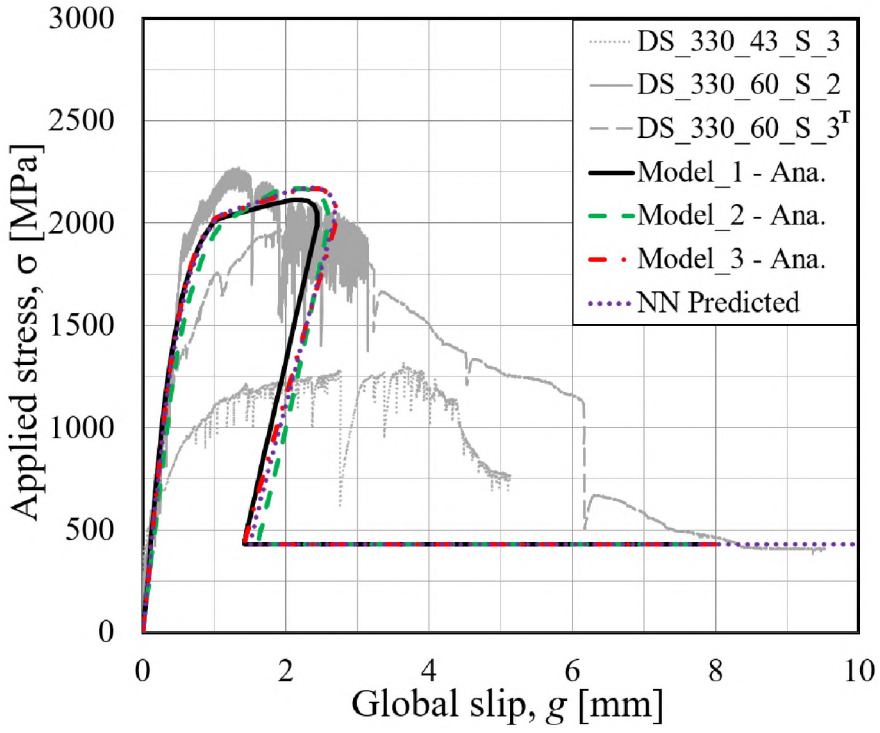


(a)

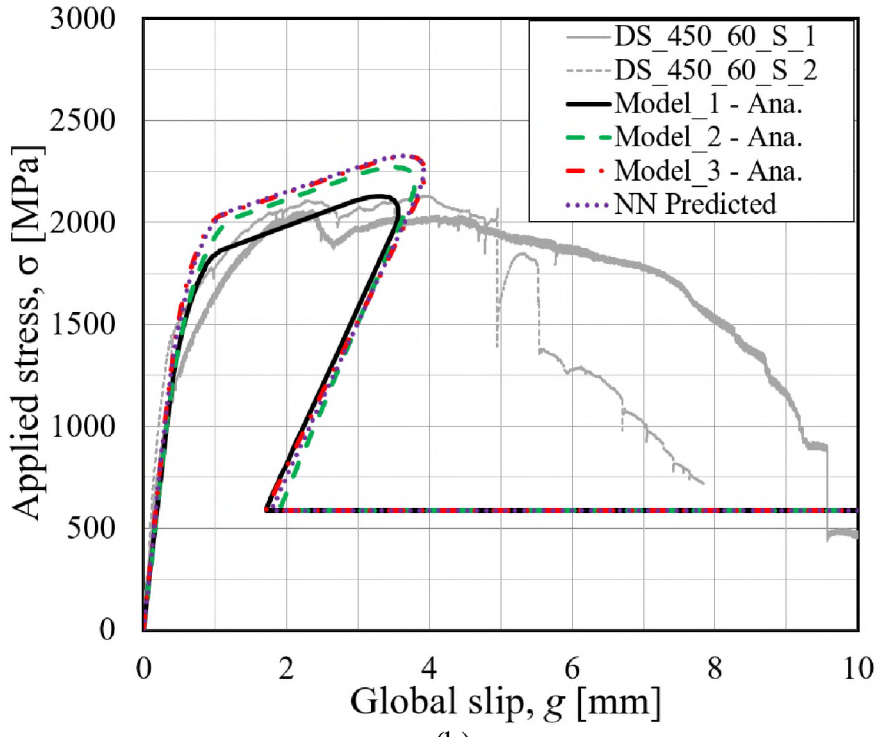


(b)

Figure 6. Comparison between analytical and experimental σ-g response: (a) DS_330 series; and (b) DS_450 series.

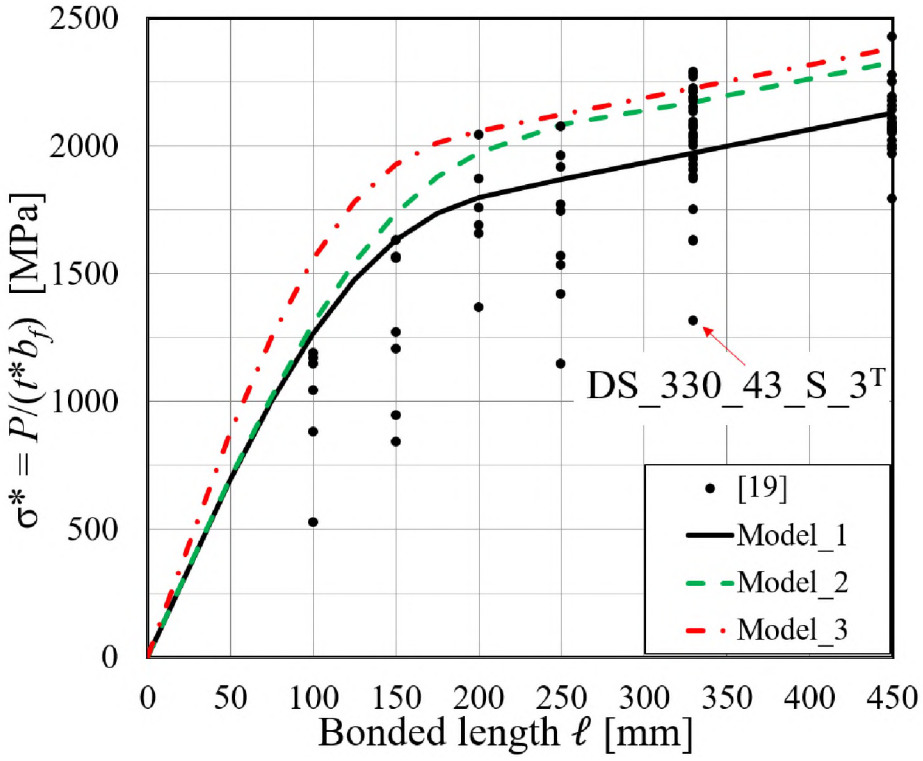


Figure 7. Comparison between analytical and experimental peak stresses for different bonded lengths.

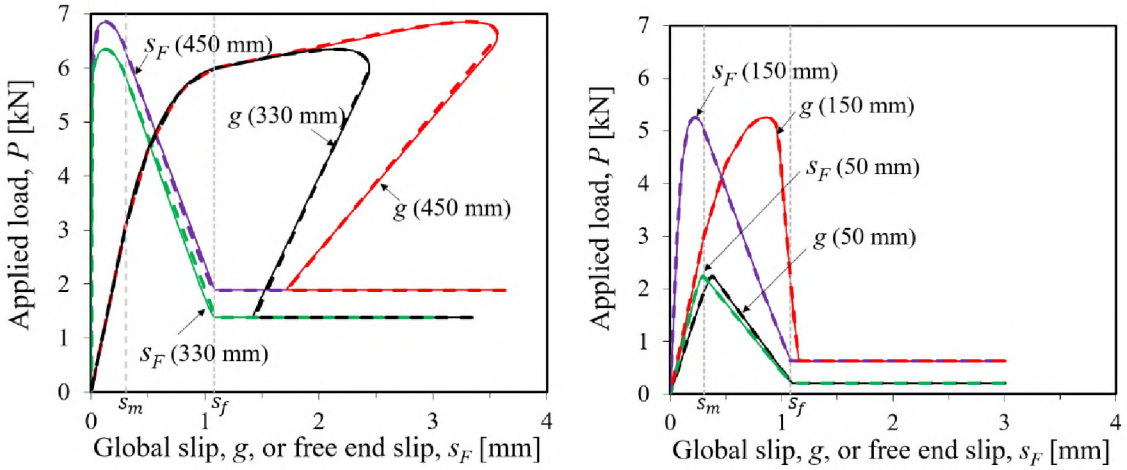


(a) (b)

Figure 8. Comparison between analytical and FDM results: (a) long bonded lengths; and (b) short bonded lengths. Solid lines indicate analytical results, and dashed lines indicate FDM results.

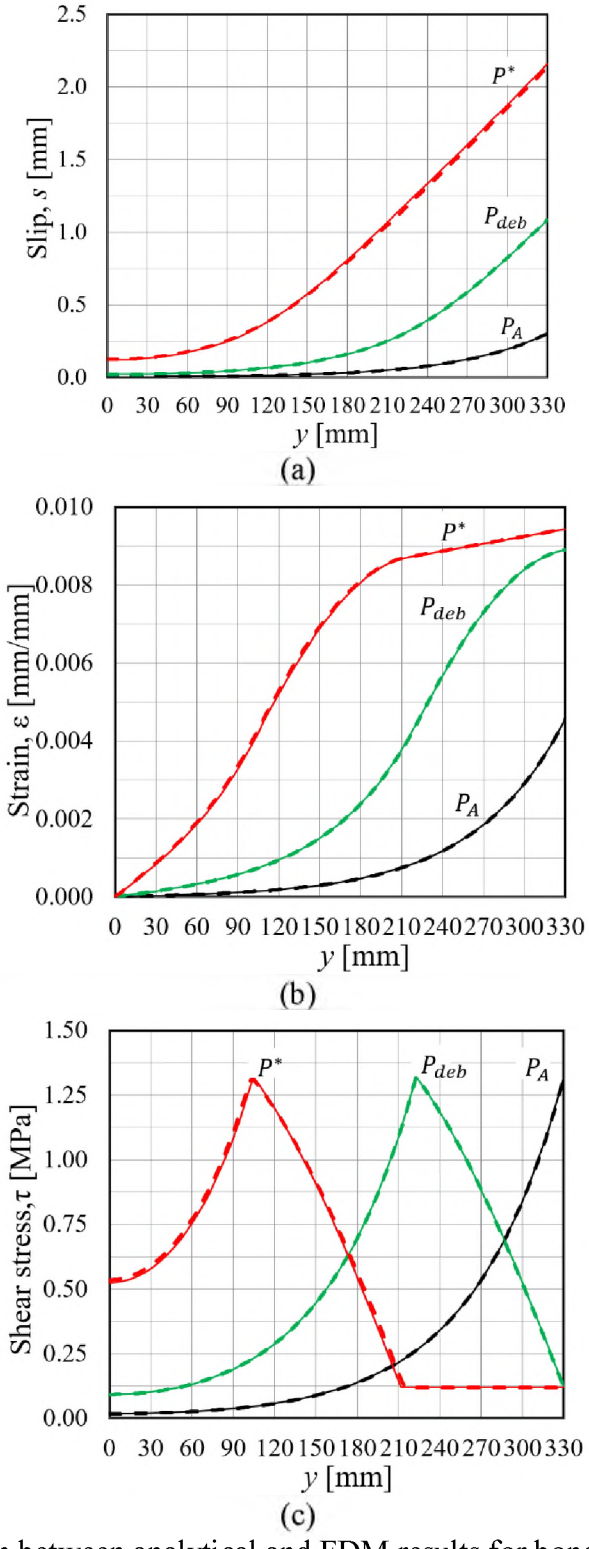


Figure 9. Comparison between analytical and FDM results for bonded length $\ell$=330 mm with Model_1: (a) slip; (b) strain; and (c) shear stress. Solid lines indicate analytical results, and dashed lines indicate FDM results.

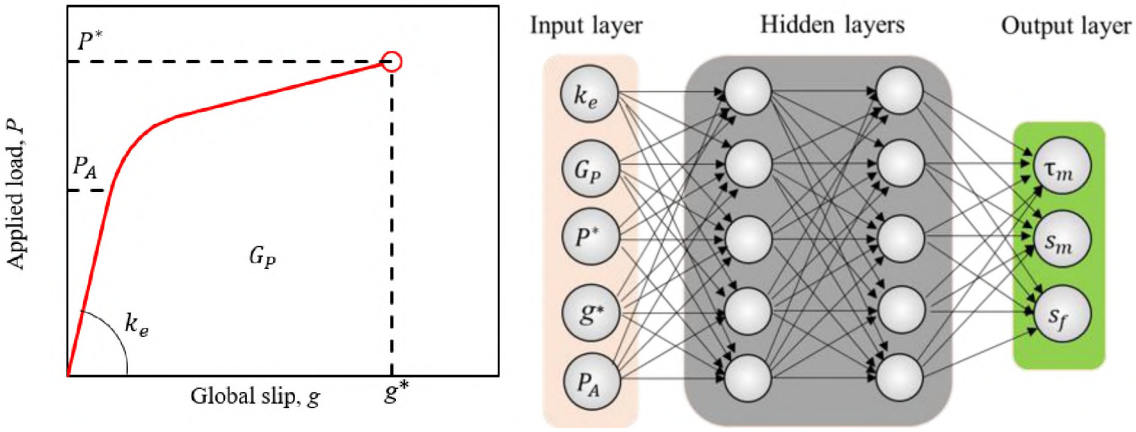


Figure 10. Illustration of the neural network used in this paper: (a) input; and (b) structure of the neural network.

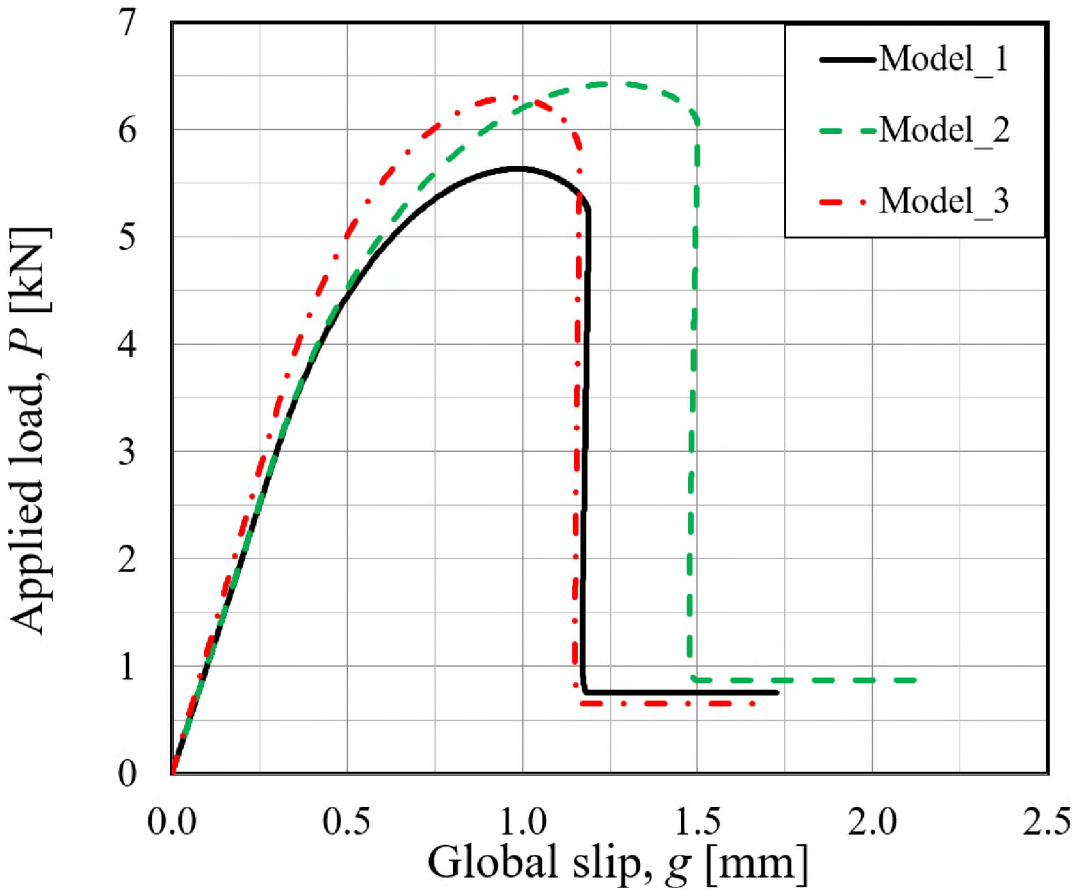


Figure 11. Applied load-global slip curves with $\ell = l_{sb}$.

Table 1. Test specimen characteristics.

| Specimen | Bonded Width (mm) | Bonded Length (mm) | Number of Longitudinal Bundles $n$ |
|---|---|---|---|
| DS_330_43_S_3 [T] | 43 | 330 | 5 |
| DS_330_60_S_2 | 60 | 330 | 7 |
| DS_330_60_S_3 | 60 | 330 | 7 |
| DS_450_60_S_1 | 60 | 450 | 7 |
| DS_450_60_S_2 | 60 | 450 | 7 |

Table 2. Parameters of the bond-slip relationships considered.

| Bond-slip relationship | Shape | $s_m$ (mm) | $\tau_m$ (MPa) | $s_f$ (mm) | $\tau_f$ (MPa) | $G_F$ (J/m$^2$) | $l_{eff}$ (mm) α=0.97 | α=0.99 | α=0.999 | $l_{sf,u}$ (mm) | $l_{sb}$ (mm) |
|---|---|---|---|---|---|---|---|---|---|---|---|
| Model_0 [40] | Continuous | 0.299 | 1.32 | 1.081 | 0.12 | 960 | | | | - | - |
| Model_1 | Trilinear | 0.299 | 1.32 | 1.081 | 0.12 | 761 | 198 | 237 | 314 | 166 | 179 |
| Model_2 | Trilinear | 0.299 | 1.32 | 1.359 | 0.12 | 960 | 215 | 254 | 332 | 193 | 209 |
| Model_3 | Trilinear | 0.299 | 1.69 | 1.081 | 0.12 | 960 | 176 | 210 | 278 | 147 | 156 |

Table 3. Features used in the neural network and the predicted parameters.

| Specimen | Input | | | | | Predicted output | | |
|---|---|---|---|---|---|---|---|---|
| | $k_e$ (kN/mm) | $G_P$ (kN·mm) | $P^*$ (kN) | $g^*$ (mm) | $P_A$ (kN) | $\tau_m$ (MPa) | $s_m$ (mm) | $s_f$ (mm) |
| DS_330_60_S_3 | 12.54 | 12.08 | 6.55 | 2.35 | 0.24 | 1.668 | 0.272 | 0.944 |
| DS_450_60_S_1 | 10.70 | 23.76 | 6.86 | 3.96 | 0.39 | 2.116 | 0.064 | 0.810 |
| DS_450_60_S_2 | 10.69 | 12.15 | 6.63 | 2.37 | 0.29 | 1.576 | 0.277 | 1.028 |
| Average | | | | | | 1.787 | 0.204 | 0.927 |
| CoV | | | | | | 0.162 | 0.595 | 0.119 |

# REFERENCES

[1] Hollaway, L. C. A review of the present and future utilisation of FRP composites in the civil infrastructure with reference to their important in-service properties. Constr Build Mater 2010; 24(12):2419-2445.

[2] Teng J. G., Chen J. F., Smith S. T., Lam L. FRP-strengthened RC structures. Wiley, New York. 2002.

[3] Raoof, S. M., Bournas, D. A. Bond between TRM versus FRP composites and concrete at high temperatures. Compos B Eng 2017; 127:150-165.

[4] Donnini, J., De Caseo y Basalo, F., Corinaldesi, V., Lancioni, G., Nanni, A. Fabric-reinforced cementitious matrix behavior at high-temperature: Experimental and numerical results. Compos B Eng 2017; 108:108-121.

[5] Trapko, T. The effect of high temperature on the performance of CFRP and FRCM confined concrete elements. Compos B Eng 2013; 54:138-145.

[6] D'Antino, T., Carloni, C., Sneed, L. H., Pellegrino, C. Matrix–fiber bond behavior in PBO FRCM composites: A fracture mechanics approach. Eng Fract Mech 2014; 117:94-111.

[7] D'Ambrisi, A., Focacci, F. Flexural strengthening of RC beams with cement-based composites. J Compos Constr 2011; 15(5):707-720.

[8] Azam, R., Soudki, K. FRCM strengthening of shear-critical RC beams. J Compos Constr 2014; 18(5), 04014012.

[9] Gonzalez-Libreros, J. H., Sneed, L. H., D'Antino, T., Pellegrino, C. Behavior of RC beams strengthened in shear with FRP and FRCM composites. Eng Struct 2017; 150:830-842.

[10] Blanksvärd, T., Täljsten, B., Carolin, A. Shear strengthening of concrete structures with the use of mineral-based composites. J Compos Constr 2009; 13(1) :25-34.

[11] Alabdulhady, M. Y., Sneed, L. H., Carloni, C. Torsional behavior of RC beams strengthened with PBO-FRCM composite–An experimental study. Eng Struct 2017; 136:393-405.

[12] Ombres, L., Verre, S. Structural behaviour of fabric reinforced cementitious matrix (FRCM) strengthened concrete columns under eccentric loading. Compos B: Eng 2015; 75:235-249.

[13] Awani, O., El Refai, A., El-Maaddawy, T. Bond characteristics of carbon fabric-reinforced cementitious matrix in double shear tests. Constr Build Mater 2015; 101:39-49.

[14] Raoof, S. M., Koutas, L. N., Bournas, D. A. Bond between textile-reinforced mortar (TRM) and concrete substrates: Experimental investigation. Compos B Eng 2016; 98:350-361.

[15] Focacci, F., Nanni, A., Bakis, C. E. Local bond-slip relationship for FRP reinforcement in concrete. J Compos Constr 2000; 4(1):24-31.

[16] D'Ambrisi, A., Feo, L., Focacci, F. (2012). Bond-slip relations for PBO-FRCM materials externally bonded to concrete. Compos B Eng 2012; 43(8):2938-2949.

[17] D'Antino, T., Sneed, L. H., Carloni, C., Pellegrino, C. Effect of the inherent eccentricity in single-lap direct-shear tests of PBO FRCM-concrete joints. Compos Struct 2016; 142:117-129.

[18] D'Ambrisi, A., Feo, L., Focacci, F. Bond-slip relations for PBO-FRCM materials externally bonded to concrete. Compos B Eng 2012; 43(8):2938-2949.

[19] Focacci, F., D'Antino, T., Carloni, C., Sneed, L. H., Pellegrino, C. An indirect method to calibrate the interfacial cohesive material law for FRCM-concrete joints. Mater Des 2017; 128:206-217.

[20] Biscaia, H. C., Borba, I. S., Silva, C., and Chastre, C. A nonlinear analytical model to predict the full-range debonding process of FRP-to-parent material interfaces free of any mechanical anchorage devices. Compos Struct, 2016; 138: 52-63.

[21] Biscaia, H. C., Chastre, C., Silva, C., and Franco, N. Mechanical response of anchored FRP bonded joints: a nonlinear analytical approach. Mech Adv Mater Struct, 2018; 25(3): 238-52.

[22] Yuan, H., Teng, J. G., Seracino, R., Wu, Z. S., Yao, J. Full-range behavior of FRP-to-concrete bonded joints. Eng Struct 2004; 26(5):553-565.

[23] Carozzi, F. G., Colombi, P., Fava, G., Poggi, C. A cohesive interface crack model for the matrix–textile debonding in FRCM composites. Compos Struct 2016; 143:230-241.

[24] Zou, X., Sneed, L. H., D'Antino, T., Carloni, C. Application of a trilinear bond-slip model to FRCM-concrete joints. 9th Int Conf on FRP Composites in Civil Engineering-CICE 2018, Hongkong, 314-321

[25] D'Antino, T., Colombi, P., Carloni, C., Sneed, L. H. Estimation of a matrix-fiber interface cohesive material law in FRCM-concrete joints. Compos Struct 2018; 193:103-112.

[26] Malena, M. Closed-form solution to the debonding of mortar based composites on curved substrates. Compos B Eng 2018; 139:249-258.

[27] Djamai, Z. I., Bahrar, M., Salvatore, F., Larbi, A. S., El Mankibi, M. Textile reinforced concrete multiscale mechanical modelling: Application to TRC sandwich panels. Finite Elem Anal Des 2017; 135:22-35.

[28] Lin, X., Zhang, Y. X. Evaluation of bond stress-slip models for FRP reinforcing bars in concrete. Compos Struct 2014; 107:131-141.

[29] Zheng, Jian-Jun, and Jian-Guo Dai. Analytical solution for the full-range pull-out behavior of FRP ground anchors. Constr Build Mater 2014; 58:129-137.

[30] Ren, F. F., Yang, Z. J., Chen, J. F., Chen, W. W. An analytical analysis of the full-range behaviour of grouted rockbolts based on a tri-linear bond-slip model. Constr Build Mater 2010; 24(3):361-370.

[31] Vaculik, J., Sturm, A. B., Visintin, P., Griffith, M. C. Modelling FRP-to-substrate joints using the bilinear bond-slip rule with allowance for friction-Full-range analytical solutions for long and short bonded lengths. Int J Solid Struct 2018; 135:245-260.

[32] D'Antino, T., Carozzi, F. G., Colombi, P., Poggi, C. Out-of-plane maximum resisting bending moment of masonry walls strengthened with FRCM composites. Compos Struct 2018; 202:881-896

[33] Bellini, A., Shahreza, S. K., Mazzotti, C. Cyclic bond behavior of FRCM composites applied on masonry substrate. Compos B Eng 2019; 169:189-199.

[34] Carloni, C., Subramaniam, K. V. Application of fracture mechanics to debonding of FRP from RC members. ACI SP 2012; 286:1-16.

[35] Martin, L. B., Tijani, M., Hadj-Hassen, F. A new analytical solution to the mechanical behaviour of fully grouted rockbolts subjected to pull-out tests. Constr Build Mater 2011; 25(2):749-755.

[36] Carrara, P., Ferretti, D., Freddi, F., Rosati, G. Shear tests of carbon fiber plates bonded to concrete with control of snap-back. Eng Fract Mech 2011; 78(15):2663-2678.

[37] He, L., Wu, Y. F., Xiao, Y. Analytical solution for externally bonded joints considering snap-back. J Compos Constr 2014; 19(5):04014077.

[38] Calabrese A. S., Colombi P., D'Antino T. Analytical solution of the bond behavior of FRCM composites using a rigid-softening cohesive material law. Compos B Eng 2019; 174:107051.

[39] Carloni C, Focacci F. FRP-masonry interfacial debonding: An energy balance approach to determine the influence of the mortar joints, Eur J Mech A/Solids 2016; 55:122-133.

[40] Zou, X., Sneed, L. H., D'Antino, T., Carloni, C. Analytical bond-slip model for fiber reinforced cementitious matrix (FRCM)-concrete joints based on strain profile measurements. J Mater Civ Eng 2019; DOI: 10.1061/(ASCE)MT.1943-5533.0002855.

[41] Carloni, C., D'Antino, T., Sneed, L. H., Pellegrino, C. Role of the matrix layers in the stress-transfer mechanism of FRCM composites bonded to a concrete substrate. J Eng Mech 2014; 141(6): 04014165.

[42] Biscaia, H. C., Chastre, C., Silva, M. A. Linear and nonlinear analysis of bond-slip models for interfaces between FRP composites and concrete. Compos B Eng 2013; 45(1):1554-1568.

[43] Colombi P., Fava G., Poggi C. End debonding of CFRP wraps and strips for the strengthening of concrete structures. Comp Struct 2014; 111:510-521.

[44] Carloni C., D'Antino T., Sneed L. H., Pellegrino C. 3-D numerical modeling of single-lap direct shear tests of FRCM-concrete joints using a cohesive contact damage approach. J Compos Constr. 2017; 22(1): 04017048.

[45] Täljsten, B. Defining anchor lengths of steel and CFRP plates bonded to concrete. Int J Adhes and Adhes 1997; 17(4): 319-327.

# III. BOND BEHAVIOR BETWEEN STEEL FIBER REINFORCED POLYMERS (SRP) AND CONCRETE

Xingxing Zou and Lesley H. Sneed

## ABSTRACT

Steel fiber reinforced polymer (SRP) composite materials, which consist of continuous unidirectional steel wires (cords) embedded in a polymeric matrix, have recently emerged as an effective solution for strengthening of reinforced concrete (RC) structures. SRP is bonded to the surface of RC structures by the same matrix to provide external reinforcement. Interfacial debonding between the SRP and concrete is a primary concern in this type of application. This study aimed to investigate the bond characteristics of between SRP and concrete determined by single-lap direct shear tests with different composite bonded lengths and fiber sheet densities (cord spacings). Specimens with medium density fibers failed mainly due to composite debonding, whereas those with low density fibers failed due to fiber rupture. Results of specimens that exhibited debonding were used to determine the bond-slip relationship of the SRP-concrete interface and to predict the full-range load response, which was in good agreement with the experimental results. A database of SRP-concrete direct shear tests reported in the literature was also established. Four analytical equations derived for fiber reinforced polymer (FRP)-concrete debonding were evaluated based on the database results and were found to predict the maximum load within approximately 15% on average, however, they all underestimated the effective bond length.

**Keywords:** Effective bond length; fiber reinforced polymer (FRP); interfacial debonding; single-lap direct shear test; steel fiber reinforced polymer (SRP).

## 1. INTRODUCTION

The increasing use of fiber reinforced polymer (FRP) composites for strengthening and repairing existing reinforced concrete (RC) structures has prompted in an extensive research effort in the last three decades [1][2]. Experimental and analytical research has shown that externally bonded (EB) FRP can provide substantial increases in flexural [3][4][5], shear [6], and torsional [7][8] strength and deformability to RC structures. Since 2004, a new type of composite comprised of high strength steel fiber cords and a polymeric matrix has been explored for the use of strengthening and repairing RC structures [9]. Steel fiber reinforced polymer composite is referred to as SRP composite in this paper. High strength steel fibers are produced in the form of steel wires twisted into cords. Typically a zinc or brass coating is provided to protect the steel cords against corrosion [9][10][11][12]. The use of steel cords results in certain advantages over other fiber types used in traditional FRP composites (e.g., carbon, glass) including relatively high stiffness, high ductility, and low vulnerability to rupture when bent or wrapped around cross sections with sharp corners [10][11][12][13]. Additionally, the higher strength perpendicular to the steel fiber axial direction can enable more effective gripping and anchoring in prestressed applications [11]. Flexural tests of RC beams strengthened with EB SRP have demonstrated the efficacy of SRP in improving the flexural strength and ductility of RC beams [9][12][14][15]. These encouraging experimental results have prompted producers and researchers to develop

commercially available products, useful laboratory data, analytical design methods, and field applications for SRP composites [10][16][17].

Interfacial debonding of the composite has been proven to be one of the most important causes of structural failure of RC members strengthened with EB FRP composites [4][6][7]. Therefore, much attention has been paid to the study of the debonding mechanism in RC structures strengthened with EB FRP composites. It is well-understood that debonding of FRP composites typically occurs at the composite-concrete interface with fracture occurring within a thin layer of concrete directly beneath the composite [18]. Likewise, many of the experimental studies on RC beams strengthened with EB SRP reported failure due to composite debonding, which occurred within a thin layer of concrete substrate beneath the composite [11][12][13][14]. Several studies have been conducted to study the SRP-concrete debonding phenomenon [10][17][19][20], although methods to predict the bond behavior are still under development. Since there has been a large number of experimental, analytical, and numerical studies on FRP-concrete debonding [21][22][23], a question faced by researchers is whether existing design methods for FRP can be used for SRP in an analogous way.

The mechanical characteristics of SRP are different from those of FRP in terms of strength, stiffness, and ductility. Pure tension tests of SRP plates showed that the stress-strain behavior is nonlinear, which is different from the elastic behavior until failure of traditional FRP [17][20][24]. Moreover, the study in [3] showed that SRP is stiffer and stronger than CFRP, and the existing equations to predict the minimum length required to fully develop the stress transfer zone (STZ) (i.e., the effective bond length, $L_e$) and the load causing interfacial debonding when the STZ is fully established ($P_{deb}$) for FRP-concrete

joints should be adjusted for SRP. Therefore, efforts to adapt existing analytical procedures and design guidelines for the FRP-concrete interface to the SRP-concrete interface are still evolving. Double-lap direct shear tests on carbon FRP (CFRP)-concrete joints and SRP-concrete joints revealed that the effective bond length of SRP is longer than that of CFRP [1]. Single-lap direct shear test results of SRP-concrete joints reported in [10] showed that: i) surface preparation influenced the bond behavior, (ii) higher density fiber sheets (i.e., smaller cord spacings) are not necessarily more effective than lower density fiber sheets since the interfacial capacity is limited by the concrete substrate, and (iii) existing semi-empirical expressions developed to predict $P_{deb}$ and $L_e$ for FRP-concrete systems could be used for SRP. Single-lap shear tests reported in [20] showed that the bond behavior of SRP composites was similar to that of FRP composites, and that the fracture energy of SRP-concrete joints was independent of the fiber sheet density, whereas the effective bond length depends on the fiber sheet density. The conflicting results described above suggest that more data are needed to understand the bond behavior of SRP-concrete joints. Additionally, the behavior of SRP-concrete joints with short bonded length (less than 120 mm) has not been heavily investigated.

This study aimed to explore the bond behavior of SRP-concrete joints tested in direct shear. This paper presents the results of an experimental campaign in which different test parameters, including composite bonded length and cord sheet density, were considered. The experimental results were used to determine the bond-slip relationship of the SRP-concrete interface and to predict the full-range load response. To consider a larger dataset, a database of SRG-concrete joint tests was established in which the test results from this study were supplemented with results of tests reported in the literature. Analytical

equations derived to predict $P_{deb}$ and $L_e$ for FRP-concrete joints were examined to determine whether they can be applied to SRP-concrete joints.

## 2. MATERIALS

### 2.1. CONCRETE

The concrete was produced from normal-weight dolomitic limestone coarse aggregate with a maximum size of 16 mm, natural river sand, and commercial Portland Type I/II cement. The concrete mixture had a design compressive strength of 30 MPa to represent concrete used in existing civil structures in need of strengthening. The mixture proportions by weight ratio were (cement: sand: aggregate) = (1:00: 3.33: 2.51), and the water-cement ratio was 0.59. The concrete compressive and splitting tensile strengths were obtained experimentally using 101.6 mm diameter × 203.2 mm long cylinders in accordance with ASTM C39/C39M [26] and ASTM C496/C496M [27], respectively. The compressive and splitting tensile strengths, each determined as the average of three tests, were 25.79 MPa (CoV = 0.08) and 2.47 MPa (CoV = 0.07), respectively.

### 2.2. MATRIX

The polymeric matrix was a thixotropic epoxy [16]. The tensile strength, shear strength, and secant Young's modulus under compression, according to the manufacturer [16], were >14 MPa, >20 MPa, and >5.3 GPa, respectively.

## 2.3. STEEL FIBERS

The composite fibers were made of unidirectional high strength steel cords, see Figure 1. Each cord had a cross sectional area ($A_{cord}$) of 0.538 mm$^2$ and consisted of five wires. Three straight wires formed the core of the cord, and two wires were twisted around them in a helical manner, see Figure 1. The wires were galvanized with a zinc coating and were laid on a fiberglass mesh backing to facilitate installation. According to the manufacturer [16], the fiber sheet had a tensile strength of >3000 MPa, and an elastic modulus of >190 GPa.

Different fiber sheet densities, defined in terms of net fiber weight per unit fiber sheet area (in g/m$^2$), were achieved by different cord spacings. Two fiber sheet densities were tested in this study, referred to herein as medium density (MD) and low density (LD) fibers, see Figure 1a. Most tests in this study were conducted using the MD fibers because the direct shear test specimens with MD fibers achieved the desired failure mode (composite debonding), whereas the specimens with LD fibers failed due to fiber rupture, as discussed in Section 4. The properties of the fiber sheets provided by the manufacturer are listed in Table 1.

It should be noted that the properties given in Table 1 generally apply to composites of relatively wide width, with a large number of cords. On the other hand, fiber strips utilized in the test specimens in this study had a finite width (assumed as 50 mm for both dry fiber sheets and SRP plates) and finite number of cords (15 cords for MD fibers, and 8 cords for LD fibers).

Three MD bare fiber tensile coupons with 15 steel cords were tested in uniaxial tension, see Table 2. Figure 1b shows the tensile test of a MD bare fiber sheet. An

extensometer was used to measure the axial strain in the fibers. The applied load-axial strain relationship of specimen BF_2 is plotted in Figure 2. As the load approached the maximum load, one fiber ruptured followed by sudden rupture of the remaining fibers, see Figs. 2b and 2c. The maximum applied load was 23.88 kN. Considering the actual cross sectional area of $15 \times 0.538$ mm$^2$ = 8.07 mm$^2$, a maximum stress of 2959 MPa can be obtained from the maximum load, which is similar to the value provided by the manufacturer. Based on the actual cross sectional area, the elastic modulus was determined from the secant slope at 5 kN, and values are reported in Table 2. The average elastic modulus for the MD bare fiber sheet was 190.8 GPa (CoV = 0.05). This value is slightly larger (approximately 5%) than the values reported in [10], where the cross sectional area of the fiber sheet were computed by multiplying the equivalent thickness of fibers (0.169 mm) with the width of the assumed equivalent strip (50 mm) instead of the area corresponding to the actual number of cords.

### 2.4. SRP PLATE

Four 50 mm wide SRP tensile coupons consisting of MD fiber sheets with 15 steel cords embedded in the polymeric matrix were fabricated and tested in tension, see Figs. 1a and 2d. The tensile coupons were the same SRP strips that were bonded to the concrete prisms and were tested in tension after the single-lap shear tests were performed. Digital image correlation (DIC) [28][29] was employed on one of the four coupons to determine the axial strain along the fiber direction on the surface of the SRP. The images were taken by a Sony$\alpha$6000 camera remotely controlled by a computer. With the control unit the camera was triggered at a selected frequency. The images were evaluated using a commercial software package [28].

The results of axial strain at different load levels are shown in Figure 2. It can be seen that at the beginning of loading, the applied load increased linearly, and no cracks were observed on the SRP surface. At a load level of approximately 12 kN, the first crack occurred within the SRP matrix along the transversal direction (perpendicular to the fibers), resulting in a reduction of the slope of the applied load-axial strain curve. With further increase in load, more cracks were observed on the surface of the SRP, and the existing cracks became wider. At the peak load, the average spacing of cracks was around 10 mm. The cracks closed to a small width after unloading.

Similar to the bare fiber test in Section 2.3, the secant slope at 5 kN was taken as the elastic modulus of the SRP plate, $E_f$, see Table 2. It should be noted that $E_f$ of the SRP was determined with respect to the equivalent thickness of the fibers ($t_f$) for comparison with values reported in previous studies [10][20] and for use in calculations later in this paper. The average $E_f$ for the SRP tensile coupon with MD fibers is 257.2 GPa (CoV = 0.08). This value is consistent with the value given by similar tests of SRP plates with the same fibers and polymer reported in [20].

## 3. METHODS

The bond behavior of SRP-concrete joints was studied using a single-lap direct shear test. The test specimen consisted of a concrete prism and a SRP strip bonded to the concrete surface using a wet lay-up process. The concrete prisms were 125 mm wide × 125 mm deep × 375 mm long. Only the longitudinal side faces cast directly against the formwork were used to bond the SRP strip, as suggested in [20]. The concrete blocks were sandblasted prior to the application of the SRP strip. All concrete prisms and cylinders

were cured under a plastic sheet for 24 hours before being removed from the forms. After the removal of the forms, they were placed in the laboratory for curing. During the curing of specimens, the room temperature was approximately 15 $^{o}$C.

The concrete specimen was mounted onto the base of a servo-hydraulic testing machine using a steel frame, see Figure 4. Prior to mounting the specimen, steel plates were attached to the end of the SRP strip using a thermosetting epoxy and four steel bolts in each corner of the steel plates, see Figure 4. The bolts were tightened to allow for better gripping during testing and to reduce the likelihood of the fibers or SRP plate from slipping between the steel plates during testing. Two brackets were mounted onto the surface of the concrete specimen to hold two linear variable displacement transducers (LVDTs) during the test procedure. A Ω-shaped, cold-formed steel plate was affixed to the SRP strip right at the loaded end of the bonded area, see Figure 4. The Ω-plate was used as a reaction surface for the LVDTs. The load was applied via displacement control where the value of displacement used to control the test was the average reading of the two LVDTs. The average reading of the two LVDTs readings was assumed to correspond to the slip at the loaded end, termed the global slip ($g$), of the SRP composite strip relative to the concrete substrate at the composite loaded end. The load was applied via displacement control at a rate of 0.00084 mm/s, which is consistent with previous research [20].

A total of 64 single lap shear test specimens were included. The specimens were designated with the following convention: XD_L_i_(D or B), in which "XD" denotes the fiber sheet density see Table 1, "L" indicates the composite bonded length (in mm), "i" denotes the specimen number within the same series, "D", where present, denotes that DIC

was used, and "B", where present, indicates that the fibers were bare outside the bonded area. All specimens are listed in Table 3.

# 4. EXPERIMENTAL RESULTS AND DISCUSSION

In this section, the experimental load responses obtained from the single-lap shear tests described in Section 3 are presented.

## 4.1. FAILURE MODE AND GENERAL OBSERVATIONS

The failure mode of each specimen is reported in Table 3. Regarding specimens with MD fibers, most specimens with MD fibers failed due to debonding of the composite, which occurred within the concrete adjacent to the matrix-concrete interface. A thin layer of concrete was still attached to the SRP strip after debonding failure (Figure 5). The failure was brittle and catastrophic. Two specimens, MD_120_8 and MD_210_7_D, failed due to fiber rupture, with a maximum load of 22.70 kN and 24.12 kN, respectively. The maximum loads achieved by these specimens were the highest of all specimens and were approximately equal to the tensile strength of the fibers (Section 2.3). All specimens with LD fibers failed due to fiber rupture, see Table 3.

From the beginning of loading to the failure of specimens, no obvious cracks were observed on the surface of the concrete substrate, nor were any cracking sounds noted. However, one salient difference between SRP- and FRP-concrete joints is that the SRP strips exhibited multiple cracks along the transversal direction (see Figure 6b), similar to the response of the SRP tensile coupons discussed in Section 2.4. In general, a relatively large piece of concrete detached from the substrate near the composite loaded end, while a smaller piece of concrete sometimes detached near the free end of the SRP strip (Figure 5).

The thickness of the concrete layer attached to the debonded SRP strip elsewhere varied approximately between 1 and 8 mm. The surface of the failure zone of the concrete prism was uneven, with the aggregate being clearly visible (Figure 5).

## 4.2. LOAD RESPONSES AND KEY VALUES OF LOAD AND GLOBAL SLIP

The load responses of the single-lap shear tests are plotted in Figs. 7, 8, and 9 for all specimens, maintaining the distinction between different bonded lengths, fiber sheet densities, and presence/absence of the matrix in the unbonded region. Figure 7 shows that, for specimens with a relatively short bonded length ($L$ = 30 and 60 mm), the load increased almost linearly until failure. There was a consistent initial slope among different specimens. For specimens with a bonded length equal to or larger than 90 mm, the initial linear response was followed by a non-linear branch until a larger load was achieved, which sometimes corresponded to the peak (maximum) load of the specimen. The drop in load that followed marks the onset of the interfacial crack propagation [20]. As the interfacial crack propagated, the load remained constant with fluctuations until the failure of the specimen.

Figure 8 shows the load responses of the specimens with LD fibers and a bonded length $L$=240 mm. It can be seen that the load response was initially linear with a slight softening behavior until around 12 kN where fiber rupture occurred, which provides lower shear capacity of the joints compared with specimens with MD fibers with the same $L$.

Figure 9 shows the load responses the specimens with MD fibers, bonded length $L$=240 mm, and bare fibers in the unbonded region. Comparing the results with those in Figure 7h, it can be seen that the load response is almost the same as the response of similar

specimens with matrix along the unbonded region. This indicates that the presence of the matrix in the unbonded region did not significantly influence the results.

Values of the peak load, $P_{max}$, and the global slip at failure (referred to as the ultimate global slip), $g_{ult}$, are listed in Table 3. Figure 10 plots the relationship between $P_{max}$ and $L$ for all specimens with MD fibers that failed due to debonding, with the exception of those with bare fibers in the unbonded region. The results in Figure 10 show that $P_{max}$ increases as $L$ increases from 30 mm to 120 mm, and then $P_{max}$ a remains nearly constant for larger values of $L$. These results are used in Section 5 to determine the bond-slip relationship for the SRP-concrete interface.

Figure 11 plots the relationship between $g_{ult}$ and $L$ for specimens with MD fibers that failed due to debonding, with the exception of those with bare fibers in the unboned region. The results in Figure 11 show that $g_{ult}$ increases with $L$, however, a large scatter was observed, especially for specimens with long bonded length.

## 5. DETERMINATION OF BOND-SLIP RELATIONSHIP FROM THE PEAK LOAD – BONDED LENGTH RELATIONSHIP

It is generally assumed that composite-concrete debonding propagation can be idealized as a Mode-II fracture problem. A fictitious interface material is usually considered with zero thickness and a well-defined constitutive response [30][31][32][33]. A relationship between interface shear stress ($\tau$) and the relative slip ($s$) between the composite and concrete can be used to characterize the interface material. The interfacial cohesive material law developed by Dai et al. [35], which has been widely used to characterize the FRP-concrete interface material, is:

$$\tau(s) = E_f t_f A^2 B(e^{-Bs} - e^{-2Bs}) \quad (1)$$

where $\tau(s)$ denotes the function of the cohesive material law, and $E_f$ and $t_f$ are the modulus of elasticity of the FRT and thickness of the fibers, respectively. $A$ and $B$ are parameters that define the peak value of shear stress and the shape of the $\tau(s)$ curve, which can be given as:

$$A = \sqrt{\frac{2G_f}{E_f t_f}} = 2.4\sqrt{\frac{\tau_m s_m}{E_f t_f}} \quad (2)$$

$$B = 0.693/s_m \quad (3)$$

where $G_f$ is the interfacial fracture energy, representing the area under the $\tau(s)$ curve, which is related to $P_{max}$ through the interface and is independent of the shape of the cohesive material law [35]. $\tau_m$ and $s_m$ are the maximum shear stress and the corresponding slip, respectively.

An analytical solution of the full-range load response of specimens with infinite bonded length has been derived in [35]. However, this solution adopted the assumption that the slip at free end, $s_F$, is zero, so it is not suitable for specimens with relatively short bonded lengths, since for short bonded lengths $s_F \neq 0$ [36].

Another solution that is suitable for all bonded lengths has been given by Liu and Wu [36], in which the solution is driven by monotonically increasing $s_F$:

$$s(y) = \frac{1}{B}\ln\left[\frac{\eta\cosh\left(AB\sqrt{1-\eta^2}y\right)+1}{1-\eta^2}\right] \quad (4)$$

$$\varepsilon(y) = A\frac{\eta(1-\eta^2)\sinh\left(AB\sqrt{1-\eta^2}y\right)}{1+\eta\cosh\left(AB\sqrt{1-\eta^2}y\right)} \quad (5)$$

$$\tau(y) = E_f t_f A^2 B\eta(1-\eta^2)\frac{\eta + \cosh\left(AB\sqrt{1-\eta^2}y\right)}{\left[1+\eta\cosh\left(AB\sqrt{1-\eta^2}y\right)\right]^2} \quad (6)$$

where $s(y)$, $\varepsilon(y)$, and $\tau(y)$ are the slip, strain, and shear stress along the bonded length of the FRP, respectively. The term $\eta$ is used to simplify the form of the equations and is given by $\eta = 1 - e^{-Bs_F}$. The global slip ($g$) and applied load ($P$) are given as:

$$g = \frac{1}{B}\ln\left[\frac{\eta\cosh\left(AB\sqrt{1-\eta^2}L\right)+1}{1-\eta^2}\right] \quad (7)$$

$$P = E_f t_f b_f A\frac{\eta\sqrt{1-\eta^2}\sinh\left(AB\sqrt{1-\eta^2}L\right)}{1+\eta\cosh\left(AB\sqrt{1-\eta^2}L\right)} \quad (8)$$

An approximate relationship between $P_{max}$ and $L$ has been given in [36] as:

$$P_{max} = AE_f t_f b_f \tanh(0.3ABL) \quad (9)$$

Using $E_f$ = 257.2 GPa determined in Section 2 of this paper and $t_f$ = 0.169 mm, the parameters of $A$ and $B$ were fitted with the experimental results in Figure 10 by Eq. (9) for all MD fiber specimens that failed due to interfacial debonding excluding the specimens with bare fibers outside the bonded area. The results are $A$ = 0.00725 mm/mm and $B$ = 7.58 /mm, with $R^2$ = 0.996, and the corresponding $\tau(s)$ determined by Eq. (1) is shown in Figure 12. Solving Eqs. (2) and (3) gives $s_m$ = 0.0915 mm and $\tau_m$= 4.386 MPa.

Substituting the fitted results of $A$ and $B$ into Eqs. (7) and (8), the full-range load response can be determined for each bonded length, and the results are shown in Figure 7 by the curves labeled as "*Ana.*". It can be seen that the analytical load response matched well with the experimental load response of the corresponding specimens. However, an important difference is that there is no experimental (measured) response after the ultimate global slip ($g_{ult}$) is reached. The reason is because for specimens with or specimens with

relatively long bonded length, there is a snap-back phenomenon in the analytical *P*-*g* response, which is attributed to the drop in strain in the fibers close to loaded end [36]. Since the experimental tests in the present study were conducted by increasing the global (loaded end) slip, the applied load will drop dramatically when snap-back phenomenon is about to occur, thereby terminating the loading process. For bonded lengths less than a critical length ($L_c$), the snap-back phenomenon does not occur. $L_c$ is given in [36] as:

$$L_c = \frac{4.57}{AB} \tag{10}$$

Considering the values of $A$ and $B$ determined above, Eq. (10) gives $L_c$= 83 mm. For $L > L_c$, the ultimate global slip will occur after the peak load is reached, and the approximate solution of η is given by [36]:

$$\eta_c = \frac{\operatorname{acoth}\left(\frac{ABL + 38.5}{42.8}\right)}{4.0} \tag{11}$$

For $L \leq L_c$ no snap-back occurs, and theoretically the experimental loading should capture the whole process including the post-peak behavior, similar to the results shown for fiber reinforced cementitious matrix (FRCM)-concrete joints in [37]. However, for specimens with short bonded lengths, since the debonding process is brittle, the loading will usually terminate suddenly at the peak load, and the global slip at peak load will be taken as the ultimate slip. Figure 11 compares the analytical and experimental $g_{ult}$ - $L$ relationships. It can be seen that the analytical $g_{ult}$ is slightly lower than the experimental results for specimens with bonded length $L \leq$ 150 mm, whereas it matched well with the experimental results for $L \geq$150 mm.

Figure 10 shows that $P_{max}$ approaches approximately 16 kN asymptotically as $L$ increases. In engineering applications, the bond length corresponding to $wP_{max}$, where $w$

is a value sufficiently close to 1.0 (typically 0.96 or larger), is estimated as the effective bond length $L_e$. $L_e$ is given as [36]:

$$L_e = \frac{\text{atanh}(w)}{0.3AB} \tag{12}$$

Using the fitted results of $A$ and $B$ in this paper and $w$ = 0.96, Eq. (12) gives $L_e = 6.48/(AB)$ =118 mm.

## 6. EVALUATION OF EQUATIONS FOR FRP-CONCRETE BOND-SLIP BEHAVIOR

Several authors have derived equations to predict the maximum load $P_{max}$ for FRP-concrete joints that fail due to debonding of the composite within the concrete substrate and the effective bond length $L_e$. This section evaluates the validity of commonly-used equations to predict $P_{max}$ and $L_e$ for SRP-concrete joints.

### 6.1. EXISTING EQUATIONS

Chen and Teng proposed a semi-empirical equation to predict $P_{max}$ and $L_e$ based on a modification of an existing fracture mechanics model [32] as:

$$P_{max} = 0.427\beta_l\beta_w b_f L_e\sqrt{f_c'} \tag{13}$$

where, $\beta_w = \sqrt{\frac{2-b_f/b_c}{1+b_f/b_c}}$, and $\beta_l = \begin{cases} 1, if\ L \geq L_e \\ \sin\left(\frac{\pi L}{2L_e}\right), if\ L < L_e \end{cases}$. The effective bond length $L_e$ is given as:

$$L_e = \sqrt{\frac{E_f t_f}{\sqrt{f_c'}}} \tag{14}$$

Lu et al. proposed the following equation based on a meso-scale finite element analysis [33]:

$$P_{max} = \beta_l b_f \sqrt{2E_f t_f G_f} \tag{15}$$

where $G_f = 0.308\beta_w^2\sqrt{f_t}$, $\beta_w = \sqrt{\frac{2.25-b_f/b_c}{1.25+b_f/b_c}}$, $\beta_l = \begin{cases} 1, if\ L \geq L_e \\ \frac{L}{L_e}\left(2-\frac{L}{L_e}\right), if\ L < L_e \end{cases}$, and $f_t$ is the tensile strength of concrete. $L_e$ is given as:

$$L_e = 1.33\frac{E_f t_f}{f_t} \tag{16}$$

Units of MPa and mm shall be used in Eqs. (13)-(16).

Neubauer and Rostasy proposed the following equation [38]:

$$P_{max} = \begin{cases} 0.64\beta_w b_f \sqrt{E_f t_f f_t}, if\ L \geq L_e \\ 0.64\beta_w b_f \sqrt{E_f t_f f_t}\frac{L}{L_e}\left(2-\frac{L}{L_e}\right), if\ L < L_e \end{cases} \tag{17}$$

where $\beta_w = \sqrt{1.125\frac{2-b_f/b_c}{1+b_f/400}}$, and $L_e$ is given by:

$$L_e = \sqrt{\frac{E_f t_f}{2f_t}} \tag{18}$$

Maeda et al. proposed the following equation [39]:

$$P_{max} = \begin{cases} \tau_u b_f L_e, if\ L \geq L_e \\ \tau_u b_f L, if\ L < L_e \end{cases} \tag{19}$$

where $\tau_u = 110.2 \times 10^{-6} E_f t_f$, and $L_e$ is given by:

$$L_e = e^{6.13-0.580\ln(10^{-3}E_f t_f)} \tag{20}$$

Units of MPa and mm shall be used in Eqs. (19) and (20).

## 6.2. COMPARISON BETWEEN EXPERIMENTAL MAXIMUM LOAD AND PREDICTION BY EXISTING EQUATIONS

In order to examine the validity of the equations described in Section 6.1 for SRP-concrete joints, a database of test results was collected from the literature [10][25]. The database included the results of the present study as well as others that met the following criteria: (1) the specimen was tested in single- or double-lap shear; and (2) the specimen failed due to interfacial debonding. In addition, specimens with a loading rate that was different from the rate utilized in this study (0.00084 mm/s) and in [20][25] were excluded. The database included 198 test results and is presented in the Appendix. Test specimens included SRP strips with four different sheet densities. The compressive strength of concrete ranged from 12.8-39.7 MPa. For the specimens reported in [10], the tensile strength of concrete was not reported; therefore the expression $f_t' = 0.3{f_c'}^{2/3}$ from Eurocode 2 [40] was used to determine the concrete tensile strength of strength classes $\leq$ C50/60.

Figure 13 plots the predicted versus experimental value of $P_{max}$ determined by Eqs. (13), (15), (17), and (19). The average ratio of $P_{max}$ predicted by Eq. (13) to the corresponding experimental value is 0.89 with a CoV of 0.24. The average ratio of $P_{max}$ predicted by Eq. (15) to the corresponding experimental value is 0.91 with a CoV of 0.25. The average ratio of $P_{max}$ predicted by Eq. (17) to the corresponding experimental value is 1.09 with a CoV of 0.24. The average ratio of $P_{max}$ predicted by Eq. (19) to the corresponding experimental value is 1.07 with a CoV of 0.26. Thus, all equations are in reasonable agreement with the experimental results but Eqs. (13) and (15) tend to

underestimate the experimental value of $P_{max}$ by around 10%, whereas Eqs. (17) and (19) tend to overestimate the experimental value of $P_{max}$ by around 8%.

For the specimens with MD fibers that exhibited the failure mode of debonding in this study, the effective bond length $L_e$ predicted by Eqs. (14), (16), (18), and (20) is 93 mm, 113 mm, 94 mm, and 51 mm, respectively. All four equations underestimated the effective bond length compared with the results given by Eq. (12) of 118 mm. Of the four equations, Eq. (16) has the best accuracy.

## 7. CONCLUSIONS

This work presented the results of an experimental study carried out to determine the load-carrying capacity of SRP-concrete joints and the bond slip model based on data acquired from single-lap direct shear test specimens. A database of SRP-concrete joint test results was established, and the results were used to examine the validity of equations to predict the maximum transferrable load and the effective bond length developed for FRP-concrete joints. Based on the findings of this study, the following conclusions are drawn:

(1) Specimens with low density fibers tended to fail in fiber rupture, whereas specimens with medium density fibers tended to fail in composite debonding. Debonding occurred due to fracture of the concrete within a thin layer beneath the SRP strip, similar to the behavior of FRP-concrete joints.

(2) The maximum load increased with the bonded length to a constant value. By fitting the maximum load-bonded length relationship, a nonlinear bond-slip relationship was obtained with a maximum shear stress of 4.386 MPa and a corresponding slip

of 0.0915 mm. The full range load response was in reasonable agreement with the experimental results.

(3) The effective bond length is approximately 118 mm for specimens with medium density fibers.A database of 198 SRP-concrete joints was established from the results of this study and supplemented with others collected from the literature. Existing equations derived for FRP-concrete debonding behavior showed reasonable prediction of the maximum loadwith an error less than 10%.

(4) Nearly all of the selected equations for FRP composites underestimated the effective bonded length for the specimens with MD fibers that failed in debonding.

## ACKNOWLEDGEMENTS

The authors would like to thank their group members: formerly master student Christoph Moore and the current undergraduate research assistant Keenan McBurney for their help in the test. Kerakoll S.p.A. of Sassuolo, Italy, is gratefully acknowledged for providing the composite materials.

## FUNDING

This work was supported by the National Science Foundation (NSF) Electrical, Communication, and Cyber Systems (ECCS) Award 1609470, “A Multi-Physics-Based Approach to Active Microwave Thermography.”

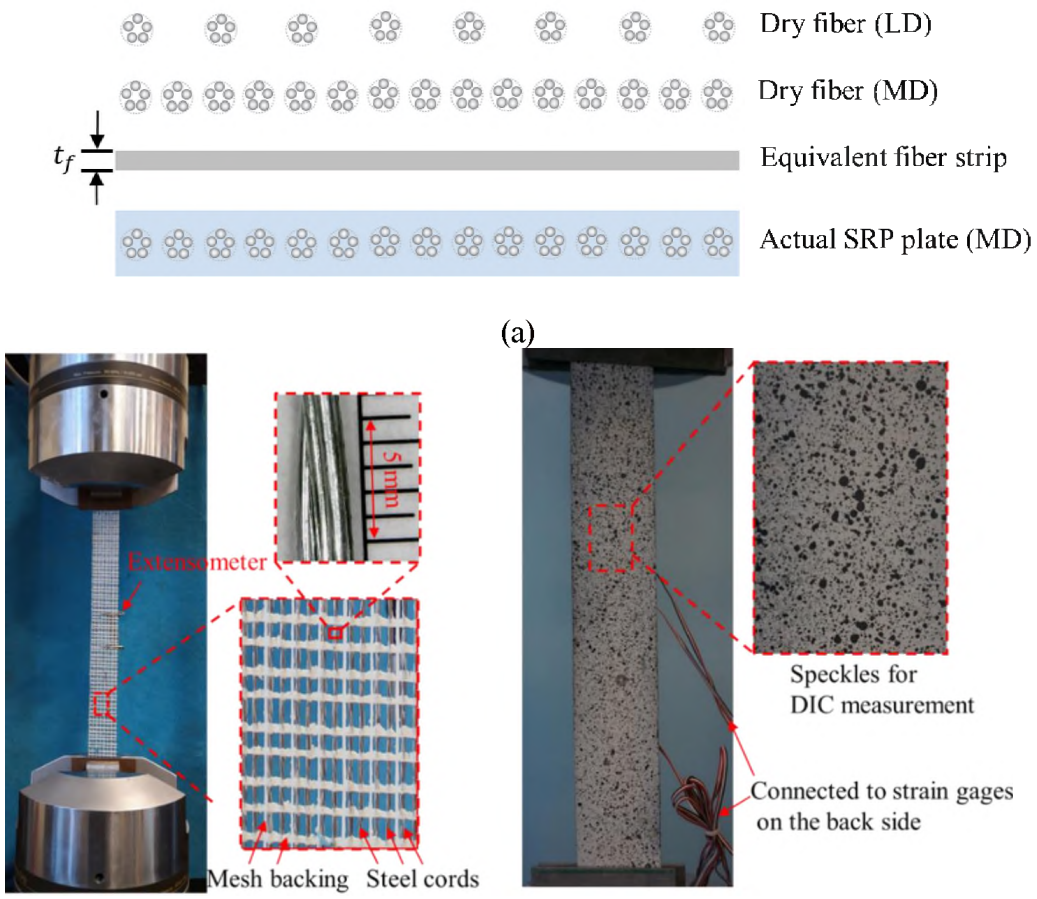


Figure 1. (a) Details of fibers and SRP plates, (b) tensile test of MD bare fiber sheet, and (c) tensile test of SRP plate with MD fibers.

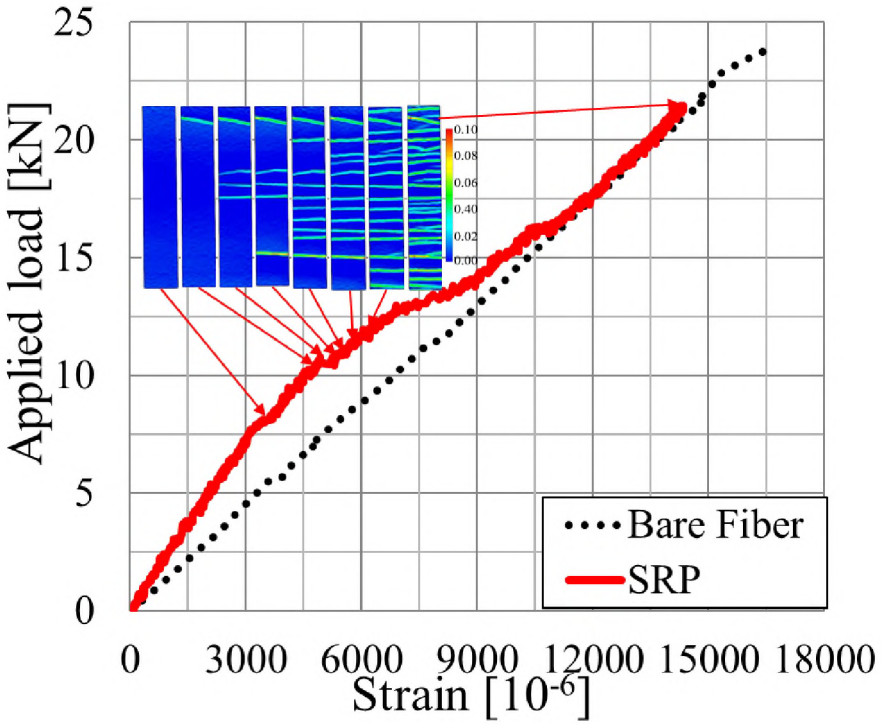


Figure 2. Typical applied load-axial strain responses of bare steel fiber sheet and SRP plate with MD fibers.

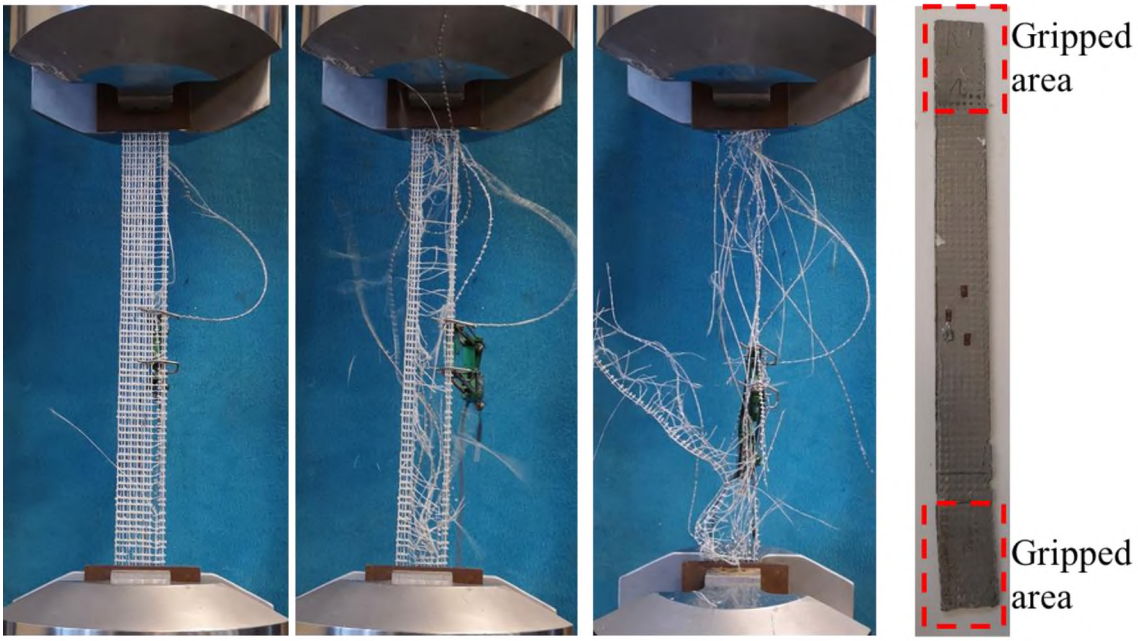


Figure 3. Failure mode of: (a) bare steel fiber sheet, and (b) a SRP plate with MD fibers.

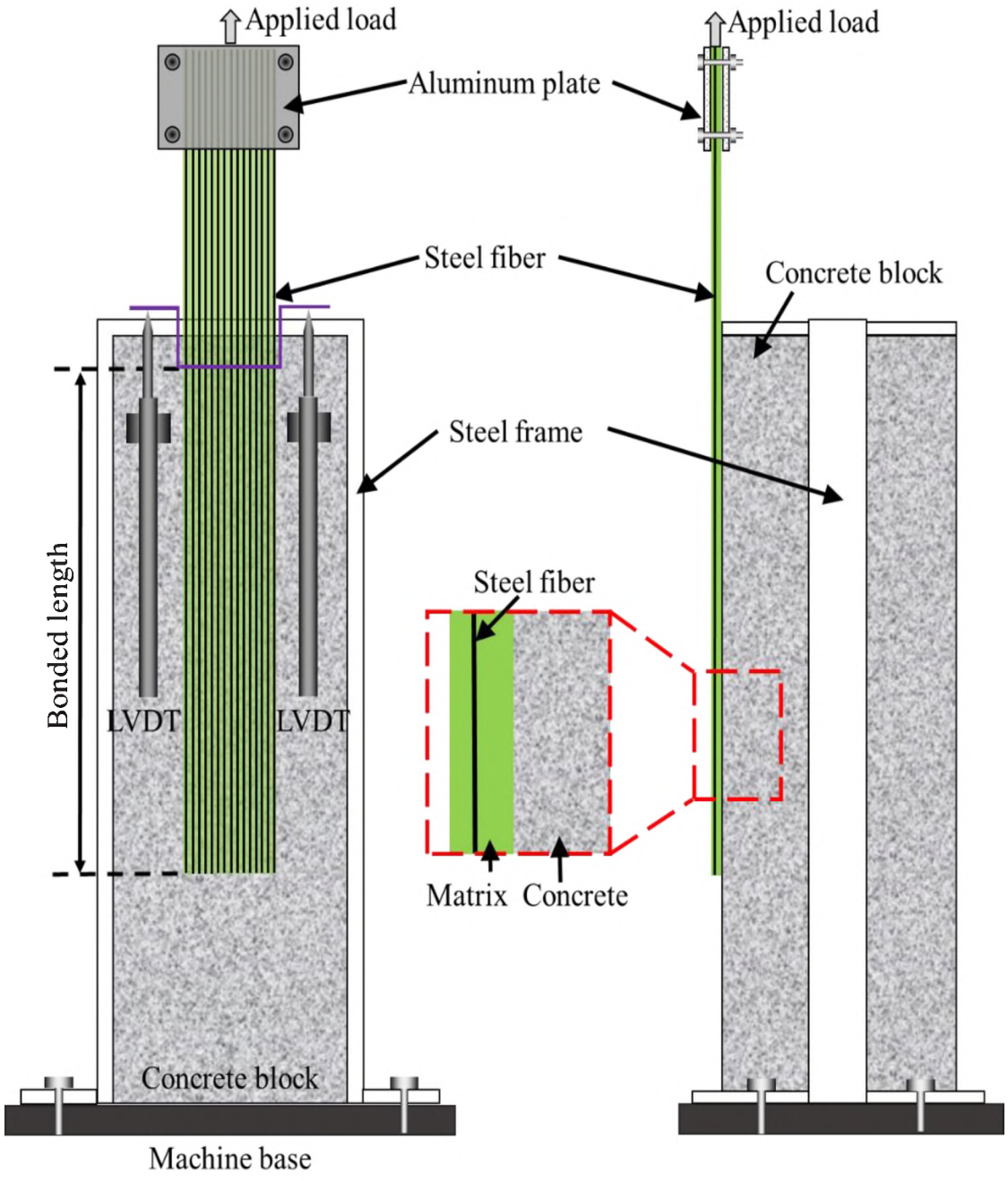


(a) (b)

Figure 4. Single-lap direct shear test setup (unit: mm): (a) front view, and (b) side view.

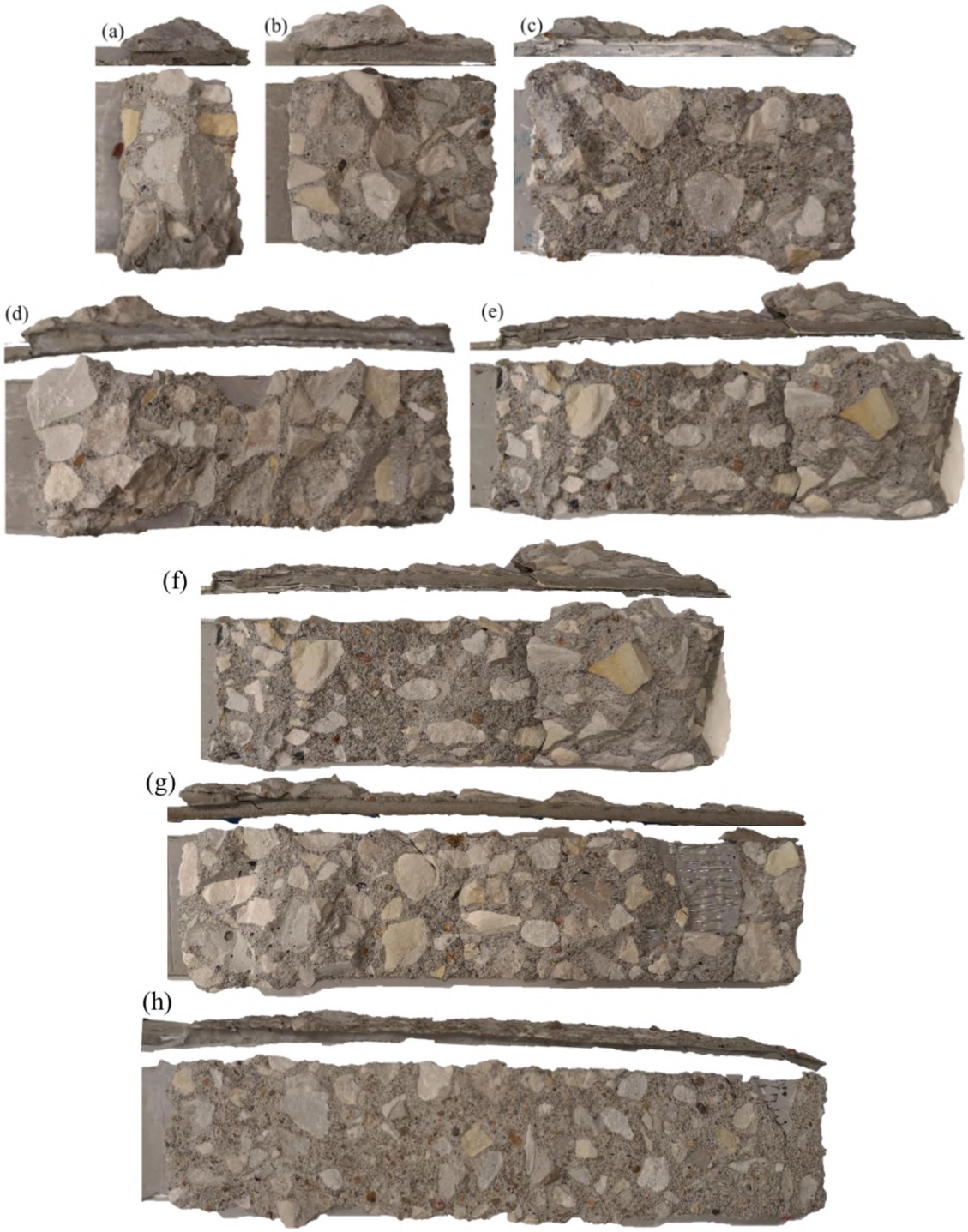


Figure 5. Typical failure mode of single-lap shear test specimens with MD fibers and bonded length of: (a) 30 mm, (b) 60 mm, (c) 90 mm, (d) 120 mm, (e) 150 mm, (f) 180 mm, (g) 210 mm, and (h) 240 mm.

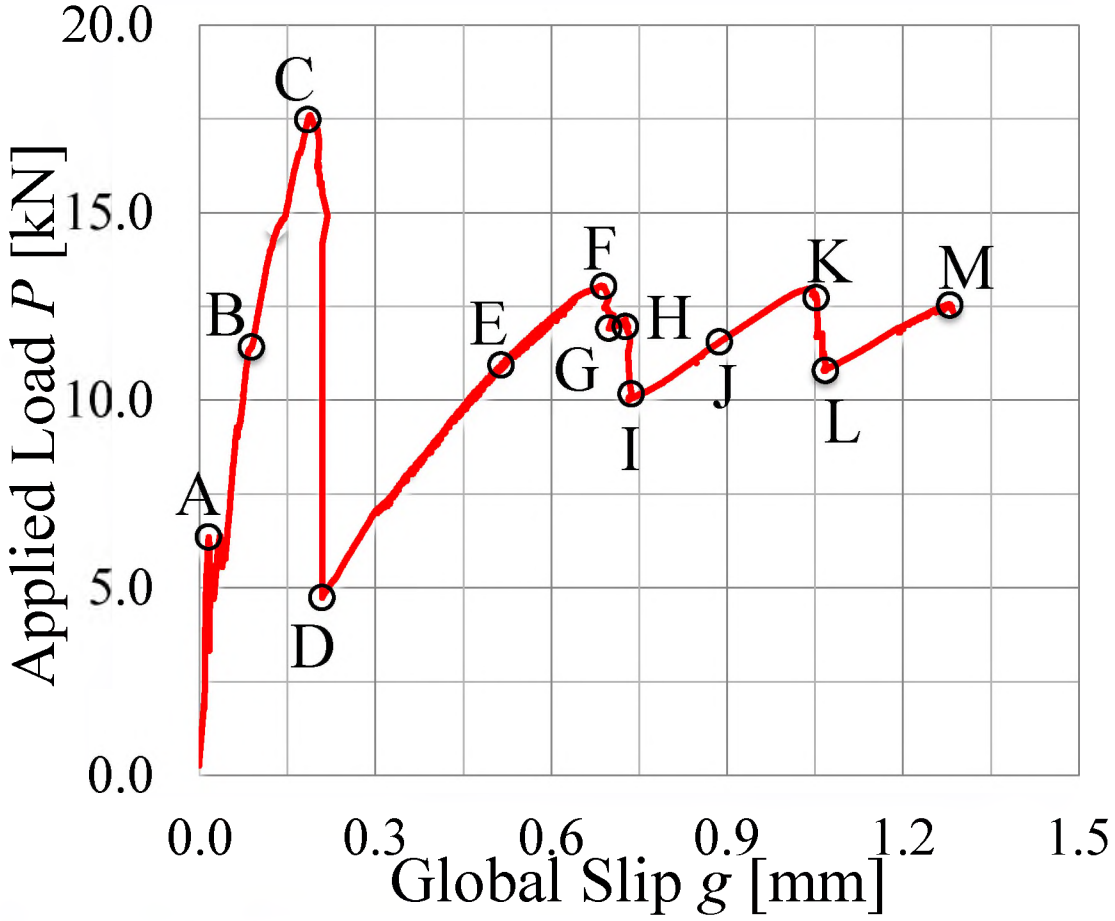


(a)

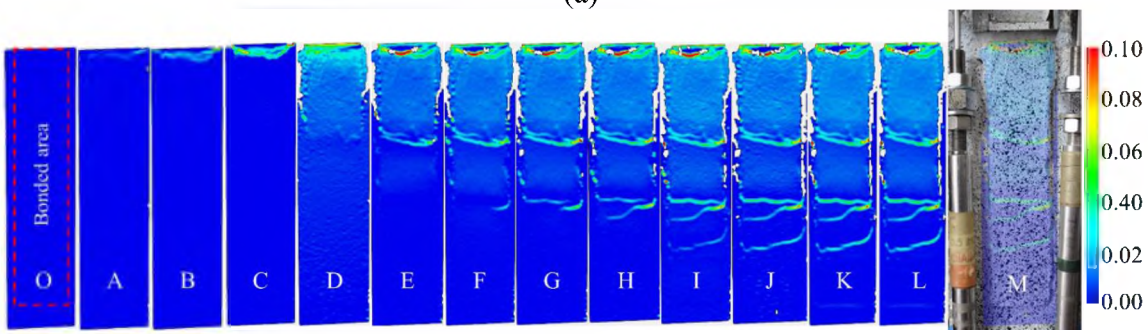


(b)

Figure 6. (a) Load-response and (b) axial strain along fiber direction of specimen MD_210_8_D.

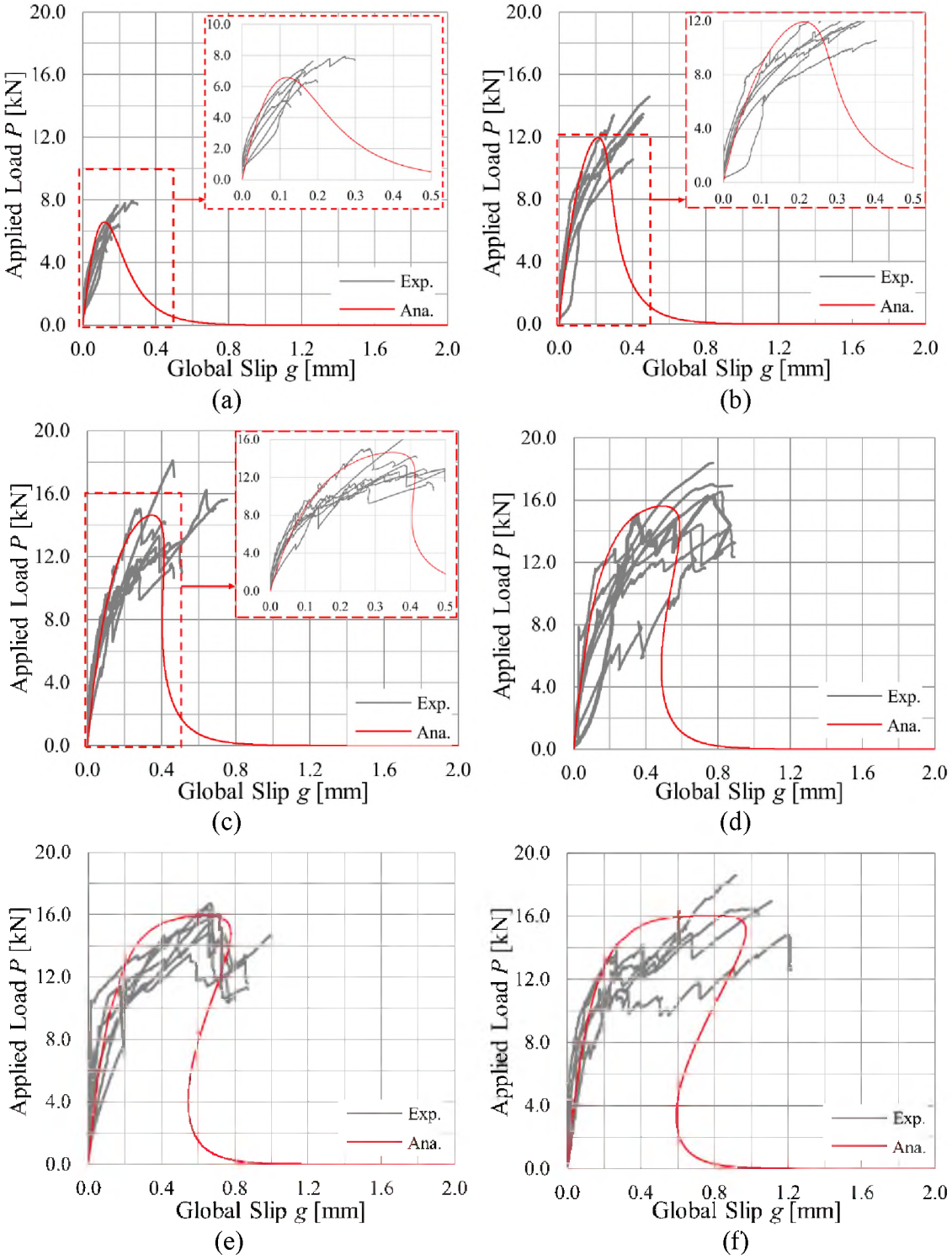


Figure 7. Loads responses of single-lap shear specimens with MD fibers and bonded length $L$ = (a) 30 mm, (b) 60 mm, (c) 90 mm, (d) 120 mm (Note MD_120_8 not shown), (e) 150 mm, (f) 180 mm, (g) 210 mm (Note MD_210_7_D not shown), and (h) 240 mm. All specimens shown failed due to debonding of the composite.

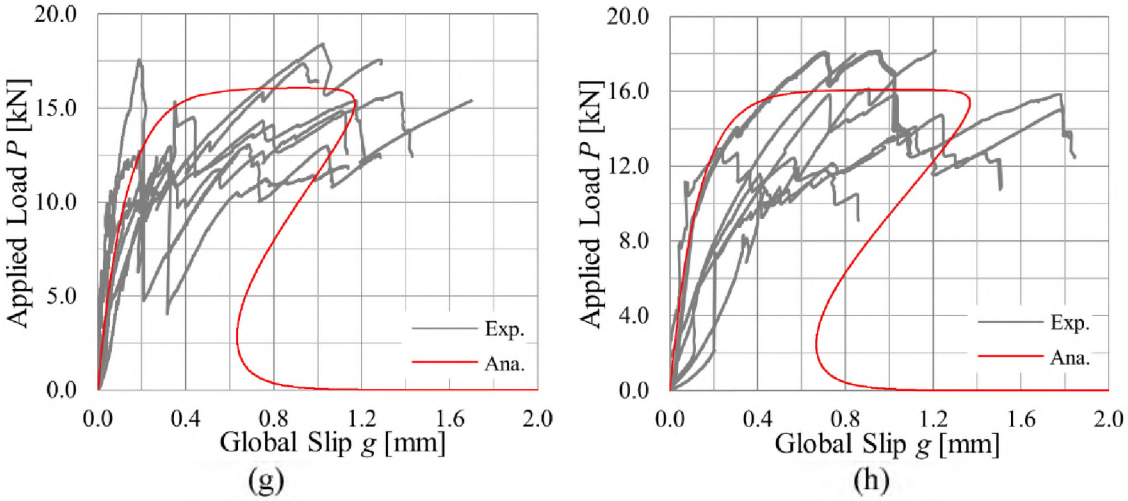


Figure 7. Loads responses of single-lap shear specimens with MD fibers and bonded length $L$ = (a) 30 mm, (b) 60 mm, (c) 90 mm, (d) 120 mm (Note MD_120_8 not shown), (e) 150 mm, (f) 180 mm, (g) 210 mm (Note MD_210_7_D not shown), and (h) 240 mm. All specimens shown failed due to debonding of the composite (continued).

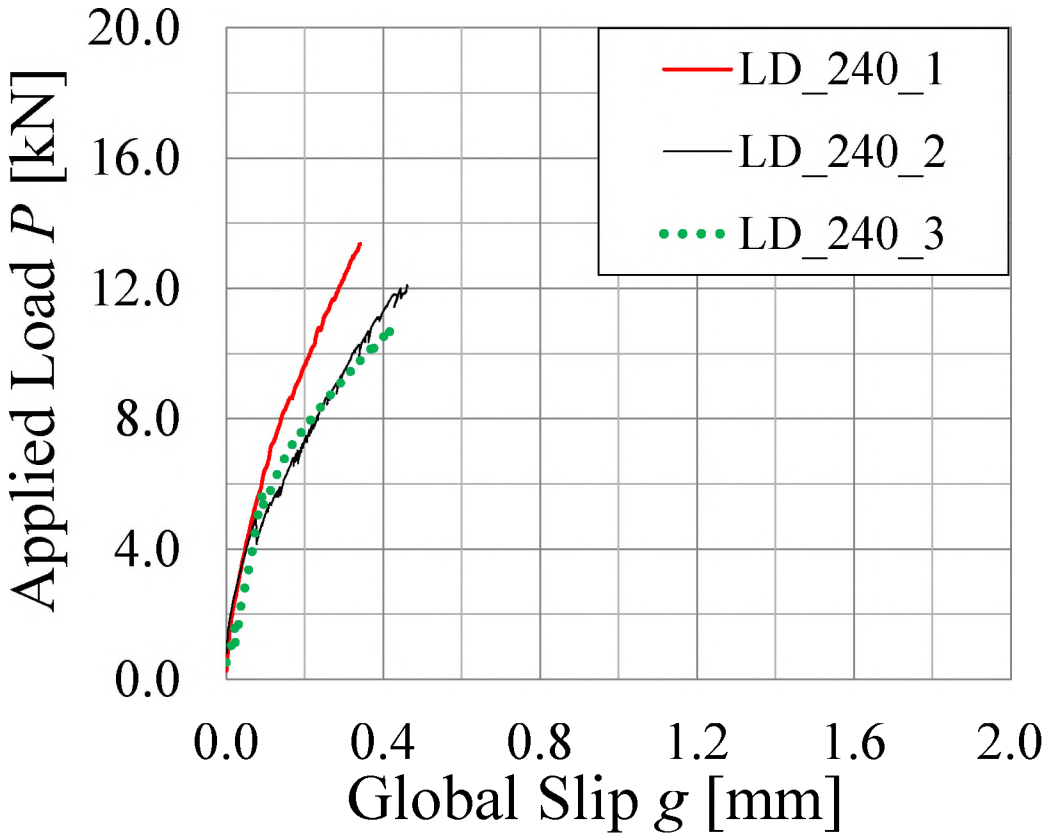


Figure 8. Load responses of single-lap shear specimens with LD fibers and bonded length $L$=240 mm. All specimens failed due to fiber rupture.

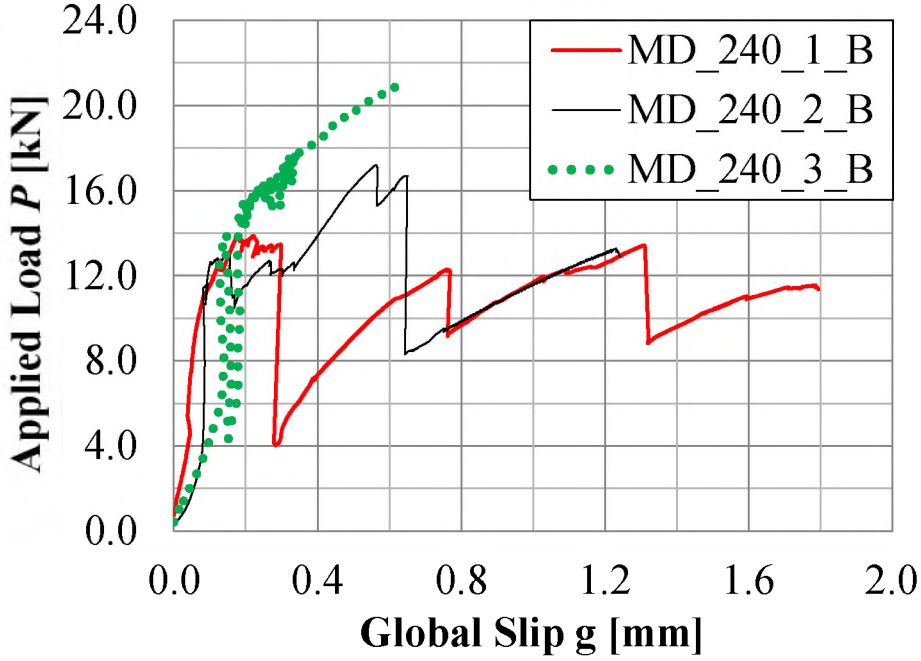


Figure 9. Load responses of single-lap shear specimens with MD fibers, bonded length $L$=240 mm, and bare fibers outside the bonded area.

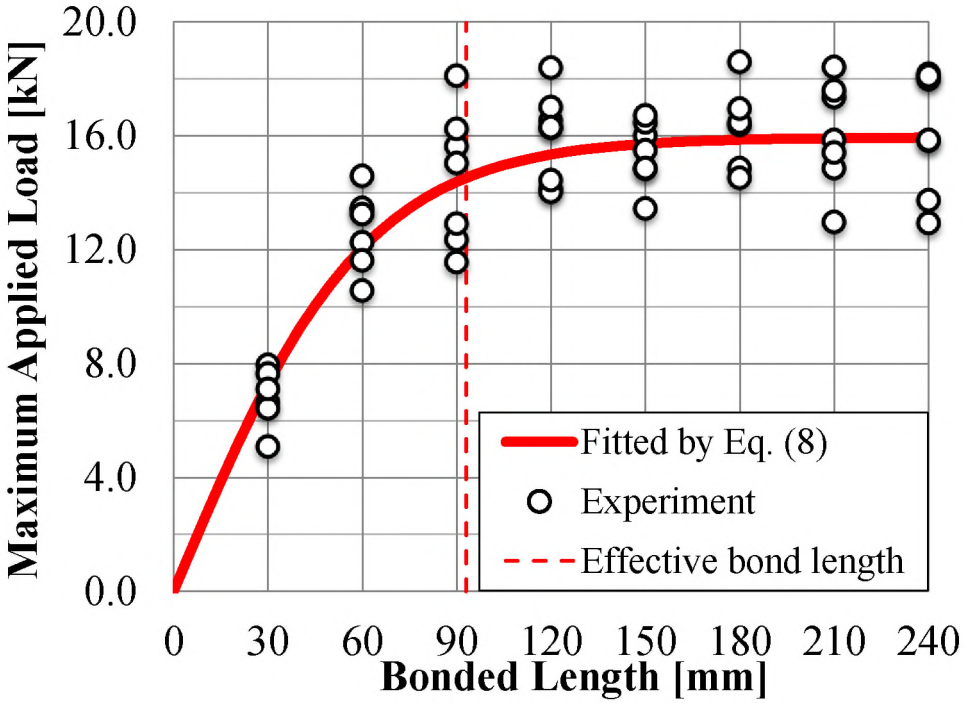


Figure 10. Peak load-bonded length relationship of specimens with MD fibers that failed due to debonding of the composite.

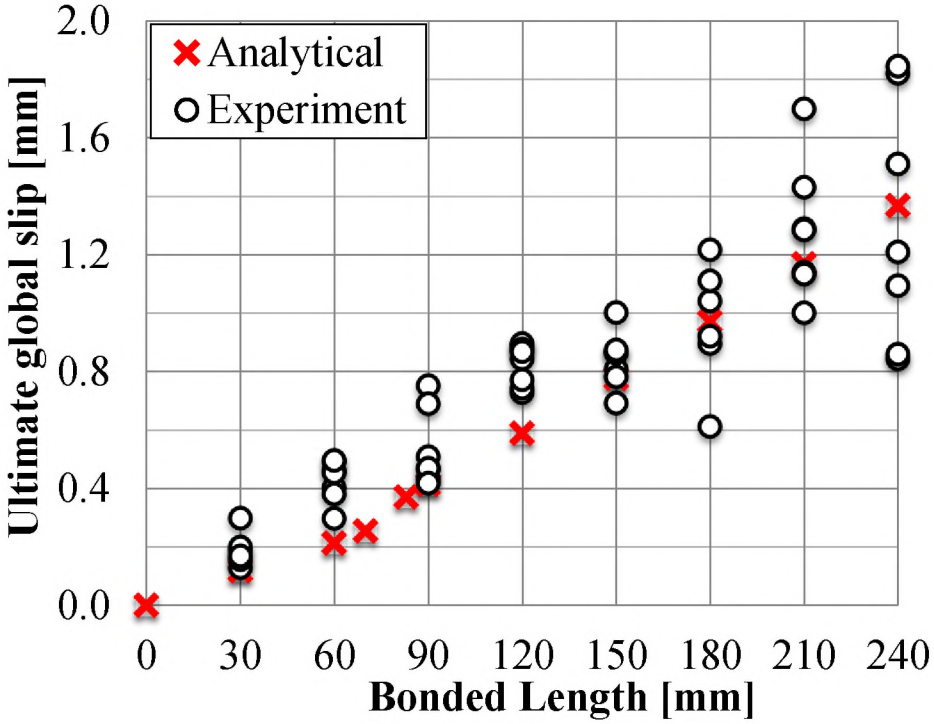


Figure 11. Ultimate global slip-bonded length relationship of specimens with MD fibers that failed due to debonding of the composite.

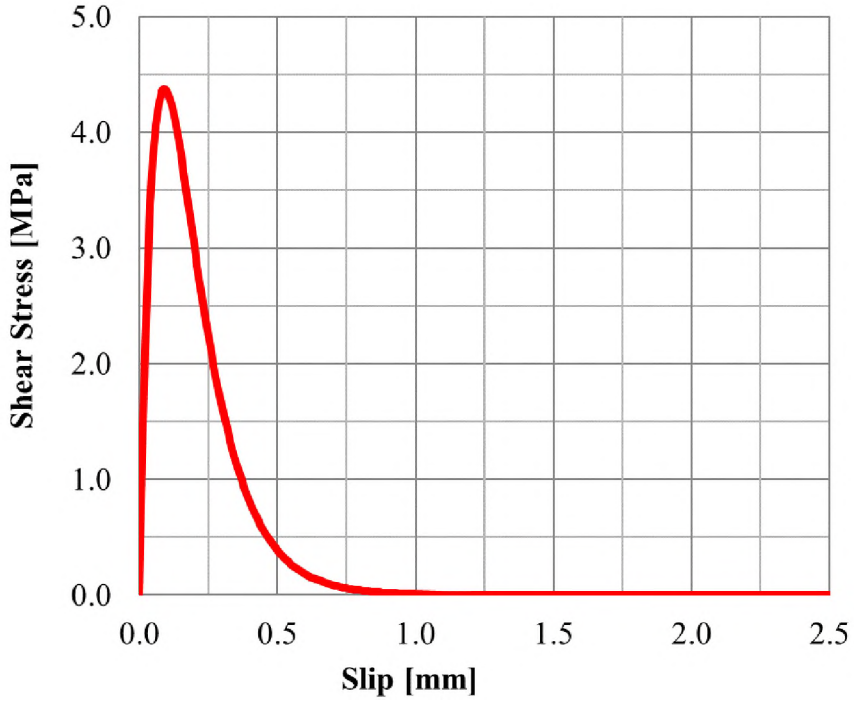


Figure 12. Bond-slip relationship for SRP-concrete joints with MD fibers determined from the experimental results.

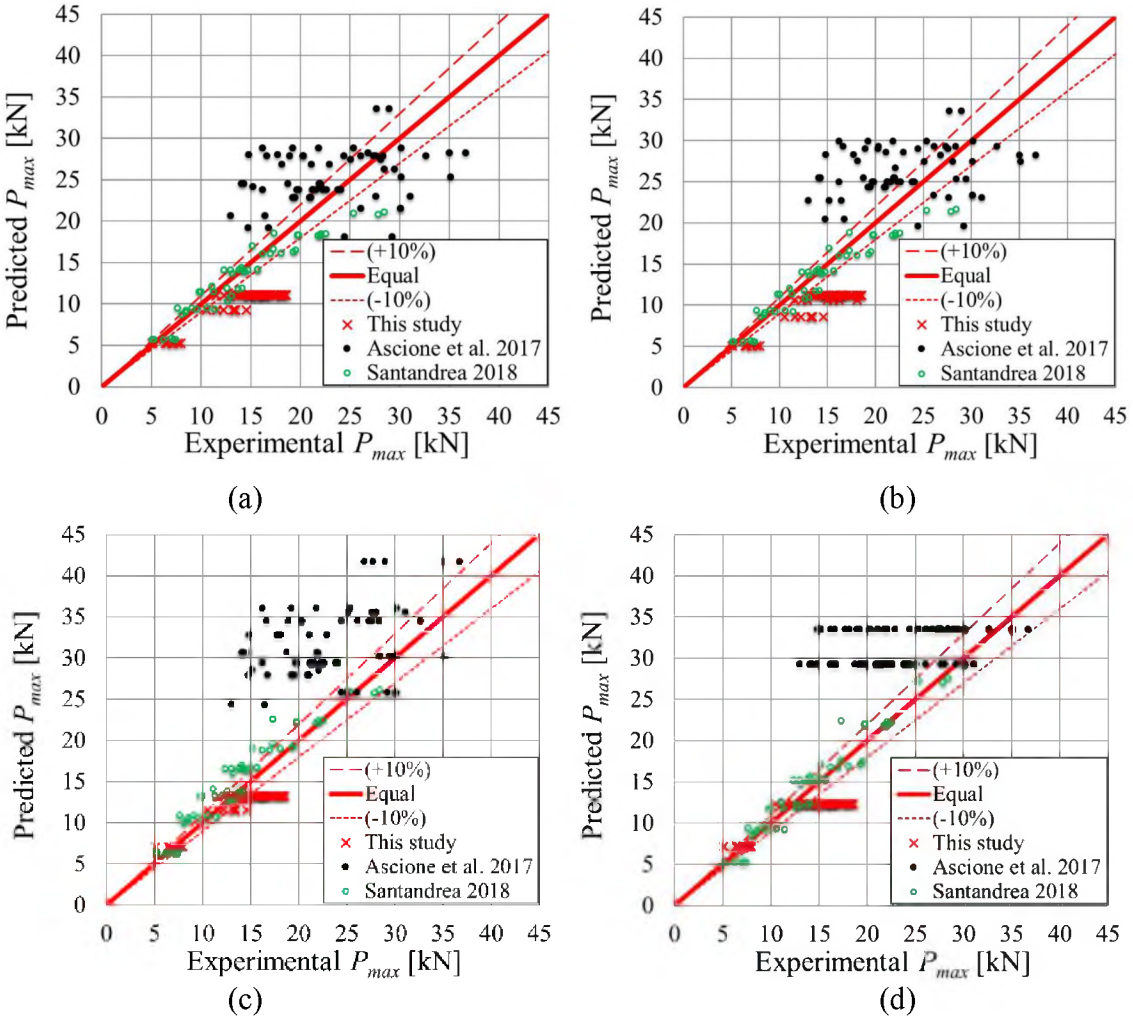


Figure 13. Evaluation of existing formulas for $P_{max}$: (a) Eq. (13), (b) Eq. (15), (c) Eq. (17), and (d) Eq. (19).

Table 1. Properties of fibers provided by the manufacturer [16].

| Fiber sheet type | Density of fiber sheets ($g/m^2$) | Number of cords (/mm) | Equivalent thickness $t_f$ (mm) | Break deformation (%) | Tensile strength (MPa) |
|---|---|---|---|---|---|
| Low density (LD) | 600 | 0.157 | 0.084 | >2 | >3000 |
| Medium density (MD) | 1200 | 0.314 | 0.169 | >2 | >3000 |

Table 2. Tensile test results of bare steel wire sheet and SRP plate with MD fibers.

| Coupon ID | Type | Strain at 5 kN ($10^{-6}$) | Elastic modulus (GPa) | | Failure mode | Ultimate load (kN) |
|---|---|---|---|---|---|---|
| | | | | Avg [CoV] | | |
| BF_1 | Bare MD fibers | 3091 | 200.4 | 190.8 [0.05] | Gripped end fracture | 16.24 |
| BF_2 | Bare MD fibers | 3285 | 188.6 | | Gripped end fracture | 17.33 |
| BF_3 | Bare MD fibers | 3380 | 183.3 | | Fiber rupture | 23.89 |
| SRP_1 | SRP with MD fibers | 2548 | 232.3 | 257.2 [0.08] | Gripped end fracture | 16.95 |
| SRP_2 | SRP with MD fibers | 2299 | 257.3 | | Fiber rupture | 21.73 |
| SRP_3 | SRP with MD fibers | 2107 | 280.8 | | Gripped end fracture | 17.01 |
| SRP_4_D | SRP with MD fibers | 2292 | 258.2 | | Fiber rupture | 21.47 |

Table 3. Direct shear test results.

| Specimen ID | Failure Mode | $P_{max}$ (kN) | | $g_{max}$ (mm) | $g_{ult}$ (mm) | |
|---|---|---|---|---|---|---|
| | | | Avg [CoV] | | | Avg [CoV] |
| MD_30_1 | Debonding | 7.95 | 6.80 [0.151] | 0.271 | 0.298 | 0.190 [0.311] |
| MD_30_2 | Debonding | 5.08 | | 0.111 | 0.128 | |
| MD_30_3 | Debonding | 7.64 | | 0.188 | 0.188 | |
| MD_30_4 | Debonding | 6.63 | | 0.147 | 0.155 | |
| MD_30_5 | Debonding | 6.42 | | 0.195 | 0.199 | |
| MD_30_6 | Debonding | 7.10 | | 0.160 | 0.169 | |
| MD_60_1 | Debonding | 14.58 | 12.73 [0.106] | 0.493 | 0.493 | 0.426 [0.168] |
| MD_60_2 | Debonding | 13.40 | | 0.297 | 0.297 | |
| MD_60_3 | Debonding | 10.56 | | 0.402 | 0.402 | |
| MD_60_4 | Debonding | 12.26 | | 0.377 | 0.380 | |
| MD_60_5 | Debonding | 13.47 | | 0.458 | 0.461 | |
| MD_60_6 | Debonding | 13.25 | | 0.453 | 0.454 | |
| MD_60_7 | Debonding | 11.62 | | 0.493 | 0.496 | |

Table 3. Direct shear test results (continued).

| Specimen ID | Failure Mode | $P_{max}$ (kN) | | $g_{max}$ (mm) | $g_{ult}$ (mm) | |
|---|---|---|---|---|---|---|
| | | | Avg [CoV] | | | Avg [CoV] |
| MD_90_1 | Debonding | 11.56 | 14.54 [0.177] | 0.452 | 0.466 | 0.534 [0.247] |
| MD_90_2 | Debonding | 12.34 | | 0.420 | 0.434 | |
| MD_90_3 | Debonding | 12.90 | | 0.498 | 0.508 | |
| MD_90_4 | Debonding | 15.63 | | 0.752 | 0.752 | |
| MD_90_5 | Debonding | 16.23 | | 0.641 | 0.690 | |
| MD_90_6 | Debonding | 18.10 | | 0.461 | 0.470 | |
| MD_90_7_D | Debonding | 15.03 | | 0.284 | 0.418 | |
| MD_120_1 | Debonding | 14.14 | 15.89 [0.098] | 0.864 | 0.889 | 0.827 [0.083] |
| MD_120_2 | Debonding | 14.02 | | 0.646 | 0.727 | |
| MD_120_3 | Debonding | 14.44 | | 0.707 | 0.895 | |
| MD_120_4 | Debonding | 16.53 | | 0.816 | 0.842 | |
| MD_120_5 | Debonding | 16.27 | | 0.741 | 0.743 | |
| MD_120_6 | Debonding | 17.00 | | 0.765 | 0.877 | |
| MD_120_7 | Debonding | 18.39 | | 0.771 | 0.771 | |
| MD_120_8 | Fiber rupture | 22.70 | | 1.365 | 1.365 | |
| MD_120_9_D | Debonding | 16.29 | | 0.776 | 0.868 | |
| MD_150_1 | Debonding | 16.00 | 15.40 [0.073] | 0.715 | 0.807 | 0.840 [0.114] |
| MD_150_2 | Debonding | 14.84 | | 0.659 | 0.866 | |
| MD_150_3 | Debonding | 15.49 | | 0.675 | 0.863 | |
| MD_150_4 | Debonding | 16.47 | | 0.651 | 1.001 | |
| MD_150_5 | Debonding | 16.71 | | 0.667 | 0.691 | |
| MD_150_6 | Debonding | 13.44 | | 0.556 | 0.873 | |
| MD_150_7 | Debonding | 14.85 | | 0.707 | 0.781 | |
| MD_180_1 | Debonding | 14.85 | 16.29 [0.091] | 1.197 | 1.216 | 0.966 [0.218] |
| MD_180_2 | Debonding | 16.38 | | 0.611 | 0.611 | |
| MD_180_3 | Debonding | 16.46 | | 0.999 | 1.041 | |
| MD_180_4 | Debonding | 14.52 | | 0.890 | 0.895 | |
| MD_180_5 | Debonding | 16.95 | | 1.110 | 1.110 | |
| MD_180_6_D | Debonding | 18.59 | | 0.919 | 0.921 | |
| MD_210_1 | Debonding | 12.97 | 16.06 [0.117] | 0.329 | 1.140 | 1.282 [0.179] |
| MD_210_2 | Debonding | 15.84 | | 1.370 | 1.430 | |
| MD_210_3 | Debonding | 14.85 | | 1.109 | 1.133 | |
| MD_210_4 | Debonding | 17.35 | | 0.934 | 1.000 | |
| MD_210_5 | Debonding | 15.40 | | 1.699 | 1.699 | |
| MD_210_6 | Debonding | 18.41 | | 1.023 | 1.289 | |
| MD_210_7_D | Fiber rupture | 24.12 | | 1.165 | 1.165 | |
| MD_210_8_D | Debonding | 17.59 | | 0.189 | 1.285 | |

Table 3. Direct shear test results (continued).

| Specimen ID | Failure Mode | $P_{max}$ (kN) | | $g_{max}$ (mm) | $g_{ult}$ (mm) | |
|---|---|---|---|---|---|---|
| | | | Avg [CoV] | | | Avg [CoV] |
| MD_240_1 | Debonding | 15.83 | 16.08 [0.133] | 0.726 | 1.820 | 1.311 [0.343] |
| MD_240_2 | Debonding | 15.84 | | 1.771 | 1.844 | |
| MD_240_3 | Debonding | 17.98 | | 0.842 | 0.842 | |
| MD_240_4 | Debonding | 12.94 | | 0.231 | 0.860 | |
| MD_240_5 | Debonding | 13.73 | | 1.081 | 1.510 | |
| MD_240_6 | Debonding | 18.17 | | 1.208 | 1.209 | |
| MD_240_7_D | Debonding | 18.10 | | 0.941 | 1.094 | |
| LD_240_1_D | Fiber rupture | 13.36 | 12.11 [0.103] | 0.341 | 0.341 | 0.412 [0.153] |
| LD_240_2_D | Fiber rupture | 12.09 | | 0.461 | 0.463 | |
| LD_240_3_D | Fiber rupture | 10.87 | | 0.432 | 0.432 | |
| MD_240_1_B | Debonding | 13.86 | 17.32 [0.204] | 0.221 | 1.794 | 1.219 [0.481] |
| MD_240_2_B | Debonding | 17.19 | | 0.562 | 1.241 | |
| MD_240_3_B | Debonding | 20.91 | | 0.621 | 0.622 | |

## REFERENCES


[1] Triantafillou, T. C., & Deskovic, N. (1991). Innovative prestressing with FRP sheets: mechanics of short-term behavior. Journal of Engineering Mechanics, 117(7), 1652-1672.

[2] Bakis, C.E., Bank, L.C., Brown, V., Cosenza, E., Davalos, J.F., Lesko, J.J., Machida, A., Rizkalla, S.H. & Triantafillou, T.C., (2002). Fiber-reinforced polymer composites for construction-State-of-the-art review. Journal of composites for construction, 6(2), 73-87.

[3] Chen, W., Pham, T. M., Sichembe, H., Chen, L., & Hao, H. (2018). Experimental study of flexural behaviour of RC beams strengthened by longitudinal and U-shaped basalt FRP sheet. Composites Part B: Engineering, 134, 114-126.

[4] Attari, N., Amziane, S., & Chemrouk, M. (2012). Flexural strengthening of concrete beams using CFRP, GFRP and hybrid FRP sheets. Construction and Building Materials, 37, 746-757.

[5] Pan, J., & Leung, C. K. (2007). Debonding along the FRP–concrete interface under combined pulling/peeling effects. Engineering Fracture Mechanics, 74(1-2), 132-150.

[6] Khalifa, A., & Nanni, A. (2000). Improving shear capacity of existing RC T-section beams using CFRP composites. Cement and Concrete Composites, 22(3), 165-174.

[7] Hii, A. K., & Al-Mahaidi, R. (2007). Torsional capacity of CFRP strengthened reinforced concrete beams. Journal of Composites for Construction, 11(1), 71-80.

[8] Alabdulhady, M. Y., & Sneed, L. H. (2019). Torsional strengthening of reinforced concrete beams with externally bonded composites: A state of the art review. Construction and Building Materials, 205, 148-163.

[9] Wobbe, E., Silva, P., Barton, B. L., Dharani, L. R., Birman, V., Nanni, A., & Tunis, G. (2004). Flexural Capacities of RC Beams Externally Bonded with SRP and SRG. http://www.hardwirellc.com/Downloads/Flex_Capacity.pdf, 2004, 8 pp.

[10] Ascione, F., Lamberti, M., Napoli, A., Razaqpur, G., & Realfonzo, R. (2017). An experimental investigation on the bond behavior of steel reinforced polymers on concrete substrate. Composite Structures, 181, 58-72.

[11] Górski, M., Krzywon, R., Dawczynski, S., & Greppi, R. (2013) Structural strengthenings based on SRP and SRG composites. International Conference on Engineering UBI, Nov 27-29, University of Beira Interior - Covilhã, Portugal.

[12] Prota, A., Manfredi, G., Nanni, A., Cosenza, E., & Pecce, M. (2004). Flexural strengthening of RC beams using emerging materials: Ultimate behavior. Proceedings of 2nd International Conference on FRP Composites in Civil Engineering, CICE 2004, Adelaide, Australia, 2004, 163-170.

[13] Figeys, W., Schueremans, L., Van Gemert, D., & Brosens, K. (2008). A new composite for external reinforcement: Steel cord reinforced polymer. Construction and Building Materials, 22(9), 1929-1938.

[14] Figeys, W., Schueremans, L., Brosens, K., & Van Gemert, D. (2005). Strengthening of concrete structures using steel wire reinforced polymer. ACI Special Publication, 230, 43.

[15] Pecce, M., Ceroni, F., Prota, A., & Manfredi, G. (2006). Response prediction of RC beams externally bonded with steel-reinforced polymers. Journal of Composites for Construction, 10(3), 195-203.

[16] ECO Products of Kerakoll: products.kerakoll.com (accessed on Feb. 2020)

[17] Matana, M., Nanni, A., Dharani, L., Silva, P., & Tunis, G. (2005). Bond performance of steel reinforced polymer and steel reinforced grout. Proceedings of the International Symposium on Bond Behaviour of FRP in Structures, BBFS, 125-132).

[18] ACI 440.2R-17 (2017) Guide for the Design and Construction of Externally Bonded FRP Systems for Strengthening Concrete Structures, American Concrete Institute, Farmington Hills

[19] Mitolidis, G. J., Salonikios, T. N., & Kappos, A. J. (2008). Mechanical and Bond Characteristics of SRP and CFRP Reinforcement- A Comparative Research. Open Construction and Building Technology Journal, 2, 207-216.

[20] Carloni, C., Santandrea, M., & Imohamed, I. A. O. (2017). Determination of the interfacial properties of SRP strips bonded to concrete and comparison between single-lap and notched beam tests. Engineering Fracture Mechanics, 186, 80-104.

[21] Mukhtar, F. M., & Faysal, R. M. (2018). A review of test methods for studying the FRP-concrete interfacial bond behavior. Construction and Building Materials, 169, 877-887.

[22] Wu, Y. F., & Jiang, C. (2013). Quantification of bond-slip relationship for externally bonded FRP-to-concrete joints. Journal of Composites for Construction, 17(5), 673-686.

[23] Zhang, D., Gu, X., Yu, Q., Huang, H., Wan, B., & Jiang, C. (2018). Fully probabilistic analysis of FRP-to-concrete bonded joints considering model uncertainty. Composite Structures, 185, 786-806.

[24] Kim, Y. J., Fam, A., Kong, A., & El-Hacha, R. (2005). Flexural strengthening of RC beams using steel reinforced polymer (SRP) composites. ACI Special Publication, 230, 93.

[25] Santandrea, M. (2018). Bond behavior between fiber reinforced composites and quasi-brittle material interfaces. Dissertation. University of Bologna.

[26] ASTM C39/C39M-17b. (2017). Standard test method for compressive strength of cylindrical concrete specimens. West Conshohocken, Pam: ASTM International.

[27] ASTM C496/C496M. (2017). Standard Test Method for Splitting Tensile Strength of Cylindrical Concrete Specimens; ASTM International: West Conshohocken, PA, USA, 2011.

[28] GOM: https://www.gom.com/3d-software/gom-correlate-professional.html (Accessed Feb. 2020)

[29] Zhu, H., Wu, G., Shi, J., Liu, C., & He, X. (2014). Digital image correlation measurement of the bond–slip relationship between fiber-reinforced polymer sheets and concrete substrate. Journal of Reinforced Plastics and Composites, 33(17), 1590-1603.

[30] Lopez, A., Galati, N., Alkhrdaji, T., & Nanni, A. (2007). Strengthening of a reinforced concrete bridge with externally bonded steel reinforced polymer (SRP). Composites Part B: Engineering, 38(4), 429-436.

[31] Casadei, P., Nanni, A., Alkhrdaji, T., & Thomas, J. (2005). Performance of double-T prestressed concrete beams strengthened with steel reinforcement polymer. Advances in Structural Engineering, 8(4), 427-442.

[32] Chen, J. F., & Teng, J. G. (2001). Anchorage strength models for FRP and steel plates bonded to concrete. Journal of structural engineering, 127(7), 784-791.

[33] Lu, X. Z., Teng, J. G., Ye, L. P., & Jiang, J. J. (2005). Bond–slip models for FRP sheets/plates bonded to concrete. Engineering structures, 27(6), 920-937.

[34] Lin, J. P., & Wu, Y. F. (2016). Numerical analysis of interfacial bond behavior of externally bonded FRP-to-concrete joints. Journal of Composites for Construction, 20(5), 04016028.

[35] Dai, J., Ueda, T., & Sato, Y. (2005). Development of the nonlinear bond stress–slip model of fiber reinforced plastics sheet–concrete interfaces with a simple method. Journal of composites for construction, 9(1), 52-62.

[36] Liu, K., & Wu, Y. F. (2012). Analytical identification of bond–slip relationship of EB-FRP joints. Composites Part B: Engineering, 43(4), 1955-1963.

[37] Zou, X., Sneed, L. H., & D'Antino, T. (2020). Full-range behavior of fiber reinforced cementitious matrix (FRCM)-concrete joints using a trilinear bond-slip relationship. Composite Structures, 112024.

[38] Neubauer, U., & Rostasy, F. S. (1997). Design aspects of concrete structures strengthened with externally bonded CFRP plates. Proc., 7th Int. Conf. on Struct. Faults and Repairs, ECS Publications, Edinburgh, Scotland, 2, 109–118.

[39] Maeda, T., Asano, Y., Sato, Y., Ueda, T., & Kakuta, Y. (1997). ''A study on bond mechanism of carbon fiber sheet.'' Non-Metallic (FRP) Reinforcement for Concrete Struct., Proc., 3rd Int. Symp., Japan Concrete Institute, Sapporo, 1, 279–285.

[40] Bamforth, P., Chisholm, D., Gibbs, J., & Harrison, T. (2008). Properties of concrete for use in Eurocode 2.

# IV. DETECTION OF CFRP-CONCRETE INTERFACIAL DEBONDING USING ACTIVE MICROWAVE THERMOGRAPHY

Xingxing Zou, Lesley H. Sneed, Ali Mirala, Mohammad Tayab Ghasr, and Kristen Donnell

## ABSTRACT

Thermographic techniques are potentially well-suited for inspection of carbon fiber reinforced polymer (CFRP)-strengthened concrete structures as air pockets caused by defects can impede heat transfer from CFRP to concrete, causing heat accumulation in the CFRP above the defect. Active microwave thermography (AMT), a thermographic technique that utilizes a microwave-based thermal excitation, is proposed as an efficient technique for non-contact, real-time inspection of embedded flaws. This study examines the use of AMT to detect interfacial debonding of the CFRP-concrete interface. This work differentiates from previous tests in that here, CFRP-concrete interfacial damage is caused by and monitored under external mechanical loading. CFRP strips bonded to the surface of concrete prisms are tested in direct shear to initiate debonding. AMT is used to monitor the CFRP surface thermal profile in an attempt to detect and monitor interfacial damage. Correlations between the mechanical load response (namely, applied load vs. composite displacement relative to the substrate, i.e., slip) and AMT results (namely, temporal CFRP thermal response) are found. A high thermal contrast, TC, defined as the CFRP surface thermal response caused by loading, is observed where interfacial debonding initiates and propagates along the composite bonded length. An increase in the TC slope occurs when a load drop occurs, which is indicative of local debonding occurrence or mobilization. Finally, at different load levels, the interfacial slip and surface temperature distributions

along the bonded length show similar trends. These correlations indicate that initiation and propagation of CFRP-concrete interfacial damage can be monitored by the AMT technique.

**Keywords:** Active microwave thermography (AMT); carbon fiber reinforced polymer (CFRP) composite material; interfacial debonding; single-lap direct shear test.

## 1. INTRODUCTION

The inspection, rehabilitation, repair, and retrofit of civil engineering structures constructed in the 20th century are becoming an increasingly important topic and a growing market. Thus, the development and widespread use of technologies that allow for effective and cost-efficient rehabilitation of civil infrastructures constitute one of the main challenges faced by civil engineers. Carbon fiber reinforced polymer (CFRP) composites, consisting of high-strength continuous fibers embedded within a high-performance thermosetting polymer matrix, have emerged since the mid-1980s as a promising technique for strengthening concrete structures such as buildings and bridges due to their high specific strength and stiffness, light weight, and durability under certain environments [1]. Many studies have shown that the flexural [2][3], shear [4][5], and torsional [6][7] strength of a reinforced concrete (RC) member can be increased by externally bonding CFRP composites to the surface of the member. In this type of application, the composite action between the CFRP and concrete plays a key role in strength improvement [8].

Many studies reported premature failure of CFRP-strengthened concrete members due to debonding of the CFRP composite with or without the concrete cover attached [9][10], which usually triggered structural failure. Long-term environmental conditions,

such as temperature, fatigue, and moisture cycles, may also cause CFRP-concrete interfacial debonding [11][12][13][14]. In addition, poor workmanship during composite installation can lead to initial defects and flaws along CFRP-concrete interface [15][16]. Therefore, effective methods are needed to determine whether the CFRP layers are properly installed and detect interfacial imperfections both initially and periodically during the life of the structure [17][18][19][20][21].

Active thermography is a nondestructive evaluation (NDE) method that has shown promise to detect interfacial imperfections hidden internally within structures in forms of defects, flaws, and local regions of debonding [22][23][24]. There are generally three steps necessary to conduct NDE using active thermography: (i) utilize an external heat excitation to induce heat in the structure, (ii) measure the thermal profile on the surface of the structure with a thermal camera, and (iii) correlate the surface temperature with inner imperfections. In the first step, a heat source is required that is capable of generating a measurable surface temperature increase for the second step in order to facilitate detection of inner structure defects. In previous works, a flash heat lamp was employed that delivers a large amount of energy to the surface of the structure under test within a very short timeframe, causing a temperature increase that may potentially change material properties [24]. Flash lamp thermography is also unable to target the incident thermal energy to an area of interest and thus is applied over an area that is larger than the area of interest [21][24][25]. Recently, utilizing a microwave heat excitation has shown advantages in certain applications of active thermography such as inspection of CFRP sheets with flat-bottom holes (FBHs) [25], covered surface cracks in metal structures [26], and chopped steel fiber distribution in cementitious materials [27]. This technique is referred to as active

microwave thermography (AMT). For the detection of CFRP-concrete interfacial debonding, significant advantages of utilizing a microwave excitation include the ability to apply the heat source for arbitrarily long durations with a constant medium power (on the order of tens of watts), and microwaves can penetrate beyond the surface of the CFRP (in the case of unidirectional CFRP).

Previous tests have been conducted to study the use of AMT on CFRP structures with man-made defects created by foam or air injection at predefined locations. However, such defects were different from those that exist in real structures in terms of material, location, and thickness [22][24][25]. In the present study, AMT is used in an attempt to detect initiation and propagation of interfacial damage of CFRP-strengthened concrete structures. CFRP strips were bonded to the surface of concrete prisms and tested in single-lap direct shear to initiate composite debonding. AMT was used to monitor the CFRP surface temperature throughout the test. Seven total single-lap shear tests are presented, including two without and five with AMT. The first two specimens were instrumented with strain gauges along the composite bonded length to quantify the distribution of the displacement of the composite relative to the concrete substrate, i.e., the interfacial slip, which is used to correlate the mechanical and thermal responses. The five specimens tested with AMT were used to explore the thermal response caused by damage to the CFRP-concrete interface. The results of this study are intended to demonstrate the feasibility of using AMT to detect the initiation and propagation of CFRP-concrete interfacial debonding and lay the groundwork for future work in this area.

## 2. PRINCIPLE AMT TO DETECT CFRP-CONCRETE INTERFACIAL DEBONDING

As mentioned in the previous section, AMT utilizes microwave heating and subsequent thermographic measurement. Regarding the microwave heat excitation, there are two different heating mechanisms that may take place, depending on the materials under test: dielectric heating and Joule heating. As it relates to dielectric heating, dielectric materials are defined by their complex relative (to free-space) dielectric properties, defined as $\varepsilon_r = \varepsilon_r' - j\varepsilon_r''$, where $\varepsilon_r'$ and $\varepsilon_r''$, or permittivity and loss factor, respectively, represent the ability of a material to store and absorb microwave energy, respectively. When a lossy dielectric is irradiated with microwave energy, the amount of dissipated heat, $Q$, inside the dielectric can be expressed as:

$$Q = 2\pi f \varepsilon_0 \varepsilon_r'' |E|^2 \quad (1)$$

where $f$ is the frequency, $\varepsilon_0$ is the free space dielectric constant, and $E$ is the RMS (root mean square) magnitude of the electric field. The second heating mechanism in AMT, Joule heating, occurs when electromagnetic waves impinge upon a conductive material. In this case, electric currents are induced on the surface of the conductive material and ohmic losses occur.

As it relates to materials with embedded carbon fibers (which are conductive), the interaction of the material with microwave energy is strongly influenced by the relative orientation of the fibers with respect to the polarization of the incident microwave signal. For CFRP with fibers aligned in a single direction (i.e., unidirectional fibers), microwave signals can penetrate through the sheet when the polarization is orthogonal to the fiber direction (CFRP⊥), and the CFRP behaves as a lossy dielectric. However, when the

microwave polarization is parallel to the CFRP fiber direction (CFRP||), the incident signal is mostly reflected, resulting in very little signal penetration. Thus, the microwave polarization is taken orthogonal to the CFRP fiber direction in the tests conducted in this study.

Subsequent to the dielectric heating, transient heat diffusion occurs that affects the temperature distribution. The temperature distribution's temporal and special variations are related to the thermal properties of material(s) and source of heat as determined by the heat equation as [24][25][26]:

$$\rho c \frac{\partial T}{\partial t} = k\nabla^2 T + Q \tag{2}$$

where $\rho$ is the density, $c$ is the specific heat, $T$ is the temperature, $t$ is time, and $k$ is the thermal conductivity. The dielectric and thermal properties of the material(s) under test (here, CFRP) determine the induced heat and subsequent heat diffusion. The electromagnetic properties and values of $k$, $c$, and $\rho$ for air, cementitious mortar, and CFRP, which were reported in [24], are summarized in Table 1.

As the frequency, $f$, and the incident electric field are constant during an AMT inspection, the energy input $Q$ can also be considered constant for the structure. However, once damage (e.g., concrete cracking, adhesive cracking, interfacial debonding of the CFRP-adhesive or adhesive-concrete interface) occurs to the interface between the CFRP and concrete, as illustrated in Figure 1, air enters the damaged area and causes $k$ (thermal conductivity) to decrease dramatically at the damaged region. Therefore, the heat generated in CFRP is impeded by the damage to be transferred from the CFRP to the concrete,

resulting in the accumulation of heat that ends in increased temperature of the CFRP at the region over the damaged area.

## 3. MATERIALS

The CFRP strips were a commercially available product (Tyfo® SCH-41 [28] that comprised of dry carbon fiber sheets and an epoxy resin. The fibers were a unidirectional carbon fabric orientated in the $0^o$ direction, see Figure 2(a). The design composite gross laminate properties provided by the manufacturer [28] were: Young's modulus, $E_f$ =82.0 GPa; ultimate tensile strength, $f_u$ = 834 MPa; ultimate tensile strain, $\varepsilon_{ult}$ = 0.0085; and nominal laminate thickness, $t_f$ = 1 mm. For the bonding system between the CFRP sheet and concrete substrate, two types of epoxy resin were used: a primer layer (MasterBrace P3500 [29]), and a saturant layer (MasterBrace P4500 [30]). The primer was a two-component solvent-less epoxy penetrating medium viscosity primer with a tensile strength and modulus of 17.2 MPa and 717 MPa, respectively [28]. The primer was used to penetrate the pore structure of cementitious substrates and to provide a high bond base coat. The saturant was used to saturate the carbon fabric sheets to create a composite with the concrete structure. The tensile strength and modulus of the saturant layer were 55.2 MPa and 3034 MPa, respectively [30].

The concrete mixture used to construct the concrete prisms had a design compressive strength of 30 MPa. The concrete batches were made of commercial Portland Type I/II cement without admixtures, dolomitic limestone coarse aggregate (Figure 2(b)) with a maximum size of 10 mm, sand from the Missouri River (Figure 2(c)), and clean water. The mixture proportions by weight ratio were (cement: sand: aggregate = 1.00: 3.86:

4.37), and the water-cement ratio was 0.76. The concrete compressive and splitting tensile strengths were obtained experimentally using 101.6 mm diameter × 203.2 mm long cylinders in accordance with ASTM C39/C39M [31] and ASTM C496/C496M [32], respectively. The average compressive strength and splitting tensile strength, determined as the average of three tests, were 30.4 MPa (CoV = 0.09) and 2.7 MPa (CoV = 0.16), respectively.

# 4. METHODS

## 4.1. FABRICATION OF SINGLE-LAP SHEAR TEST SPECIMENS

Seven CFRP-concrete joint specimens are included in the present study. Each specimen was comprised of a concrete prism and a CFRP strip bonded to one face. All specimens had the same nominal geometrical size and mechanical properties. The composite bonded area was 50 mm wide × 270 mm long. In order to capture the gradual debonding process, the bonded length was selected to be longer than the estimated value of the effective bond length, i.e., the length needed to fully establish the stress transfer mechanism at the CFRP-concrete interface

Two specimens, named CFRP-S-i (i = 1, 2), had strain gauges mounted onto the surface of the CFRP strip along the bonded length. These two specimens were used to quantify the distribution of slip along the composite bonded length at different load levels (times). The remaining five specimens, named AMT-CFRP-j (j = 1, 2, 3, 4, 5), were monitored by AMT during the test. These specimens were used to examine the thermal response along the composite bonded length at different load levels (times). The test specimens are listed in Table 2.

## 4.2. SINGLE-LAP SHEAR TEST SETUP WITH AMT MONITORING

Wood forms were used to construct the concrete prisms (Figure 3(a)), which were 125 mm wide × 125 mm deep × 375 mm long. All prisms and cylinders were cast from the same batch of concrete. After the concrete was cast, the prisms and cylinders were cured under wet towels for 24 hours before being removed from the forms. After the removal of the forms, they were placed in the laboratory for curing and covered by wet towels for at least 28 days. During the curing period, the room temperature was approximately 15 °C. After curing the concrete prisms, the two side (formed) faces of the prisms were sandblasted. The sandblasting was conducted to expose the aggregates (Figure 3(c)) thereby obtaining a stronger surface strength.

The CFRP strips were applied to the concrete prisms using a wet layup procedure. The first layer of epoxy (primer) was applied and allowed to cure 6 hours. Next, formwork was applied to the surface of the prism to control the location of the composite bonded area and the thickness of the composite. Precut carbon fiber strips were saturated in the saturant and applied to the prism in the designated location. Finally, the fiber strip was rolled onto the surface to fully impregnate the strip and coat it with saturant. The CFRP strip was allowed to harden at least 7 days prior to testing.

## 4.3. LOAD RESPONSE MEASUREMENT PROCEDURE

The classical single-lap direct shear test configuration was adopted in which the CFRP strip was pulled from the concrete prism as the prism was restrained (see Figure 4). The specimen was mounted onto the base of a servo hydraulic universal testing machine using a Π-shaped steel frame (Figure 4(b)). Steel plates were mounted to the end of the

CFRP strip using thermosetting epoxy and four bolts in each corner of the plates to allow for better gripping of the CFRP strip during testing.

Brackets were attached to the concrete surface to hold two linear variable displacement transformers (LVDTs) during the testing process. Two L-shaped aluminum plates were clamped to the CFRP strip just outside the bonded area to serve as a reaction surface for the LVDTs. The average of the two LVDT measurements was used to control the mechanical loading rate of the specimens, which was held constant at a rate of 0.0001084 mm/s. The average of the two LVDT measurements was taken as the global (or loaded end) slip in this study. For two specimens, nine uniaxial electrical resistance strain gauges were attached to the CFRP surface at different positions along the bonded length (see Figure 4(a)). Applied load, machine stroke, LVDT displacements, and strain gauge measurements (where applicable) were recorded at a rate of 2 Hz throughout the test. All specimens were loaded until failure (complete debonding of the composite) occurred.

## 4.4. AMT MEASUREMENT PROCEDURE

The AMT measurements were conducted on the surface of the specimen to which the CFRP strip was applied, see Figure 5(a). All measurements were conducted at a constant frequency of 2.4 GHz and a fixed power level of 50 W. The horn antenna used in this work (aperture dimensions of 230×170 $mm^2$) is capable of handling high-power microwave radiation. It was placed directly toward the specimen surface in order to maximize the microwave-induced heat over the surface. The distance between the antenna aperture and the specimen was 400 mm to allow viewing of the inspection area with the thermal camera. A FLIR T430sc thermal camera was used in this work that is capable of producing thermal images of 320×240 pixels. It should be noted that the thermal camera

was capable of covering the region from $y$ = ~30 mm to ~290 mm, where $y$ is defined in Figure 4a. A control unit synchronized the microwave and thermal segments of the AMT system. The temperature profile was acquired at a rate of 2 Hz. A photo of the AMT system is shown in Figure 5(b).

The thermal profiles of the tests were recorded and compared. To this end, $\Delta T$ is defined as the temperature increase caused by the microwave heating, which is defined as the temperature value at any time ($t$) relative to its initial value immediately prior to heating ($t$=0). The AMT measurement procedure consisted of three stages: heating without loading (Stage-I), cooling (Stage-II), and heating with loading (Stage-III), see Figure 6. In Stage-I, the CFRP-concrete joint specimen was placed into the test frame, and the microwave heating was conducted. This stage aimed to detect if the specimen had any initial defects or anomalous regions that occurred during composite installation. Additionally, the quality of the thermal field created by AMT system could be evaluated. $\Delta T$ in this stage, denoted by $\Delta T_I(t)$, where $t$ is the time of heating in Stage-I, was used to normalize the temperature increase in Stage-III, which will be introduced below. The duration of Stage-I was 45 minutes. Stage-II was a cooling process where the microwave was shut down, and cooling was driven by the convection effect with the air with relatively lower room temperature. In Stage-III, the specimen was heated using the same process as Stage-I, and at the same time, external loading was applied as discussed in Section 4.2. $\Delta T$ in Stage-III is denoted by $\Delta T_{III}(t)$, where $t$ is the heating time in Stage-III.

In Stage-III, if the CFRP-concrete interface has been damaged by the loading, cracks occur along the interface which causes air injection. The air gap serves as a thermal insulating layer that prevents the heat transfer from the CFRP to the concrete substrate,

thereby leading to an increase of $\Delta T$ compared to Stage I. Therefore, the thermal contrast $TC(t)$ caused by loading (see Figure 7) is taken as the difference between $\Delta T$ of Stage-I and $\Delta T$ of Stage-III at a given time as follows:

$$TC(t) = \Delta T_{III}(t) - \Delta T_I(t) \quad (3)$$

# 5. EXPERIMENTAL RESULTS AND DISCUSSION

## 5.1. FAILURE MODE AND APPLIED LOAD – GLOBAL SLIP RESPONSE

All seven specimens failed due to debonding of the CFRP strip, which was characterized by cohesive fracture of the concrete in a thin layer beneath the composite strip, with the concrete attached to the CFRP strip after failure (see Figs. 8 and 9). The failure process started with the formation of an interfacial crack near the loaded end of the CFRP strip, which was visible from the sides of the specimen. The interfacial crack progressed to the free end of the CFRP strip until the entire strip detached from the concrete prism. The surface of the failed zone on the concrete prism was uneven, with the aggregates being clearly visible (Figs. 8 and 9). A relatively thick piece of concrete usually attached to the debonded CFRP strip near the loaded end, while a relatively smaller piece was sometimes attached near the free end of the CFRP strip (Figure 9a, c, d, and e). The thickness of the concrete layer attached to the debonded CFRP strip elsewhere varied between approximately 1 and 5 mm.

The applied load $P$ – global slip $g$ response of each specimen is plotted in Figure 10. Despite the scatter, which can be attributed to experimental variability and randomly distributed interfacial properties, the $P$–$g$ responses exhibit similar trends. It can be seen that the applied load increased nearly linearly at the beginning of test, and then the slope

of $P$–$g$ curve reduced slightly at an applied load of approximately 10 kN. The applied load reached a plateau of around 16 kN when the global slip was around 0.5 mm until the failure of the specimen. The start of the plateau in the $P$–$g$ response is associated with full establishment of the so-called stress transfer zone (STZ), defined as the zone in which the stress is transferred between the concrete and the composite, and is followed by translation of the fully-established STZ along the bonded length to the free end of the composite (i.e., initiation and propagation of debonding) [35][36]. Fluctuations in applied load (load drops) were observed during this phase of loading until failure of specimen, as reported by other researchers [9][33][34][35]. The load drops were caused by localized bond failure, which results in an abrupt reduction in strain until the bond is transferred to a new region down the bonded length.

Table 2 reports the maximum applied load $P^*$, the global slip at maximum applied load $g^*$, and the global slip at debonding $g_{ult}$ for each specimen. The average peak load of the specimens was 18.18 kN with a CoV of 0.10. The average $g^*$ was 1.79 with a CoV of 0.33. The large variation is because the peak load is generally caused by the first wave of debonding, which is a brittle process. The average value of $g_{ult}$ was 2.21 with a CoV of 0.05.

## 5.2. DETERMINATION OF SLIP DISTRIBUTION OF SPECIMENS WITH STRAIN GAGES

The axial strain measurments acquired from specimens CFRP-S-1 and CFRP-S-2 were used to quantify the distribution of interfacial slip at different load (or global slip) levels. Figure 11 shows the variation in the axial strain $\varepsilon(y)$ measured at the midwidth of the CFRP sheet along the bonded length for different points of the load response of Figure

10 for specimen CFRP-S-2, where $y$ is the distance along the composite bonded length with the origin at the free end of the bonded area, see Figure 4(a). The locations of the strain gauges are also shown in Figure 4(a). Figure 11 shows that the strain distribution along the CFRP is close to zero at the free end ($y$ = 0 mm). There is a rapid increase in strain approaching the loaded end ($y$ = 270 mm). Fluctuations in the measured strain along the bonded length of the CFRP composite are due to local material variations in the concrete substrate and to possible bond defects in the adhesive.

Interfacial debonding creates both relative displacement along the loading direction (slip) and separation in the normal plane of the bonded surface (i.e., mixed-mode fracture). Usually these two effects have similar trends, so one effect is adequate to indicate interfacial debonding. Herein, the interfacial slip is used as an index to represent the degree of interfacial debonding. In order to quantitively determine the slip distribution along the bonded region of the CFRP from the strain measurements, the following assumptions were made: (1) axial deformation of concrete is negligible with respect to the CFRP, which is justified because the axial stiffness of the concrete substrate is much larger than that of the CFRP strip [33]; (2) strains in the CFRP vary linearly between two subsequent strain gauges, see Figure 4(a); and (3) the strain in the unbonded region of the CFRP strip is equal to the strain measured at the loaded end, see Figure 4(a). Assumption (3) gives the strain at the reaction plate $\varepsilon_9 = \varepsilon_8$ (see Figure 4(a)). Integration of the strain profile, starting from the composite loaded end with the bondary condition of global slip $s(y_9) = g$, where $g$ is the global slip measured by the LVDTs, see Figure 4a, gives the following expression for the slip

at a general $y$:

$$s(y_i) = s(y_{i+1}) - \int_{y_i}^{y_{i+1}} \varepsilon(y)\, dy,\ i = 8,7,\ldots,0 \tag{4}$$

The geometric relationship of assumption (2) gives:

$$\int_{y_i}^{y_{i+1}} \varepsilon(y)\, dy = \frac{\varepsilon_i + \varepsilon_{i+1}}{2}(y_{i+1} - y_i),\ i = 8,7,\ldots,0 \tag{5}$$

Substituting Eq. (5) into Eq. (4) provides the slip distribution at any global slip level of the load response.

The following bond-slip law $\tau(s)$ was used to quantify the relationship between the interfacial shear stress and slip of CFRP-concrete joints [33][35][37]:

$$\tau(s) = E_f t_f \frac{\alpha}{\beta^2} e^{-\frac{s}{\alpha}}\left(1 - e^{-\frac{s}{\alpha}}\right) \tag{6}$$

where the maximum shear stress $\tau_m$ and the corresponding slip $s_m$ can be given by [37]:

$$\tau_m = E_f t_f \frac{\alpha}{4\beta^2} \tag{7}$$

$$s_m = 0.693\alpha \tag{8}$$

Based on Eq. (6) and assuming zero slip at the free end of the CFRP strip at low global slip levels for long bonded length, the strain can be solved as [35][37]:

$$\varepsilon(y) = \frac{\alpha}{1 + e^{-(y - y_0)/\beta}} \tag{9}$$

where $\alpha$, $\beta$, and $y_0$ are parameters determined using nonlinear regression analysis of the measured strains. $\alpha$ and $\beta$ are parameters that determine the bond-slip law, and $y_0$ is a parameter that reflects the load and global slip levels.

Previous studies have shown that after debonding initiates, the fully-established STZ self-similarly translates along the bonded length with increasing global slip [35]. Therefore, the axial strain profiles can be evaluated for any point of the load response after

debonding occurs. Five global slip levels ($g$ = 0.75, 1.00, 1.25, 1.50, and 1.75 mm) were chosen to fit the parameters for specimens CFRP-S-1 and CFRP-S-2. The fitting results are summarized in Table 3. Considering the results of both specimens, the average values of $\alpha$ and $\beta$ are $7839\times10^{-6}$ mm/mm and 22.5 mm, respectively. Therefore, $\tau_m$ and $s_m$ are 2.85 MPa, and 0.125 mm, respectively, according to Eqs. (7) and (8).

With the fitted results of $\alpha$ and $\beta$, the shape of $\tau(s)$ is plotted in Figure 12. It can be seen that the shear stress increases with increasing slip until the shear stress reaches $\tau_m$.This phase of $\tau(s)$ is an elastic phase [34]. As the slip continues to increase, the shear stress decreases, which is the result of damage to the interface. Herein, a damage index $D(s)$ is introduced to quantify the damage of the interface. $D(s)$ is a damage parameter that defines the softening behavior of $\tau(s)$ [38]. The damage parameter is based on a nonlinear softening branch of $\tau(s)$ and can be written as [38]:

$$D(s) = \begin{cases} 0, 0 \le s \le s_m \\ \dfrac{s_f(s - s_m)}{s(s_f - s_m)}, s_m \le s \le s_f \\ 1, s \ge s_f \end{cases} \tag{10}$$

where $s_f$ is the displacement at complete debonding. According to the damage parameter, no damage occurs before the shear stress reaches the peak value, which indicates the interface is in the elastic stage. When the slip is larger than the slip at the peak shear stress, a non-zero damage is attained, indicating that interfacial damage starts to occur. The value of $D$ increases to 1.0 when the slip reaches $s_f$. The value of $s_f$ is taken as 1.5 mm in this paper, based on the value at which $\tau(s)$ decreases to nearly zero (<0.1% of $\tau_m$). $D(s)$ and $\tau(s)$ are shown together in Figure 12.

## 5.3. OBSERVATIONS OF THERMAL RESPONSE

As mentioned, five specimens were subjected to loading and inspected via AMT. Three points were selected along the midwidth of the bonded CFRP strip surface to study the temporal thermal response of areas close to the loaded end (Point A), at the middle of the bonded length (Point B), and close to the free end (Point C). Points A, B, and C are located at $y$ = 260 mm, 150 mm, and 40 mm, respectively ($y$ is defined in Figure 4(a)). Values of $\Delta T$ at time $t$ were obtained by averaging the values determined from the pixels within a 5 mm wide × 5 mm long square centered on the corresponding point. The thermal contrast caused by loading at any given time, $TC(t)$, was obtained by Eq. (3), as shown in Figure 7.

Figure 13 shows the time histories of $\Delta T_I$, $\Delta T_{III}$, and $TC$ of Points A, B, and C on the CFRP surface of representative specimen AMT-CFRP-2. Both $\Delta T_I(t)$ and $\Delta T_{III}(t)$ showed similar trends: $\Delta T$ increased rapidly at the beginning of heating, and then the slope decreased gradually with heating time. The reason for the rapid increase of $\Delta T$ at the beginning of heating is that with a fixed input of heat, see $Q$ in Eq. (2), heat generation within the CFRP layer caused immediate heat increase of the CFRP itself. Then, with the increase of time, more heat transferred from the CFRP to the epoxy and concrete, and the convection effect kept working to dissipate the heat generated within CFRP, which resulted in the decrease of slope. The generation and transferring of the heat is illustrated in Figure 14. For all three points, the magnitude of $\Delta T_{III}$ was similar to $\Delta T_I$ at the beginning of heating (i.e., $TC$ was approximately zero), which means that for low load levels, the temperature increase was not affected by the applied load. After a certain time, $\Delta T_{III}$ was larger than $\Delta T_I$ (resulting in a positive value of $TC$), which indicates that the temperature

increase was, in part, due to the applied load. At Point A, near the loaded end, $\Delta T_{III}$ was larger than $\Delta T_I$ after ~600 s. At Point B, at the midlength, $\Delta T_{III}$ was larger than $\Delta T_I$ after ~1300 s. At Point C, near the free end, $\Delta T_{III}$ was close to $\Delta T_I$ from the beginning of heating to the end, which means that the temperature increase near the free end was not significantly affected by the load until failure of the specimen. The $TC(t)$ responses for Points A, B, and C are compared in Figure 13(d).

Figure 15(a) shows sequential $TC(t)$ profiles captured over the surface of specimen AMT-CFRP-2 from the beginning of loading to failure of the specimen (Points a-k are indicated on the load time history response in Figure 13(d)). The Stage-III heating period lasted for 1963 s (until debonding failure occurred). It can be seen that at the beginning of Stage-III, the temperature was relatively low for the entire monitored bonded area (the monitored area is indicated by the dashed red box in Figure 15(a)). At 200 s, some local fluctuations in temperature were observed along the bonded area, although the $TC$ response at Points A, B, and C in Figs. 13(a)-(c) were nearly zero, as mentioned above. The reason for the local fluctuations can be attributed to localized initial flaws caused by workmanship during composite installation. With increasing time, the area close to the loaded end exhibited an increased temperature distribution, and the area of increased temperature progressed toward the free end.

Figure 16 shows the $TC$ profile corresponding to the second before debonding failure occurred for each of the five specimens monitored with AMT. It can be seen that there was an area with high $TC$ response close to the loaded end for each specimen, which indicates the newly formed debonded region. For areas close to the free end, the temperature was relatively low for all $t$, even when the specimen was close to the failure.

The $TC$ profiles immediately prior to failure also show significant variability among the different specimens, which can be attributed to non-uniform bond properties and interfacial crack propagation as discussed in Section 5.1.

## 6. CORRELATION BETWEEN MECHANICAL AND THERMAL RESPONSES

Figure 13(d) compares the time history of load and temperature of Points A, B, and C of specimen AMT-CFRP-2. The load time history shows a drop in applied load around $t$ = 550 s, and a noise was heard during the test at that time. As discussed in Section 5.1, the load drop was caused by localized bond failure at regions of high shear stress, which results in an abrupt reduction in strain until the bond is transferred to a new region down the bonded length. Simultaneously, $TC$ at Point A, near the loaded end of the CRP strip, increased in slope (see also Figure 13(a)). Another load drop occurred at approximately $t$ = 910 s, at which time $TC$ at Point B, at the CFRP strip midlength, increased in slope (see also Figure 13(b)). These results demonstrate that the progression of damage that occurs at the CFRP-concrete interface as the STZ translates along the composite bonded length from the loaded end to the free end could be detected by AMT.

In this work, a first attempt to correlate the mechanical and thermal responses was made by comparing the $TC(t)$ profile with the damage parameter $D(s)$. The damage parameter was herein determined from the softening branch of $\tau(s)$, which in turn, was obtained from axial strain profiles $\varepsilon(y)$ along the composite bonded length (as discussed in Section 5.2). The axial strain profiles were obtained by fitting the strain measurements from specimens CFRP-S-1 and CFRP-S-2. It should be noted that $TC(t)$ and $D(s)$ profiles were not determined from the same specimen, and therefore the resulting trends should be

considered qualitative in nature. However, the approach developed herein is intended to shed light on correlations the mechanical and thermal responses and could be used in future studies in which data can be acquired from the same specimen.

Figure 15(b) shows the distribution of slip, determined by Eqs. (4) and (5) using the average value of the axial strains measured along the bonded length of specimens CFRP-S-1 and CFRP-S-2, at the times corresponding to Points a-k of the time history response of specimen AMT-CFRP-2 in Figure 13(d). It is interesting to note that the slip profiles have the same tendency as the thermal contrast profiles shown in Figure 15(a). The slip was relatively small for the entire bonded area at the beginning of the test, and then it increased with increasing time (global slip). The area close to the composite loaded end attained large slip when the time (global slip) was large.

Figure 15(c) shows the damage parameter, $D$, determined by Eq. (10) using the average value of the axial strains measured along the bonded length of specimens CFRP-S-1 and CFRP-S-2, at the times corresponding to Points a-k of the time history response of specimen AMT-CFRP-2 in Figure 13(d). It can be seen that for $t \leq 400$ s, the damage was almost zero, which means that the first wave of debonding had not been achieved (see the load drop at ~550 s in Figure 13(d)). Then, with the increase of time (global slip), the damage started to occur at the loaded end and propagated to the free end.

Figure 16 shows the distribution of $TC$ along the bonded length $y$ of specimen AMT-CFRP-2, along with the distributions of slip and $D$ determined using the average value of the axial strains measured along the bonded length of specimens CFRP-S-1 and CFRP-S-2 at four global slip levels ($g$ = 0.5 mm, $g$ = 1.0 mm, $g$ = 1.5 mm and $g$ = 2.0 mm, see Figure 10). Note that the slip distribution was obtained by using the analytical approach

given in Eqs. (5) and (6), and $D$ was determined by Eq. (10). Because the temperature profile was highly variable across the width of the specimen (see Figure 15(a)), the $TC$ distribution was obtained by averaging the values of temperature determined from the pixels across the width of the specimen at the corresponding position $y$. It can be seen that the $TC$, slip, and $D$ all have an decreasing tendency from the loaded end to the free end of the CFRP strip. The tendencies of $TC$ and $D$ matched well at $g$ = 0.5 mm, see Figure 17(a). At $g$ = 2.0 mm, see Figure 17(d), the tendencies of $TC$ and slip matched well. At $g$ = 1.0 mm and $g$ = 1.5 mm, all three curves have similar tendencies. These results show that the thermal contrast is caused by CFRP-concrete interfacial slip and damage, although further work is needed to quantify these relationships.

## 7. CONCLUSION

This paper presented a study of using AMT as a NDE method to detect and monitor CFRP-concrete interfacial debonding. The following four correlations between interfacial slip and CFRP outer surface $TC$ were found, which show that AMT can detect the interfacial damage caused by load:

(1) At the beginning of loading, high $TC$ occurred within the areas close to the CFRP strip loaded end where interfacial debonding initiates.

(2) With the increase of load, the interfacial debonded area propagated towards the free end, which correlated well with the $TC(t)$ profiles of the CFRP surface.

(3) The slope of $TC$ changed when there was a load drop, which indicates local debonding occurrence or mobilization.

(4) At different loading levels, the interfacial slip, damage, and $TC$ distributions along the bonded area showed similar trends.

These correlations indicate that the initiation and propagation of CFRP-concrete interfacial damage can be monitored by AMT. The experimental work presented here represents a first step in the study of the non-destructive evaluation of CFRP–concrete interfacial damage using AMT technology. Studies considering a variety of other factors are required to establish the full relationship between the damage and the thermal contrast at CFRP surface. A numerical investigation that can integrate microwave energy input and the mechanical response can also be conducted to further understand this relationship.

## ACKNOWLEDGEMENT

This work was supported by the National Science Foundation (NSF) Electrical, Communication, and Cyber Systems (ECCS) Award 1609470, "A Multi-Physics-Based Approach to Active Microwave Thermography".

## AVAILABILITY OF DATA AND MATERIALS

Not applicable.

## COMPETING INTERESTS

The authors declare that they have no competing interests.

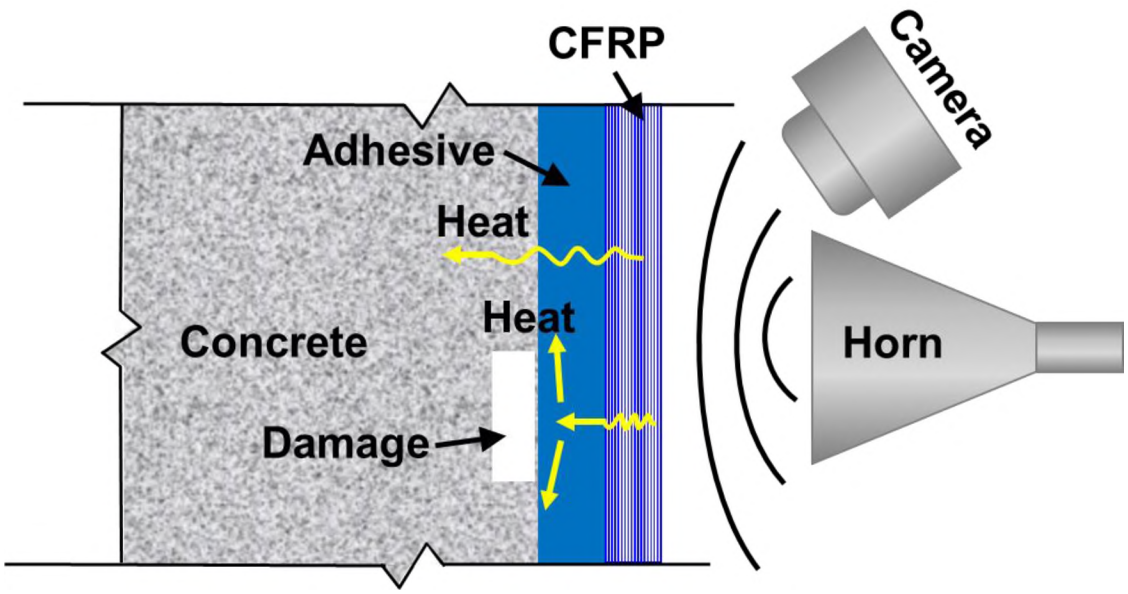


Figure 1. Illustration of AMT test on CFRP bonded to a concrete substrate.


(a) (b) (c)

Figure 2. Raw materials used for the test specimens: (a) CFRP sheets, (b) sand, and (c) coarse aggregate.

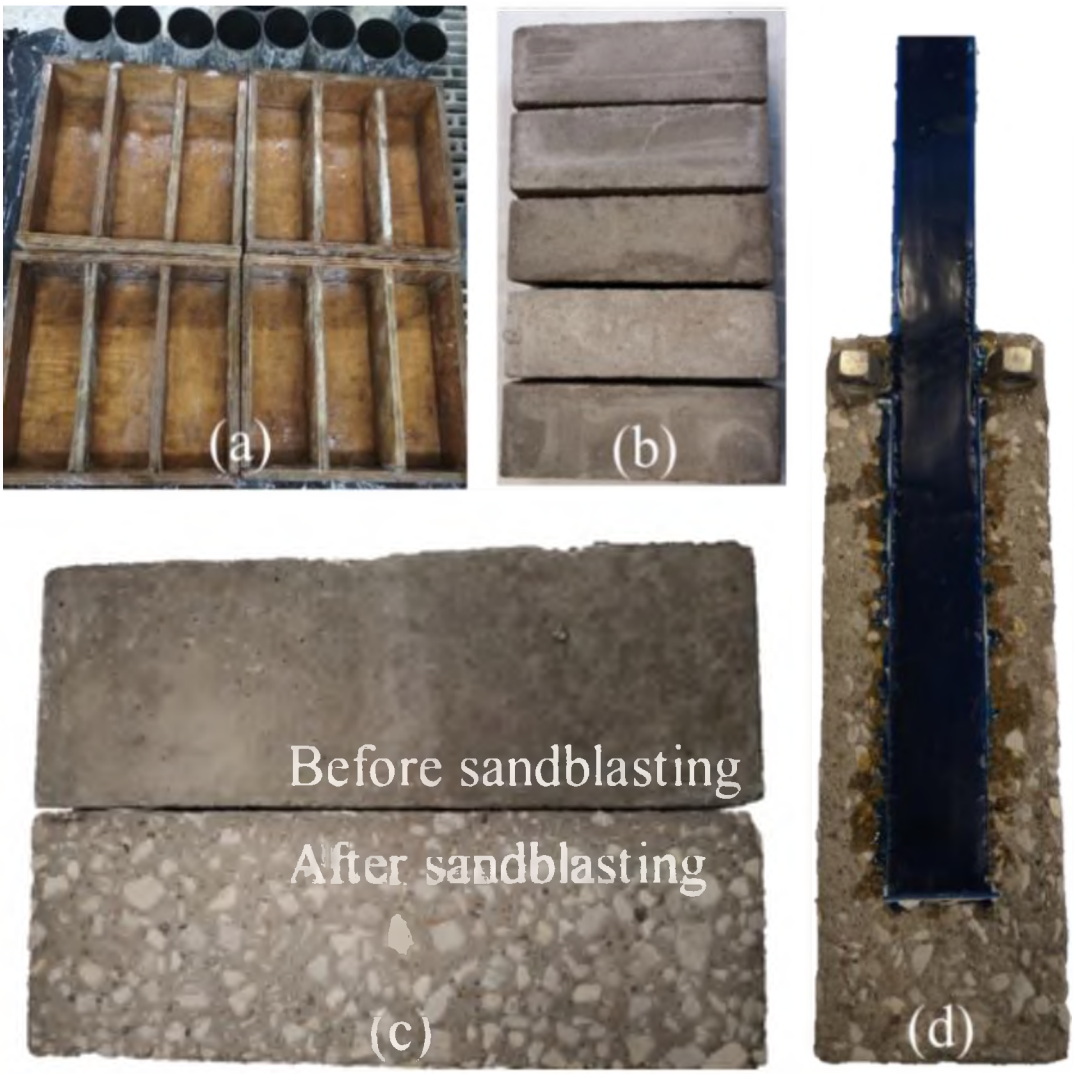


Figure 3. Construction of single-lap shear test specimens: (a) forms for concrete prisms and material property cylinders; (b) concrete blocks; (c) concrete surface before and after sandblasting; and (d) single-lap shear test specimen with concrete block and CFRP strip.

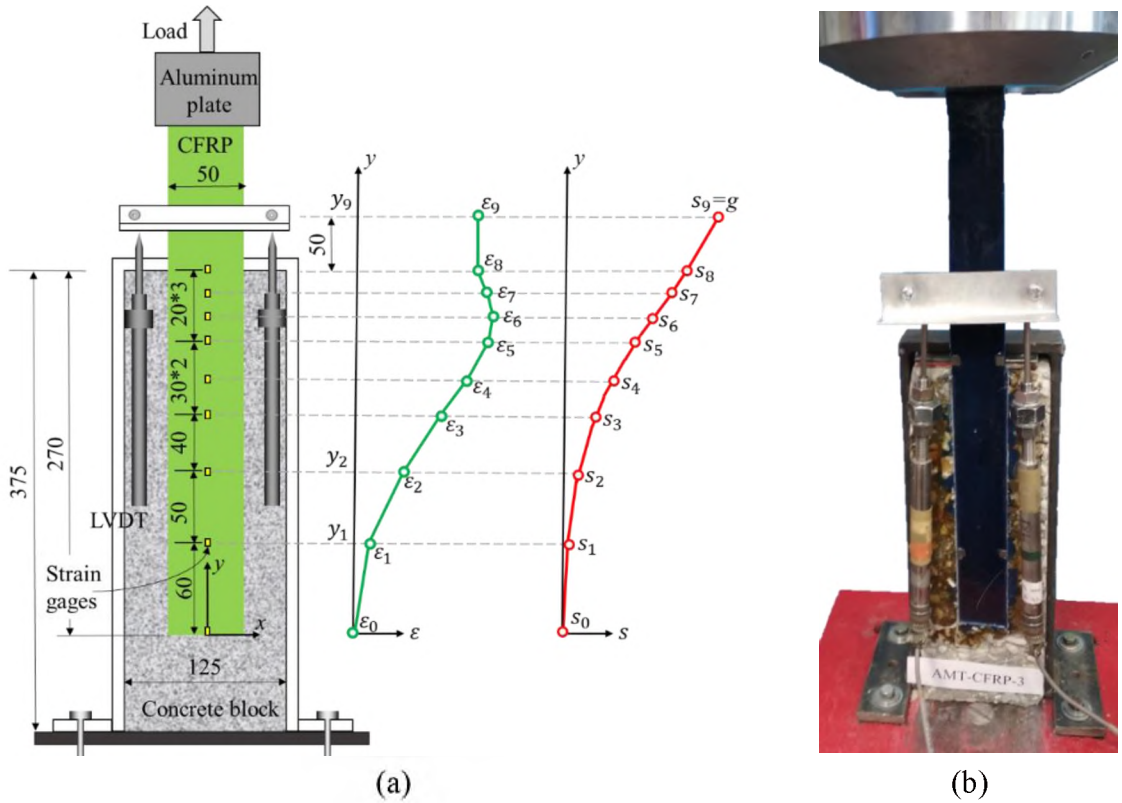


Figure 4. Single-lap direct shear test setup (unit: mm): (a) schematic front view, and (b) photo of front view.

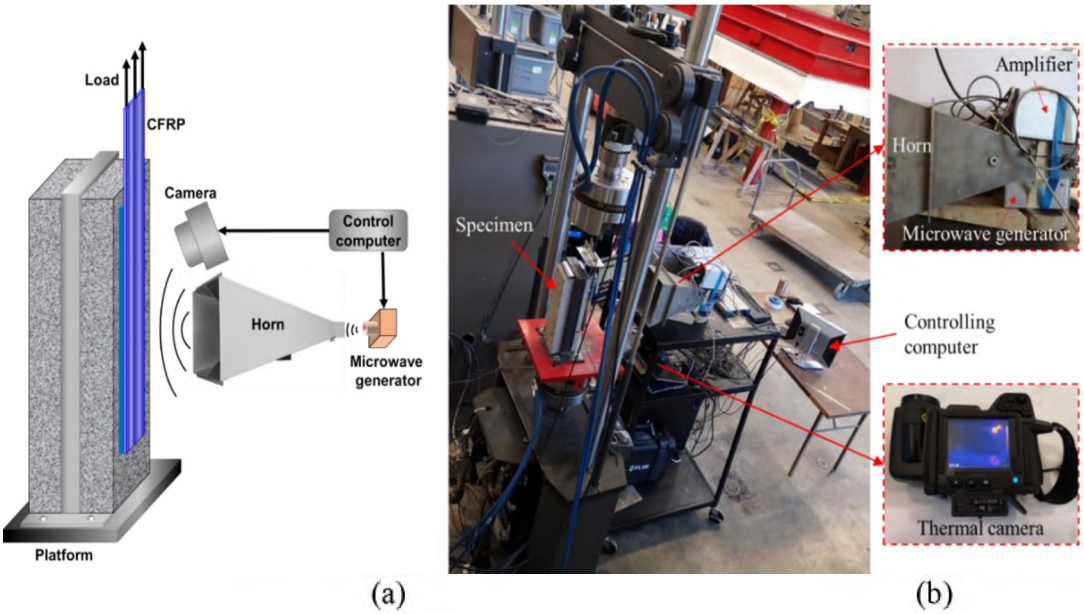


Figure 5. Illustration of AMT measurement set-up: (a) schematic view, and (b) photo showing components.

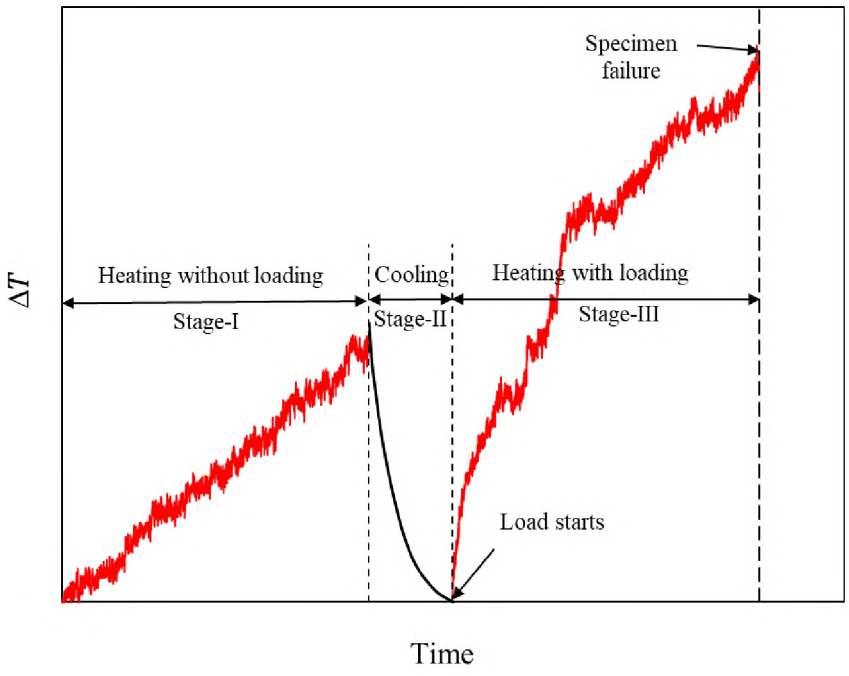


Figure 6. AMT test procedure.

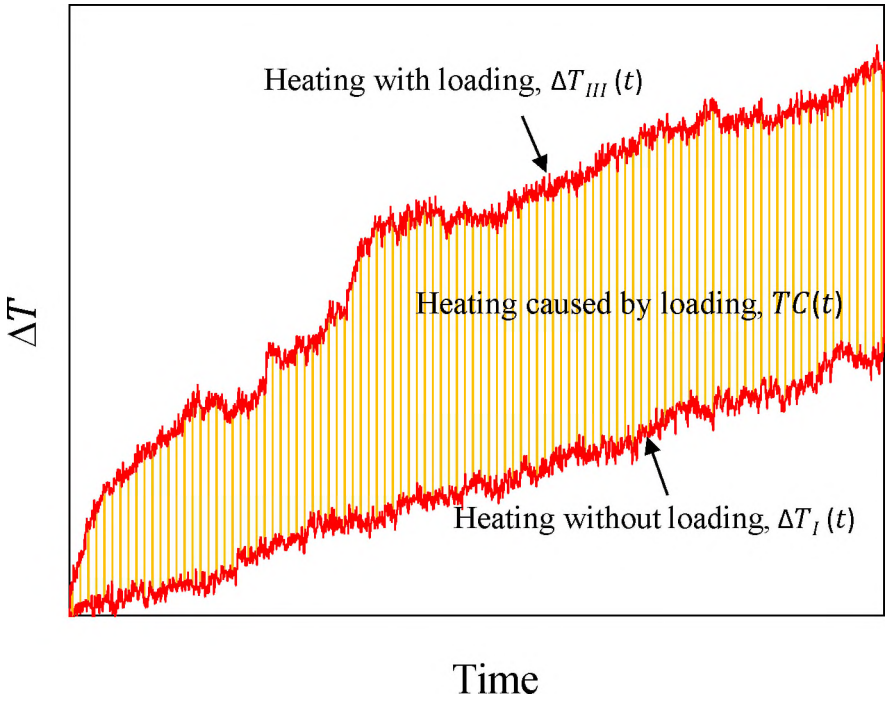


Figure 7. Illustration of thermal contrast caused by loading.

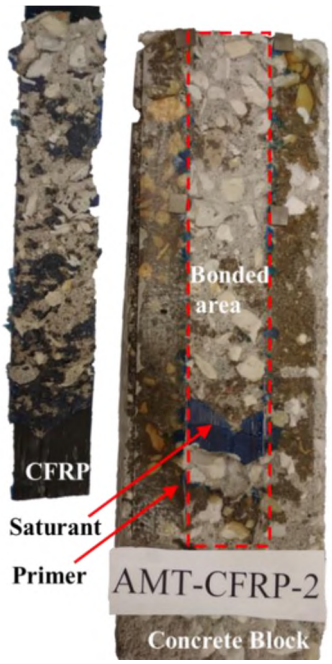


Figure 8. Failure mode of AMT-CFRP-2.

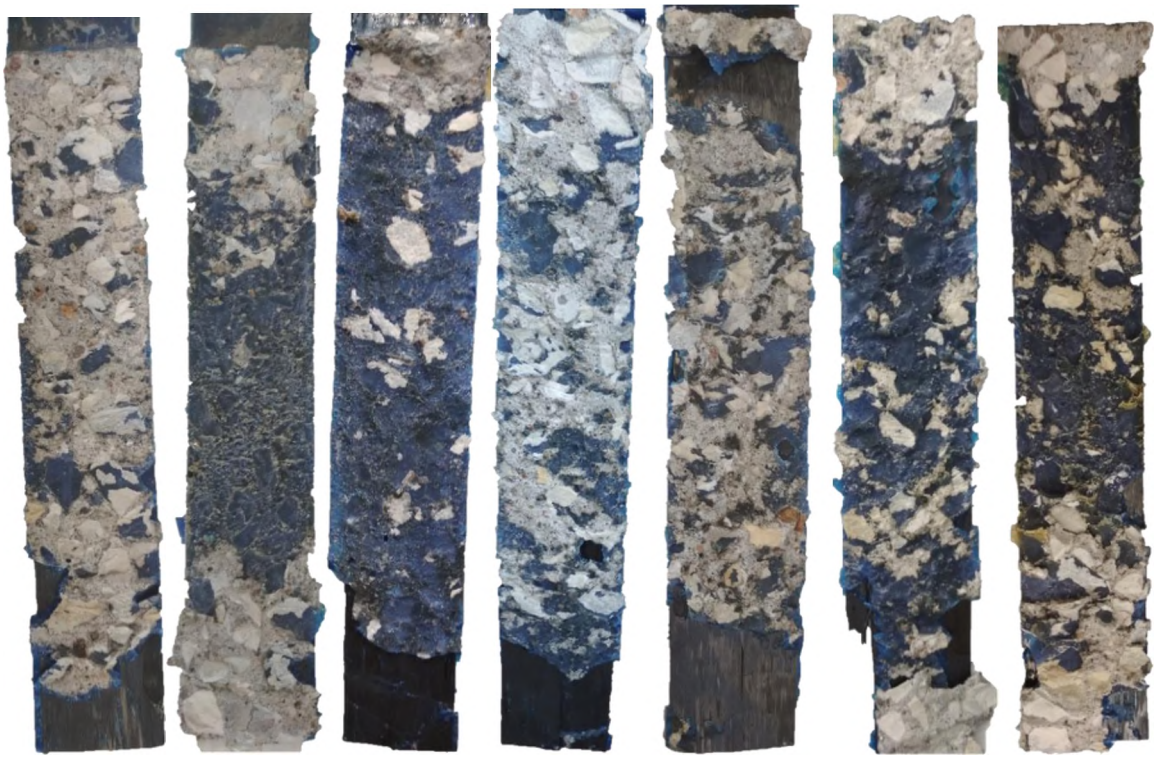

(a) (b) (c) (d) (e) (f) (g)

Figure 9. Photos showing the inside surface of the CFRP strips after failure: (a) CFRP-S-1; (b) CFRP-S-2; (c) AMT-CFRP-1; (d) AMT-CFRP-2; (e) AMT-CFRP-3; (f) AMT-CFRP-4; and (g) AMT-CFRP-5.

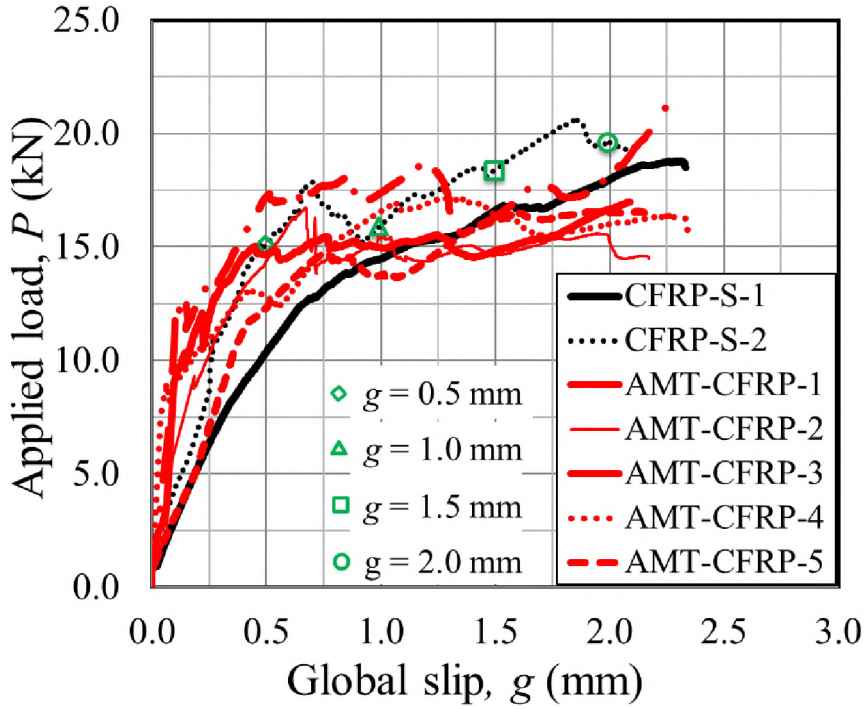


Figure 10. Applied load-global slip response of all specimens.

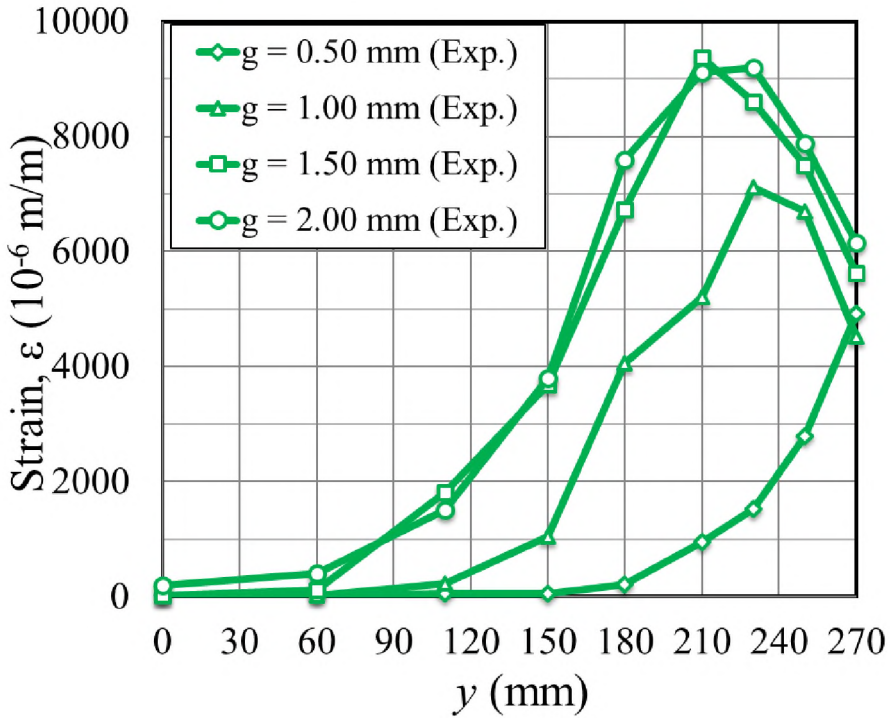


Figure 11. Measured axial strains in CFRP along the bonded length of specimen CFRP-S-2 at g = 0.5 mm, 1.0 mm, 1.5 mm, and 2.0 mm.

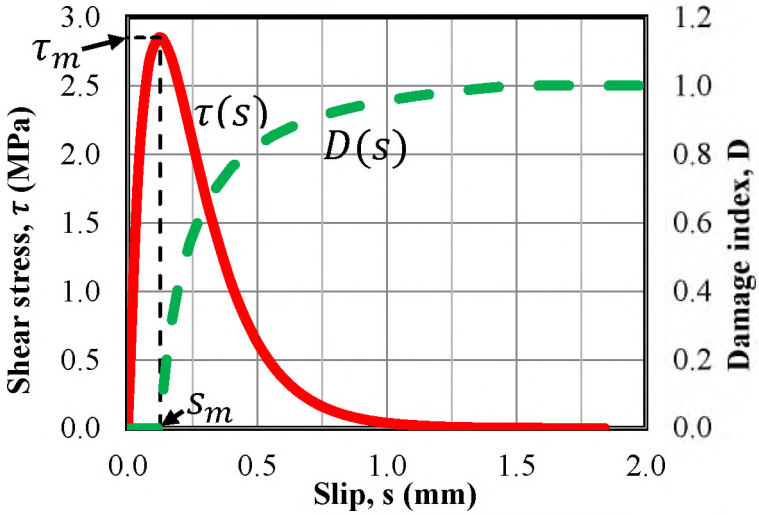


Figure 12. Bond-slip law τ(s) and the damage index $D$(s).

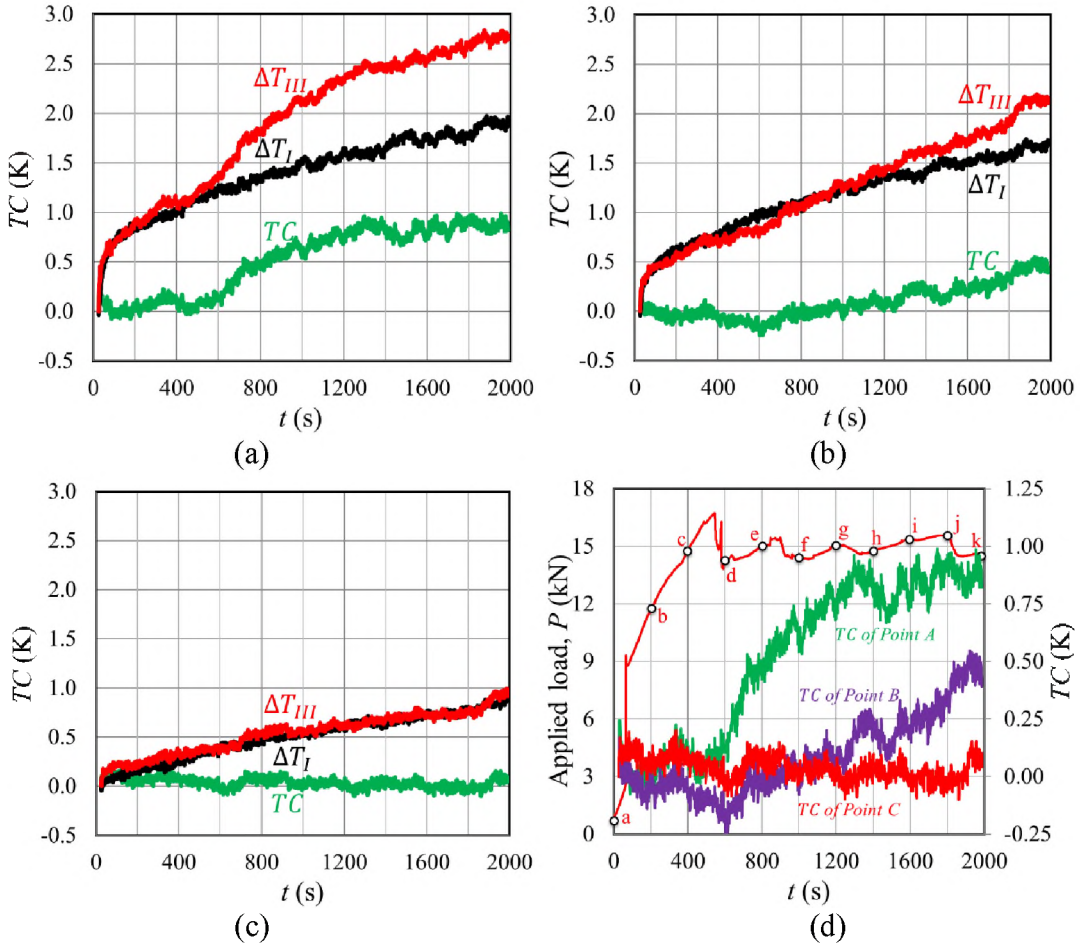


Figure 13. $\Delta T$ of (a) point A, (b) point B, (c) point C of specimen AMT-CFRP-2, and (d) comparison of time history of applied load and temperature contrast of specimen AMT-CFRP-2.

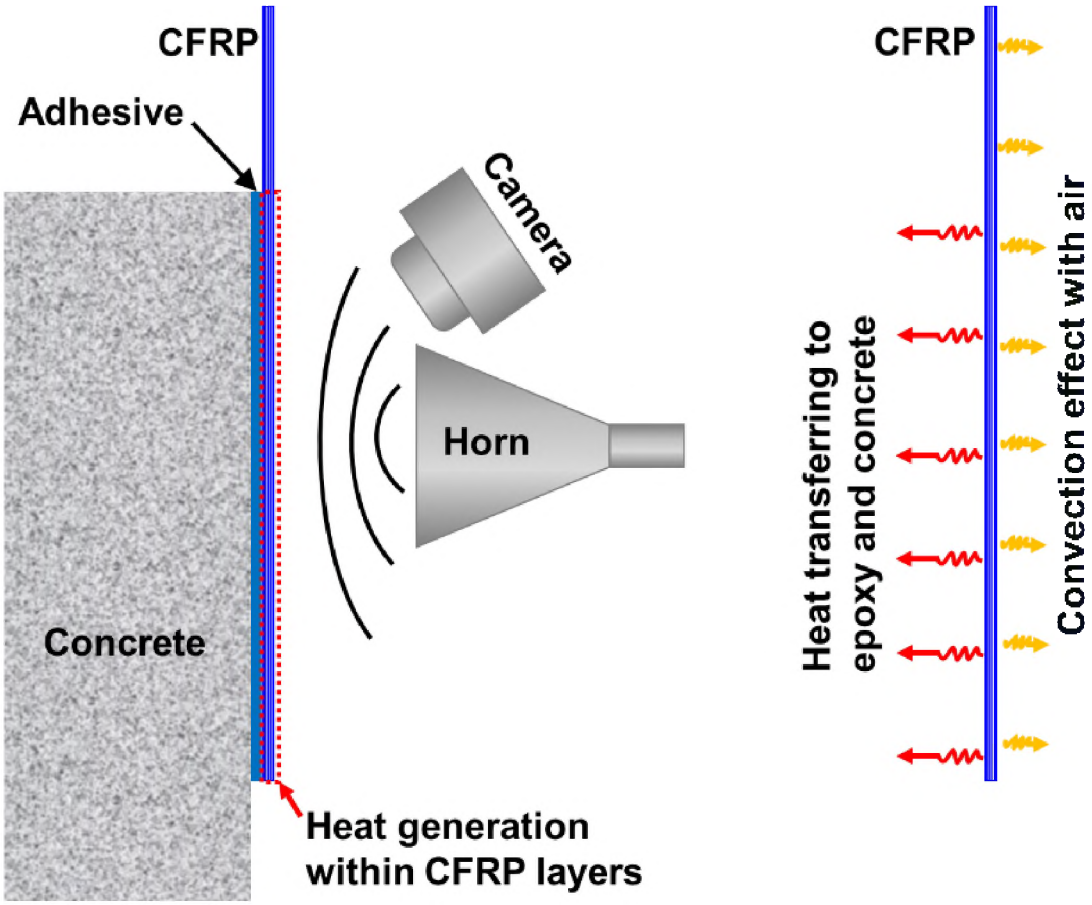


Figure 14. Illustration of heat generation within CFRP layer and heat transferring.

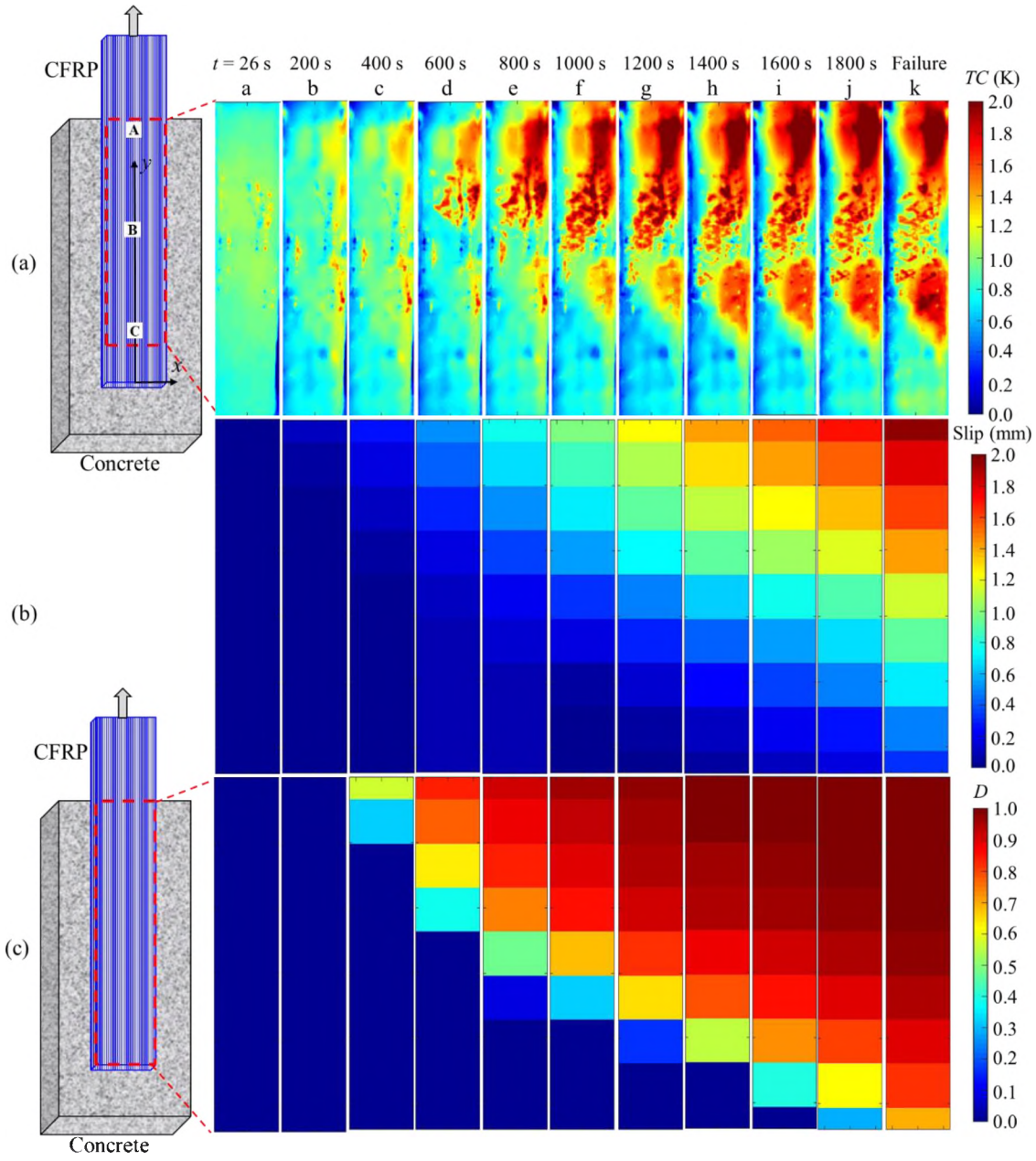


Figure 15. (a) Thermal contrast *TC*(t) profiles on the surface of specimen AMT-CFRP-2, and the (b) slip and (c) damage distributions determined from strain measurements from specimens CFRP-S-1 and CFRP-S-2 (Points a-k are shown in Figure 13).

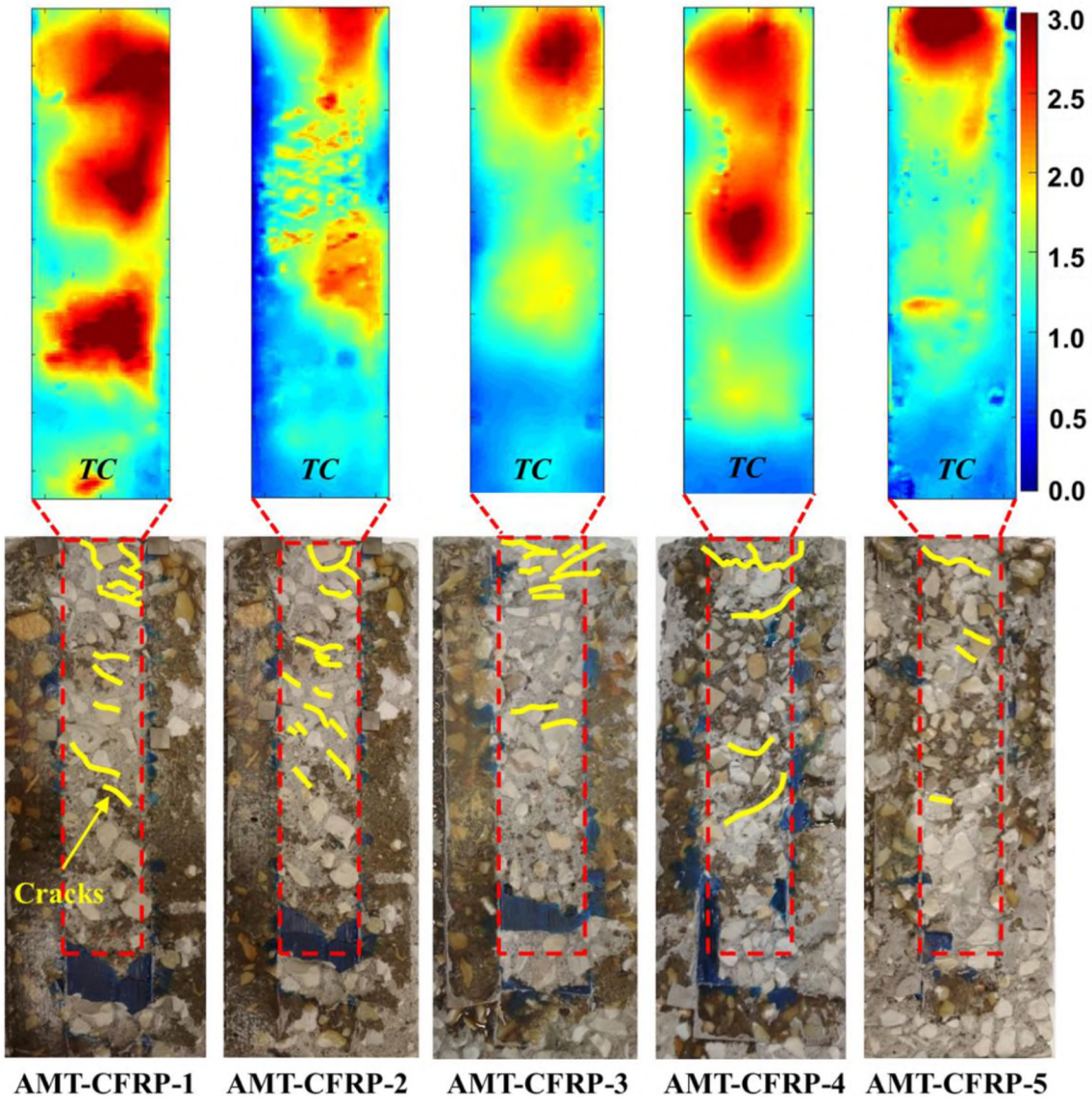


Figure 16. *TC* profiles the second before composite debonding occurred.

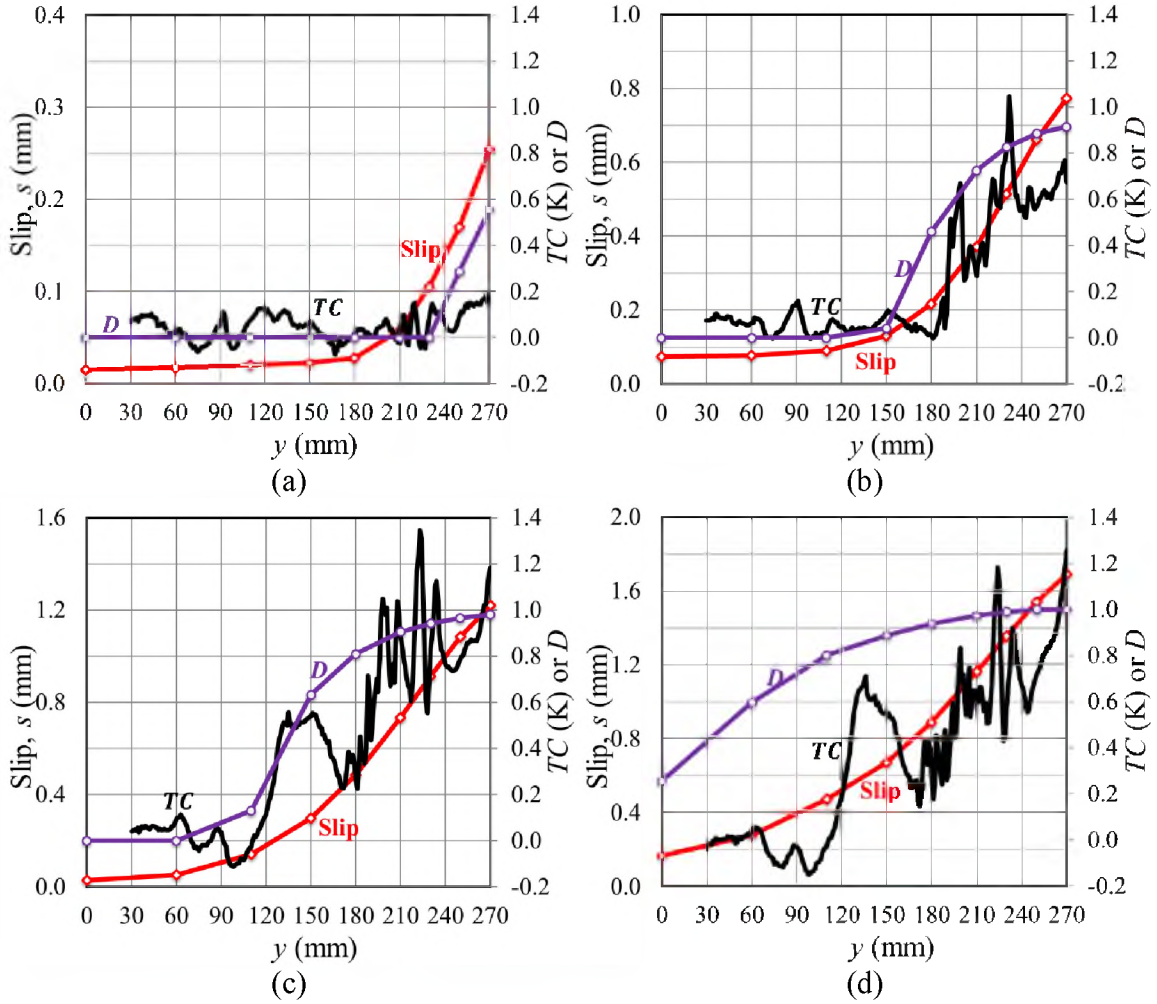


Figure 17. Distribution of *TC* for specimen AMT-CFRP-2 and distribution of slip and D determined from strain measurements from specimens CFRP-S-1 and CFRP-S-2 along the bonded length y for $g$ = (a) 0.5 mm, (b) 1.0 mm, (c) 1.5 mm, and (d) 2.0 mm.

Table 1. Electromagnetic and thermal properties of materials.

| Material | Electromagnetic Properties | $K_T$ (W/m·K) | $C_T$ (J/g·K) | $\rho$ (kg/m$^3$) |
|---|---|---|---|---|
| Air | $\varepsilon_r = 1$ | 0.026 | 1.005 | 1.204 |
| Epoxy | $\varepsilon_r \approx 6 - 0.6j$ | 1.0 | 3.7 | 1100 |
| Cementitious mortar | $\varepsilon_r \approx 4.7 - 0.7j$ | 1.7 | 0.8 | 2400 |
| CFRP‖ | $\sigma = 10^4$ | 7 | 1.2 | 1600 |
| CFRP⊥ | $\varepsilon_r \approx 7 - 2.5j$ | 0.8 | 1.2 | 1600 |

Note that ‖ and ⊥ indicate the direction parallel and perpendicular to the fiber direction, respectively.

Table 2. Single-lap shear specimen parameters and test results.

| Specimen | AMT | Strain gages | $P^*$ (kN) | $g^*$ (mm) | $g_{ult}$ (mm) |
|---|---|---|---|---|---|
| CFRP-S-1 | | √ | 18.76 | 2.30 | 2.33 |
| CFRP-S-2 | | √ | 20.60 | 1.85 | 2.12 |
| AMT-CFRP-1 | √ | | 16.97 | 2.08 | 2.09 |
| AMT-CFRP-2 | √ | | 16.72 | 0.67 | 2.17 |
| AMT-CFRP-3 | √ | | 20.48 | 2.20 | 2.26 |
| AMT-CFRP-4 | √ | | 17.15 | 1.28 | 2.34 |
| AMT-CFRP-5 | √ | | 16.55 | 2.12 | 2.18 |
| Average | | | 18.18 | 1.79 | 2.21 |
| CoV | | | 0.10 | 0.33 | 0.05 |

Table 3. Fitting parameters determined by nonlinear regression analysis.

| Specimen | $g$ (mm) | $\alpha$ ($10^{-6}$) | $\beta$ (mm) | $y_0$ (mm) |
|---|---|---|---|---|
| CFRP-S-1 | 0.75 | 7420 | 18.9 | 196.9 |
| | 1.00 | 8082 | 19.4 | 173.1 |
| | 1.25 | 8852 | 28.0 | 138.8 |
| | 1.50 | 9176 | 31.9 | 120.2 |
| | 1.75 | 9979 | 40.6 | 100.5 |
| CFRP-S-2 | 0.75 | 5811 | 13.5 | 210.1 |
| | 1.00 | 5985 | 13.4 | 170.5 |
| | 1.25 | 6891 | 19.9 | 149.3 |
| | 1.50 | 7794 | 18.6 | 146.1 |
| | 1.75 | 8396 | 20.5 | 143.7 |
| Average | | 7839 | 22.5 | 154.9 |
| CoV | | 0.17 | 0.38 | 0.22 |

## REFERENCES

[1] Hollaway, L. C. (2010). A review of the present and future utilisation of FRP composites in the civil infrastructure with reference to their important in-service properties. Construction and Building Materials, 24(12), 2419-2445.

[2] Shi JW, Cao WH, Wu ZS. Effect of adhesive properties on the bond behaviour of externally bonded FRP-to-concrete joints. Compos B Eng 2010; 177, 107365.

[3] He, R., Grelle, S., Sneed, L. H., & Belarbi, A. (2013). Rapid repair of a severely damaged RC column having fractured bars using externally bonded CFRP. Composite Structures, 101, 225-242.

[4] Khalifa, A., Gold, W. J., Nanni, A., & MI, A. A. (1998). Contribution of externally bonded FRP to shear capacity of RC flexural members. Journal of composites for construction, 2(4), 195-202.

[5] Gonzalez-Libreros, J. H., Sneed, L. H., D'antino, T., & Pellegrino, C. (2017). Behavior of RC beams strengthened in shear with FRP and FRCM composites. Engineering Structures, 150, 830-842.

[6] Ameli, M., Ronagh, H. R., & Dux, P. F. (2007). Behavior of FRP strengthened reinforced concrete beams under torsion. Journal of Composites for Construction, 11(2), 192-200.

[7] Alabdulhady, M. Y., & Sneed, L. H. (2019). Torsional strengthening of reinforced concrete beams with externally bonded composites: A state of the art review. Construction and Building Materials, 205, 148-163.

[8] Grelle, S. V., & Sneed, L. H. (2013). Review of anchorage systems for externally bonded FRP laminates. International Journal of Concrete Structures and Materials, 7(1), 17-33.

[9] Lu, X. Z., Teng, J. G., Ye, L. P., & Jiang, J. J. (2005). Bond–slip models for FRP sheets/plates bonded to concrete. Engineering structures, 27(6), 920-937.

[10] Chen, G. M., Chen, J. F., & Teng, J. G. (2012). Behaviour of FRP-to-concrete interfaces between two adjacent cracks: A numerical investigation on the effect of bondline damage. Construction and building materials, 28(1), 584-591.

[11] Cromwell JR, Harries KA, Shahrooz BM. Environmental durability of externally bonded FRP materials intended for repair of concrete structures. Constr Build Mater 2011, 25(5), 2528-2539.

[12] Carloni C, Subramaniam KV, Savoia M, Mazzotti C. Experimental determination of FRP–concrete cohesive interface properties under fatigue loading. Compos Struct 2012; 94(4), 1288-1296.

[13] Tuakta C, Büyüköztürk O. Deterioration of FRP/concrete bond system under variable moisture conditions quantified by fracture mechanics. Compos B Eng 2012; 42(2), 145-154.

[14] Subramaniam KV, Ali-Ahmad M, Ghosn M. Freeze–thaw degradation of FRP–concrete interface: impact on cohesive fracture response. Eng Fract Mech 2008; 75(13), 3924-3940.

[15] Zhou A, Qin R, Feo L, Penna R, Lau D. Investigation on interfacial defect criticality of FRP-bonded concrete beams. Compos B Eng 2017; 113, 80-90.

[16] Wan B, Jiang C, Wu YF. Effect of defects in externally bonded FRP reinforced concrete. Constr Build Mater 2018; 172, 63-76.

[17] Mahmoud AM, Ammar HH, Mukdadi OM, Ray I, Imani FS, Chen A, Davalos JF. Non-destructive ultrasonic evaluation of CFRP–concrete specimens subjected to accelerated aging conditions. NDT & E Int 2010; 43(7), 635-641.

[18] Li J, Lu Y, Guan R, Qu W. Guided waves for debonding identification in CFRP-reinforced concrete beams. Constr Build Mater 2017; 131, 388-399.

[19] Qiu Q, Lau D. A novel approach for near-surface defect detection in FRP-bonded concrete systems using laser reflection and acoustic-laser techniques. Constr Build Mater 2017; 141, 553-564.

[20] Yazdani N, Beneberu E. Riad M. Nondestructive Evaluation of FRP-Concrete Interface Bond due to Surface Defects. Adv Civ Eng 2019; 2563079

[21] Shih JKC, Tann DB, Hu CW, Delpak R, Andreou E. Remote sensing of air blisters in concrete–FRP bond layer using IR thermography. Int J Mater Prod Technol 2003; 19(1-2), 174-187.

[22] Gu JC, Unjoh S, Naito H. Detectability of delamination regions using infrared thermography in concrete members strengthened by CFRP jacketing. Compos Struct 2020; 112328.

[23] Hong X, Lin J, Liu Y, Xu W. Active Thermal Sensing for Bonding Structure Damage Detection of Hidden Frame Glass Curtain Wall. Sens 2018; 18(11), 3594.

[24] Foudazi A, Edwards CA, Ghasr MT, Donnell KM. Active microwave thermography for defect detection of CFRP-strengthened cement-based materials. IEEE Trans Instrum Meas 2016; 65(11), 2612-2620.

[25] Mirala A, Foudazi A, Ghasr MT, Donnell KM. Detection of Flat-Bottom Holes in Conductive Composites Using Active Microwave Thermography. Nondestr Eval Diagn Progn Eng Syst 2018; 1(4).

[26] Foudazi A, Mirala A, Ghasr, MT, Donnell K M. Active Microwave Thermography for Nondestructive Evaluation of Surface Cracks in Metal Structures. IEEE Trans Instrum Meas 2018; (99), 1-10.

[27] Foudazi A, Mehdipour I, Donnell KM, Khayat KH. Evaluation of steel fiber distribution in cement-based mortars using active microwave thermography. Mater Struct 2016; 49(12), 5051-5065.

[28] https://www.aegion.com/-/media/Files/Fyfe/2013-Products/Tyfo%20SCH%2041.ashx (accessed April 2020)

[29] https://assets.master-builders-solutions.basf.com/en-ru/basf-masterbrace-p3500-tds.pdf (accessed April 2020)

[30] https://assets.master-builders-solutions.basf.com/en-bd/basf-masterbrace-4500-v1-tds.pdf (accessed April 2020)

[31] ASTM C39/C39M-17b. Standard test method for compressive strength of cylindrical concrete specimens. ASTM International: West Conshohocken. PA, USA, 2017.

[32] ASTM C496/C496M. Standard Test Method for Splitting Tensile Strength of Cylindrical Concrete Specimens. ASTM International: West Conshohocken. PA, USA, 2011.

[33] He L, Wu YF, Xiao Y. Analytical solution for externally bonded joints considering snap-back. J Compos Constr 2014; 19(5), 04014077.

[34] Wu YF, Jiang C. Quantification of bond-slip relationship for externally bonded FRP-to-concrete joints. J Compos Constr 2013; 17(5), 673-686.

[35] Carloni C, Subramaniam KV. Direct determination of cohesive stress transfer during debonding of FRP from concrete. Compos Struct 2010; 93(1), 184-192.

[36] Carloni C, Subramaniam KV. Application of fracture mechanics to debonding of FRP from RC members. SP-286, ACI 2012;10-1-10-14

[37] Dai J, Ueda T, Sato Y. Unified analytical approaches for determining shear bond characteristics of FRP-concrete interfaces through pullout tests. J Adv Concr Technol 2006; 4(1), 133-145.

[38] Carrara P. Interface behavior of fiber reinforced polymer composites externally glued to quasi-brittle substrates. Doctoral dissertation 2014; University of Florence.

# V. NONDESTRUCTIVE EVALUATION OF INITIAL DEFECTS AND PROGRESSIVE DEBONDING OF CFRP-CONCRETE JOINTS USING ACTIVE MICROWAVE THERMOGRAPHY (AMT)

Xingxing Zou, Lesley H. Sneed, Ali Mirala, Mohammad Tayab Ghasr, and Kristen Donnell

## ABSTRACT

This study presents an investigation of non-destructive evaluation (NDE) of carbon fiber reinforced polymer (CFRP)-concrete interfacial debonding by using a novel technology- active microwave thermography (AMT). AMT utilizes microwave energy as a heating excitation to the structure and captures the anomalies of temperature contrast ($TC$) at the surface of the structure by a thermal camera. First, AMT was used to detect the initial man-made defect of CFRP-concrete joints by comparative tests on specimens without or with initial defects. Test results showed that AMT can detect the initial defects at the interface of CFRP and concrete in around 10 s heating. Secondly, the time-history AMT was used to monitor the progressive interfacial debonding process of the CFRP-concrete joints under monotonic loading of single-lap shear test. The test results showed that the bonded interface failed first at the loaded end of bonded area due to the increasing of load. Then, debonding occurred to the area adjacent to the initially debonded region. A loaded drop was marked by a change of slope of local CFRP surface $TC$.

**Keywords:** Active microwave thermography (AMT); interfacial debonding; defect; carbon fiber reinforced polymer (CFRP); single-lap shear test.

# 1. INTRODUCTION

Externally bonded carbon fiber-reinforced polymer (CFRP) composites, consisting of high-strength fibers impregnated by high-performance thermosetting polymer, have been widely used to strengthen concrete structures [1]. The interfacial bonding quality plays a pivotal role in the composite action between CFRP and concrete. Previous researches showed that interfacial debonding can be caused by the poor workmanship during the installation, the environmental damage, and the load effects [1][2]. Once there is debonded area along the interface, the capacity, ductility, and durability of CFRP strengthened structures can be substantially decreased. Therefore, the quality of the bonded interface of CFRP strengthened structures should be checked both after installation and during the long-term service [2][3]. Several NDT methods including microwave imaging [4][5], ultrasound [6], and shearography [7] have been applied to detect the debonding between CFRP and concrete industry with varying levels of success.

Since CFRP are usually bonded to the concrete substrate and the interfacial debonding at a fairly shallow surface beneath CFRP layers, active thermography have been proven to be an effective, low-cost, and potable approach to detect this kind of debonding [8][9][10][11][12][13]. There are generally three steps to conduct the active thermography approach [14]: (i) utilizing an external heat excitation to penetrate a certain thickness in structures, (ii) capturing the thermal field on outer surfaces of structures with a thermal camera, and (iii) correlating the surface temperature with the inner imperfections. In the first step, powerful heat source is required to generate enough heat to the structures [8][9][10]. Flash heat lamp was employed in some researches, however, lamps cannot be focused to an area of interest, but rather are applied over a larger area. Moreover, powerful

lamp heating system increases the risk of fire disaster and damage to the structural regions with interest [14]. Instead, microwave excitations offer unique advantages, including the application of controlled and localized microwave energy, remote (noncontact) inspection, and the ability to tailor the evaluation to the inspection need through choice of frequency and polarization of the microwave signal (amongst others). In the second step, AMT utilizes commercially available thermal cameras to capture easy-to-interpret surface thermal images of a structure under test.

AMT was successfully used to detect the presence of steel reinforcement in a depth of about 38 mm for outdoor uses [15], to inspect flat-bottom holes (FBHs) underneath CFRP sheets [16], covered surface cracks in metal structures [17], and chopped steel fibers' distribution in cementitious materials [18]. In this paper, AMT will be used to detect the initial debonding at the CFRP-concrete interface. Firstly, comparative AMT tests were conducted to inspect the initial defect on two specimens with or without initial man-made detects. Then, AMT was used to monitor the initiation and propagation of interfacial debonding on the same two specimens under single-lap shear test.

## 2. ACTIVE MICROWAVE THERMOGRAPHY (AMT)

As mentioned before, AMT uses microwave energy as a heat excitation. The main heating mechanism is dielectric heating. When a lossy dielectric is irradiated with microwave energy, the amount of dissipated heat $Q$ at each point inside the dielectric at that point can be expressed as:

$$Q = 2\pi f \varepsilon_0 \varepsilon_r'' |E|^2 \tag{1}$$

where $f$ is the frequency, $\varepsilon_0$ is the free space dielectric constant, $\varepsilon_r''$ is the loss factor, which represents the ability of a material to absorb microwave energy, and $E$ is the RMS (root mean square) magnitude of the electric field, which is related to the microwave power source. The dielectric and thermal properties of material(s) under test determine the induced heat and subsequent heat diffusion. Assuming that the energy input is the heat $Q$, in Eq. (1) which serves as the external input to the structural part being heated, transient heat diffusion occurs and is related to the thermal properties of material(s) and source of heat as follows:

$$\rho C_T \frac{\partial T}{\partial t} = K_T \nabla^2 T + Q \tag{2}$$

where $\rho$ is the density, $C_T$ is the specific heat, $T$ is the temperature, $t$ is the time, and $K_T$ is the thermal conductivity. The thermal properties and values of $K_T$, $C_T$, and $\rho$ are summarized in Table 1, which have been reported in [14].

If $f$ and the $E$ are constant values during the test and no loading is applied, the material properties will remain the same and the thermal response will reach a stable state. However, once damage (e.g., concrete cracking, adhesive cracking, interfacial debonding of CFRP-adhesive, or adhesive-concrete interface) occurs to the interface between CFRP and concrete due to the load (see Figure 1), air pocket formed within the damaged area. Since $K_T$, $C_T$, and $\rho$ of air are dramatically lower than epoxy, concrete, and CFRP, see Table 1, temperature will increase within the regions close to interfacial cracking. To sum, the interfacial debonding can cause increase of anomalies of temperature of CFRP outer surface which will be monitored by the thermal camera in AMT system.

# 3. MATERIALS

The unidirectional CFRP sheets was a commercially available product [21], with design composite gross laminate properties provided by the manufacturer [21] of: Young's modulus, $E_{FRP}$ =82.0 GPa; ultimate tensile strength, $f_u$ =834 MPa; ultimate tensile strain, $\varepsilon_{ult}$ = 0.0085; and nominal laminate thickness, $t_f$ =1 mm. For the bonding system between CFRP sheet and concrete substrate, two types of epoxy resin were used: a primer layer (MasterBrace P 3500), and a saturant layer (MasterBrace 4500). The primer was a two-component solvent-less epoxy penetrating medium viscosity primer with a tensile strength and modulus, according to the manufacture [22], of 17.2 MPa and 717 MPa, respectively. The primer was used to penetrate the pore structure of cementitious substrates and to provide a high bond base coat. The tensile strength and modulus of the saturant layer, according to the manufacture [23], are 55.2 MPa and 3034 MPa, respectively. It is used to saturate the carbon fabric sheets to create a composite with the concrete structure.

All concrete batches consisted of commercial Portland Type I/II cement without admixtures, normal-weight coarse aggregate with a maximum size of 10 mm, sand from Missouri River, and clean water. The concrete mixture had a designed compressive strength of 30 MPa to simulate the massive concrete used in existing civil structures awaiting strengthening by CFRP. The mixture proportions by weight ratio were (cement: sand: aggregate = (1:00: 3.86: 4.37), and the water-cement ratio was 0.76. The concrete compressive and splitting tensile strength was experimentally obtained using six 101.6 mm (4 inches) diameter 203.2 mm (8 inches) long cylinders in accordance with ASTM C39/C39M [24] and ASTM C496/C496M [25], respectively. The typical failure modes can

be seen in Figure 3. The average compressive strength and splitting tensile strength measured were 30.4 MPa (CoV = 0.09) and 2.7 MPa (CoV = 0.16), respectively.

# 4. METHODS

## 4.1. CFRP-CONCRETE JOINTS

There were two specimens in the form of CFRP-concrete joint reported in this paper. Each specimen consists of a CFRP sheet bonded to a concrete prism by a layer of epoxy (see Figure 1). The first specimen, named as AMT-CFRP-2, had no initial man-made defect. The second specimens has initial man-made defects between the CFRP layer and the concrete substrate, named AMT-CFRP-D-1. A plastic plates was first applied to the interface (see Figure 2b), and then the epoxy and CFRP were applied (see Figs. 2c and 2d), finally before the hardening of epoxy, the plate was pull out (Figure 2e).

The concrete prisms were dimensioned as 125 mm wide × 125 mm deep × 375 mm long. All concrete prisms and cylinders for material property tests were cured under towels for 24 hours before being removed from the forms. After the removal of the forms, they were placed into moisture lab for curing. During the curing of specimens, the room temperature was approximate 15 $^{o}$C. After 28 days of curing of concrete prisms, the side faces that will be used to apply CFRP, were sandblasted until the aggregates were exposed thereby obtaining a stronger strength at the concrete surface.

## 4.2. COMPARATIVE TESTS ON SPECIMENS WITH OR WITHOUT A MAN-MADE DEFECT

The non-uniformity of the microwave energy absorbed by the CFRP-concrete joint, caused by its reflection from the specimen with the antenna, generates an inhomogeneous

volumetric heating in the sample and may lead to misinterpret raw thermographs [15]. Thus, the first round of test was to carry out AMT tests on all the three specimens without any loading separately. The method used to analyze thermograph series is based on a contrast algorithm between the specimens. First, the temperature field of specimen $T_S(x, y, t)$ and $T_D(x, y, t)$, respectively, represent the temperature of specimens without defects (AMT-CFRP-2) or with man-made defects (see Figs. 3a and 3b). To this end, thermal contrast ($TC$) is defined as the difference between the temperature increase which is defined as the temperature value at any time relative to its initial value. Letting $t$ = 1 (s) in $T_S(x, y, t)$ and $T_D(x, y, t)$ denotes the beginning of the heating process (see Figure 3), which serves as a starting point to compute $TC$. Therefore, $TC_S(x, y, t)$ and $TC_D(x, y, t)$ were taken as $TC$ for specimen with solid or defected interface, respectively, see Figure 3. The calculation principle is to subtract first thermograph series recorded on a specimen without defect with a series recorded on a specimen containing some inclusions (see Figure 3). This subtraction is carried out on each point and at the same times. This approach can reduce the non-uniformity effect of the excitation. The initial temperature value is then subtracted from the resulting contrast sequence which allowed to consider only the temperature rise in case of the temperatures of the two specimens would not be identical. The calculation principle is shown in Figure 3. This approach can reduce the influence of the room temperature at the beginning of the excitation.

## 4.3. COMPARATIVE TEST OF SPECIMENS AMT-CFRP-D-1 WITHOUT LOADING OR UNDER SINGLE-LAP SHEAR TEST WITH AMT MONITORING

The set-up for the single-lap shear test involved using a servo-hydraulic universal testing machine in a tension procedure. The single-lap shear test configuration was adopted where the fibers were pulled on the top gripped area and the concrete prism was mounted onto the base of the machine by a Π-shaped steel frame.

The AMT measurements were conducted on the front surface on which the CFRP stripe was applied, see Figure 1. All microwaves were generated at a constant frequency of 2.45 GHz and a fixed power level of 50 W. The horn antenna had an aperture size of A×B = 230×170 $mm^2$ and can handle high-power microwave radiation, faced directly toward the specimen surface to maximize the microwave-induced heat over the surface. The distance between the antenna aperture and the specimen, which is called strand-off distance, was 400 mm to ensure that the microwave excitation was sufficiently uniform over the inspection area but also allowed viewing of the inspection area with the thermal camera. The thermal camera used in this work was the FLIR T430sc that can produce thermal images of 320×240 pixels at the temperature resolution of less than 30 mK. The temperature profile was acquired at a rate of 1 Hz. The control unit synchronized the microwave and thermal segments of the AMT system. The mechanical loading was controlled by monotonically increasing average value of the displacements measured by the two LVDTs, which is defined as global slip, with a constant rate of 0.001084 mm/s.

For each specimen, the test procedure consisted of three stages: heating without loading (Stage-I), cooling (Stage-II), and heating with loading (Stage-III), see Figure 3. In Stage-I, the specimen was placed into the test frame, and the microwave heating was

conducted, the temperature was recorded as $T_I(t)$, see Figure 4. This stage aimed to detect if the specimen had any initial defects or anomalous regions that occurred during composite installation. In addition, the temperature increase in this stage was used to normalize the temperature increase in Stage-III, which will be explained later. Stage-II was a cooling process where the microwave was shut down, and cooling was driven by convection effect with the relatively lower room temperature (compared with that of the specimen). In Stage-III, the specimen was heated using the same process as Stage-I, and at the same time, external loading was applied, see Figure 3, the temperature was recorded as $T_{III}(t)$, see Figure 4.

In each stage, thermal contrast ($TC$) is defined as the difference in temperature increase, which is defined as the temperature value at any time ($t$) relative to its initial value ($t = 0$), thus the influence of different room temperature can be eliminated. $TC$ in Stage-I is denoted by $TC_I(t)$, where $t$ is the time of heating in Stage-I. The duration of this stage was approximately 45 minutes. $TC$ in Stage-III is denoted by $TC_{III}(t)$, where $t$ is the time of heating in Stage-III. One has $TC_I(t)$ and $TC_{III}(t)$, from the definition as

$$TC_I(t) = T_I(1) - TC_I(t) \tag{3a}$$

$$TC_{III}(t) = T_{III}(1) - TC_{III}(t) \tag{3b}$$

In Stage-III, if the CFRP-concrete interface has been damaged by the loading, cracks occur along the interface which causes air injection thereby leading to $TC$ increase compared to Stage I. Therefore, the temperature change $TC_c(t)$ caused by loading (see Figure 4) is taken as the difference between the Stage-I and Stage-III $TC$ at time $t$ as:

$$TC_c(t) = TC_{III}(t) - TC_I(t) \tag{4}$$

# 5. EXPERIMENTAL RESULTS AND DISCUSSION

## 5.1. INITIAL DEFECTS INSPECTION

Figure 5 shows the $TC_I$ thermographs for $t$ = 1 s (beginning), 100 s, 500 s, 1000 s, 1500 s, and 2000 s for specimens AMT-CFRP-2 and AMT-CFRP-D-1. It can be seen that the initial defect at specimens AMT-CFRP-D-1 caused dramatic $TC_I$ anomaly than the rest areas. $TC_I$ for specimen AMT-CFRP-2 without loading shows that there are some speckles at the bonded area, which might be caused be the workmanship. Let the maximum label of temperature reduce from the value of 3 K in Figure 5 to 0.3 K in Figure 6, the results of $TC_I$ for specimen AMT-CFRP- D-1 is plotted for $t$ = 5 s, 10 s, and 15 s. It is clear seen that the original defect can be detected at 10 s, which means AMT is a fast and effective NDT method to detect the CFRP-concrete interfacial debonding.

Figure 7 shows the average $TC_I$ distribution along $y$ direction for the two specimens. It can be seen that $TC_I$ shows a constant distribution along $y$ direction for specimen AMT-CFRP-2, thought there are some fluctuations. As a comparison, $TC_I$ for specimen AMT-CFRP-D-1 shows dramatically high values at the location ($150 \ll y \ll 180$) with man-made defects.

Figure 8 shows the time-history responses of $TC_I$ for the both specimens. D1, D2, and D3 are rectangular regions on the surface of CFRP, see Figure 5. D1 denotes an area close to the loaded end, D2 denotes the area at the debonded area, and D2 denotes the area closed to the free end. $TC_I$ for Specimen AMT-CFRP-2 in Figure 8a shows that D1 has higher $TC$ than D2 and D3. However, $TC_D$ for Specimens AMT-CFRP-D-1~2 shows D2 has much larger $TC$ than D1 and D3, which denotes that the defected area induced higher $TC$.

## 5.2. TIME-HISTORY MONITORING OF SINGLE-LAP SHEAR TEST

The load responses of the two specimens were summarized in Table 2. It is shown that the specimen AMT-CFRP-D-1 has a lower peak load, ($P_{max}$), and a similar ultimate global slip ($g_{ult}$).

Figure 9 shows the load response of the two tested specimens in Stage-III. It can be seen that, from the beginning to 7 kN, the two specimens behaved similarly, with nearly the same global slip and load. Then from 7 kN to around 12.5 kN, both curves exhibit decreased slope which means damage formed. When the global slip was around 0.6 mm, the two specimens both had a load drop of around 2 kN, and 10 kN, respectively, for specimens AMT-CFRP-2 and AMT-CFRP-D-1~2. The difference in load drop indicates the initial defected area substantially decreased the capacity of the interface.

$TC_C$ distribution among the width of the bonded area for specimens AMT-CFRP-D-1 can be seen in Figure 10. It can be seen that the there is higher $TC_C$ response at the debonded areas, which is the same as the response compared with Figs. 7b. There is higher $TC_C$ close to the loaded end, which is attributed to the load induced debonding.

Figure 11 shows the sequential $TC_C$ responses of specimens AMT-CFRP-2 and AMT-CFRP-D-1. It can be clearly seen that the $TC_C$ responses are different. For specimen AMT-CFRP-2, initial defect formed at the region close to the loaded end, and then propagates to the free end. For specimen AMT-CFRP-D-1, the initial defect was already at the region in the middle of the bonded length, as the load increase, new defected area formed at loaded end, and propagates to the free end. When the new defect is close to the defected area, there is a severe load drop, which can be seen in Figure 9. At then, the defected area kept propagating to the free end.

It is interesting to see that the defected area in specimen AMT-CFRP-D-1 has a lower $TC_C$ responses, the value could be negative when the load was large. This phenomenon can be explained by the fact that with the increase of load, the CFRP fibers were stretched to a straight line, which reduced the thickness of the defected region, see Figure 12.

Figure 13 shows the correlation between the applied load and the $TC_{III}$ responses for specimen AMT-CFRP-D-1. It can be seen that when load dropped at around 600 s, the slope of $TC_{III}$ for point D1 increased suddenly, which means the region close to the loaded end was debonded. When the load had another drop at around 1450 s, the slope of $TC_{III}$ for point D2 increased suddenly, which means the region close to the initial man-made defect was debonded.

Figure 14 shows the correlation between the applied load and the $TC_C$ responses for specimen AMT-CFRP-D-1. It can be seen that when load dropped at around 600 s, the slope of $TC_{III}$ for point D1 increased suddenly, which means the region close to the loaded end was debonded. When the load had another drop at around 1450 s, the slope of $TC_C$ for point D2 changed from negative to positive suddenly, which means the region close to the initial man-made defect started to debond.

To summary from the load and thermal responses of specimens AMT-CFRP-2 and AMT-CFRP-D-1 in Stage-III, it can be found that the existence of the initial man-made defect can influence the CFRP-concrete interface in the following aspects: (i) reducing the load capacity, and (ii) making the load drop caused by local debonding more severe.

## 6. CONCLUSION

This study reveals that the initiation and propagation of CFRP-concrete interfacial damage can be detected and monitored by AMT. Salient findings are:

(1) The AMT technology can detect the man-made defect in 10 s heating.

(2) For the specimen without man-made defect, at the beginning of loading, dense $TC_c$ responses occurred within the areas close to loaded end where interfacial debonding initiates. With the increase of load, the interfacial debonded area transferred towards the free end which correlated well with the local $TC_c$ of CFRP surface.

(3) The presence of an initial defect changes the debonding process by reducing the load capacity, and making the load drop caused by local debonding more severe.

(4) $TC_{III}$ and $TC_C$ can both be used to correlate with the load resposnse.

## ACKNOWLEDGEMENT

This work was supported by the National Science Foundation (NSF) Electrical, Communication, and Cyber Systems (ECCS) Award 1609470, "A Multi-Physics-Based Approach to Active Microwave Thermography". Many thanks to undergraduate students Lia Vanzant and Daniel Bishof from Department of Electrical and Computer Engineering, Missouri University of Science and Technology, for their contributions to the test.

## AVAILABILITY OF DATA AND MATERIALS

Not applicable.

## FUNDING

This work was supported by the National Science Foundation (NSF) Electrical, Communication, and Cyber Systems (ECCS) Award 1609470, "A Multi-Physics-Based Approach to Active Microwave Thermography."

## COMPETING INTERESTS

The authors declare that they have no competing interests.

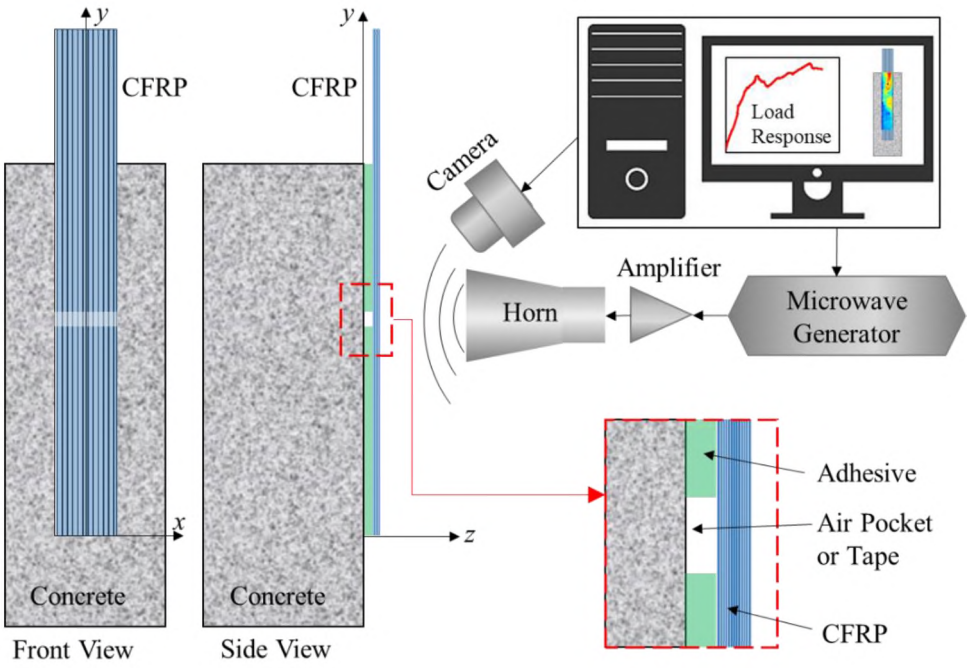


Figure 1. Setup of AMT testing on single-lap shear test of CFRP-concrete joint.

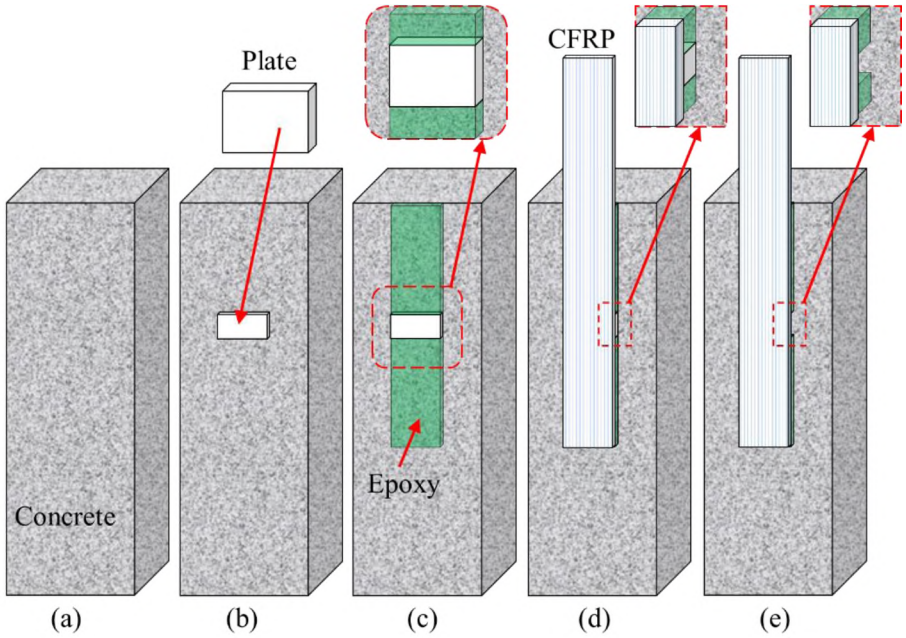


Figure 2. Construction of CFRP-concrete joints: (a) concrete prism, (b) attach tap or plate at predefined location of defects, (c) apply epoxy, (d) apply CFRP sheets, and (e) remove the plate before the hardening of epoxy (for Specimen AMT-CFRP-D-1).

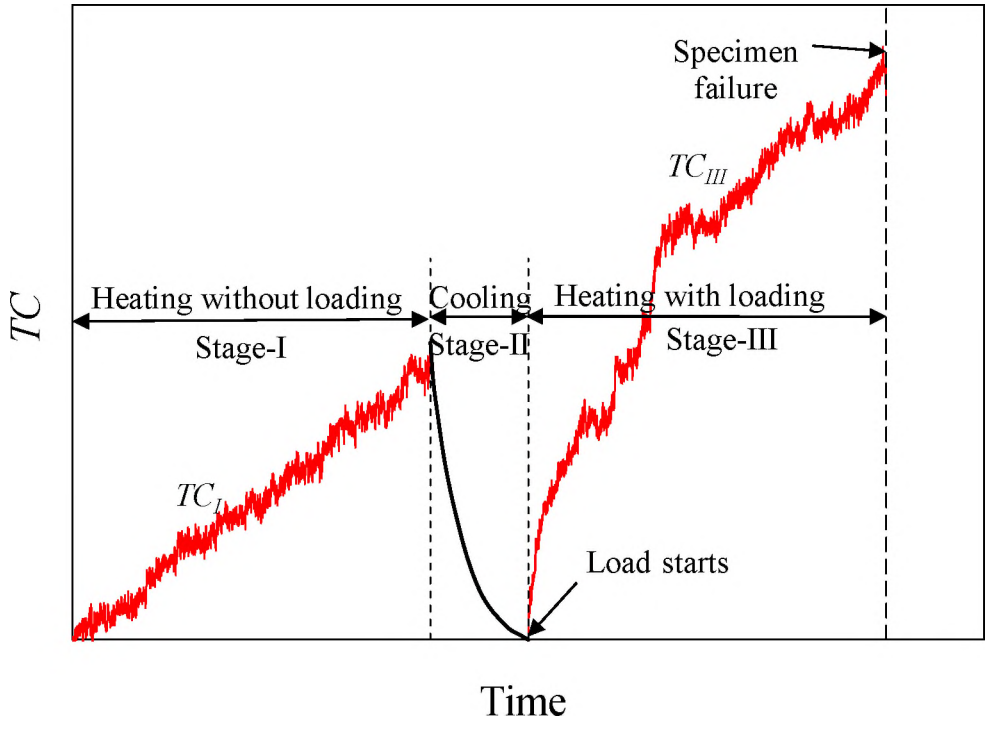


Figure 3. AMT test procedure for each specimen.

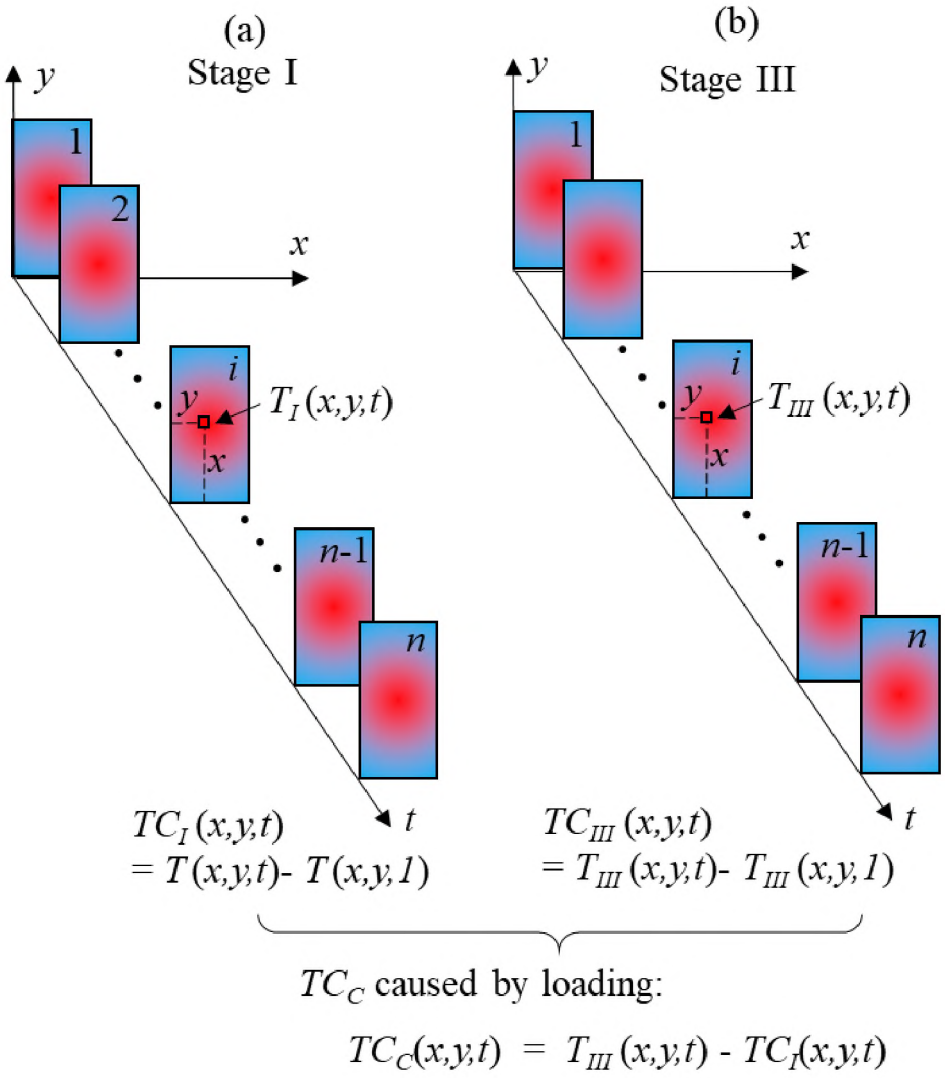


Figure 4. Thermographs analysis principle.

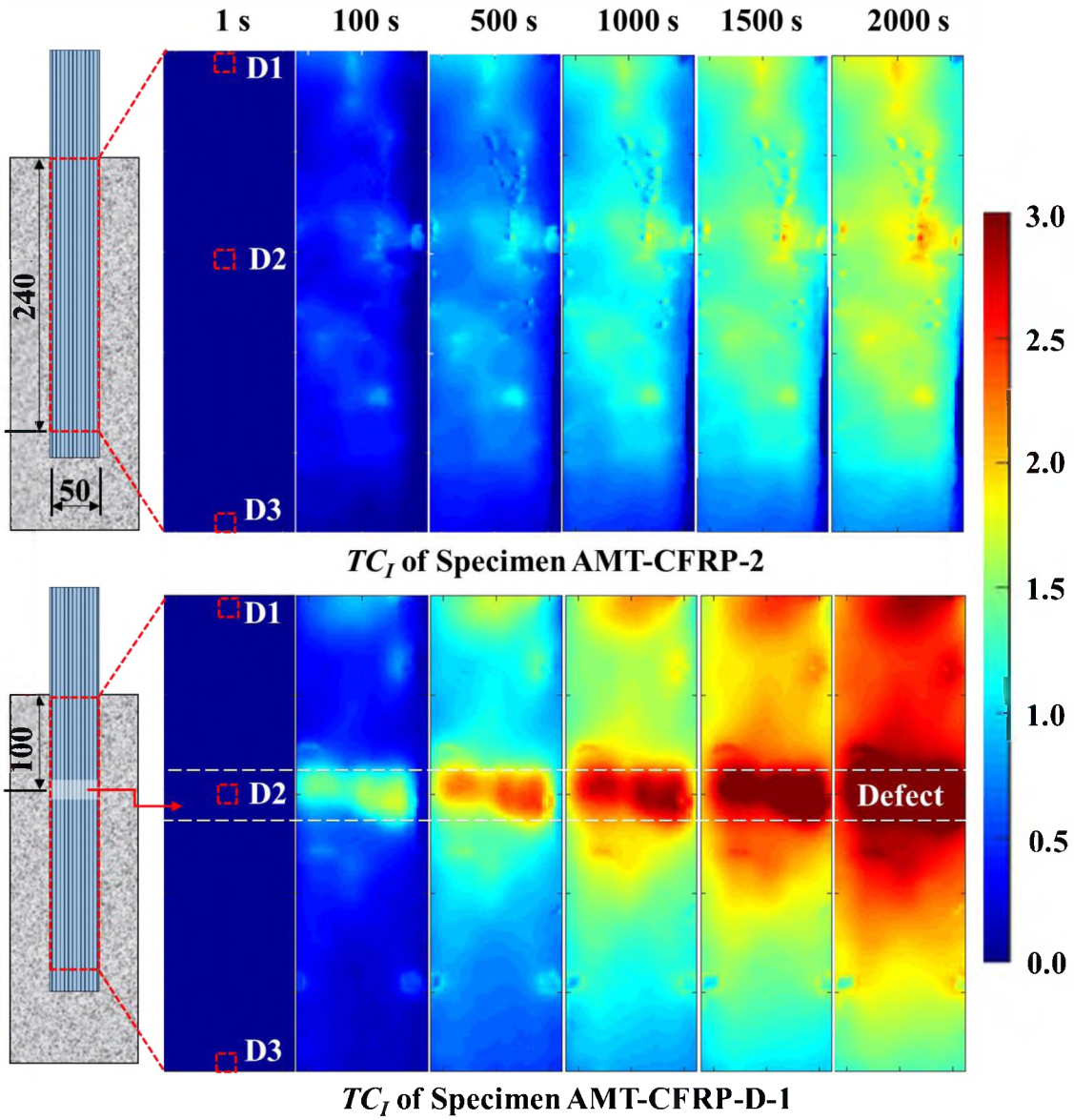


Figure 5. Comparative $TC_I$ response of specimens without and with initial defect (Units in K and mm).

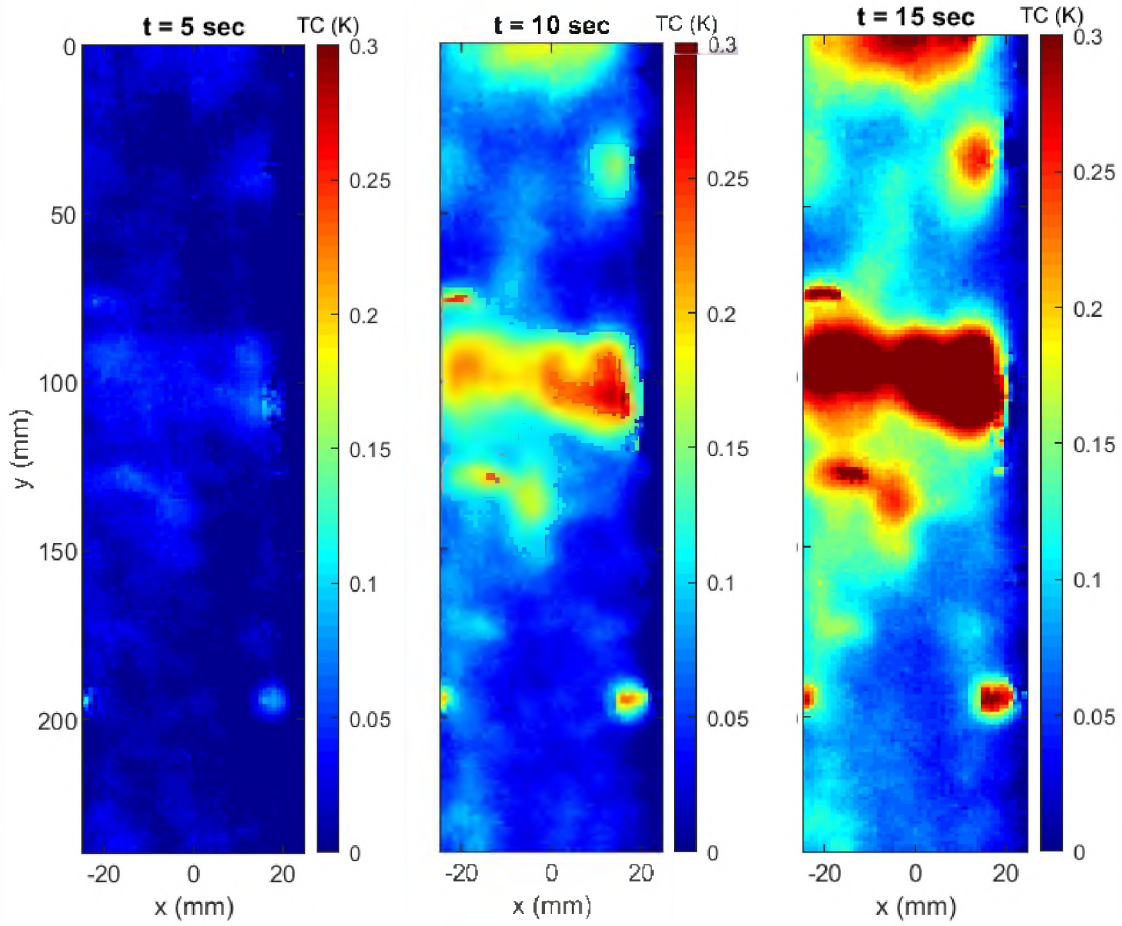


Figure 6. $TC_I$ response of Specimen AMT-CFRP-D-1 at 5 s, 10 s, and 15 s (Units in K and mm).

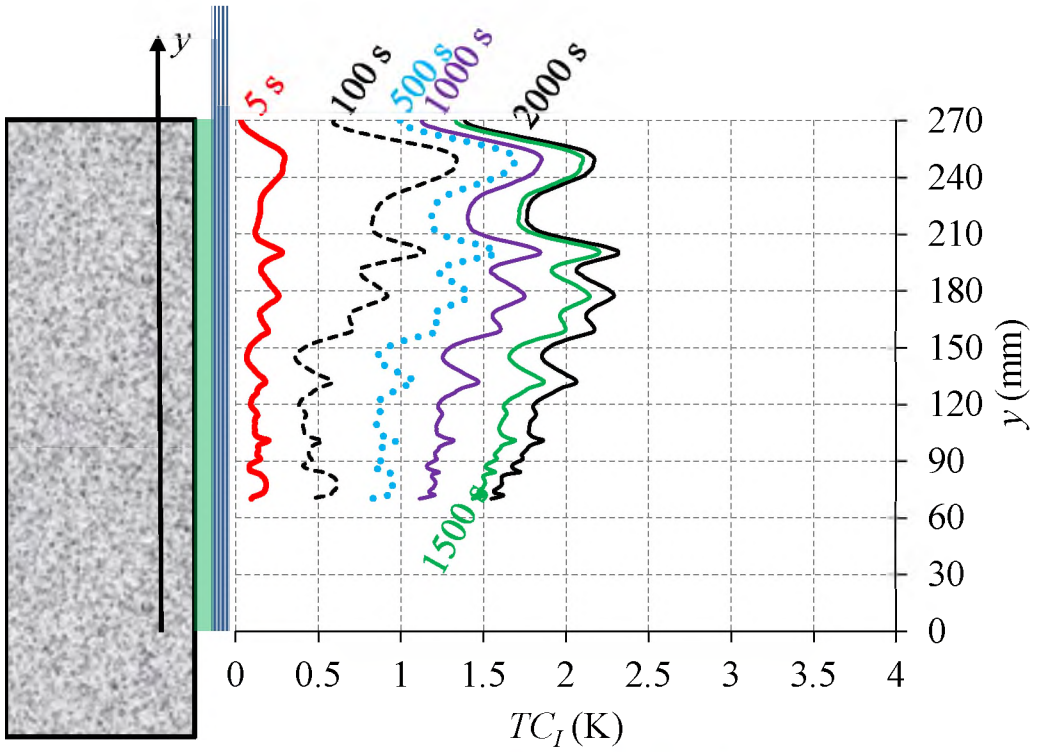


(a)

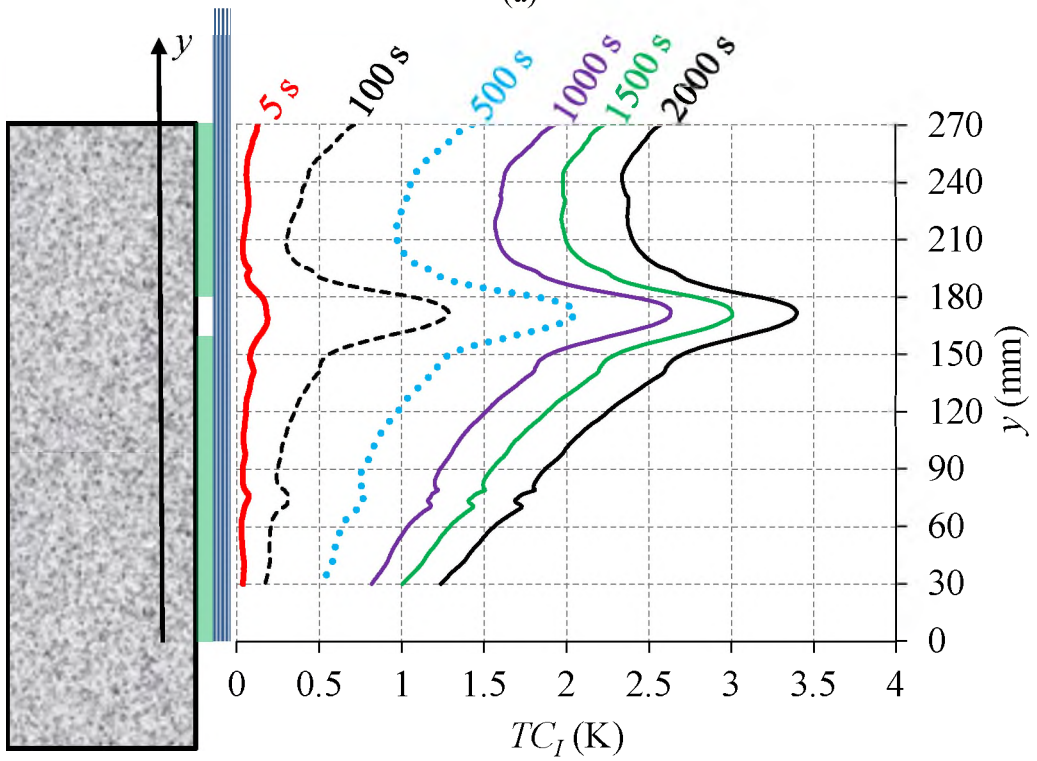


(b)

Figure 7. Average $TC_I$ distribution among $y$ direction for specimen (a) AMT-CFRP-2, and (b) AMT-CFRP-D-1.

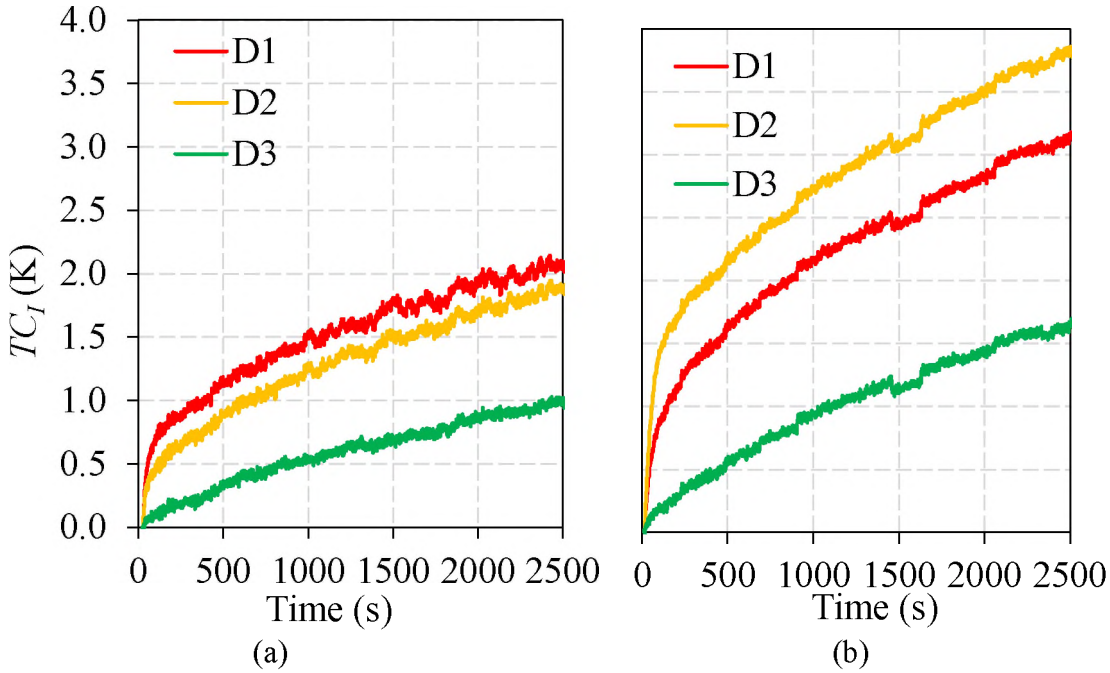


Figure 8. Time-history $TC_1$ responses in Stage-I of Specimen: (a) AMT-CFRP-2, and (b) AMT-CFRP-D-1.

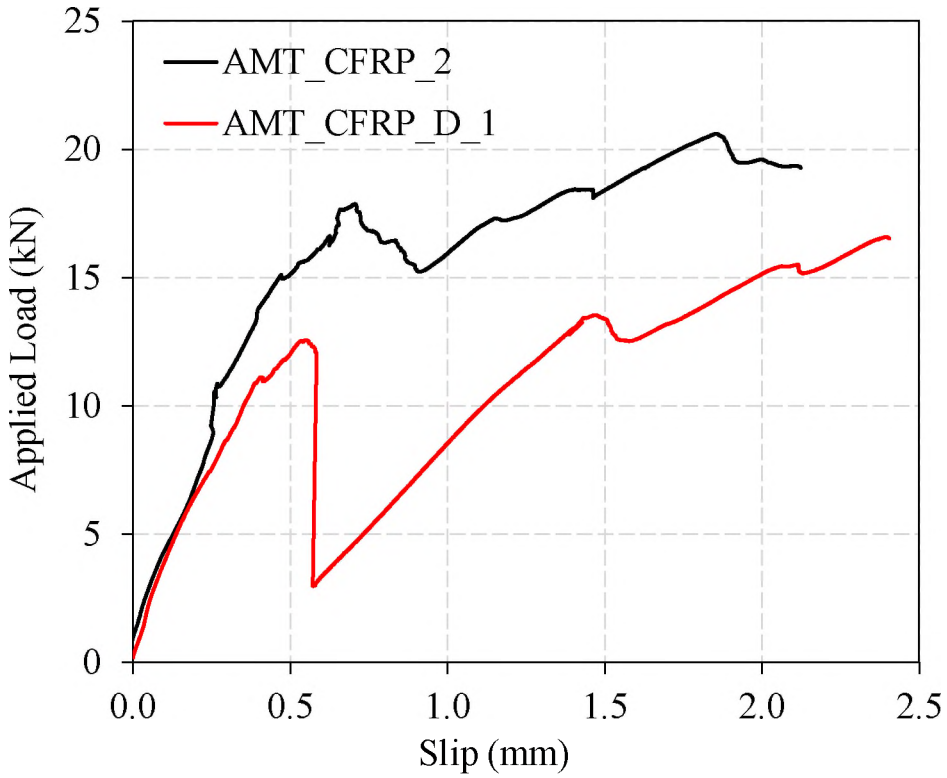


Figure 9. Load responses of the tested specimens.

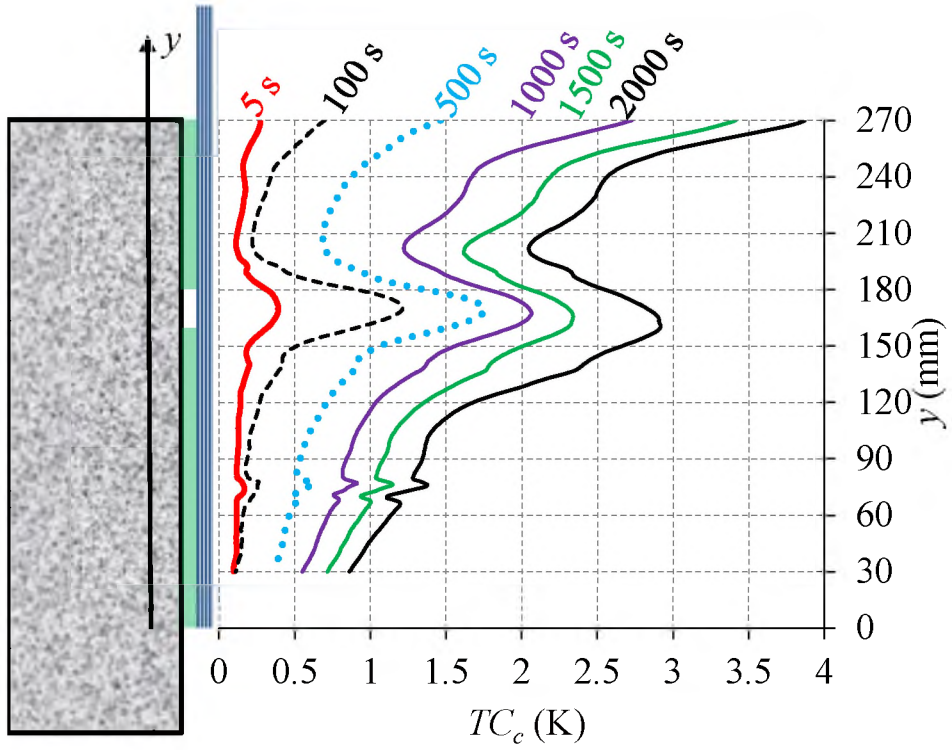


Figure 10. Average $TC_C$ distribution among y direction for specimen AMT-CFRP-D-1.

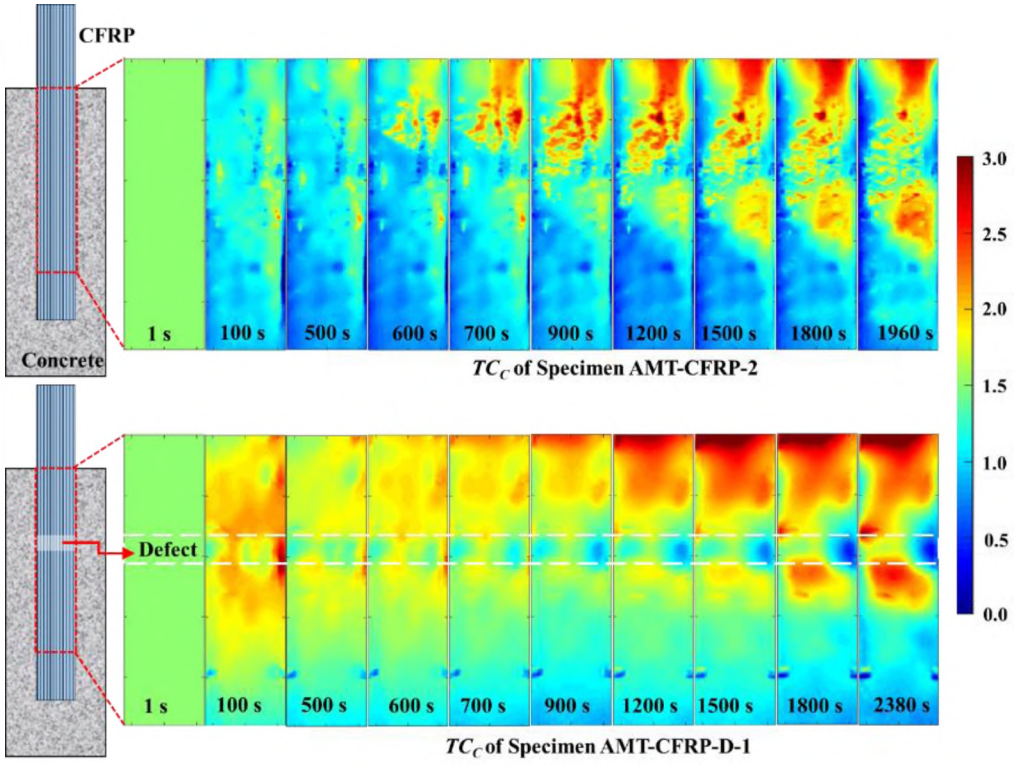


Figure 11. $TC_C$ response of specimens.

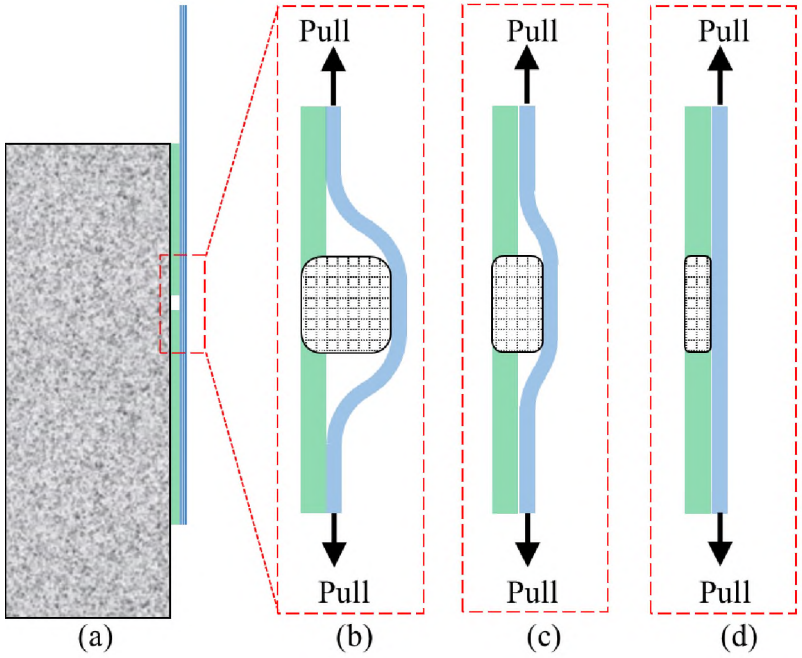


Figure 12. Illustration of the change of thickness of the defected area during loading for specimen AMT-CFRP-D-1.

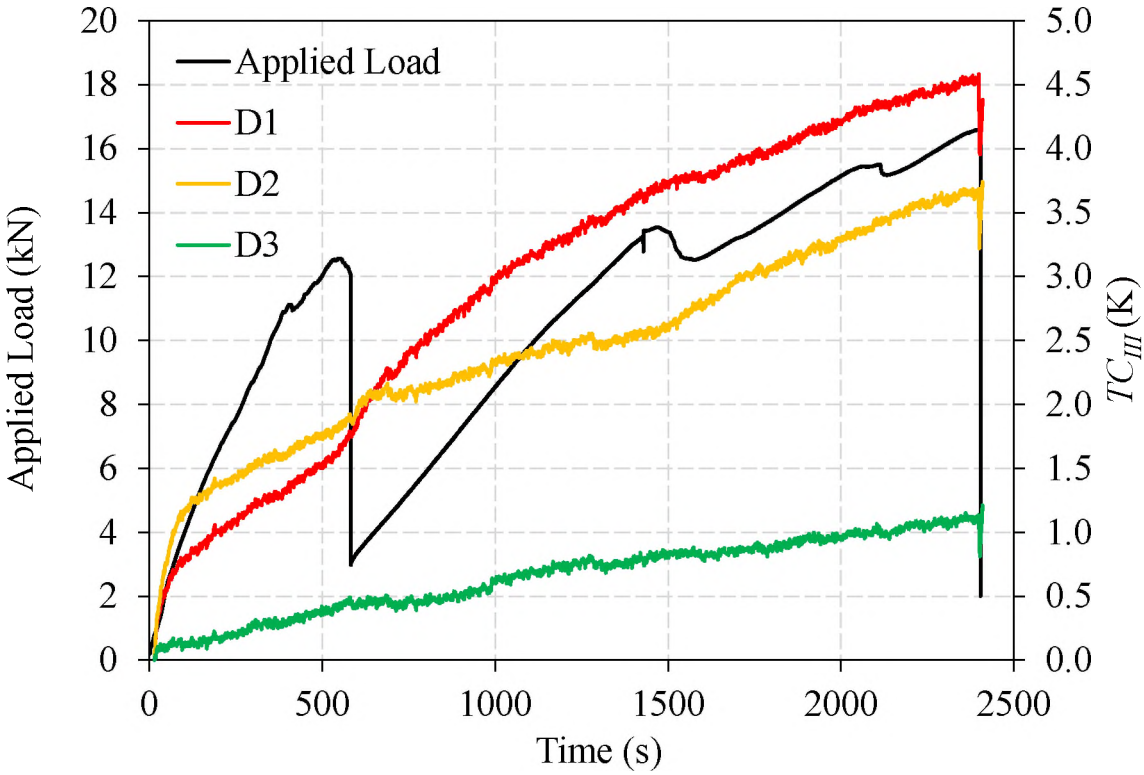


Figure 13. Correlation between applied load and $TC_{III}$ response for specimen AMT-CFRP-D-1.

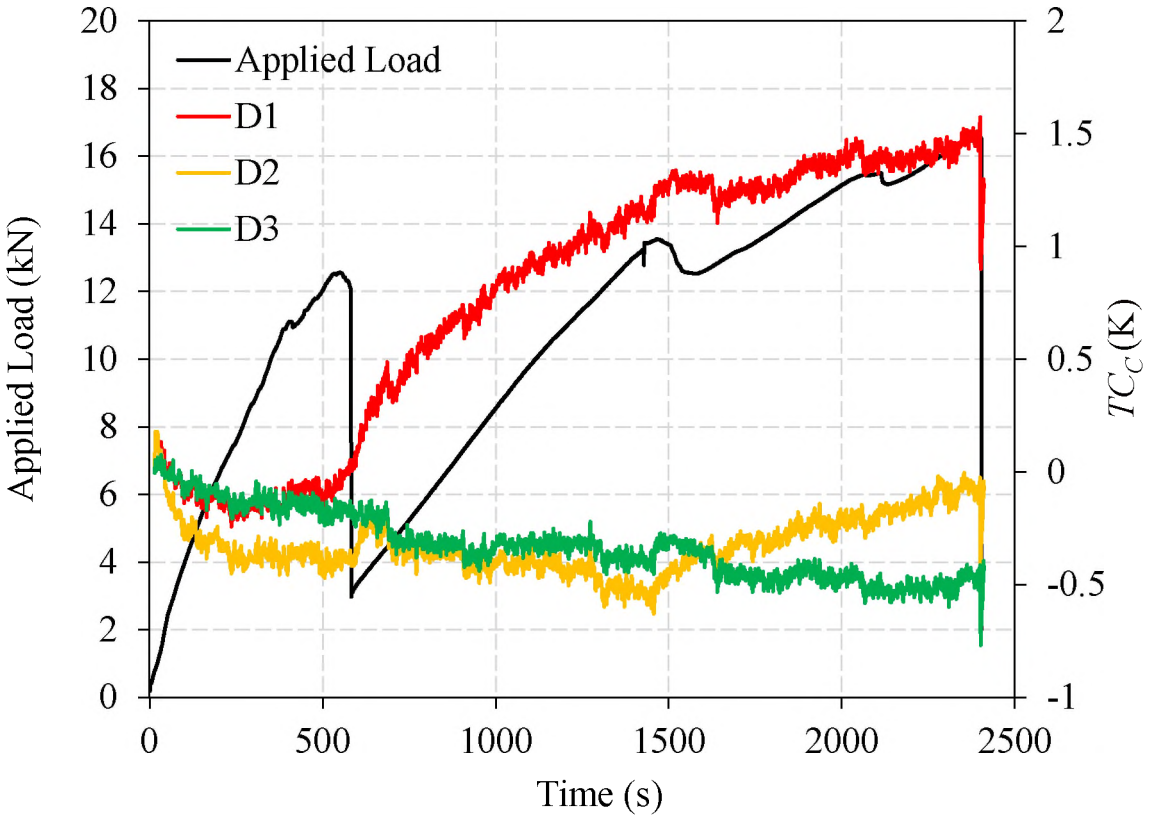


Figure 14. Correlation between applied load and $TC_C$ response for specimen AMT-CFRP-D-1.

Table 1. Thermal properties of materials.

| Material | $K_T$ (W/m·K) | $C_T$ (J/g·K) | $\rho$ (kg/m$^3$) |
|---|---|---|---|
| Air | 0.026 | 1.005 | 1.204 |
| Epoxy | 1.0 | 3.7 | 1100 |
| Cementitious mortar | 1.7 | 0.8 | 2400 |
| CFRP‖ | 7 | 1.2 | 1600 |
| CFRP⊥ | 0.8 | 1.2 | 1600 |

Table 2. Parameters of single-lap shear test.

| Specimen | Initial Defect | $P^*$ (kN) | $g_{ult}$ (mm) |
|---|---|---|---|
| AMT-CFRP-2 | No | 20.61 | 2.12 |
| AMT-CFRP-D-2 | Air | 16.59 | 2.40 |

# REFERENCES

[1] Hollaway, L. C. (2010). A review of the present and future utilisation of FRP composites in the civil infrastructure with reference to their important in-service properties. Construction and Building Materials, 24(12), 2419-2445.

[2] Yazdani, N., Beneberu, E., & Riad, M. (2019). Nondestructive Evaluation of FRP-Concrete Interface Bond due to Surface Defects. Advances in Civil Engineering, 2019.

[3] Ekenel, M., & Myers, J. J. (2007). Nondestructive evaluation of RC structures strengthened with FRP laminates containing near-surface defects in the form of delaminations. Science and Engineering of Composite Materials, 14(4), 299-316.

[4] Fallahpour, M., & Zoughi, R. (2015). Fast 3-D qualitative method for through-wall imaging and structural health monitoring. IEEE Geoscience and Remote Sensing Letters, 12(12), 2463-2467.

[5] Kharkovsky, S., Ryley, A. C., Stephen, V., & Zoughi, R. (2007). Dual-polarized near-field microwave reflectometer for noninvasive inspection of carbon fiber reinforced polymer-strengthened structures. IEEE Transactions on Instrumentation and Measurement, 57(1), 168-175.

[6] Ricci, M., Senni, L., & Burrascano, P. (2012). Exploiting pseudorandom sequences to enhance noise immunity for air-coupled ultrasonic nondestructive testing. IEEE Transactions on Instrumentation and Measurement, 61(11), 2905-2915.

[7] Taillade, F., Quiertant, M., Benzarti, K., & Aubagnac, C. (2011). Shearography and pulsed stimulated infrared thermography applied to a nondestructive evaluation of FRP strengthening systems bonded on concrete structures. Construction and Building Materials, 25(2), 568-574.

[8] Taillade, F., Quiertant, M., Benzarti, K., Dumoulin, J., & Aubagnac, C. (2012). Nondestructive evaluation of FRP strengthening systems bonded on RC structures using pulsed stimulated infrared thermography. In Infrared thermography. IntechOpen.

[9] Valluzzi, M. R., Grinzato, E., Pellegrino, C., & Modena, C. (2009). IR thermography for interface analysis of FRP laminates externally bonded to RC beams. Materials and Structures, 42(1), 25-34.

[10] Halabe, U. B., Vasudevan, A., Klinkhachorn, P., & GangaRao, H. V. (2007). Detection of subsurface defects in fiber reinforced polymer composite bridge decks using digital infrared thermography. Nondestructive Testing and Evaluation, 22(2-3), 155-175.

[11] Shih, J. K. C., Tann, D. B., Hu, C. W., Delpak, R., & Andreou, E. (2003). Remote sensing of air blisters in concrete–FRP bond layer using IR thermography. International Journal of Materials and Product Technology, 19(1-2), 174-187.

[12] Galietti, U., Luprano, V., Nenna, S., Spagnolo, L., & Tundo, A. (2007). Non-destructive defect characterization of concrete structures reinforced by means of FRP. Infrared physics & technology, 49(3), 218-223.

[13] Górski, M., Krzywoń, R., Białozor, R., Białecki, R., Adamczyk, W., & Ostrowski, Z. (2019). IRT research on influence of long-term loads on defects in FRP strengthened RC beams. In MATEC Web of Conferences (Vol. 262, p. 08002). EDP Sciences.

[14] Foudazi, A., Edwards, C. A., Ghasr, M. T., & Donnell, K. M. (2016). Active microwave thermography for defect detection of CFRP-strengthened cement-based materials. IEEE Transactions on Instrumentation and Measurement, 65(11), 2612-2620.

[15] Keo, S. A., Brachelet, F., Breaban, F., & Defer, D. (2014). Steel detection in reinforced concrete wall by microwave infrared thermography. Ndt & E International, 62, 172-177.

[16] Mirala, A., Foudazi, A., Ghasr, M. T., & Donnell, K. M. (2018). Detection of Flat-Bottom Holes in Conductive Composites Using Active Microwave Thermography. Journal of Nondestructive Evaluation, Diagnostics and Prognostics of Engineering Systems, 1(4).

[17] Foudazi, A., Mirala, A., Ghasr, M. T., & Donnell, K. M. (2018). Active Microwave Thermography for Nondestructive Evaluation of Surface Cracks in Metal Structures. IEEE Transactions on Instrumentation and Measurement, (99), 1-10.

[18] Foudazi, A., Mehdipour, I., Donnell, K. M., & Khayat, K. H. (2016). Evaluation of steel fiber distribution in cement-based mortars using active microwave thermography. Materials and Structures, 49(12), 5051-5065.

[19] Layssi, H., Ghods, P., Alizadeh, A. R., & Salehi, M. (2015). Electrical resistivity of concrete. Concrete International, 37(5), 41-46.

[20] Foudazi, A., Edwards, C., Ghasr, M. T., Sneed, L. H., & Donnell, K. M. (2019). Active Microwave Thermography for Evaluation of FRP-Rehabilitated Cement-Based Structures. Materials Evaluation, 77(6), 810-821.

[21] https://www.aegion.com/-/media/Aegion2017/Files/Literature/Fyfe/Tyfo%20SCH-41%20Composite.ashx?la=en (Accessed on August 21, 2019)

[22] https://assets.master-builders-solutions.basf.com/en-my/basf-masterbrace-p3500-tds.pdf (Accessed on August 21, 2019)

[23] https://assets.master-builders-solutions.basf.com/en-bd/basf-masterbrace-4500-v1-tds.pdf (Accessed on August 21, 2019)

[24] ASTM C39/C39M-17b. (2017). Standard test method for compressive strength of cylindrical concrete specimens. West Conshohocken, Pam: ASTM International.

[25] ASTM C496/C496M. (2017). Standard Test Method for Splitting Tensile Strength of Cylindrical Concrete Specimens; ASTM International: West Conshohocken, PA, USA, 2011.

[26] Mirala, A., Zou, X., Ghasr, M. T., Sneed, L., & Donnell, K. M. (2019, May). Active Microwave Thermography: A Real-Time Monitoring Tool for CFRP-Concrete Bond Testing. In 2019 IEEE International Instrumentation and Measurement Technology Conference (I2MTC) (pp. 1-6). IEEE.

# SECTION

# 2. SUMMARY, CONCLUSIONS, AND RECOMMENDATIONS

## 2.1. SUMMARY OF RESEARCH WORK

The aim of this research was to study the bond behavior of the fiber reinforced composite-concrete interface. Analytical derivations, numerical simulations, and experimental tests are the main tools to solve the above problem. The scope of work includes the following six tasks:

1. An analytical procedure was developed to determine the bond-slip relationship of FRCM-concrete joints that fail due to debonding at the matrix–fiber interface and to determine expressions to predict key values of load and slip based on discrete measurements of longitudinal fiber strain. Experimental results from single-lap shear test specimens of FRCM-concrete joints with strain gauges mounted on the longitudinal fiber bundles along the composite bonded length were used to calibrate the model.

2. An indirect approach was developed to determine the simplified bond-slip relationship of FRCM-concrete joints tested in direct shear. Specifically, analytical equations were derived to predict the full-range load response of FRCM-concrete joints by adopting a trilinear bond-slip relationship consisting of a linear-elastic branch, a softening branch, and a friction branch. Closed-form solutions of the interfacial slip, shear stress, and axial stress (or strain) distribution along the bonded length were provided. Experimental results were used to calibrate the parameters of the assumed simplified bond-slip relationship.

3. A numerical method was developed that is capable of validating the analytical solutions for FRP/FRCM-concrete joints using different bond-slip models (e.g., bilinear, trilinear, exponential, and others) and predicting the results when analytical solutions were not available for other bond-slip models.

4. The bond-slip relationship of the SRP-concrete interface was experimentally and analytically determined. The debonding load and effective bond length were determined.

5. The use of AMT to study the initiation and propagation of interfacial debonding in CFRP-concrete joints subjected to mechanical loading was explored.

6. The use of AMT to study the effect of initial defects on the initiation and propagation of interfacial debonding in CFRP-concrete joints subjected to mechanical loading was studied.

## 2.2. CONCLUSIONS

This section summarizes the conclusions from the experimental, numerical, and analytical studies on bond behavior of advanced composite – concrete joints. With respect to the strain-based analytical results of FRCM-concrete joints, the following conclusions are presented:

1. The strain profiles of FRCM-concrete joints can be described by the continuous function $\varepsilon(y)$. Based on the proposed equation, the peak load and the debonding load and the corresponding global slips can be predicted with good agreement.

2. The bond–slip model of FRCM-concrete joints can be represented by a continuous, closed-form function. Based on the continuous closed-form function, the fracture energy can be predicted at a good accuracy.

With respect to the analytical results of FRCM-concrete joints using a trilinear bond-slip model, the following conclusions are presented:

1. The applied load-global slip behavior for long bonded lengths features an elastic stage, an elastic-softening stage, an elastic-softening-debonding stage, a softening-debonding stage, and a debonding stage. For bonded lengths less than the fully established softening length, the third stage is a pure softening stage.

2. The trilinear $\tau(s)$ provides closed-form solutions for the debonding and peak loads and corresponding slips at the composite free and loaded ends.

3. The analytical solution is in good agreement with strain and peak load results of test specimens reported in the literature, as well as with the numerical results obtained using a finite difference method (FDM).

4. Results obtained by an inverse determination of the parameters in the trilinear bond-slip relationship using the experimental load-slip response as input of the neural network were in good agreement with the experimental load responses.

5. An approximate solution for the minimum length needed to develop the snap-back phenomenon was derived.

6. The effective bond length determined using the analytical approach was in good agreement with experimental results reported in the literature.

With respect to the experimental and analytical results based on SRP-concrete single-lap shear tests, the following conclusions are presented:

1. Specimens with low density fibers tended to fail in fiber rupture, whereas specimens with medium density fibers tended to fail in composite debonding. Debonding

occurred due to fracture of the concrete within a thin layer beneath the SRP strip, similar to the behavior of FRP-concrete joints.

2. The maximum load increased with the bonded length to a constant value. By fitting the maximum load-bonded length relationship, a nonlinear bond-slip relationship was obtained with a maximum shear stress of 4.386 MPa and a corresponding slip of 0.0915 mm. The full range load response was in reasonable agreement with the experimental results.

3. The effective bond length is approximately 118 mm for specimens with medium density fibers.

4. A database of 198 SRP-concrete joints was established from the results of this study and supplemented with others collected from the literature. Existing equations derived for FRP-concrete debonding behavior showed reasonable prediction of the maximum load with an error less than 10%.

5. Nearly all of the selected equations for FRP composites underestimated the effective bonded length for the specimens with MD fibers that failed in debonding.

With respect to the experimental study of using AMT as a NDE method to detect the CFRP-concrete interfacial debonding, the following conclusions are presented:

1. Four strong correlations between interfacial slip and CFRP outer surface thermal contrast were found, which showed that the AMT can detect the interfacial damage caused by load;

2. At the beginning of loading, dense thermal contrast occurred within the areas close to loaded end where interfacial debonding initiates.

3. With the increase of load, the interfacial debonded area transferred towards the free end which correlated well with the local thermal contrast of CFRP surface.

4. The slope of the thermal contrast at the CFRP surface suddenly changed when there was a load drop, which indicates a local debonding occurrence or mobilization.

5. At different loading moments, the slip and thermal contrast distributions along the bonded area all show positive correlations.

6. These correlations indicate that the initiation and propagation of CFRP-concrete interfacial damage can be monitored by AMT.

With respect of the experimental study of using AMT as a NDE method to detect initial defects and the progression of CFRP-concrete interfacial debonding with defects, the following conclusions are presented:

1. The AMT technology can detect the man-made defect in 10 s heating.

2. For the specimen without man-made defect, at the beginning of loading, dense $TC_c$ responses occurred within the areas close to loaded end where interfacial debonding initiates. With the increase of load, the interfacial debonded area transferred towards the free end which correlated well with the local temperature contrast of CFRP surface.

3. The presence of an initial defect changes the debonding process by reducing the load capacity, and making the load drop caused by local debonding more severe.

4. Temperature contrast in loading stage and relative temperature contrast can both be used to correlate with the load response.

## 2.3. RECOMMENDATIONS

Based on the objective and scope of work of this study, the following aspects are recommended for future research:

1. Different types of strain measurements could be applied to obtain the data of axial strain of fibers in FRCM-concrete joints. For example, the use of optical fibers to provide continuous strain measurements along the bonded length should be explored.
2. Experimental data related to short bonded length FRCM-concrete joints are scare. More data are needed to provide validation of analytical results of load responses of specimens with short bonded length.
3. More shear tests on SRP-concrete joints should be conducted to validate the equations to predict the responses of FRP-concrete joints, especially those with fiber sheet densities larger than those studied in this work.
4. Further investigations are needed to develop AMT to provide a more uniform electromagnetic heating pattern, so the initial heat stage can become unnecessary.
5. The mixed failure mode of concrete cracking and interfacial debonding should be separately researched by AMT.

# REFERENCES

ASTM C496/C496M. (2017). Standard Test Method for Splitting Tensile Strength of Cylindrical Concrete Specimens; ASTM International: West Conshohocken, PA, USA, 2011.

ACI 440.2R-17 (2017) Guide for the Design and Construction of Externally Bonded FRP Systems for Strengthening Concrete Structures, American Concrete Institute, Farmington Hills

ACI Committee 549. (2013). Guide to Design and construction of externally bonded fabric-reinforced cementitious matrix (FRCM) systems for repair and strengthening concrete and masonry structures, ACI 549.4R-13, American Concrete Institute, Farmington Hills, USA.

Alabdulhady, M. Y., & Sneed, L. H. (2019). Torsional strengthening of reinforced concrete beams with externally bonded composites: A state of the art review. Construction and Building Materials, 205, 148-163.

Alabdulhady, M. Y., Sneed, L. H., & Carloni, C. (2017). Torsional behavior of RC beams strengthened with PBO-FRCM composite–An experimental study. Engineering Structures, 136, 393-405.

Alecci, V., Focacci, F., Rovero, L., Stipo, G., & De Stefano, M. (2016). Extrados strengthening of brick masonry arches with PBO–FRCM composites: Experimental and analytical investigations. Composite Structures, 149, 184-196.

Ameli, M., Ronagh, H. R., & Dux, P. F. (2007). Behavior of FRP strengthened reinforced concrete beams under torsion. Journal of Composites for Construction, 11(2), 192-200.

Ascione, F., Lamberti, M., Napoli, A., Razaqpur, G., and Realfonzo, R. (2017). An experimental investigation on the bond behavior of steel reinforced polymers on concrete substrate. Composite Structures, 181, 58-72.

ASTM C39/C39M-17b. (2017). Standard test method for compressive strength of cylindrical concrete specimens. West Conshohocken, Pam: ASTM International.

Attari, N., Amziane, S., & Chemrouk, M. (2012). Flexural strengthening of concrete beams using CFRP, GFRP and hybrid FRP sheets. Construction and Building Materials, 37, 746-757.

Awani, O., El Refai, A., & El-Maaddawy, T. (2015). Bond characteristics of carbon fabric-reinforced cementitious matrix in double shear tests. Construction and Building Materials, 101, 39-49.

Awani, O., El Refai, A., El-Maaddawy, T. (2015). Bond characteristics of carbon fabric-reinforced cementitious matrix in double shear tests. Constr Build Mater 2015; 101:39-49.

Azam, R., & Soudki, K. (2014). FRCM strengthening of shear-critical RC beams. Journal of Composites for Construction, 18(5), 04014012.

Babaeidarabad S., Loreto G, & Nanni A. (2014). Flexural strengthening of RC beams with an externally bonded fabric-reinforced cementitious matrix. Journal of Composites for Construction,18(5), 04014009.

Bakis, C.E., Bank, L.C., Brown, V., Cosenza, E., Davalos, J.F., Lesko, J.J., Machida, A., Rizkalla, S.H. & Triantafillou, T.C., (2002). Fiber-reinforced polymer composites for construction-State-of-the-art review. Journal of composites for construction, 6(2), 73-87.

Bamforth, P., Chisholm, D., Gibbs, J., & Harrison, T. (2008). Properties of concrete for use in Eurocode 2.

Bellini, A., Shahreza, S. K., Mazzotti, C. Cyclic bond behavior of FRCM composites applied on masonry substrate. Compos B Eng 2019; 169:189-199.

Bilotta, A., Ceroni, F., Lignola, G. P., & Prota, A. (2017). Use of DIC technique for investigating the behaviour of FRCM materials for strengthening masonry elements. Composites Part B: Engineering.

Biscaia, H. C., Borba, I. S., Silva, C., and Chastre, C. A nonlinear analytical model to predict the full-range debonding process of FRP-to-parent material interfaces free of any mechanical anchorage devices. Compos Struct, 2016; 138: 52-63.

Biscaia, H. C., Chastre, C., Silva, C., and Franco, N. Mechanical response of anchored FRP bonded joints: a nonlinear analytical approach. Mech Adv Mater Struct, 2018; 25(3): 238-52.

Biscaia, H. C., Chastre, C., Silva, M. A. Linear and nonlinear analysis of bond-slip models for interfaces between FRP composites and concrete. Compos B Eng 2013; 45(1):1554-1568.

Blanksvärd, T., Täljsten, B., & Carolin, A. (2009). Shear strengthening of concrete structures with the use of mineral-based composites. Journal of Composites for Construction, 13(1), 25-34.

Bournas, D. A., Lontou, P. V., Papanicolaou, C. G., & Triantafillou, T. C. (2007). Textile-reinforced mortar versus fiber-reinforced polymer confinement in reinforced concrete columns. ACI Structural Journal, 104(6), 740.

Brückner, A., Ortlepp, R., & Curbach, M. (2008). Anchoring of shear strengthening for T-beams made of textile reinforced concrete (TRC). Materials and Structures, 41(2), 407-418.

Caggegi, C., Sciuto, D., & Cuomo, M. (2018). Experimental study on effective bond length of basalt textile reinforced mortar strengthening system: Contributions of digital image correlation. Measurement, 129, 119-127.

Calabrese A. S., Colombi P., D'Antino T. Analytical solution of the bond behavior of FRCM composites using a rigid-softening cohesive material law. Compos B Eng 2019; 174:107051.

Carloni C, Focacci F. FRP-masonry interfacial debonding: An energy balance approach to determine the influence of the mortar joints, Eur J Mech A/Solids 2016; 55:122-133.

Carloni C., D'Antino T., Sneed L. H., Pellegrino C. 3-D numerical modeling of single-lap direct shear tests of FRCM-concrete joints using a cohesive contact damage approach. J Compos Constr. 2017; 22(1): 04017048.

Carloni, C., & Subramaniam, K. V. (2010). Direct determination of cohesive stress transfer during debonding of FRP from concrete. Composite Structures, 93(1), 184-192.

Carloni, C., & Subramaniam, K. V. (2012). Application of fracture mechanics to debonding of FRP from RC members. Special Publication, 286, 1-16.

Carloni, C., D'Antino, T., Sneed, L. H., & Pellegrino, C. (2014). Role of the matrix layers in the stress-transfer mechanism of FRCM composites bonded to a concrete substrate. Journal of Engineering Mechanics, 141(6), 04014165.

Carloni, C., Santandrea, M., & Imohamed, I. A. O. (2017). Determination of the interfacial properties of SRP strips bonded to concrete and comparison between single-lap and notched beam tests. Engineering Fracture Mechanics, 186, 80-104.

Carloni, C., Sneed, L.H., & D'Antino, T. (2013). Interfacial bond characteristics of fiber reinforced concrete mortar for external strengthening of reinforced concrete members. In: FraMCos-8, 8th International Conference on Fracture Mechanics of Concrete and Concrete Structures, Toledo, Spain, 1-9.

Carloni, C., Subramaniam, K. V. Application of fracture mechanics to debonding of FRP from RC members. ACI SP 2012; 286:1-16.

Carozzi, F. G., Colombi, P., Fava, G., Poggi, C. A cohesive interface crack model for the matrix–textile debonding in FRCM composites. Compos Struct 2016; 143:230-241.

Carrara, P., Ferretti, D., Freddi, F., Rosati, G. Shear tests of carbon fiber plates bonded to concrete with control of snap-back. Eng Fract Mech 2011; 78(15):2663-2678.

Casadei, P., Nanni, A., Alkhrdaji, T., & Thomas, J. (2005). Performance of double-T prestressed concrete beams strengthened with steel reinforcement polymer. Advances in Structural Engineering, 8(4), 427-442.

Chen, G. M., Chen, J. F., & Teng, J. G. (2012). Behaviour of FRP-to-concrete interfaces between two adjacent cracks: A numerical investigation on the effect of bondline damage. Construction and building materials, 28(1), 584-591.

Chen, J. F., & Teng, J. G. (2001). Anchorage strength models for FRP and steel plates bonded to concrete. Journal of structural engineering, 127(7), 784-791.

Chen, W., Pham, T. M., Sichembe, H., Chen, L., & Hao, H. (2018). Experimental study of flexural behaviour of RC beams strengthened by longitudinal and U-shaped basalt FRP sheet. Composites Part B: Engineering, 134, 114-126.

Colombi P., Fava G., Poggi C. End debonding of CFRP wraps and strips for the strengthening of concrete structures. Comp Struct 2014; 111:510-521.

Cromwell, J. R., Harries, K. A., & Shahrooz, B. M. (2011). Environmental durability of externally bonded FRP materials intended for repair of concrete structures. Construction and Building Materials, 25(5), 2528-2539.

D'Ambrisi, A., Feo, L., & Focacci, F. (2013). Experimental analysis on bond between PBO-FRCM strengthening materials and concrete. Composites Part B:

D'Ambrisi, A., Feo, L., Focacci, F. (2012). Bond-slip relations for PBO-FRCM materials externally bonded to concrete. Compos B Eng 2012; 43(8):2938-2949.

D'Ambrisi, A., Focacci, F. Flexural strengthening of RC beams with cement-based composites. J Compos Constr 2011; 15(5):707-720.

D'Ambrisi, A., Focacci, F., & Caporale, A. (2013). Strengthening of masonry–unreinforced concrete railway bridges with PBO-FRCM materials. Composite Structures, 102, 193-204.

D'Antino, T., Carloni, C., Sneed, L. H., & Pellegrino, C. (2014). Matrix–fiber bond behavior in PBO FRCM composites: A fracture mechanics approach. Engineering Fracture Mechanics, 117, 94-111.

D'Antino, T., Sneed, L. H., Carloni, C., & Pellegrino, C. (2016). Effect of the inherent eccentricity in single-lap direct-shear tests of PBO FRCM-concrete joints. Composite Structures, 142, 117-129.

D'Antino, T., Sneed, L.H., Carloni, C., & Pellegrino, C. (2015). Influence of the substrate characteristics on the bond behavior of FRCM-concrete joints. Construction and Building Materials, 101(1), 838-850.

Dai, J., Ueda, T., & Sato, Y. (2005). Development of the nonlinear bond stress–slip model of fiber reinforced plastics sheet–concrete interfaces with a simple method. Journal of composites for construction, 9(1), 52-62.

Dai, J., Ueda, T., & Sato, Y. (2006). Unified analytical approaches for determining shear bond characteristics of FRP-concrete interfaces through pullout tests. Journal of Advanced Concrete Technology, 4(1), 133-145.

D'Antino, T., Carozzi, F. G., Colombi, P., Poggi, C. Out-of-plane maximum resisting bending moment of masonry walls strengthened with FRCM composites. Compos Struct 2018; 202:881-896

D'Antino, T., Colombi, P., Carloni, C., & Sneed, L. H. (2018). Estimation of a matrix-fiber interface cohesive material law in FRCM-concrete joints. Composite Structures.

De Felice, G., De Santis, S., Garmendia, L., Ghiassi, B., Larrinaga, P., Lourenco, P. B., Oliveira, D. V., Paolacci, F., & Papanicolaou, C. G. (2014) Mortar-based systems for externally bonded strengthening of masonry. Materials and Structures, 47:2021-2037.

Djamai, Z. I., Bahrar, M., Salvatore, F., Larbi, A. S., El Mankibi, M. Textile reinforced concrete multiscale mechanical modelling: Application to TRC sandwich panels. Finite Elem Anal Des 2017; 135:22-35.

Donnini, J., De Caseo y Basalo, F., Corinaldesi, V., Lancioni, G., Nanni, A. Fabric-reinforced cementitious matrix behavior at high-temperature: Experimental and numerical results. Compos B Eng 2017; 108:108-121.

Donnini, J., Lancioni, G., Bellezze, T., Corinaldesi, V. (2017). Bond behavior of FRCM carbon yarns embedded in a cementitious matrix: Experimental and numerical results. Key Engineering Materials, 747, 305-312.

ECO Products of Kerakoll: products.kerakoll.com (accessed on Feb. 2020)

Ekenel, M., & Myers, J. J. (2007). Nondestructive evaluation of RC structures strengthened with FRP laminates containing near-surface defects in the form of delaminations. Science and Engineering of Composite Materials, 14(4), 299-316.

Fallahpour, M., & Zoughi, R. (2015). Fast 3-D qualitative method for through-wall imaging and structural health monitoring. IEEE Geoscience and Remote Sensing Letters, 12(12), 2463-2467.

Figeys, W., Schueremans, L., Brosens, K., & Van Gemert, D. (2005). Strengthening of concrete structures using steel wire reinforced polymer. ACI Special Publication, 230, 43.

Figeys, W., Schueremans, L., Van Gemert, D., & Brosens, K. (2008). A new composite for external reinforcement: Steel cord reinforced polymer. Construction and Building Materials, 22(9), 1929-1938.

Focacci, F., D'Antino, T., Carloni, C., Sneed, L. H., & Pellegrino, C. (2017). An indirect method to calibrate the interfacial cohesive material law for FRCM-concrete joints. Materials & Design, 128, 206-217.

Focacci, F., D'Antino, T., Carloni, C., Sneed, L. H., Pellegrino, C. An indirect method to calibrate the interfacial cohesive material law for FRCM-concrete joints. Mater Des 2017; 128:206-217.

Focacci, F., Nanni, A., Bakis, C. E. Local bond-slip relationship for FRP reinforcement in concrete. J Compos Constr 2000; 4(1):24-31.

Foudazi, A., Edwards, C. A., Ghasr, M. T., & Donnell, K. M. (2016). Active microwave thermography for defect detection of CFRP-strengthened cement-based materials. IEEE Transactions on Instrumentation and Measurement, 65(11), 2612-2620.

Foudazi, A., Edwards, C., Ghasr, M. T., Sneed, L. H., & Donnell, K. M. (2019). Active Microwave Thermography for Evaluation of FRP-Rehabilitated Cement-Based Structures. Materials Evaluation, 77(6), 810-821.

Foudazi, A., Mehdipour, I., Donnell, K. M., & Khayat, K. H. (2016). Evaluation of steel fiber distribution in cement-based mortars using active microwave thermography. Materials and Structures, 49(12), 5051-5065.

Foudazi, A., Mirala, A., Ghasr, M. T., & Donnell, K. M. (2018). Active Microwave Thermography for Nondestructive Evaluation of Surface Cracks in Metal Structures. IEEE Transactions on Instrumentation and Measurement, (99), 1-10.

Galietti, U., Luprano, V., Nenna, S., Spagnolo, L., & Tundo, A. (2007). Non-destructive defect characterization of concrete structures reinforced by means of FRP. Infrared physics & technology, 49(3), 218-223.

Genest, M., and Li, G. (2018). Induction thermography of steel coupons with cracks. Applied optics, 57(18), 40-48.

GOM: https://www.gom.com/3d-software/gom-correlate-professional.html (Accessed Feb. 2020)

Gonzalez-Libreros, J. H., Sabau, C., Sneed, L. H., Pellegrino, C., & Sas, G. (2017). State of research on shear strengthening of RC beams with FRCM composites. Construction and Building Materials, 149, 444-458.

Gonzalez-Libreros, J. H., Sneed, L. H., D'antino, T., & Pellegrino, C. (2017). Behavior of RC beams strengthened in shear with FRP and FRCM composites. Engineering Structures, 150, 830-842.

Gonzalez-Libreros, J. H., Sneed, L. H., D'Antino, T., Pellegrino, C. Behavior of RC beams strengthened in shear with FRP and FRCM composites. Eng Struct 2017; 150:830-842.

Gonzalez-Libreros, J., D'Antino, T., & Pellegrino, C. (2017). Experimental Behavior of Glass-FRCM Composites Applied onto Masonry and Concrete Substrates. Key Engineering Materials, 747, 390-397.

Górski, M., Krzywoń, R., Białozor, R., Białecki, R., Adamczyk, W., & Ostrowski, Z. (2019). IRT research on influence of long-term loads on defects in FRP strengthened RC beams. In MATEC Web of Conferences (Vol. 262, p. 08002). EDP Sciences.

Górski, M., Krzywon, R., Dawczynski, S., & Greppi, R. (2013) Structural strengthenings based on SRP and SRG composites. International Conference on Engineering UBI, Nov 27-29, University of Beira Interior - Covilhã, Portugal.

Grelle, S. V., & Sneed, L. H. (2013). Review of anchorage systems for externally bonded FRP laminates. International Journal of Concrete Structures and Materials, 7(1), 17-33.

Halabe, U. B., Vasudevan, A., Klinkhachorn, P., & GangaRao, H. V. (2007). Detection of subsurface defects in fiber reinforced polymer composite bridge decks using digital infrared thermography. Nondestructive Testing and Evaluation, 22(2-3), 155-175.

He, L., Wu, Y. F., & Xiao, Y. (2014). Analytical solution for externally bonded joints considering snap-back. Journal of Composites for Construction, 19(5), 04014077.

He, R., Grelle, S., Sneed, L. H., & Belarbi, A. (2013). Rapid repair of a severely damaged RC column having fractured bars using externally bonded CFRP. Composite Structures, 101, 225-242.

He, Y., Tian, G., Pan, M., and Chen, D. (2014). Impact evaluation in carbon fiber reinforced plastic (CFRP) laminates using eddy current pulsed thermography. Composite Structures, 109, 1-7.

Hii, A. K., & Al-Mahaidi, R. (2007). Torsional capacity of CFRP strengthened reinforced concrete beams. Journal of Composites for Construction, 11(1), 71-80.

Hollaway, L. C. (2010). A review of the present and future utilisation of FRP composites in the civil infrastructure with reference to their important in-service properties. Construction and Building Materials, 24(12), 2419-2445.

Hong, X., Lin, J., Liu, Y., & Xu, W. (2018). Active Thermal Sensing for Bonding Structure Damage Detection of Hidden Frame Glass Curtain Wall. Sensors, 18(11), 3594.

https://assets.master-builders-solutions.basf.com/en-bd/basf-masterbrace-4500-v1-tds.pdf (Accessed on August 21, 2019)

https://assets.master-builders-solutions.basf.com/en-my/basf-masterbrace-p3500-tds.pdf (Accessed on August 21, 2019)

https://www.aegion.com/-/media/Aegion2017/Files/Literature/Fyfe/Tyfo%20SCH-41%20Composite.ashx?la=en (Accessed on August 21, 2019)

Keo, S. A., Brachelet, F., Breaban, F., & Defer, D. (2014). Steel detection in reinforced concrete wall by microwave infrared thermography. Ndt & E International, 62, 172-177.

Khalifa, A., & Nanni, A. (2000). Improving shear capacity of existing RC T-section beams using CFRP composites. Cement and Concrete Composites, 22(3), 165-174.

Khalifa, A., Gold, W. J., Nanni, A., & MI, A. A. (1998). Contribution of externally bonded FRP to shear capacity of RC flexural members. Journal of composites for construction, 2(4), 195-202.

Kharkovsky, S., Ryley, A. C., Stephen, V., & Zoughi, R. (2007). Dual-polarized near-field microwave reflectometer for noninvasive inspection of carbon fiber reinforced polymer-strengthened structures. IEEE Transactions on Instrumentation and Measurement, 57(1), 168-175.

Kim, Y. J., Fam, A., Kong, A., & El-Hacha, R. (2005). Flexural strengthening of RC beams using steel reinforced polymer (SRP) composites. ACI Special Publication, 230, 93.

Layssi, H., Ghods, P., Alizadeh, A. R., & Salehi, M. (2015). Electrical resistivity of concrete. Concrete International, 37(5), 41-46.

Li, J., Lu, Y., Guan, R., & Qu, W. (2017). Guided waves for debonding identification in CFRP-reinforced concrete beams. Construction and Building Materials, 131, 388-399.

Lin, J. P., & Wu, Y. F. (2016). Numerical analysis of interfacial bond behavior of externally bonded FRP-to-concrete joints. Journal of Composites for Construction, 20(5), 04016028.

Lin, X., Zhang, Y. X. Evaluation of bond stress-slip models for FRP reinforcing bars in concrete. Compos Struct 2014; 107:131-141.

Liu, K., & Wu, Y. F. (2012). Analytical identification of bond–slip relationship of EB-FRP joints. Composites Part B: Engineering, 43(4), 1955-1963.

Lopez, A., Galati, N., Alkhrdaji, T., & Nanni, A. (2007). Strengthening of a reinforced concrete bridge with externally bonded steel reinforced polymer (SRP). Composites Part B: Engineering, 38(4), 429-436.

Lu, X. Z., Teng, J. G., Ye, L. P., & Jiang, J. J. (2005). Bond–slip models for FRP sheets/plates bonded to concrete. Engineering structures, 27(6), 920-937.

Maeda, T., Asano, Y., Sato, Y., Ueda, T., & Kakuta, Y. (1997). ''A study on bond mechanism of carbon fiber sheet.'' Non-Metallic (FRP) Reinforcement for Concrete Struct., Proc., 3rd Int. Symp., Japan Concrete Institute, Sapporo, 1, 279–285.

Mahmoud, A. M., Ammar, H. H., Mukdadi, O. M., Ray, I., Imani, F. S., Chen, A., & Davalos, J. F. (2010). Non-destructive ultrasonic evaluation of CFRP–concrete specimens subjected to accelerated aging conditions. NDT & E International, 43(7), 635-641.

Malena, M. Closed-form solution to the debonding of mortar based composites on curved substrates. Compos B Eng 2018; 139:249-258.

Martin, L. B., Tijani, M., Hadj-Hassen, F. A new analytical solution to the mechanical behaviour of fully grouted rockbolts subjected to pull-out tests. Constr Build Mater 2011; 25(2):749-755.

Matana, M., Nanni, A., Dharani, L., Silva, P., & Tunis, G. (2005). Bond performance of steel reinforced polymer and steel reinforced grout. Proceedings of the International Symposium on Bond Behaviour of FRP in Structures, BBFS, 125-132).

Mirala, A., Foudazi, A., Ghasr, M. T., & Donnell, K. M. (2018). Detection of Flat-Bottom Holes in Conductive Composites Using Active Microwave Thermography. Journal of Nondestructive Evaluation, Diagnostics and Prognostics of Engineering Systems, 1(4), 041005.

Mirala, A., Foudazi, A., Ghasr, M. T., & Donnell, K. M. (2018). Detection of Flat-Bottom Holes in Conductive Composites Using Active Microwave Thermography. Journal of Nondestructive Evaluation, Diagnostics and Prognostics of Engineering Systems, 1(4).

Mirala, A., Zou, X., Ghasr, M. T., Sneed, L., & Donnell, K. M. (2019, May). Active Microwave Thermography: A Real-Time Monitoring Tool for CFRP-Concrete Bond Testing. In 2019 IEEE International Instrumentation and Measurement Technology Conference (I2MTC) (pp. 1-6). IEEE.

Mitolidis, G. J., Salonikios, T. N., & Kappos, A. J. (2008). Mechanical and Bond Characteristics of SRP and CFRP Reinforcement- A Comparative Research. Open Construction and Building Technology Journal, 2, 207-216.

Mukhtar, F. M., & Faysal, R. M. (2018). A review of test methods for studying the FRP-concrete interfacial bond behavior. Construction and Building Materials, 169, 877-887.

Mukhtar, F. M., and Faysal, R. M. (2018). A review of test methods for studying the FRP-concrete interfacial bond behavior. Construction and Building Materials, 169, 877-887.

Neubauer, U., & Rostasy, F. S. (1997). Design aspects of concrete structures strengthened with externally bonded CFRP plates. Proc., 7th Int. Conf. on Struct. Faults and Repairs, ECS Publications, Edinburgh, Scotland, 2, 109–118.

Ombres, L., Mancuso, N., Mazzucca, S., & Verre, S. (2017). Bond between carbon fabric-reinforced cementitious matrix and masonry substrate. Journal of Materials in Civil Engineering, 31(1), 1-11.

Ombres, L., Verre, S. Structural behaviour of fabric reinforced cementitious matrix (FRCM) strengthened concrete columns under eccentric loading. Compos B: Eng 2015; 75:235-249.

Pan, J., & Leung, C. K. (2007). Debonding along the FRP–concrete interface under combined pulling/peeling effects. Engineering Fracture Mechanics, 74(1-2), 132-150.

Pecce, M., Ceroni, F., Prota, A., & Manfredi, G. (2006). Response prediction of RC beams externally bonded with steel-reinforced polymers. Journal of Composites for Construction, 10(3), 195-203.

Prota, A., Manfredi, G., Nanni, A., Cosenza, E., & Pecce, M. (2004). Flexural strengthening of RC beams using emerging materials: Ultimate behavior. Proceedings of 2nd International Conference on FRP Composites in Civil Engineering, CICE 2004, Adelaide, Australia, 2004, 163-170.

Qiu, Q., & Lau, D. (2017). A novel approach for near-surface defect detection in FRP-bonded concrete systems using laser reflection and acoustic-laser techniques. Construction and Building Materials, 141, 553-564.

Raoof, S. M., Bournas, D. A. Bond between TRM versus FRP composites and concrete at high temperatures. Compos B Eng 2017; 127:150-165.

Raoof, S. M., Koutas, L. N., Bournas, D. A. Bond between textile-reinforced mortar (TRM) and concrete substrates: Experimental investigation. Compos B Eng 2016; 98:350-361.

Ren, F. F., Yang, Z. J., Chen, J. F., Chen, W. W. An analytical analysis of the full-range behaviour of grouted rockbolts based on a tri-linear bond-slip model. Constr Build Mater 2010; 24(3):361-370.

Ricci, M., Senni, L., & Burrascano, P. (2012). Exploiting pseudorandom sequences to enhance noise immunity for air-coupled ultrasonic nondestructive testing. IEEE Transactions on Instrumentation and Measurement, 61(11), 2905-2915.

Sabau, C., Gonzalez-Libreros, J. H., Sneed, L. H., Sas, G., Pellegrino, C., & Täljsten, B. (2017). Use of image correlation system to study the bond behavior of FRCM-concrete joints. Materials and Structures, 50(3), 172.

Santandrea, M. (2018). Bond behavior between fiber reinforced composites and quasi-brittle material interfaces. Dissertation. University of Bologna.

Shih, J. K. C., Tann, D. B., Hu, C. W., Delpak, R., & Andreou, E. (2003). Remote sensing of air blisters in concrete–FRP bond layer using IR thermography. International Journal of Materials and Product Technology, 19(1-2), 174-187.

Sneed, L. H., D'Antino, T., Carloni, C., & Pellegrino, C. (2015). A comparison of the bond behavior of PBO-FRCM composites determined by double-lap and single-lap shear tests. Cement and Concrete Composites, 64, 37-48.

Sneed, L.H., D'Antino, T., and Carloni, C. (2014). Investigation of bond behavior of PBO fiber-reinforced cementitious matrix-composite concrete interface. ACI Materials Journal, 111(5), 569-580.

Subramaniam, K. V., Ali-Ahmad, M., & Ghosn, M. (2008). Freeze–thaw degradation of FRP–concrete interface: impact on cohesive fracture response. Engineering Fracture Mechanics, 75(13), 3924-3940.

Taillade, F., Quiertant, M., Benzarti, K., & Aubagnac, C. (2011). Shearography and pulsed stimulated infrared thermography applied to a nondestructive evaluation of FRP strengthening systems bonded on concrete structures. Construction and Building Materials, 25(2), 568-574.

Taillade, F., Quiertant, M., Benzarti, K., Dumoulin, J., & Aubagnac, C. (2012). Nondestructive evaluation of FRP strengthening systems bonded on RC structures using pulsed stimulated infrared thermography. In Infrared thermography. IntechOpen.

Täljsten, B. Defining anchor lengths of steel and CFRP plates bonded to concrete. Int J Adhes and Adhes 1997; 17(4): 319-327.

Teng, J. G., Chen, J.F., Smith, S.T., & Lam, L. (2002). FRP-strengthened RC structures. UK: John Wiley & Sons.

Trapko, T. (2013). The effect of high temperature on the performance of CFRP and FRCM confined concrete elements. Composites Part B: Engineering, 54, 138-145.

Triantafillou, T. C., & Deskovic, N. (1991). Innovative prestressing with FRP sheets: mechanics of short-term behavior. Journal of Engineering Mechanics, 117(7), 1652-1672.

Triantafillou, T. C., & Matthys, S. (2001). Flexural strengthening with externally bonded FRP reinforcement. In Composites in Construction: A Reality (pp. 194-202).

Tuakta, C., & Büyüköztürk, O. (2011). Deterioration of FRP/concrete bond system under variable moisture conditions quantified by fracture mechanics. Composites Part B: Engineering, 42(2), 145-154.

Vaculik, J., Sturm, A. B., Visintin, P., Griffith, M. C. Modelling FRP-to-substrate joints using the bilinear bond-slip rule with allowance for friction-Full-range analytical solutions for long and short bonded lengths. Int J Solid Struct 2018; 135:245-260.

Valluzzi, M. R., Grinzato, E., Pellegrino, C., & Modena, C. (2009). IR thermography for interface analysis of FRP laminates externally bonded to RC beams. Materials and Structures, 42(1), 25-34.

Wakjira, T. G., & Ebead, U. (2018). Hybrid NSE/EB technique for shear strengthening of reinforced concrete beams using FRCM: Experimental study. Construction and Building Materials, 164, 164-177.

Wobbe, E., Silva, P., Barton, B. L., Dharani, L. R., Birman, V., Nanni, A., & Tunis, G. (2004). Flexural Capacities of RC Beams Externally Bonded with SRP and SRG. http://www.hardwirellc.com/Downloads/Flex_Capacity.pdf, 2004, 8 pp.

Wu, Y. F., & Jiang, C. (2013). Quantification of bond-slip relationship for externally bonded FRP-to-concrete joints. Journal of Composites for Construction, 17(5), 673-686.

Yazdani, N., Beneberu, E., & Riad, M. (2019). Nondestructive Evaluation of FRP-Concrete Interface Bond due to Surface Defects. Advances in Civil Engineering, 2019.

Younis, A., & Ebead, U. (2018). Bond characteristics of different FRCM systems. Construction and Building Materials, 175, 610-620.

Yuan, H., Teng, J. G., Seracino, R., Wu, Z. S., Yao, J. Full-range behavior of FRP-to-concrete bonded joints. Eng Struct 2004; 26(5):553-565.

Zhang, D., Gu, X., Yu, Q., Huang, H., Wan, B., & Jiang, C. (2018). Fully probabilistic analysis of FRP-to-concrete bonded joints considering model uncertainty. Composite Structures, 185, 786-806.

Zheng, Jian-Jun, and Jian-Guo Dai. Analytical solution for the full-range pull-out behavior of FRP ground anchors. Constr Build Mater 2014; 58:129-137.

Zhou, A., Qin, R., Feo, L., Penna, R., & Lau, D. (2017). Investigation on interfacial defect criticality of FRP-bonded concrete beams. Composites Part B: Engineering, 113, 80-90.

Zhu, H., Wu, G., Shi, J., Liu, C., & He, X. (2014). Digital image correlation measurement of the bond–slip relationship between fiber-reinforced polymer sheets and concrete substrate. Journal of Reinforced Plastics and Composites, 33(17), 1590-1603.

Zou, X., Sneed, L. H., & D'Antino, T. (2020). Full-range behavior of fiber reinforced cementitious matrix (FRCM)-concrete joints using a trilinear bond-slip relationship. Composite Structures, 112024.

Zou, X., Sneed, L. H., D'Antino, T., Carloni, C. Analytical bond-slip model for fiber reinforced cementitious matrix (FRCM)-concrete joints based on strain profile measurements. J Mater Civ Eng 2019; DOI: 10.1061/(ASCE)MT.1943-5533.0002855.

Zou, X., Sneed, L. H., D'Antino, T., Carloni, C. Application of a trilinear bond-slip model to FRCM-concrete joints. 9th Int Conf on FRP Composites in Civil Engineering-CICE 2018, Hongkong, 314-321

# VITA

Xingxing Zou was born in 1989 in a beautiful village called Red Flag, which is near Yangtze River, Hubei, China. He received his bachelor degree in Civil Engineering from Wuhan University of Science and Technology, China, in 2011. Then he enrolled in Southeast University, China, with the first class fellowship as a master student. He earned his master degree in Bridge Engineering in 2014. He started his research in the field of fiber reinforced polymer bridges, and seismic behavior of bridges. In 2016, he enrolled in Missouri University of Science and Technology as a Ph.D. student, advised by Dr. Lesley Sneed. His Ph.D. research focused on the bond behavior between advanced composite materials and concrete substrate.

Xingxing Zou published several journal papers in Elsevier {Composite Structures, Engineering Structures} journals and ASCE (Journal of Composites for Construction, Journal of Civil Engineering Materials) journals. He also delivered presentations in several academic conferences. He received his Ph.D. in Civil Engineering from Missouri University of Science and Technology in August 2020.